
JSCSEN 79(8)911–1049(2014)

ISSN 1820-7421(Online)

Journal of the Serbian Chemical Society

e
Version
electronic

VOLUME 79

No 8

BELGRADE 2014

Available on line at



www.shd.org.rs/JSCS/

The full search of JSCS

is available through

DOAJ DIRECTORY OF

OPEN ACCESS

JOURNALS

www.doaj.org



CONTENTS

Organic Chemistry

- M. Hamzehlouiean, S. Yeganegi, Y. Sarrafi, K. Alimohammadi and M. Sadatshahabi:* A theoretical investigation on the regioselectivity of the intramolecular hetero Diels–Alder and 1,3-dipolar cycloaddition reactions of 2-(vinyloxy)benzaldehyde derivatives 911

- O. Marvi, M. Giahi, P. P. Ayub and M. Nikpasand:* K-10 clay as a reusable catalyst for the solvent-free, MW-induced synthesis of enaminones (Short communication)..... 921

Biochemistry and Biotechnology

- E. Sulejmani, V. Rafajlovska and O. Guneser:* Characterization of volatiles in Beaten cheeses "Bieno sirenje" by SPME/GC-MS: Influence of geographical origin..... 927

Inorganic Chemistry

- N. Tasić, J. Rogan, D. Poleti, L. Radovanović and G. Branković:* Synthesis and characterization of μ -hydroxido- and μ -polycarboxylato-bridged iron(III) complexes with 2,2'-bipyridine 941

- S. A. Osman, H. A. Mousa, H. A. A. Yosef, T. S. Hafez, A. A. El-Sawy, M. M. Abdallah and A. S. Hassan:* Synthesis, characterization and cytotoxicity of mixed ligand Mn(II), Co(II) and Ni(II) complexes 953

Theoretical Chemistry

- L. Jiao, X. Wang, H. Li and Y. Wang:* QSPR study on the gas/particle partition coefficient of polychlorinated biphenyls using the molecular distance-edge vector index 965

Physical Chemistry

- J. Nešić, D. D. Manojlović, M. Jović, B. P. Dojčinović, P. J. Vulić, J. Krstić and G. M. Roglić:* Fenton-like oxidation of an azo dye using mesoporous Fe/TiO₂ catalysts prepared by a microwave-assisted hydrothermal process 977

Electrochemistry

- N. D. Nikolić, K. I. Popov, E. R. Ivanović and G. Branković:* Effect of the orientation of the initially formed grains on the final morphology of electrodeposited lead 993

Materials

- M. Abdollahifar, M. R. Zamani, E. Beiyyigie and H. Nekouei:* Synthesis of micro–mesopores flower-like γ -Al₂O₃ nano-architectures 1007

Environmental

- E. Levei, M. Ponta, M. Senila, M. Miclean and T. Frentiu:* Assessment of contamination and origin of metals in mining affected river sediments: a case study of the Aries River catchment, Romania 1019

- O. N. Kononova, M. A. Kuznetsova, A. M. Mel'nikov, N. S. Karplyakova and Y. S. Kononov:* Sorption recovery of copper(II) and zinc(II) from aqueous chloride solutions ... 1037

Published by the Serbian Chemical Society
Karnegijeva 4/III, P. O. Box 36, 11120 Belgrade 35, Serbia
Printed by the Faculty of Technology and Metallurgy
Karnegijeva 4, P. O. Box 35-03, 11120 Belgrade, Serbia



A theoretical investigation on the regioselectivity of the intramolecular hetero Diels–Alder and 1,3-dipolar cycloaddition reactions of 2-(vinyloxy)benzaldehyde derivatives

MAHSHID HAMZEHLOUEIAN^{1*}, SAEID YEGANEKI², YAGHOUB SARRAFI³, KAMAL ALIMOHAMMADI⁴ and MARZIEH SADAT SHAHABI³

¹Department of Chemistry, Islamic Azad University, Jouybar Branch, Jouybar 47715-195, Iran, ²Department of Physical Chemistry, Faculty of Chemistry, University of Mazandaran, Babolsar, Iran, ³Department of Organic Chemistry, Faculty of Chemistry, University of Mazandaran, Babolsar, Iran and ⁴Department of Chemistry, Dr. Ali Shariati Branch, University of Farhangian, Sari, Iran

(Received 23 January, revised 5 February, accepted 5 February 2014)

Abstract: The present paper reports a systematic computational analysis study of the two possible pathways, fused and bridged, for an intramolecular hetero Diels–Alder (IMHDA) and an intramolecular 1,3-dipolar cycloaddition (IMDCA) of 2-(vinyloxy)benzaldehyde derivatives. The potential energy surface analyses for both reactions are in agreement with the experimental observations. The activation energies associated with the two regioisomeric channels in the IMHDA reaction showed that the bridged product is favored, although in the IMDCA, the most stable transition state results in the fused product. The global electronic properties of the fragments within each molecule were studied to discuss the reactivity patterns and charge transfer direction in the intramolecular processes. The asynchronicity of the bond formation and aromaticity of the optimized TSs in the Diels–Alder reaction as well as cycloaddition reaction were evaluated. Finally, the ¹H-NMR chemical shifts of the possible regiosomers were calculated using the GIAO method, the values of which for the most stable products were in agreement with the experimental data for both reactions.

Keywords: intramolecular hetero Diels–Alder; intramolecular 1,3-dipolar cycloaddition; charge transfer; DFT calculation; fragment electrophicity analysis.

INTRODUCTION

Pericyclic reactions are of particular interest because of their broad preparative significance in the chemistry of drugs and natural products.^{1–6} Intramolecular hetero Diels–Alder reactions appeared to be a versatile strategy for the

*Corresponding author. E-mail: m.hamzehlooian@gmail.com
doi: 10.2298/JSC140121012H

formation of novel polycyclic systems, which were successfully employed in the design of skeletons for some natural products and potent anti-tumor agents.^{7–10} 1,3-Dipolar cycloaddition reactions (DCA) also provide an efficient approach for the synthesis of five-membered heterocyclic units in a highly regio- and stereo-selective manner.¹¹ Five-membered heterocycles are an important class of compounds, not only because of their natural abundance, but also for their chemical and biological importance.¹²

Steric and electronic effects are two major factors that could influence the selectivity of these reactions. Domingo *et al.*¹³ proposed that the global electrophilicity index introduced by Parr¹⁴ could be used as a reliable quantity to classify the electrophilicity of a series of dienes/dipoles (D) and dienophiles/dipolarophiles (Dp) involved in intermolecular Diels–Alder and 1,3-dipolar cycloaddition reactions within a unique relative scale. Useful information about the polarity at the transition state (TS) for a given reaction could be obtained from the difference in global electrophilicity $\Delta\omega$ of the D/Dp interacting pair. Thus, small electrophilicity differences are related to non-polar mechanisms, while large electrophilicity differences are associated with polar mechanisms.¹³ Soto-Delgado and coworkers established that these rules could be transferred to an intramolecular a Diels–Alder process by introducing electrophilicity and nucleophilicity indices of the fragment.^{15,16} These analyses indicated that electronic effects, such as charge transfer (CT) along the reaction coordinate are invariant in both inter- and intra-molecular processes.¹⁶

The global electrophilicity index, ω , which measures the stabilization energy when the system acquires an additional electronic charge, ΔN , from the environment, is given by the following simple expression:¹⁴

$$\omega = \frac{\mu^2}{2\eta} \quad (1)$$

where μ is the electronic chemical potential and η is the chemical hardness at the ground state of the molecules. This index was used to classify the dienes/dipoles and dienophiles/dipolarophiles used in Diels–Alder and 1,3-dipolar cycloaddition reactions within a unique scale of electrophilicity.¹³ Furthermore, both the electronic chemical potential and chemical hardness may be approached in terms of the one electron energies of the frontier molecular orbitals HOMO and LUMO, ε_H and ε_L , using the expressions:

$$\mu = \frac{(\varepsilon_H + \varepsilon_L)}{2} \quad (2)$$

and

$$\eta = \varepsilon_L - \varepsilon_H \quad (3)$$



On the other hand, the nucleophilicity index, N , for a given system is defined as:

$$N = \varepsilon_{\text{HOMO}} - \varepsilon_{\text{HOMO(TCE)}} \quad (4)$$

where $\varepsilon_{\text{HOMO}}$ is the HOMO energy of the nucleophile and $\varepsilon_{\text{HOMO(TCE)}}$ corresponds to the HOMO energy of tetracyanoethylene (TCE), taken as reference.¹⁷

The fragment electrophilicity and nucleophilicity indices are given as follows:

$$\omega_{(\text{fragment})} = \omega_F = \omega \sum_{k \in F} f_k^+ \quad (5)$$

and

$$N_{(\text{fragment})} = N_F = \omega \sum_{k \in F} f_k^- \quad (6)$$

where $F = D$ or Dp .^{15,16} The regional Fukui functions at the atomic center k for electrophilic (f_k^+) and nucleophilic (f_k^-) attacks can be obtained from single point calculations at the optimized structures of the ground state of the molecules.¹⁸ The direction of the electronic flux within an IMHDA and IMDCA reagent may be determined by introducing the following dual indices:

$$EI = \omega_{Dp} + N_D \quad (7)$$

and

$$E2 = \omega_D + N_{Dp} \quad (8)$$

Accordingly, the charge transfer (CT) can be estimated from the relative values of EI and $E2$. The process will be characterized by a Dp to D electronic flux if $EI < E2$, whereas the electronic flux occurs from D to Dp if $EI > E2$. The charge transfer along the reaction coordinates can be elucidated by the regional electrophilicity:¹⁷

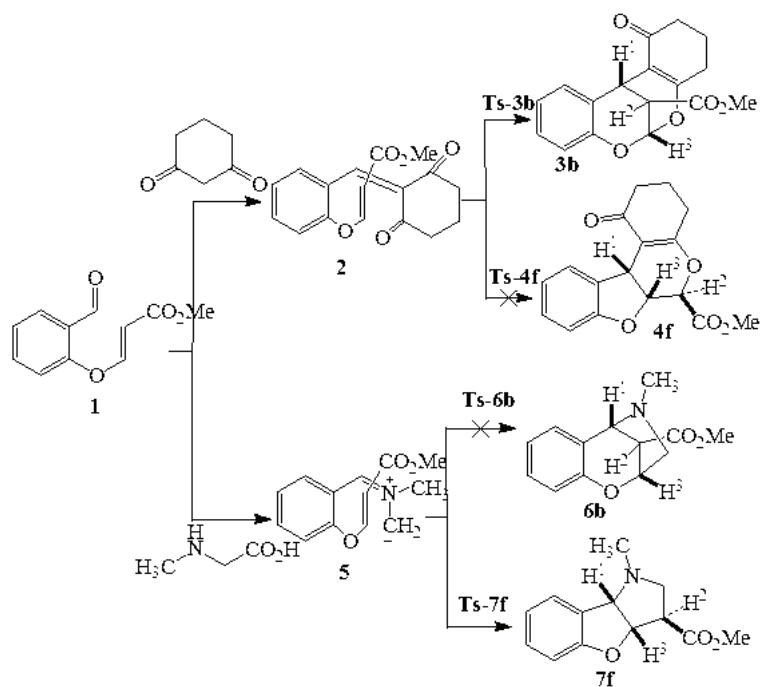
$$\alpha_\Omega = \frac{\mu_\Omega^2}{2\eta_\Omega} \quad (9)$$

where Ω is A or B.

In the past decades, in addition to the selectivity behavior, the understanding of the underlying principles in pericyclic reactions has grown from a fruitful interplay between theory and experiment and continues to present a real challenge.¹⁹ Recently, Kim *et al.* reported the synthesis of benzo-fused 2,8-dioxabicyclo[3.3.1]nonane (**3**) utilizing a domino Knoevenagel condensation hetero Diels–Alder reaction of 2-(vinyloxy)benzaldehyde (**1**).²⁰ Then, it was expected that the 1,3-dipole (**5**), generated from **1** with sarcosine, would react with the neighboring double bond to give a structurally novel bicyclo[3.2.1]octane ring system (**6b**), Scheme 1.²¹ However, contrary to anticipation, a linearly fused tricyclic



compound **7f** was obtained as the major product instead (Scheme 1). In the present work, as a part of an ongoing theoretical and experimental research program on 1,3-dipolar cycloaddition reactions,²² a theoretical study on the observed difference in regioselectivity of the above reactions was performed, in order to achieve a deeper insight to IMHDA and IMDCA.



Scheme 1. Possible reaction channels for the IMHDA and the IMDCA reactions of 2-(vinyloxy)benzaldehyde derivatives.

COMPUTATIONAL DETAILS

All calculations were performed using Gaussian09²³ suite of programs. The full geometrical optimization of all structures and transition states (TSs) was realized with the Density Functional Theory (DFT) using non-local B3LYP hybrid functional and the 6-31G(d,p) basis set. The nature of stationary geometries was characterized by calculating the frequencies in order to verify that the transition states have only one imaginary frequency with the corresponding eigenvector involving the formation of the newly created C–C bonds.

RESULT AND DISCUSSION

Energies of transition state structures

The intramolecular hetero Diels–Alder and intramolecular 1,3-dipolar cycloaddition reactions are kinetically controlled reactions with early transition states.²⁴ Theoretical calculations are the only way to study these TSs. For each of

the IMHDA and IMDCA reactions, two regiochemical channels, namely, the fused (**TS-f**) and the bridged (**TS-b**) modes, were studied. The optimized transition structures are shown in Figs. 1 and 2. The activation energies, enthalpies and Gibbs free energies as well as energies, enthalpies, Gibbs free energies of the reactions are reported in Table I.

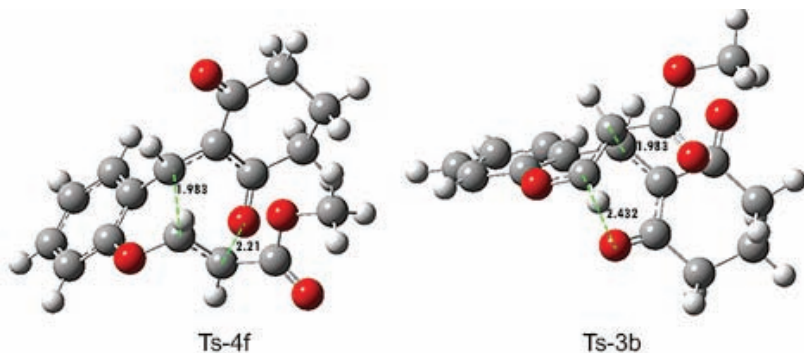


Fig. 1. Optimized structures of the transition states for the IMHDA reaction at B3lyp/6-31G(d,p) level. The lengths of the bonds directly involved in the reactions are given in angstroms.

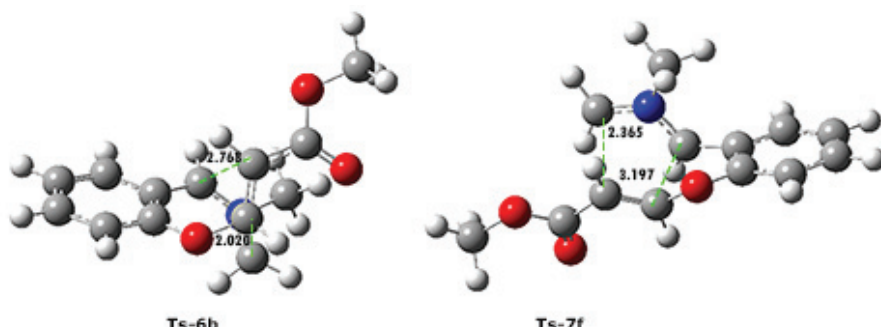


Fig. 2. Optimized structures of transition states for the IMDCA reaction at B3lyp/6-31G(d,p) level. The lengths of the bond directly involved in the reactions are given in angstroms.

TABLE I. Calculated electronic activation energies E_a , reaction Gibbs free energies ΔG , reaction enthalpies ΔH , reaction energies ΔE_{rxn} , activation Gibbs free energies $\Delta G^\#$, activation enthalpies $\Delta H^\#$ (all energies are in kcal mol⁻¹; 1 kcal = 4.184 kJ), charge transfers CT and nucleus-independent chemical shifts $NICS$

Structure	E_a	$\Delta G^\#$	$\Delta H^\#$	ΔE_{rxn}	ΔG	ΔH	CT a.u.	$NICS$ ppm mol ⁻¹
Ts-3b	20.33	1.03	0.84	-20.39	-21.84	-16.94	0.08 ^a	-11.79
Ts-4f	31.61	1.51	1.32	-12.11	-13.49	-8.91	0.32 ^b	-10.10
Ts-7f	2.87	0.19	0.10	-48.38	-49.95	-46.00	0.03 ^a	-13.94
Ts-6b	5.06	0.27	0.17	-42.61	-44.17	-40.16	0.16 ^a	-12.17

^aFrom D to Dp; ^bfrom Dp to D

The computed activation energies associated with the two regioisomeric channels for the IMHDA reaction of **2** are 31.61 (**TS-4f**) and 20.33 (**TS-3b**) kcal mol⁻¹. Therefore, the bridge mode **3b** is favored over the fused one by 11.28 kcal mol⁻¹. The activation barriers associated with the IMDCA reaction of **5** are 2.87 (**TS-7f**) and 5.06 (**Ts-6b**) kcal mol⁻¹. Accordingly, it could be predicted that the regioisomer **7f** would be formed preferentially. These results are in agreement with the experimental findings that for the IMHDA reaction of compound **2**, the bridged product **3b** is the major product²⁰ but for the IMDCA reaction of **5**, the fused product **7f** is favored.²¹

In order to calculate the charge transfer and reactivity indices for an intramolecular reaction, it is necessary to consider a molecule as two fragments: diene (D) and dienophile (Dp) for IMHDA and dipole (D) and dipolarophile (Dp) for IMDCA. The embedded fragments in **2** and **5** are shown in Fig. 3. For the IMHDA reaction, the calculated *CTs* present diene–dienophile fragments electron flux in **TS-3b**, while a reversed flux was predicted for **TS-4f**. However, the calculated *CTs* in both TS of IMDCA are from dipole to dipolarophile fragments.

The extent of the asynchronicity of the bond formation in a Diels–Alder or cycloaddition reaction can be measured through the difference between the lengths of the two σ bonds that are being formed in the reaction. The computed ΔR_s are 0.368, 0.227, 0.832 and 0.748 Å for **TS-3b**, **TS-4f**, **TS-7f** and **TS-6b**, respectively. This data indicates that the TSs associated with the more favorable stereoisomeric channels (**TS-3b** and **TS-7f**) have more asynchronous character than those associated with the other channels.

In order to evaluate the aromaticity of the optimized TSs, the nucleus-independent chemical shifts (*NICS*)²⁵ at the center of the forming ring were computed using the gauge invariant atomic orbital (GIAO)²⁶ approach at the B3LYP/6-31G(d,p) level. The calculated *NICS* values are presented in Table I. All of the transition structures in Table I have large negative *NICS* values, which indicate the aromatic characters of TSs due to the six electrons undergoing bond change.

Reactivity indices analysis for the IMHDA and IMDCA reactions

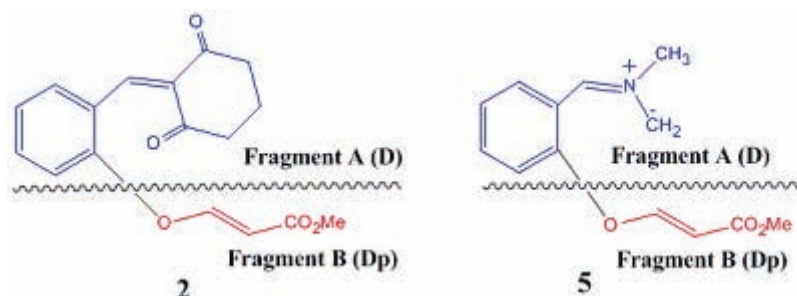
The computed electronic chemical potentials μ , chemical hardness η , global electrophilicities ω and nucleophilicities N of **2** and **5** are given in Table II. The global electrophilicity indices of **2** and **5** are 2.49 and 0.97 eV and their nucleophilicities are 2.72 and 4.86 eV, respectively. Compound **2** is classified as a strong electrophile and two compounds are described as excellent nucleophiles.

Frontier molecular orbital (FMO) analysis cannot be applied for IMHDA and IMDCA reactions when the HOMO and LUMO orbitals of the D and Dp fragments belong to a molecule. Thus, the electrophilicity and nucleophilicity indices of fragments were employed to analyze the polar interactions in the IMHDA and IMDCA reactions. The two considered fragments in compounds **2** and **5** are shown

in Fig. 3 and their computed electrophilicity and nucleophilicity indices are given in Table III. For compounds **2**, $E1 = 2.99$ and $E2 = 2.84$ (Eqs. (7) and (8)) and for **5**, $E1 = 5.13$ and $E2 = 1.28$. The larger $E1$ for both compounds indicates that CT will occur from D to Dp (Table I). The analysis of the fragment electrophilicity and nucleophilicity indices is in agreement with the estimated *CTs* for both TSs (**TS-7f** and **TS-6b**) of the IMDCA reaction (D to Dp). However for the IMHDA reaction, the analysis of fragment indices only agree with the direction of estimated charge transfer for the most stable TS (**TS-3b**) (Table I).

TABLE II. Global properties of **2** and **5**

Structure	μ / a.u	η / a.u	ω / eV	N / eV
2	-0.1641	0.1423	2.49	2.72
5	-0.0941	0.1246	0.97	4.86

Figure 3. The diene (D)/dienophile (Dp) and dipole (D)/dipolarophile (Dp) fragments in compounds **2** and **5**.

For compounds **2** and **5**, the values of the ω_Ω index of the D fragments are 2.95 and 1.08 eV, and the values of the Dp fragments are 0.27 and 0.25 eV, respectively. The fragment electrophilicity difference $\Delta\omega_\Omega = |\omega_B - \omega_A|$ was used to estimate the CT at the TSs associated with the IMHDA/IMDCA reactions. The IMHDA processes involving **2** are expected to follow a polar mechanism with significant CT at the TS, $\Delta\omega_\Omega > 1.50$, while the IMDCA reaction in compound **5** is predicted to undergo a polar mechanism with marginal CT at the TS, $0.5 < \Delta\omega_\Omega < 1.50$.

TABLE III. Local electronic properties (in eV) of the embedded fragments of **2** and **5**

Structure	ω_D	N_D	ω_{Dp}	N_{Dp}	$\omega_{(\Omega=A)}$	$\omega_{(\Omega=B)}$	$\Delta\omega_\Omega = \omega_B - \omega_A $
2	2.81	2.90	0.10	0.03	2.95	0.27	2.85
5	1.13	5.01	0.12	0.15	1.08	0.25	0.83

NMR chemical shifts

Owing to similar splitting pattern for the two regioisomers of these reactions, evaluation between the experimental data and calculated chemical shifts of pos-

sible regioisomers could be useful. Thus, the $^1\text{H-NMR}$ chemical shifts of regioisomers were calculated using the GIAO method and the results (values in ppm) are summarized in Table IV. The theoretical values of H-1, H-2 and H-3 of compound **3** for IMHDA reaction and compound **7** for IMDCA reaction are closer to the experimental values, as can be seen in Table IV. Therefore, the estimated chemical shift values of the more stable regioisomers **3** and **7** correspond well with the experimental data.

TABLE IV. Comparison of the theoretical $^1\text{H-NMR}$ chemical shifts data (δ / ppm) of H-1, H-2 and H-3 of each pair of regioisomers with those obtained from the experimental spectroscopy

Atom number	IMHDA			IMDCA		
	3	4	Experimental ²⁰	6	7	Experimental ²¹
H-1	4.7	4.3	4.54	4.0	4.9	4.59
H-2	2.8	2.1	3.12	2.9	3.0	3.52
H-3	6.4	5.6	6.30	5.1	6.0	5.67

CONCLUSIONS

A systematic theoretical study on the regioselectivity in the intramolecular hetero Diels–Alder (IMHDA) and intramolecular 1,3-dipolar cycloaddition reactions (IMDCA) of 2-(vinyloxy)benzaldehyde derivatives using DFT method was conducted. A potential energy surface analysis in the IMHDA and IMDCA reactions demonstrated that the preferred products would be bridged and fused, respectively, in agreement with experimental observations. The charge transfer direction in these intramolecular processes was studied in terms of the global electronic properties of fragments within each molecule.

Acknowledgment. The authors acknowledge the University of Jouybar for financial support of this research.

ИЗВОД

ТЕОРИЈСКО ИСПИТИВАЊЕ РЕГИОСЕЛЕКТИВНОСТИ ИНТРАМОЛЕКУЛСКЕ DIELS–ALDER И 1,3-ДИПОЛАРНЕ ЦИКЛОАДИЦИЈЕ ДЕРИВАТА 2-(ВИНИЛОКСИ)БЕНЗАЛДЕХИДА

MAHSHID HAMZEHLOUEIAN¹, SAEID YEGANEGI², YAGHOUB SARRAFI³, KAMAL ALIMOHAMMADI⁴
И MARZIEH SADATSHAHABI³

¹Department of Chemistry, Islamic Azad University, Jouybar Branch, Jouybar, Iran, ²Department of Physical Chemistry, University of Mazandaran, Babolsar, Iran, ³Department of Organic Chemistry, University of Mazandaran, Babolsar, Iran и ⁴Department of Chemistry, Dr. Ali Shariati Branch, University of Farhangian, Sari, Iran

Извршена је систематска компјутерска анализа двају могућих реакционих путева интрамолекулске хетеро Diels–Alder (IMHDA) и интрамолекулске 1,3-диполарне циклоадиције (IMDCA) деривата 2-(венилокси)бензалдехида. Анализа површине потенцијалне енергије за обе реакције је у сагласју с експерименталним опажањима. Енергије активације за два посматрана механизма показују да у IMHDA реакцији фаворизован



премошћени продукт, док у IMDCA је то кондензовани продукт. Проучене су глобалне електронске особине фрагмената, и дискутована реактивност и правац преноса наелектрисања у интрамолекулским процесима. Одређени су асинхроницитет грађења веза и ароматичност у оптимизованим прелазним стањима истраживаних реакција. Израчуната су $^1\text{H-NMR}$ хемијска померања насталих региоизомера и нађена да су у складу са експерименталним подацима.

(Примљено 21. јануара, ревидирано и прихваћено 5. фебруара 2014)

REFERENCES

1. K. N. Houk, Y. Li, J. D. Evanseck, *Angew. Chem. Int. Ed.* **31** (1992) 682
2. J. March, *Advanced Organic Chemistry*, Wiley, New York, 1992
3. R. B. Woodward, R. Hoffmann, *Angew. Chem. Int. Ed.* **8** (1969) 781
4. H. E. Zimmerman, *Acc. Chem. Res.* **4** (1971) 272
5. M. J. S. Dewar, *Angew. Chem. Int. Ed.* **10** (1971) 761
6. K. Fukui, *Acc. Chem. Res.* **4** (1971) 57; G. Desimoni, G. Tacconi, A. Barco, G. P. Pollini, *Natural product synthesis through pericyclic reactions*, in *ACS monograph*, Vol. 180, American Chemical Society, Washington DC, 1983
7. A. G. Fallis, *Acc. Chem. Res.* **32** (1999) 464
8. D. Craig, *Chem. Soc. Rev.* **16** (1987) 187
9. A. G. Fallis, *Pure Appl. Chem.* **69** (1997) 495
10. J. R. Bull, R. Gordon, R. Hunter, *J. Chem. Soc., Perkin Trans. I* (2000) 3129
11. J. W. Lown, in *1,3-Dipolar Cycloaddition Chemistry*, Vol. 1, A. Padwa, Ed., Wiley, New York, 1984, pp. 653–732; W. Carruthers, *Cycloaddition Reactions in Organic Synthesis*, Pergamon Press, Elmsford, New York, 1990; *Synthetic Applications of 1,3-Dipolar Cycloaddition Chemistry toward Heterocycles and Natural Products*, A. Padwa, W. H. Pearson, Eds., Wiley, New York, 2002
12. O. Tsuge, S. Kanemasa, in *Advances in Heterocyclic Chemistry*; A. R. Katritzky, Ed., Academic Press, San Diego, CA, 1989, Vol. 45, pp. 231–349
13. L. R. Domingo, M. J. Aurell, P. Pérez, R. Contreras, *Tetrahedron* **58** (2002) 4417; P. Pérez, L. R. Domingo, M. J. Aurell, R. Contreras, *Tetrahedron* **39** (2003) 3117
14. P. G. Parr, L. von Szentpaly, S. Liu, *J. Am. Chem. Soc.* **121** (1999) 1922
15. J. Soto-Delgado, L. R. Domingo, R. Contreras, *Org. Biomol. Chem.* **8** (2010) 3678
16. J. Soto-Delgado, A. Aizman, L. R. Domingo, R. Contreras, *Chem. Phys. Lett.* **499** (2010) 272
17. L. R. Domingo, E. Chamorro, P. Pérez, *J. Org. Chem.* **73** (2008) 4615
18. R. Contreras, P. Fuentealba, M. Galván, P. Pérez, *Chem. Phys. Lett.* **304** (1999) 405; M. C. Rezende, *J. Braz. Chem. Soc.* **12** (2001) 73
19. G. Bentabed-Ababsa, A. Derdour, T. Roisnel, J. A. Saez, P. Perez, E. Chamorro, L. R. Domingo, F. Mongin, *J. Org. Chem.* **74** (2009) 2120; A. K. Nacereddine, W. Yahia, S. Bouacha, A. Djerourou, *Tetrahedron Lett.* **51** (2010) 2617; W. Benchouk, S. M. Mekelleche, M. J. Aurell, L. R. Domingo, *Tetrahedron* **65** (2009) 4644; M. Bakavoli, F. Moeinpour, A. Davoodnia, A. Morsali, *J. Mol. Struct.: THEOCHEM* **969** (2010) 139; P. Merino, J. Revuelta, T. Tejero, U. Chiacchio, A. Rescifinab, G. Romeoc, *Tetrahedron* **59** (2003) 3581; S. Špirtović-Halilović, M. Salihović, H. Džudžević-Čančar, S. Trifunović, S. Roca, D. Softić, D. Završnik, *J. Serb. Chem. Soc.* **78** (2013) 1
20. I. Kim, H.-K. Kim, S. G. Choi, G. H. Lee, *Tetrahedron* **64** (2008) 664
21. I. Kim, H.-K. Na, K. R. Kim, S. G. Kim, G. H. Lee, *Synlett* **13** (2008) 2069



22. Y. Sarrafi, M. Sadatshahabi, M. Hamzehloueian, K. Alimohammadi, M. Tajbakhsh, *Synthesis* **45** (2013) 2294; K. Alimohammadi, Y. Sarrafi, M. Tajbakhsh, S. Yeganegi, M. Hamzehloueian, *Tetrahedron* **67** (2011) 1589; Y. Sarrafi, M. Hamzehlouian, K. Alimohammadi, H. R. Khavasi, *Tetrahedron Lett.* **51** (2010) 4734; Y. Sarrafi, M. Hamzehloueian, K. Alimohammadi, S. Yeganegi, *J. Mol. Struct.* **1030** (2012) 168.
23. Gaussian 09, Revision A.1Gaussian, Inc., Wallingford, CT, 2009
24. W. R. Roush, S. E. Hall, *J. Am. Chem. Soc.* **103** (1981) 5200; F. K. Brown, K. N. Houk, *Tetrahedron Lett.* **26** (1985) 2297
25. P. V. R. Schleyer, C. Maerker, A. Dransfeld, H. Jiao, N. J. R. V. E. Hommes, *J. Am. Chem. Soc.* **118** (1996) 6317
26. K. Wolinski, J. F. Hilton, P. Pulay, *J. Am. Chem. Soc.* **112** (1990) 8251.



SHORT COMMUNICATION

**K-10 clay as a reusable catalyst for the solvent-free,
MW-induced synthesis of enaminones**

OMID MARVI^{1*}, MASOUD GIAHI², POURAN PUR AYUB¹
and MOHAMMAD NIKPASAND³

¹Department of Chemistry, Faculty of Science, Payam Noor University (PNU), P. O. Box 19395-3697, Tehran, Iran, ²Department of Chemistry, Faculty of Science, Islamic Azad University, Lahijan Branch, Lahijan, Iran and ³Department of Chemistry, Rasht Branch, Islamic Azad University, Rasht, Iran

(Received 26 January, revised 14 May, accepted 3 June 2014)

Abstract: A series of β -amino- α,β -unsaturated ketones and esters were synthesized in good to excellent yields from the reaction of different amines with 1,3-dicarbonyl compounds in solvent-free media using montmorillonite K-10 clay as a solid recyclable heterogeneous acidic catalyst and microwave irradiation.

Keywords: montmorillonite K-10 clay; β -amino- α,β -unsaturated esters and ketones; solvent-free; microwave.

INTRODUCTION

β -Amino- α,β -unsaturated esters and ketones are useful synthetic intermediates,¹ particularly in the construction of heterocyclic compounds such as dihydropyridines,^{2–5} pyridines,⁶ pyrimidines,⁷ indoles,⁸ isothiazoles,⁹ oxazolidinones, pyrrole and α -amino- β -lactams.^{10–13} A number of reviews have been published concerning the chemistry of β -amino- α,β -unsaturated esters and ketones, their hydrolysis, physicochemical properties and uses.¹⁴ The standard methods for the preparation of β -enamino ketones involve the direct condensation of amines and diketones using a stream of gaseous amine, ammonium acetate and reflux in aromatic solvent with azeotropic removal of the water¹⁵ or the reaction of a lithiated Schiff's base from imines with esters.¹⁶ Consequently, the development of more efficient methods and exploring proper reagents as catalysts are still in demand to make the available procedures more convenient and simple.

Application of naturally benign substances like montmorillonite clays as catalysts for chemical reactions constitutes an exciting component of green

*Corresponding author. E-mail: omid_marvi@pnu.ac.ir
doi: 10.2298/JSC140112061M

chemistry. The use of K-10 clay as solid support has become very useful in synthetic organic chemistry because of its enhanced selectivity due to its lamellar swelling structure, large surface area, the availability of both Brønsted and Lewis surface acidic sites, milder reaction conditions and ease of workup.¹⁷ The combined use of montmorillonite and microwave irradiation (MWI) showed rate enhancements, high yields and short reaction times. In addition, the use of solvent-free conditions with heterogeneous media under microwave irradiation is a useful alternative and has received considerable attention due to its greater efficiency from economic as well as ecological points of view.¹⁸

In continuation of ongoing investigations exploring the use of montmorillonite as a solid support in the synthesis and reactivity of organic compounds using microwave irradiation,¹⁹ this paper reports a simple, selective and environmentally acceptable microwave promoted synthesis of β -amino- α,β -unsaturated esters and ketones using montmorillonite K-10 clay as an efficient heterogeneous acid catalyst.

RESULTS AND DISCUSSION

As shown in Table I, a variety of β -amino- α,β -unsaturated esters and ketones were obtained using this procedure and no by-products were observed. In general, for a wide variety of amines, the condensation reactions usually afforded the corresponding β -amino- α,β -unsaturated esters and ketones in over 90 % yields in a short reaction time (Scheme 1). The presence of an electron-withdrawing group on the benzene ring decreased the reactivity of the substrate (entry 14). The solid clay portion applied in the first cycle was washed with methanol and dried at 120 °C under reduced pressure to be reused in the subsequent reactions, which showed a gradual decrease in the activity (Table I).

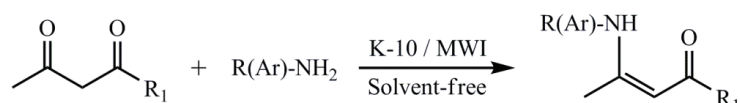
TABLE I. K-10 clay supported microwave-induced synthesis of β -amino- α,β -unsaturated esters and ketones

Entry	Dicarbonyl Compound	Amine	Product ^a	Yield, % ^b	Time, min
1				96 (92)	2
2				98 (91)	2.5
3				95 (89)	3
4				96 (92)	2.5

TABLE I. Continued

Entry	Dicarbonyl Compound	Amine	Product ^a	Yield, % ^b	Time, min
5		CH ₃ NH ₂		96 (90)	2.5
6				98 (95)	2
7				95 (91)	2.5
8				94 (90)	2.5
9				92 (87)	2.5
10		CH ₃ NH ₂		94 (90)	2.5
11				95 (92)	2
12				97 (92)	3
13				95 (88)	3
14				87 (82)	3.5
15				92 (88)	2.5

^aAll products were identified by comparison of their physical and spectral data with those of authentic samples;²⁰ ^bisolated yields. Yields indicated in the parenthesis correspond to those reactions in which recovered K-10 clay was used. The fresh solid clay portion applied in the first cycle, was filtered off, washed with methanol (2×30 mL) and dried at 120 °C under reduced pressure to be reused in the subsequent reaction.



R₁: OEt, OMe, Me

Scheme 1. Synthesis of β -amino- α,β -unsaturated esters and ketones on K-10 clay under MWI.

EXPERIMENTAL

General

Melting points were determined on an Electrothermal 9100 apparatus. The ^1H -NMR and ^{13}C -NMR spectra were recorded on a FT-NMR BRUKER DRX 500 Avance spectrometer. Chemical shifts were measured in ppm from TMS. CDCl_3 was used as the solvent as well as the internal standard. The IR spectra were recorded on a Perkin-Elmer FT-IR GX instrument in KBr discs. Physical and spectral data of the synthesized compounds are given in the Supplementary material to this paper.

Microwave irradiations were realized with a Synthewave 402[®] (Prolabo, France) single mode focused microwave reactor.²¹ The chemicals used in this work were purchased from Merck and Fluka.

Typical procedure

In a typical experiment (entry **11**), acetylacetone (3 mmol) and aniline (5 mmol) were dispersed on K-10 clay (1 g). The heterogeneous mixture was submitted into a single mode focused microwave reactor with continuous rotation for 3 min (optimized time) at 40 °C. The product was extracted by washing the K-10 clay with ethyl acetate. The organic layer was washed with water, dried with MgSO_4 , filtered and the solvent was removed under vacuum to afford the relevant β -amino- α,β -unsaturated ketone **11**.

CONCLUSIONS

In conclusion, the supported reaction using K-10 clay and MWI provides a general procedure for a highly selective method for the synthesis of β -amino- α,β -unsaturated esters and ketones. The major advantages of this methodology are mild reaction conditions and faster reaction rates. The K-10 clay catalyst is inexpensive, non-toxic and reusable, which makes the process convenient, more economic and benign. The notable features of this procedure are the solvent-free conditions, high yields of products, cleaner reaction profiles, and availability of the reagents.

SUPPLEMENTARY MATERIAL

Physical and spectral data of the synthesized compounds are available electronically at <http://www.shd.org.rs/JSCS/>, or from the corresponding author on request.

Acknowledgment. Financial support from Payam Noor University (PNU), Roodsar, Guilan, Iran is gratefully appreciated.

И З В О Д

ГЛИНА К-10 КАО КАТАЛИЗАТОР СА ВИШЕКРАТНОМ УПОТРЕБОМ ЗА СИНТЕЗУ
ЕНАМИНОНА ПОД УСЛОВИМА ГРЕЈАЊА МИКРОТАЛАСИМА У ОДСУСТВУ
РАСТВАРАЧА

OMID MARVI¹, MASOUD GIAHI², POURAN PUR AYUB¹ и MOHAMMAD NIKPASAND³

¹Department of Chemistry, Faculty of Science, Payam Noor University (PNU), P. O. Box 19395-3697, Tehran, Iran, ²Department of Chemistry, Faculty of Science, Islamic Azad University, Lahijan Branch, Lahijan, Iran и ³Department of Chemistry, Rasht Branch, Islamic Azad University, Rasht, Iran

Извршена је синтеза серије β -амино- α,β -незасићених кетона и естара реакцијом различитих амина и 1,3-дикарбонилних једињења, у одсуству растварача, коришћењем

мономоријонит К-10 глине, као чврстог катализатора са вишекратном употребом, под условима загревања реакционе смеше микроталасима. Производи су добијени у добром до одличном приносу.

(Примљено 26. јануара, ревидирано 14 маја, прихваћено 3. јуна 2014)

REFERENCES

1. J. V. Greenhill, *Chem. Soc. Rev.* **6** (1977) 277
2. H. H. Fox, J. I. Lewis, W. J. Wenner, *Chem. Soc.* (1951) 1259
3. J. E. Arrowsmith, S. F. Campbell, P. E. Cross, J. K. Stubbs, R. A. Burges, *J. Med. Chem.* **29** (1986) 1696
4. D. Alker, S. F. Campbell, P. E. Cross, R. A. Burges, A. J. Carter, *J. Med. Chem.* **33** (1990) 1805
5. K. Miyashita, M. Nishimoto, T. Ishino, H. Murafuji, S. Obika, O. Muraoka, T. Imanishi, *Tetrahedron* **53** (1997) 4279
6. G. Horlein, B. Kubel, A. Studeneer, G. Salbeck, *Liebigs Ann. Chem.* (1979) 371
7. K. Grohe, H. Heitzer, *Liebigs Ann. Chem.* (1973) 1025
8. D. Raileaunu, M. Palaghita, C. D. Nenitzescu, *Tetrahedron* **27** (1971) 5031
9. R. K. Howe, T. A. Grumer, L. G. Garter, J. E. Frans, *J. Heterocycl. Chem.* **15** (1978) 1001
10. C. M. Kascheres, *J. Braz. Chem. Soc.* **14** (2003) 945
11. G. Negri, C. Kascheres, A. J. Kascheres, *J. Heterocycl. Chem.* **41** (2004) 461
12. H. M. C. Ferraz, F. L. C. Pereira, *Quim. Nova* **27** (2004) 89
13. H. K. Hombrecher, G. Horts, *Synthesis* (1990) 389
14. a) A.-Z. A. Elassar, A. A. El-Khair, *Tetrahedron* **59** (2003) 8463; b) J. P. Michael, C. B. De Koning, D. Gravestock, G. D. Hosken, A. S. Howard, C. M. Jungmann, R. W. M. Krause, A. S. Parsons, S. C. Pelly, T. V. Stanbury, *Pure Appl. Chem.* **71** (1999) 979; c) T. Ueda, H. Konishi, K. Manabe, *Tetrahedron Lett.* **53** (2012) 5171; d) J. Sun, L.-L. Zhang, C.-G. Yan, *Tetrahedron* **69** (2013) 5451; e) M. Youness El Kadiri, E. Framery, B. Andrioletti, *Tetrahedron Lett.* **53** (2012) 6335; f) T. Muraoka, E. Hiraiwa, M. Abe, K. Ueno, *Tetrahedron Lett.* **54** (2013) 4309
15. P. G. Baraldi, D. Simoni, S. Manfredini, *Synthesis* (1983) 902
16. a) G. Bartoli, C. Cimarelli, G. Palmieri, M. Bosco, R. Dalpozzo, *Synthesis* (1990) 895; b) C. J. Valduga, A. Squizani, H. S. Braibante, M. E. F. Braibante, *Synthesis* (1998) 1019
17. a) P. Lasszlo, *Science*, **235** (1987) 1473; b) B. Baghernejad, *Lett. Org. Chem.* **7** (2010) 255; c) S. Agarwal, J. N. Ganguli, *J. Mol. Catal. A: Chem.* **372** (2013) 44; d) N. Kaur, D. Kishore, *J. Chem. Pharm. Res.* **4** (2012) 991; e) M. R. Dintzner, *Synlett* **24** (2013) 1091; f) G. Baishya, B. Sarmah, N. Hazarika, *Synlett* **24** (2013) 1137; g) M. V. Reddy, G. C. S. Reddy, Y. T. Jeong, *Tetrahedron* **68** (2012) 6820; h) K. C. Majumdar, S. Ponra, T. Ghosh, *Synthesis* **44** (2012) 2079; i) W. Chen, M.-X. Zhang, C. Li, Y.-L. Li, *J. Serb. Chem. Soc.* **78** (2013) 537
18. a) P. Lidström, J. Tierney, B. Wathey, J. Westman, *Tetrahedron* **57** (2001) 9225; b) M. E. F. Braibante, H. T. S. Braibante, A. F. Morel, C. C. Costa, M. G. Lima, *J. Braz. Chem. Soc.* **17** (2006) 184; c) *Microwave-Assisted Organic Synthesis*, P. Lidstrom, J. P. Tierney, Eds., Blackwell, Oxford, 2005; d) *Microwave Methods in Organic Synthesis*, M. Larhed, K. Olofsson, Eds., Springer, Berlin, 2006; e) D. Dallinger, C. O. Kappe, *Chem. Rev.* **107** (2007) 2563; f) P. Belov, V. L. Campanella, A. W. Smith, R. Priefer, *Tetrahedron Lett.* **52** (2011) 2776

19. a) D. Habibi, O. Marvi, *Can. J. Chem.* **85** (2007) 81; b) D. Habibi, O. Marvi, *Catal. Commun.* **8** (2007) 127; c) D. Habibi, O. Marvi, *Arkivoc* (2006) 8; d) D. Habibi, O. Marvi, *J. Serb. Chem. Soc.* **70** (2005) 579; e) D. Habibi, O. Marvi, *Chin. J. Chem.* **26** (2008) 522; f) O. Marvi, M. Nikpasand, *Lett. Org. Chem.* **10** (2013) 353
20. a) Y. Gao, Q. Zhang, J. Xu, *Synth. Commun.* **34** (2004) 909; b) M. E. F. Braibante, H. S. Braibante, L. Missio, A. Andricopulo, *Synthesis* (1994) 898; c) Z.-H. Zhang, Z.-C. Ma, L.-P. Mo, *Indian J. Chem., B* **46** (2007) 535
21. a) Prolabo, Fr. Pat. 62241/D, 14669 FR, December 23th 1991; b) R. Commarmot, R. Didenot, Gardais, JF Rhône-Poulenc/Prolabo Patent No. 84/03496 – October 27th 1986.



SUPPLEMENTARY MATERIAL TO
**K-10 clay as a reusable catalyst for the solvent-free,
MW-induced synthesis of enaminones**

OMID MARVI^{1*}, MASOUD GIAHI², POURAN PUR AYUB¹
and MOHAMMAD NIKPASAND³

¹Department of Chemistry, Faculty of Science, Payam Noor University (PNU), P. O. Box 19395-3697, Tehran, Iran, ²Department of Chemistry, Faculty of Science, Islamic Azad University, Lahijan Branch, Lahijan, Iran and ³Department of Chemistry, Rasht Branch, Islamic Azad University, Rasht, Iran

J. Serb. Chem. Soc. 79 (8) (2014) 921–926

PHYSICAL AND SPECTRAL DATA FOR THE SYNTHESIZED ENAMINONES

3-Phenylamino-but-2-enoic acid ethyl ester (1). Oil, IR (neat, cm⁻¹): 3429, 3018, 2959, 1630, 1508, 1293, 1128, 1085, 921, 796; ¹H-NMR (500 MHz, CDCl₃, δ / ppm): 1.22 (3H, t, J = 7.3 Hz), 1.92 (3H, s), 4.12 (2H, q, J = 7.3 Hz), 4.61 (1H, s), 6.68–7.35 (5H, m, aromatic), 11.38 (1H, s, NH); ¹³C-NMR (125 MHz, CDCl₃, δ / ppm): 15.8 (CH₂CH₃), 18.7 (CH₃), 57.6 (CH₂), 92.7 (=CH), 123.9 (CH), 125.3 (CH), 128.4 (CH), 138.8 (qC), 158.0 (N=C=), 189.2 (O=C).

3-Benzylamino-but-2-enoic acid ethyl ester (2). Oil, IR (neat, cm⁻¹): 3292, 3074, 2951, 1655, 1608, 1512, 1229, 1173, 1151, 1068, 928, 756; ¹H-NMR (500 MHz, CDCl₃, δ / ppm): 1.20 (3H, t, J = 7.3 Hz), 1.89 (3H, s), 4.15 (2H, q, J = 7.3 Hz), 4.33 (2H, d, J = 6.4 Hz), 4.54 (1H, s), 7.08–7.29 (5H, m, aromatic), 11.21 (1H, s, NH); ¹³C-NMR (125 MHz, CDCl₃, δ / ppm): 14.2 (CH₂CH₃), 18.6 (CH₃), 46.3 (PhCH₂), 57.6 (CH₂), 82.8 (=CH), 126.2 (CH), 126.4 (CH), 128.4 (CH), 138.4 (qC), 161.5 (N=C=), 171.2 (O=C).

3-(1-Phenylethanamino)-but-2-enoic acid ethyl ester (3). Oil, IR (neat, cm⁻¹): 3298, 3019, 2996, 1686, 1616, 1541, 1229, 1182, 1163, 1055, 980, 745; ¹H-NMR (500 MHz, CDCl₃, δ / ppm): 1.27 (3H, s), 1.32 (3H, t, J = 7.3 Hz), 2.04 (3H, d, J = 4.7 Hz), 4.09 (1H, m), 4.29 (2H, q, J = 7.3 Hz), 4.68 (1H, s), 7.15–7.41 (5H, m, aromatic), 11.06 (1H, s, NH); ¹³C-NMR (125 MHz, CDCl₃, δ / ppm): 14.3 (CH₂CH₃), 18.5 (CH₃), 22.3 (CH₃CH), 56.0 (CH₂CH₃), 61.4 (CHCH₃), 82.3 (=CH), 116.9 (CH), 126.7 (CH), 128.5 (CH), 129.9 (qC), 162.2 (N=C=), 170.4 (O=C).

*Corresponding author. E-mail: omid_marvi@pnu.ac.ir

3-Allylamino-but-2-enoic acid ethyl ester (4). Oil, IR (neat, cm^{-1}): 3297, 3064, 2975, 1668, 1611, 1508, 1284, 1169, 1058, 949, 766; $^1\text{H-NMR}$ (500 MHz, CDCl_3 , δ / ppm): = 1.23 (3H, *t*, J = 7.3 Hz), 3.61 (3H, *s*), 3.81–3.86 (2H, *m*), 4.14 (2H, *q*, J = 7.3 Hz), 4.83 (1H, *s*), 5.16–5.24 (2H, *m*), 5.82–5.90 (1H, *m*), 8.64 (1H, *s*, NH); $^{13}\text{C-NMR}$ (125 MHz, CDCl_3 , δ / ppm): 14.2 (CH_2CH_3), 24.5 (CH_3), 49.7 ($\text{CH}_2\text{C=}$), 61.4 (CH_2CH_3), 82.3 (=CH), 116.9 (=CH₂), 134.4 (=CH–CH₂), 161.8 (N–C=), 170.5 (O=C).

3-Methylamino-but-2-enoic acid ethyl ester (5). Oil, IR (neat, cm^{-1}): 3288, 3046, 2989, 1645, 1602, 1529, 1274, 1154, 1138, 1072, 943, 792; $^1\text{H-NMR}$ (500 MHz, CDCl_3 , δ / ppm): 1.21 (3H, *t*, J = 7.3 Hz), 1.93 (3H, *s*), 2.81 (3H, *d*, J = 7.4 Hz), 4.11 (2H, *q*, J = 7.3 Hz), 4.52 (1H, *s*), 11.82 (1H, *s*, NH); $^{13}\text{C-NMR}$ (125 MHz, CDCl_3 , δ / ppm): 14.2 (CH_2CH_3), 18.7 (CH_3), 46.3 (NCH₃), 57.3 (CH_2CH_3), 80.3 (=CH), 162.3 (N–C=), 171.3 (O=C).

3-Phenylamino-but-2-enoic acid methyl ester (6). Oil, IR (neat, cm^{-1}): 3454, 3092, 2940, 1639, 1524, 1252, 1149, 1125, 1078, 912, 737; $^1\text{H-NMR}$ (500 MHz, CDCl_3 , δ / ppm): 1.42 (3H, *s*), 2.19 (3H, *s*), 4.70 (1H, *s*), 7.02–7.48 (5H, *m*, aromatic), 11.19 (1H, *s*, NH); $^{13}\text{C-NMR}$ (125 MHz, CDCl_3 , δ / ppm): 14.6 (CH_2CH_3), 54.3 (OCH₃), 91.2 (=CH), 122.4 (CH), 129.1 (CH), 129.6 (CH), 139.1 (qC), 160.2 (N–C=), 179.9 (O=C).

3-(2-Methyl-phenylamino)-but-2-enoic acid methyl ester (7). M.p. 65–67 °C; IR (KBr, cm^{-1}): 3435, 2692, 1648, 1590, 1442, 1284, 1141, 880, 791; $^1\text{H-NMR}$ (500 MHz, CDCl_3 , δ / ppm): = 1.38 (3H, *s*), 1.80 (3H, *s*), 3.43 (3H, *s*), 4.61 (1H, *s*), 6.75–7.19 (4H, *m*, aromatic), 10.48 (1H, *s*, NH); $^{13}\text{C-NMR}$ (125 MHz, CDCl_3 , δ / ppm): 14.0 (CH_2CH_3), 18.5 (CH_3), 51.9 (PhCH₃), 84.4 (=CH), 123.8 (CH), 126.5 (CH), 127.2 (CH), 131.3 (CH), 135.0 (qC), 136.1 ($\text{CH}_3\text{--C}$ aromatic), 160.4 (N–C=), 170.8 (O=C).

3-(4-Ethoxy-phenylamino)-but-2-enoic acid methyl ester (8). M.p. 60–62 °C; IR (KBr, cm^{-1}): 3445, 2681, 1635, 1587, 1429, 1248, 1159, 869, 776; $^1\text{H-NMR}$ (500 MHz, CDCl_3 , δ / ppm): 1.44 (3H, *t*, J = 7.2 Hz), 1.92 (3H, *s*), 3.65 (3H, *s*), 4.1 (2H, *q*, J = 7.2 Hz), 4.68 (1H, *s*), 6.81 (2H, *d*, J = 8.7 Hz), 7.09 (2H, *d*, J = 8.7 Hz), 10.12 (1H, *s*, NH); $^{13}\text{C-NMR}$ (125 MHz, CDCl_3 , δ / ppm): 14.8 (OCH₂CH₃), 20.1 (CH₃), 50.1 (OCH₃), 62.3 (OCH₂CH₃), 84.3 (=CH), 115.2 (CH), 127.1 (CH), 131.8 (qC), 156.9 (O–C aromatic), 160.1 (N–C=), 170.5 (O=C).

4-(1-Phenylethanamino)-3-penten-2-one (9). M.p. 58–61 °C; IR (KBr, cm^{-1}): 3438, 3016, 1657, 1593, 1242, 1179, 1025, 941, 883; $^1\text{H-NMR}$ (500 MHz, CDCl_3 , δ / ppm): 1.26 (3H, *s*), 1.97 (3H, *d*, J = 4.7 Hz), 2.25 (3H, *s*), 4.23 (1H, *m*), 5.11 (1H, *s*), 7.24–7.45 (5H, *m* aromatic), 10.56 (1H, *s*, NH); $^{13}\text{C-NMR}$ (125 MHz, CDCl_3 , δ / ppm): 22.4 (CH₃), 24.6 (CHCH₃), 27.4 (COCH₃), 56.2 (CHCH₃), 95.0 (=CH), 126.4 (CH), 126.5 (CH), 128.3 (CH), 141.5 (qC), 160.1 (N–C=), 195.7 (O=C).

4-Methylamino-3-penten-2-one (10). M.p. 36–38 °C; IR (KBr, cm⁻¹): 3269, 3082, 2988, 1651, 1639, 1560, 1281, 1154, 1063, 974, 787; ¹H-NMR (500 MHz, CDCl₃, δ / ppm): 1.94 (3H, s), 1.98 (3H, s), 2.85 (3H, d, J = 5.6 Hz), 11.86 (1H, s, NH); ¹³C-NMR (125 MHz, CDCl₃, δ / ppm): 18.1 (CH₃), 28.3 (NCH₃), 29.1 (OCCH₃), 94.8 (=CH), 163.7 (N=C=), 192.8 (O=C).

4-phenylamino-3-penten-2-one (11). M.p. 47–49 °C; IR (KBr, cm⁻¹): 3432, 3058, 1629, 1587, 1255, 1194, 1068, 859; ¹H-NMR (500 MHz, CDCl₃, δ / ppm): 1.95 (3H, s), 2.28 (3H, s), 5.19 (1H, s), 7.12–7.49 (5H, m, aromatic), 12.45 (1H, s, NH); ¹³C-NMR (125 MHz, CDCl₃, δ / ppm): 19.5 (CH₃), 28.7 (OCCH₃), 96.9 (=CH), 124.5 (CH), 125.3 (CH), 128.7 (CH), 139.0 (qC), 159.8 (N=C=), 195.2 (O=C).

4-(2-Ethoxy-phenylamino)-3-penten-2-one (12). M.p. 56–58 °C; IR (KBr, cm⁻¹): 3448, 3071, 1627, 1564, 1249, 1173, 1028, 872, 747; ¹H-NMR (500 MHz, CDCl₃, δ / ppm): 1.36 (3H, t, J = 7.2 Hz), 1.93 (3H, s), 2.56 (3H, s), 4.09 (2H, q, J = 7.2 Hz), 4.68 (1H, s), 6.61–6.98 (4H, m, aromatic), 10.18 (1H, s, NH); ¹³C-NMR (125 MHz, CDCl₃, δ / ppm): 14.8 (CH₂CH₃), 19.8 (CH₃), 27.8 (COCH₃), 63.5 (CH₂CH₃), 96.4 (=CH), 113.5 (CH), 121.1 (CH), 122.3 (CH), 123.8 (CH), 130.4 (qC), 154.2 (O-C aromatic), 159.6 (N=C=), 195.6 (O=C).

4-(2-Methyl-phenylamino)-3-penten-2-one (13). M.p. 52–55 °C. IR (KBr, cm⁻¹): 3435, 3042, 1624, 1571, 1239, 1187, 1058, 854, 762; ¹H-NMR (500 MHz, CDCl₃, δ / ppm): 1.96 (3H, s), 2.16 (3H, s), 2.26 (3H, s), 5.21 (1H, s), 6.29–7.32 (4H, m, aromatic), 10.79 (1H, s, NH); ¹³C-NMR (125 MHz, CDCl₃, δ / ppm): 17.8 (PhCH₃), 19.6 (CH₃), 27.5 (COCH₃), 97.6 (=CH), 123.5 (CH), 126.4 (CH), 127.4 (CH), 131.3 (CH₃–C aromatic), 135.8 (CH), 136.6 (qC), 159.7 (N=C=), 196.1 (O=C).

4-(3-Chloro-phenylamino)-3-penten-2-one (14). M.p. 75–78 °C; IR (KBr, cm⁻¹): 3424, 3156, 1691, 1621, 1524, 1486, 1264, 1145, 1039, 894; ¹H-NMR (500 MHz, CDCl₃, δ / ppm): 1.97 (3H, s), 2.21 (3H, s), 5.20 (1H, s), 6.31–7.14 (4H, m, aromatic), 11.68 (1H, s, NH); ¹³C-NMR (125 MHz, CDCl₃, δ / ppm): 18.5 (CH₃), 23.4 (COCH₃), 96.8 (=CH), 122.3 (CH), 124.7 (CH), 125.6 (CH), 134.7 (CH), 135.6 (C-Cl), 141.1 (qC), 158.2 (N=C=), 195.9 (O=C).

4-Benzylamino-3-penten-2-one (15). Oil, IR (neat, cm⁻¹): 3288, 3046, 2989, 1645, 1602, 1529, 1274, 1138, 1154, 1072, 943, 792; ¹H-NMR (500 MHz, CDCl₃, δ / ppm): 1.81 (3H, s), 2.07 (3H, s), 4.38 (2H, d), 4.93 (1H, s), 6.81–7.29 (5H, m, aromatic), 11.19 (1H, s, NH); ¹³C-NMR (125 MHz, CDCl₃, δ / ppm): 18.7 (CH₃), 22.6 (COCH₃), 57.3 (CH₂), 80.3 (=CH), 123.9 (CH), 125.3 (CH), 127.2 (CH), 136.8 (qC), 162.3 (N=C=), 191.3 (O=C).



Characterization of volatiles in Beaten cheeses “Bieno sirenje” by SPME/GC-MS: Influence of geographical origin

ERHAN SULEJMANI^{1,2*}, VESNA RAFAJLOVSKA³ and ONUR GUNESER²

¹Department of Food Technology, State University of Tetovo, 1200 Tetovo, FYR Macedonia,

²Department of Food Engineering, Canakkale Onsekiz Mart University, 17020 Canakkale,

Turkey and ³Department of Food Technology and Biotechnology – Skopje, Ss. Cyril and Methodius University, 1000 Skopje, FYR Macedonia

(Received 17 September, revised 17 November, accepted 18 November 2013)

Abstract: In this study, the volatile profiles of an economically important type of cheeses for the FYR Macedonian dairy sector were characterized. A total of eighteen samples belonging to 6 different geographical regions of Beaten cheese, including cheeses from Kumanovo, Tetovo, Struga, Resen, Veles and Radoviš, were comparatively studied for their volatile profiles. Sixty one volatile compounds were identified in the cheeses by solid-phase micro-extraction combined with gas chromatography–mass spectrometry. The results are discussed based on their chemical classes (17 esters, 9 ketones, 10 acids, 8 alcohols, 6 terpenes and 11 miscellaneous compounds). Acids, esters and alcohols were the most abundant classes identified and were highly dependent on the geographical origin of the cheeses. Beaten cheese from Struga had the highest levels of carboxylic acids, ketones, alcohols, esters and terpenes. The Beaten cheese of other geographical origin had low levels of volatiles, probably due to the effects of the variable characteristics of the employed milk and differences in the cheese making processes, which affected the biochemical processes. The results suggested that each cheese from different geographical regions had a different volatiles profile and that the manufacturing technique and the ripening stage of the cheeses played major roles in determining the distribution of the volatile compounds.

Keywords: Beaten cheese; geographical regions; volatile compounds; SPME; GC-MS.

INTRODUCTION

Several reviews summarize the present knowledge of volatile formation, profiling in different types of cheese and the analytical techniques for their study.^{1,2} The typical flavour of each cheese variety is determined by the presence of volatile compounds and their relative concentrations. Although over 600 vola-

*Corresponding author. E-mail: erhan.sulejmani@unite.edu.mk
doi: 10.2298/JSC130917135S

tile compounds have been identified in cheeses, only a small fraction can be considered as "flavour impact" compounds. The most potent flavour compounds in cheeses are aldehydes, alcohols, carboxylic acids and esters derived from the catabolism of amino acids. The main agents related to flavour formation in cheese are indigenous milk enzymes, rennet and microbial enzymes from the wild microbial flora and/or commercial starters or adjunct cultures used.

For some cheese varieties, a specific compound group is recognized as being the major contributor to flavour. In general, raw milk cheeses contain a more diverse group of volatile compounds than cheeses made from pasteurized milk, as pasteurization of milk promotes changes that affect the flavour. In hard Italian cheese varieties, free fatty acids (FFAs) are the important contributors, while in blue-veined ripened cheeses, the impact of FFAs on the flavour is less owing to the dominant influence of methyl ketones. The volatile chromatographic pattern was used in the classification of some cheese varieties.³ The formation of these compounds in cheese results from proteolysis, lipolysis and the metabolism of lactose and lactate.⁴

Beaten cheese is an autochthonous product in the FYR Macedonia, which originates from the territory of Mariovo where it is manufactured on the pasture land exclusively from sheep's milk. It is characterized by extremely salty flavour and a firm texture with visible holes (eye). This kind of cheese is named after the manufacturing process: the cheese curd is beaten; therefore, it is called "Beaten cheese" or "*Bieno sirenje*". Beaten cheeses are produced almost exclusively on state territory mainly from raw milk of cows, ewes and goats. The production of cheese varies in different regions, which results in the appearance of different cheese varieties. The characteristics of the milk used for cheese production are also variable and depend on the geographical region, season of milking and the nutrition method. Following coagulation of the milk at 34 °C for 45 min using animal rennet, the curd is stirred and beaten manually or mechanically until a homogenous compact structure is obtained. After drainage, the curd is cooked in a hot water at 70 to 90 °C for 20 min. Following the cooking, the curd is beaten for 5 to 10 min. The curd is then moulded and transferred to a cotton cloth for hanging for about 24 h. Then the curd is pre-ripened for 3 days. During this period, the curd gains a specific yellowish colour, a hard texture and visible holes. The cheese loafs are cut in slices 30 to 40 cm long and 4 to 5 cm wide. The cheese blocks are salted by dry-salting for 24 h and then brine salting. Finally the pieces are packed in plastic barrels containing brine with concentration of 18 to 20 % (w/V) NaCl for long-term storage. Such differences in manufacture procedure have strong influence on the characteristics and appearance of the cheese varieties.⁵

The aim of this study was to determine and compare the volatile compounds of Beaten cheeses produced in different geographical regions. Due to the lack of

information on such cheeses, the results should provide a better understanding and notification of these cheeses, which would lead to a protected designation.

EXPERIMENTAL

Cheese samples

Eighteen samples from 6 different regions of Beaten cheese (three samples per region) were collected from FYR Macedonia in 2012. The ages of the cheeses were between 1–9 months old (Table I). As far as possible, ripened or ready for sale cheese samples were collected. Production dates were noted when known; however, some samples were produced by artisanal methods without packaging and labelling. Thus, to assess the production dates for these, the manufacturer's declarations were taken into account. The cheese samples were stored in sterile plastic bags and transported to the laboratory of the Food Engineering Department, Canakkale Onsekiz Mart University, Turkey. The cheese samples were vacuum-packed and stored at –20 °C until analysis, which was performed within 1 month of sample collection.

TABLE I. Short summary of the production characteristics of the analysed cheeses

Characteristic	Geographical origin of Beaten cheeses (<i>n</i> = 18)					
	Kumanovo	Tetovo	Struga	Resen	Veles	Radoviš
Milk type	Ewe/Goat	Ewe/Cow	Ewe	Cow/Ewe	Cow	Ewe/Goat
Pasteurisation	No	No	No	Yes	Yes	No
Rennet type	Home made	Home made	Chymosin	Chymosin	Chymosin	Home made
Cooking temperature, °C	80	90	80	70	70	60
Ripening type	Under brine	Under brine	Under brine	Vacuum packed	Vacuum packed	Under brine or dry
Ripening period	> 9 months	8–9 months	> 9 months	< 2 months	< 1 months	9 months
Industrialised	No	No	No	Yes	Yes	No

SPME GC/MS

The volatile compounds were isolated from Beaten cheese by solid-phase microextraction (SPME) methods. For this purpose, 5 g of grated and homogenized cheese sample was placed in a 40-mL amber-coloured SPME vial and then 1 g of NaCl was added and 10 µL of internal standard (0.8 µg 2-methyl-3-heptanone for basic/neutral compounds and 55.2 µg 2-methylvaleric acid for acidic compounds). The vial was vortexed for one min, and held in a water bath for 20 min at 40 °C. Volatile compounds were extracted by placing a SPME fibre (2 cm – 50/30 µm divinylbenzene (DVB)/Carboxen/polydimethylsiloxane (PDMS), Supelco) into a vial and exposing it to a head-space (HS) vial for 20 min at 40 °C. The volatile compounds were determined using a HS-GC-MS system, which consisted of a HP 6890 GC and a 7895C mass selective detector (Agilent Technologies, Wilmington, DE, USA). Helium was used as the carrier gas. The total flow was 1.2 mL min⁻¹. The GC was fitted with a HP5 MS column (30 m×0.25 mm id×0.25-µm film thickness, J and W Scientific, Folsom, CA, USA). The mass spectra were recorded in the electron impact mode at an ionization voltage of 70 eV in the 33–300 a.m.u. mass range. Oven temperature was programmed from 40 to 230 °C at rate of 10 °C min⁻¹, with initial and final hold times of 5 and 20 min, respectively. The volatiles were tentatively identified by comparison of the mass spectra of the unknown

compounds with those in the National Institute of Standards and Technology (NIST 08) and Wiley Registry of Mass Spectral Data, 7th edition (Wiley 05) mass spectral databases. The retention indices were calculated using an *n*-alkane series.⁶ Quantification of flavour compounds were realised from the relative abundances of the volatiles compounds positively using Eq. (1):⁷

$$\text{Mean abundance } (\mu\text{g/kg}) = c_{\text{IS}} \times A_{\text{C}} / A_{\text{IS}}. \quad (1)$$

where, c_{IS} is concentration of internal standard (lg/kg), A_{C} is peak area of compound, A_{IS} is peak area of the internal standard.

Statistical analysis

Data from GC-MS measurements were analyzed using one-way analysis of variance (ANOVA). The HSD Tukey's test was applied to compare the mean values of the volatile compounds. These statistical treatments were performed using the SPSS program for Windows, version 9.0 (SPSS Inc., Chicago, IL, USA).

RESULTS AND DISCUSSION

Volatile compounds

A total of 62 volatile compounds were identified in Beaten cheeses from 6 different geographical regions. These compounds were grouped into chemical classes including 10 acids, 8 alcohols, 17 esters, 9 ketones, 6 terpenes and 11 miscellaneous compounds. Duplicate analyses for all samples were performed and the average values with standard deviation (*SD*) are listed in Tables II–VII. The volatiles of Beaten cheeses have not hitherto been characterized and the results are discussed by comparison to data reported by other researchers for different cheeses.

Carboxylic acids

Carboxylic acids were the most abundant chemical family isolated from the headspace of the Beaten cheeses from the different regions. A high concentration ($173624.6 \mu\text{g } 100 \text{ g}^{-1}$) of these acids was detected in the Struga cheeses. A low concentration ($1863.6 \mu\text{g } 100 \text{ g}^{-1}$) was detected in the samples of Resen cheeses. Five different acids were identified in the Kumanovo and Resen Beaten cheeses, and their concentrations were 13347.2 and $1863.6 \mu\text{g } 100 \text{ g}^{-1}$, respectively. Six different acids were identified in the Tetovo and Radoviš Beaten cheeses, and their concentration were 4220.8 and $13773.8 \mu\text{g } 100 \text{ g}^{-1}$, respectively. Acetic acid was identified in the Veles Beaten cheese ($371.9 \mu\text{g } 100 \text{ g}^{-1}$), while considerably higher levels of butanoic ($59993.8 \mu\text{g } 100 \text{ g}^{-1}$) and hexanoic acid ($84803.1 \mu\text{g } 100 \text{ g}^{-1}$) were detected in the Struga cheeses. Throughout the ripening period of the cheeses, most of carboxylic acids came from lipolysis of triglycerides followed by those produced from lactate metabolism; therefore, lipolysis was the main pathway responsible for the release of carboxylic acids in Beaten cheeses. Acetic acid was probably the product of citrate or lactate fermentation of amino acid catabolism by bacteria.

TABLE II. Contents of acids in the Beaten cheeses, $\mu\text{g } 100 \text{ g}^{-1}$ ($n = 18$); * – significant statistical differences (Tukey's test, $P < 0.05$); n.q.: not quantified; NS – not significant; RI – retention index

Compound	RI	Geographical origin						<i>P</i> value
		Kumanovo (<i>n</i> = 3)	Tetovo (<i>n</i> = 3)	Struga (<i>n</i> = 3)	Resen (<i>n</i> = 3)	Veles (<i>n</i> = 3)	Radoviš (<i>n</i> = 3)	
Acetic acid	614	n.q.	n.q.	n.q.	n.q.	371.9 ± 71.2	n.q.	*
Pentanoic acid	882	n.q.	1088.9 ±47.3	928.8 ±13.9	188.5 ±52.3	0.7 ± 0.06	437.5 ±80.0	*
2-Methylbutanoic acid	889	n.q.	361.2 ±420.5	n.q. ±0.1	0.6	0.6 ± 0.07	n.q.	NS
Butanoic acid	890	7493.6 ±3141.7	1137.8 ±8.5	59993.8 ±1509.1	501.5 ±22.1	1090.1 ± 37.7	12850.2 ±1409.9	*
3-Methylbutanoic acid	909	n.q.	n.q.	n.q.	n.q.	n.q.	41.9 ± 4.9	*
Hexanoic acid	1060	3253.4 ±1344.4	n.q.	84803.1 ±2095.1	23.9 ±9.5	489.7 ± 19.1	263.1 ±28.8	*
Octanoic acid	1204	169.5 ±54.6	1259.1 ±485.3	1981.6 ±37.5	819.4 ±259.4	191.4 ± 16.6	175.9 ±8.5	*
Nonanoic acid	1276	6.8 ±0.04	n.q. ±54.1	665	n.q. ±54.1	n.q.	n.q.	*
Decanoic acid	1379	2423.6 ±1007.2	373.8 ±179.3	25234.4 ±3261.4	330.02 ±210.3	42.3 ± 5.9	5.1 ±0.6	*
Dodecanoic acid	1556	n.q.	n.q.	17.8 ± 1.2	n.q.	n.q.	n.q.	*
Total acids		13347.1	4220.8	173624.6	1863.6	2186.8	13773.8	

The differences between cheeses in the volatile acid concentrations are associated with the maturation periods since the longer maturation period results in higher amount of carboxylic acids (Tables I and II). The variabilities in the milk composition during the seasonal production of the used milk could also impact these differences.⁸ Acid compounds constituted 97 % of the volatile compounds isolated from the Beaten cheeses. Significant differences ($P < 0.05$) for all acids were found, except for 2-methylbutanoic acid. Other carboxylic acids detected in Beaten cheese are listed in Table II.

Hexanoic acid, a short-chain carboxylic acid, contributes to the typical aroma of Struga Beaten cheese. The fatty acids hexanoic, octanoic and decanoic acids were widely recognized as being responsible for the characteristic aroma of goat cheeses, giving rise to the trivial terms caproic, caprylic and capric acids, respectively,⁹ and their contribution to the volatile profile of Beaten cheeses has been showed in this study as well.

Acetic and propanoic acids were associated with the slight sour taste of Veles Beaten cheeses. Branched-chain fatty acids (BCFA) were not characteristic active compounds of Beaten ewe's cheeses in general. 2-Methylbutanoic acid was the most abundant acid found in Tetovo Beaten cheese and it provides a rancid cheese and sweaty odours.¹⁰ In this case, as raw sheep milk was used for

some cheese manufacture, the native microorganisms of non-pasteurized milk may have a significant contribution on its final volatile profile.¹¹

Ketones

Most of the ketones in Beaten cheeses were methyl ketones (Table III). There were significant differences among the cheeses ($P < 0.05$) from different origin. The highest ($755.5 \mu\text{g } 100 \text{ g}^{-1}$) and lowest ($27.5 \mu\text{g } 100 \text{ g}^{-1}$) concentration were identified in Kumanovo and Radoviš Beaten cheeses, respectively. Methyl ketones are produced from free fatty acids by an alternative pathway to β -oxidation.¹¹ About 7 ketones were identified in Kumanovo Beaten cheese and the highest concentration of 2-heptanone was detected in Kumanova Beaten cheese. In addition, some identified ketones, including 2-octanone, 8-nonen-2-one and 2-nonanone were rarely found in cheeses from other regions. 2-Butanone, with a butterscotch odour, was identified as the main odorant in Cheddar cheese¹² and 2-heptanone, with a herbaceous odour, is an important flavour compound of Emmentaler and natural creamy Gorgonzola cheeses.¹³ Fruity, floral and musty notes are associated with various methyl ketones, such as 2-octanone, 2-nonanone and 2-undecanone, so the presence of these volatile compounds could be considered beneficial to the flavour of cheese.¹⁴ 2-Butanone

TABLE III. Contents of ketones in the Beaten cheeses, $\mu\text{g } 100 \text{ g}^{-1}$ ($n = 18$); * – significant statistical differences (Tukey's test, $P < 0.05$); n.q.: not quantified; NS – not significant; RI – retention index

Compound	RI	Geographical origin						P value
		Kumanovo ($n = 3$)	Tetovo ($n = 3$)	Struga ($n = 3$)	Resen ($n = 3$)	Veles ($n = 3$)	Radoviš ($n = 3$)	
Acetone	<600	n.q.	14.6 ± 0.5	n.q.	n.q.	n.q.	n.q.	*
2-Butanone	612	n.q.	n.q. ± 1.6	385.2 ± 1.6	n.q.	n.q.	n.q.	*
2-Pentanone	684	92.2 ± 6.3	4.7 ± 1.6	231.5 ± 1.5	n.q.	5.4 ± 0.2	n.q.	*
3-Hydroxy-2-butanone	711	n.q.	448.2 ± 37.1	n.q. ± 37.1	100 ± 25.8	115.3 ± 18.4	26.5 ± 4.1	*
2-Hexanone	790	16 ± 1.7	n.q. ± 2	16.7 ± 2	n.q.	n.q.	n.q.	*
2-Heptanone	896	520 ± 50.9	6.3 ± 5.9	62.1 ± 3.7	32.5 ± 0.7	24.7 ± 6.5	n.q.	*
2-Octanone	991	12.2 ± 2.8	–	0.6 ± 0.1	n.q.	n.q.	n.q.	*
8-Nonen-2-one	1088	11.2 ± 1.2	n.q. ± 0	0.05 ± 0	n.q.	n.q.	n.q.	*
2-Nonanone	1094	103.9 ± 10.2	1.8 ± 2.2	0.06 ± 0	8.3 ± 1.8	6.2 ± 2	1 ± 0.2	*
Total ketones		755.5	475.6	796.0	140.9	151.5	27.4	

and 2-pentanone were the main ketones in Struga Beaten cheese, similar to Malatya cheeses made from raw milk.¹⁵ Resen and Veles Beaten cheeses were differentiated from the other cheeses due to their similar ketone concentration of 140.9 and 151.5 µg 100 g⁻¹, respectively. On the other hand, 2-butanone was identified only in Struga Beaten cheese. Seven different types of ketones were identified in Tetovo Beaten cheese with the concentrations of 3-hydroxy-2-butanone or acetoin (448.2 µg 100 g⁻¹) and acetone (14.6 µg 100 g⁻¹) being the greatest (Table III). Veles Beaten cheese was also rich in ketones (7 types) with acetoin (115.3 µg 100 g⁻¹) and 2-heptanone (24.7 µg 100 g⁻¹) being predominant, while the others were present at considerably lower levels (0.2–6.2 µg 100 g⁻¹). The ketones followed a similar trend as was described for the acids. However, the reduction in the concentration of ketones was higher in cheese from the Radoviš region. 2-Pentanone and 2-heptanone were previously identified as the prevailing ketones in the volatile fraction of Parmigiano,¹⁶ whereas acetoin was identified at higher concentrations in pasteurized milk cheeses than in raw milk cheeses.¹⁷ Similar results were found in Spanish regional raw milk cheeses with protected designation of origin (PDO).¹⁸ Therefore, they could play an important role in the final aroma of these cheeses made from raw milk.

Alcohols

Eight different alcohols consisting of primary, secondary, and branched-chain alcohols were present in the cheese samples. The levels of the alcohols were significantly affected ($P < 0.05$) by the different methods of cheese manufacture. Generally, primary alcohols originate from the corresponding aldehydes produced from fatty acids and from amino acid metabolism. Among these, ethanol may be formed by lactose metabolism or by reduction of acetaldehyde.¹⁶ Secondary alcohols are obtained by the enzymatic reduction of methyl ketones.⁴ Alcohols were quantitatively the most abundant volatiles in Kumanovo Beaten cheese (Table IV) with 7 different alcohols being identified in this cheese. 2-Heptanol, 2-pentanol and benzyl alcohol were the most abundant alcohols in the cheeses from Kumanovo (Table IV). The concentration of alcohols in the cheeses from other regions may have been higher than the reported levels as it was reported that the level of alcohols can fluctuate during ripening.¹⁹ Thus, at the time of analysis, the cheeses examined in the present study were not sampled at the time where the levels of the various alcohols were at their maximal. Similar concentrations of total alcohols were isolated in Tetovo (74.1 µg 100 g⁻¹) and Struga (88.6 µg 100 g⁻¹) Beaten cheeses, although the predominant alcohols differed between these cheeses. 2-Pentanol was detected in the Struga Beaten cheeses, while, on the other hand, 1-butanol was detected in the Tetovo Beaten cheese. Two alcohols were identified in Resen and Veles Beaten cheeses with the

main one being 3-methyl-1-butanol. Radoviš Beaten cheese did not contain high levels of alcohols, however, the concentration of alcohols was similar with the Veles ($9.9 \mu\text{g } 100 \text{ g}^{-1}$) Beaten cheese.

TABLE IV. Contents of alcohols in the Beaten cheeses, $\mu\text{g } 100 \text{ g}^{-1}$ ($n = 18$); * – significant statistical differences (Tukey's test, $P < 0.05$); n.q.: not quantified; RI – retention index

Compound	RI	Geographical origin						<i>P</i> value
		Kumanovo (<i>n</i> = 3)	Tetovo (<i>n</i> = 3)	Struga (<i>n</i> = 3)	Resen (<i>n</i> = 3)	Veles (<i>n</i> = 3)	Radoviš (<i>n</i> = 3)	
2-Pentanol	701	249.6 ± 28.9	n.q.	83.3 ± 1.7	n.q.	n.q.	n.q.	*
1-Butanol	729	99.6 ± 12.9	71.7 ± 18.2	n.q.	n.q.	n.q.	4.1 ± 0.7	*
3-Methyl-1-butanol	730	n.q.	n.q.	5.1 ± 0.07	180.4 ± 44.9	8.2 ± 0.8	3.2 ± 0.6	*
2-Heptanol	914	277.8 ± 35.2	n.q.	n.q.	n.q.	1.5 ± 0.1	n.q.	*
3-(Methylthio)-1- -propanol	983	1.04 ± 0.2	n.q.	n.q.	n.q.	n.q.	n.q.	*
Benzyl alcohol	1039	161.1 ± 32.3	n.q.	n.q.	n.q.	n.q.	0.1 ± 0.01	*
2-Nonanol	1104	19.9 ± 1.2	n.q.	n.q.	n.q.	n.q.	0.01 ± 0	*
Benzenethanol	1118	17.2 ± 0.5	2.4 ± 0.8	n.q.	n.q.	n.q.	2.9 ± 0.5	*
Total alcohols		826.4	74.1	88.5	180.7	9.8	10.4	

2-Heptanol was the highest secondary alcohol isolated in the artisanal Kumanovo cheese, which was previously identified as a key odorant of Gorgonzola and Grana Padano cheeses,¹³ and was detected in the highest concentrations in semi-hard Spanish goat cheeses.²⁰ 2-Pentanol has lower detection thresholds,¹⁸ which plays an important role in the aroma of ewe raw milk La Serena cheese. The present results indicated that 2-butanol was the most abundant compound, followed by 3-methyl-1-butanol, 1-propanol and ethanol. Similar results were observed in the case of the aromatic fraction of other raw milk cheeses, in which all these components were found in high amounts.¹⁸ The large amount of 2-butanol was formed by the reduction of 2,3-butanedione to 2-butanol during ripening, due to the high activity of non-starter lactic acid bacteria.²¹

Esters

These compounds are produced by enzymatic or chemical reactions of fatty acids with primary alcohols, so the alcohol concentration is a limiting factor in ester production.²² Seventeen esters were found in the 6 Beaten cheeses of different geographical origin and the most frequently identified sub-groups were seven

ethyl, four methyl, two isopropyl, two isobutyl, one isoamyl and one methylbutyl esters (Table V). The amounts of esters were significantly different ($P < 0.05$) in the cheeses, except for octanoic acid methyl ester. Esters were the unique chemical family with a high presence in Radoviš Beaten cheese because these cheeses had the longest maturation period (Table V). This increase could be due to the esterification of acids and alcohols. The ethyl esters of hexanoic acid and butanoic acid were the most abundant esters isolated in the Kumanovo and Resen Beaten cheese. These esters were obtained from esterification reactions occurring with hexanoic and butanoic acids, respectively. The ethyl esters of butanoic and hexanoic acids were identified as two of the most potent odorants of Cheddar, Emmentaler, creamy Gorgonzola, Grana Padano and Pecorino cheeses.¹³ These two esters, in addition to ethyl acetate, were the major esters identified in

TABLE V. Contents of esters in the Beaten cheeses, $\mu\text{g } 100 \text{ g}^{-1}$ ($n = 18$); * – significant statistical differences (Tukey's test, $P < 0.05$); n.q.: not quantified; NS – not significant; RI – retention index

Compound	RI	Geographical origin						<i>P</i> value
		Kumanovo (n = 3)	Tetovo (n = 3)	Struga (n = 3)	Resen (n = 3)	Veles (n = 3)	Radoviš (n = 3)	
Ethyl acetate	603	126.3±16.3	n.q.	n.q.	n.q.	n.q.	n.q.	*
Methyl butanoate	716	n.q.	n.q.	n.q.	3.8 ±0.7	n.q.	n.q.	*
Ethyl butanoate	804	9.1±0.8 ±35.9	156.5 ±1.4	65.3 ±1	4.6 ±0.3	2.7	n.q.	*
Methyl hexanoate	927	4.5±0.2	n.q.	10.2 ±1.7	0.8 ±0.2	0.6 ±0.1	n.q.	*
Isobutyl butanate	959	13.4±1.7	n.q.	n.q.	n.q.	n.q.	n.q.	*
Ethyl hexanoate	1006	287.8±33.7	120.6	8.7	n.q.	n.q.	n.q.	*
				±52.4 ±0.7				
Isoamyl butyrate	1058	1.4±0.2	n.q.	n.q.	n.q.	n.q.	n.q.	*
Methyl octanoate	1124	2.4±2.6	7.5	8.3	n.q.	n.q.	n.q.	NS
				±6 ±0.6				
Isobutyl hexanoate	1136	2.2±0.2	n.q.	n.q.	n.q.	n.q.	n.q.	*
Ethyl octanoate	1202	21.6±1.8	8.3	11.4	n.q.	n.q.	0.7 ±0.01	*
				±4.1 ±0.5				
Isopropyl octanoate	1232	2.2±0.2	n.q.	0.04 ±0.0	n.q.	n.q.	n.q.	*
2-Methylbutyl hexanoate	1252	9.1±0.1	n.q.	5.1 ±0.3	n.q.	n.q.	n.q.	*
Ethyl 9-deenoate	1389	3.5±0.1	n.q.	n.q.	n.q.	n.q.	n.q.	*
Ethyl decanoate	1397	55.2±1	2.0	16.8	n.q.	0.1 ±0	n.q.	*
				±1.3 ±1.6				
Isopropyl decanoate	1428	1.5±0.5	n.q.	n.q.	n.q.	n.q.	n.q.	*
Ethyl dodecanoate	1598	2.9±0.4	n.q.	n.q.	n.q.	n.q.	n.q.	*
Methyl palmitate	1889	8.2±1.1	n.q.	n.q.	n.q.	n.q.	n.q.	*
Total esters		552.1	294.9	125.8	9.3	3.2	0.7	

Majorero goat cheese.²³ The most abundant ester was ethyl acetate, followed by ethyl butanoate, ethyl propanoate and propyl acetate. It is notable that in Manchego cheese, ethyl esters were reported at higher levels in raw milk cheeses than in pasteurized ones.¹⁸

Terpenes

Six terpenes were identified in the cheese samples; however, higher concentrations were isolated in Kumanovo and Veles Beaten cheese (Table VI). On the contrary, terpenes were not detected in Radoviš cheeses. The most abundant terpene in the majority of the cheese samples was limonene, which is associated with citrus-like note,²⁴ and was the most abundant terpene in eleven varieties of Turkish cheese.²⁵ Three different terpene compounds were determined in Tetovo Beaten cheese, with α -pinene being the main one. α -Pinene was also identified in Kuflu²⁶ and Manchego cheeses.¹⁷ These compound originate from pasture plants and are transferred to the milk and milk products.²⁴ High levels of terpenes were detected in Resen cheese ($32.3 \mu\text{g } 100 \text{ g}^{-1}$), with limonene being the main one. Low levels of terpenes were detected in Tetova ($8.7 \mu\text{g } 100 \text{ g}^{-1}$) and Radoviš ($6.9 \mu\text{g } 100 \text{ g}^{-1}$) Beaten cheese. The majority of terpenes that were identified in the Beaten cheeses were also isolated from other types of brined cheese.²⁷ It is thought that the high level of terpenes in the cheeses could be due to the high levels of terpenes in the plants consumed by the animals. In traditional cheeses manufactured in Alpine regions, terpenes are important volatile compounds with origins in the plants that constitute the forage mixture of the pastures.²⁸ In another study, terpenes were considered to be important compounds due to their

TABLE VI. Terpenes in the Beaten cheeses, $\mu\text{g } 100 \text{ g}^{-1}$ ($n = 18$); * – significant statistical differences (Tukey's test, $P < 0.05$); n.q.: not quantified; RI – retention index

Compound	RI	Geographical origin						P value
		Kumanovo ($n = 3$)	Tetovo ($n = 3$)	Struga ($n = 3$)	Resen ($n = 3$)	Veles ($n = 3$)	Radoviš ($n = 3$)	
α -Pinene	934	0.13 ± 0.02	4.3 ± 1.4	n.q.	3.9 ± 0.7	2.1 ± 0.3	1.15 ± 0.17	*
β -Pinene	980	n.q.	n.q.	n.q.	1.2 ± 1.45	n.q.	n.q.	NS
β -Myrcene	990	n.q.	n.q.	n.q.	n.q.	0.2 ± 0.1	n.q.	*
<i>p</i> -Cymene	1025	n.q.	1.3 ± 1.4	n.q.	n.q.	4.2 ± 0.5	n.q.	*
l-Limonene	1033	90.5 ± 7.3	2.9 ± 1.1	n.q.	27.1 ± 3.7	56.2 ± 8.4	5.71 ± 1.80	*
γ -Terpinene	1061	0.54 ± 0.08	0.1 ± 0.02	n.q.	0.1 ± 0.1	0.4 ± 0.1	0.04 ± 0.01	*
Total terpenes	91.2	8.7	n.q.	32.3	62.9	6.9		

low odour thresholds and they were thought to originate from the plants that constituted the forage mixture of the grazing pastures.²⁸

Miscellaneous

Eleven miscellaneous compounds, including eight hydrocarbons, one phenol, one aldehyde and one sulphur compound (carbon disulfide), were detected (Table VII). Carbon disulfide was the most abundant miscellaneous compound, while toluene was isolated at various levels, as a result of contamination.²⁹

TABLE VII. Miscellaneous compounds in the Beaten cheeses, $\mu\text{g } 100 \text{ g}^{-1}$ ($n = 18$); * – significant statistical differences (Tukey's test, $P < 0.05$); n.q.: not quantified; RI – retention index

Compound	RI	Geographical origin						<i>P</i> value
		Kumanovo (n = 3)	Tetovo (n = 3)	Struga (n = 3)	Resen (n = 3)	Veles (n = 3)	Radoviš (n = 3)	
Carbon disulfide	<600	223.7 ±18.7	17.98 ±7	231.1 ±16.9	513.3 ±52.8	469.6 ±110.4	167.5 ±44.4	
2-Methyloctane	866	n.q.	n.q.	n.q.	n.q.	0.4	n.q.	*
						±0.1		
3,7-Dimethyl-1,6-octadiene	945	2.9 ±0.15	4.6 ±0.9	3.3 ±0.6	n.q.	3.3 ±2.9	n.q.	NS
3,7-dimethyl-2-octene	970	n.q. ±5.4	4.6 ±0.1	0.7	n.q.	n.q.	n.q.	NS
2-Butenal	643	n.q. ±3.9	n.q.	104.8	n.q.	n.q.	n.q.	*
Toluene	763	n.q. ±2.8	2.4 ±3.2	24.8 ±0.7	2.8 ±0.2	2.03 ±0.08	0.5	*
<i>m</i> -Cresol	1076	4.9 ±0.4	n.q. ±0	0.09	n.q.	n.q.	0.1 ±0.01	*
Undecane	1098	n.q. ±3.9	9.9	n.q.	n.q.	15.6 ±2.6	0.01 ±0.00	*
Dodecane	1199	n.q. ±1.3	n.q.	n.q.	n.q.	6.2	n.q.	*
Tridecane	1301	n.q. ±0.4	n.q.	n.q.	n.q.	2.1	n.q.	*
Nonadecane	1846	1.5 ±0.2	n.q.	n.q.	n.q.	n.q.	n.q.	*
Total miscellaneous	229.4	30.2	355.9	516.1	495.5	168.1		

One of the hydrocarbons, toluene, which provides nutty odour, was the most abundant hydrocarbon, already identified at high levels in Feta-type cheese.³⁰ High levels of octane were previously found in other raw milk cheeses, *e.g.*, in Spanish Manchego cheese.¹⁷ Hydrocarbons originate from fodder,¹⁸ and are also produced during the ripening as a result of lipid autoxidation.¹⁶ Volatile sulphur

compounds greatly contribute to the flavour of many cheeses¹¹ and interact with each other and with other compounds in cheese.

CONCLUSIONS

The aim of this study was to characterize the volatile profile of the cheeses that are important for the dairy sector of the FYR Macedonia. Volatile acids were the most abundant compounds isolated in the headspace analyses of Beaten cheese. These acids are of the highest importance for the aromatic profile of this type of cheese. The pattern of volatile acids formation according to their most probable origin could be associated with the different and typical characteristics in each cheese from different regions. The concentration of volatile compounds varied greatly with high standard deviations, due to the lack of standard manufacturing protocols and age-related differences. In general, the highest concentration of alcohols, esters and ketones were observed in Kumanovo, whereas the highest concentration of the miscellaneous compounds was observed in Resen Beaten cheese. This study highlights the fact that the manufacturing technique and ripening conditions of the cheeses play important roles on the formation of volatile compounds. The data presented in this article provide new information on the volatile characterization of some Beaten cheeses from different regions of the FYR Macedonian. In addition, the volatile profiles could be applied for quality control of Beaten cheeses. Complementary sensory and microbial analyses should be performed in the future to develop further the relationship between manufacturing factors and the formation of volatiles in Beaten cheese.

ИЗВОД

КАРАКТЕРИЗАЦИЈА ИСПАРЉИВИХ СУПСТАНЦИ ИЗ БИЈЕНОГ СИРА „БИЕНО СИРЕЊЕ“ МЕТОДОМ SPME/GC-MS: УТИЦАЈ ГЕОГРАФСКОГ ПОРЕКЛА

ERHAN SULEJMANI^{1,3}, VESNA RAFAJLOVSKA² и ONUR GUNESER³

¹Department of Food Technology, State University of Tetova, 1200 Tetovo, FYR Macedonia, ²Department of Food Engineering, Canakkale Onsekiz Mart University, 17020 Canakkale, Turkey и ³Department of Food Technology and Biotechnology – Skopje, Ss. Cyril and Methodius University, 1000 Skopje, FYR Macedonia

У овом раду су окарактерисани испарљиви састојци сира који је, са економског аспекта, веома важан за БЈР Македонију. Упоредно је испитивано 18 узорака бијеног сира, из 6 различитих географских области, укључујући Куманово, Тетово, Стругу, Ресен, Велес и Радовиш. Методом екстракције у чврстој фази и гасно–масеном спектрометријом идентификован је 61 испарљив састојак. Резултати су обрађени према њиховој хемијској класификацији (17 естара, 9 кетона, 10 киселина, 8 алкохола, 6 терпена и 11 осталих једињења). Најприсутнија једињења су киселине, естри и алкохоли, а њихов састав је веома зависио од географског порекла сира. Бијени сир из Струге је имао највећи садржај карбоксилних киселина, кетона, алкохола, естара и терпена. Бијени сир из других региона је имао мали садржај испарљивих састојака, што се може сматрати последицом састава млека и начина обраде сира, који утичу на биохемијске процесе. Резултати су показали да је сир из сваке области имао различит профил

испарљивих супстанци, као и да је техника производње и стадијум зрелости сира од одлучујућег значаја за те профиле.

(Примљено 17. септембра, ревидирано 17. новембра, прихваћено 18. новембра 2013)

REFERENCES

1. J. Adda, *Le Fromage*, Lavoisier, Paris, 1984, p. 320
2. H. T. Badings, *Dairy Chem. Phys.*, Wiley, New York, 1984, p. 336
3. T. Aishima, S. Nakai, *J. Food Sci.* **152** (1987) 939
4. P. Molimard, H. Spinnler, *J. Dairy Sci.* **79** (1996) 169
5. V. Levkov, V. Kakurinov, *J. Hyg. Eng. Des.* **1** (2012) 325
6. H. Van den Dool, P. D. Kratz, *J. Chromatogr., A* **11** (1963) 463
7. Y. K. Avsar, Y. Karagul-Yuceer, M. A. Drake, T. K. Singe, Y. Yoon, K. R. Cadwallader, *J. Dairy Sci.* **87** (2004) 1999
8. J. F. R. Lues, *J. Food Comp. Anal.* **13** (2000) 819
9. J. M. Poveda, L. Cabezas, *Food Chem.* **95** (2006) 307
10. M. Yvon, L. Rijnen, *Int. Dairy J.* **11** (2001) 185
11. P. L. H. McSweeney, M. J. Sousa, *Lait* **80** (2000) 293
12. G. Arora, F. Cormier, B. Lee, *J. Agric. Food Chem.* **43** (1995) 748
13. P. M. G. Curioni, J. O. Bosset, *Int. Dairy J.* **12** (2002) 959
14. F. J. Delgado, J. González-Crespo, R. Cava, J. García-Parra, R. Ramírez, *Food Chem.* **118** (2010) 182
15. A. A. Hayaloglu, E. Y. Brechany, *Lait* **87** (2007) 39
16. G. Barbieri, L. Bolzoni, M. Careri, A. Mangia, G. Parolari, S. Spagnoli, R. Virgilli, *J. Agric. Food Chem.* **42** (1994) 1170
17. E. Fernandez-Garcia, M. Carbonell, M. Nunez, *J. Dairy Res.* **69** (2002) 579
18. M. Carbonell, M. Núñez, E. Fernández-García, *Lait* **82** (2002) 683
19. A. A. Hayaloglu, S. Cakmakci, E. Y. Brechany, K. C. Deegan, P. L. H. McSweeney, *J. Dairy Sci.* **90** (2007) 1102
20. J. M. Poveda, E. Sánchez-Palomo, M. S. Pérez-Coello, L. Cabezas, *Dairy Sci. Technol.* **88** (2008) 355
21. G. Urbach, *Int. Dairy J.* **3** (1993) 389
22. J. Berard, F. Bianchi, M. Carer, A. Chatel, A. Mangia, M. Musci, *Food Chem.* **105** (2007) 293
23. I. Castillo, M. V. Calvo, L. Alonso, M. Juárez, J. Fontecha, *Food Chem.* **100** (2007) 590
24. M. Correa Lelles Nogueira, G. Luachevsky, S. A. Rankin, *Lebensm.-Wiss. Technol.* **38** (2005) 555
25. A. A. Hayaloglu, I. Karabulut, *Int. J. Food Prop.* **13** (2013) 1630
26. A. A. Hayaloglu, E. Y. Brechany, K. C. Deegan, P. L. H. McSweeney, *LWT-Food Sci. Technol.* **41** (2008) 1323
27. P. Papademas, R. K. Robinson, *Lebensm.-Wiss. Technol.* **35** (2002) 512
28. R. G. Mariaca, T. F. H. Berger, R. Gauch, M. I. Imhof, B. Jeangros, J. O. Bosset, *J. Agric. Food Chem.* **45** (1997) 4423
29. L. Moio, F. Addeo, *J. Dairy Res.* **65** (1998) 317
30. T. Bintis, R. K. Robinson, *Food Chem.* **88** (2004) 435.



Synthesis and characterization of μ -hydroxido- and μ -polycarboxylato-bridged iron(III) complexes with 2,2'-bipyridine

NIKOLA TASIĆ^{1*}, JELENA ROGAN^{2#}, DEJAN POLETI^{2#}, LIDIJA RADOVANOVIĆ^{2#}
and GORAN BRANKOVIĆ^{1#}

¹Department of Materials Science, Institute for Multidisciplinary Research, University of Belgrade, Kneza Višeslava 1, 11030 Belgrade, Serbia and ²Department of General and Inorganic Chemistry, Faculty of Technology and Metallurgy, University of Belgrade, Karnegijeva 4, 11120 Belgrade, Serbia

(Received 28 October 2013, revised 10 January, accepted 17 January 2014)

Abstract: Four novel polymeric iron(III) complexes with 2,2'-bipyridine (bipy) and different aromatic polycarboxylato ligands as anions of phthalic (pht), isophthalic (ipht), terephthalic (tpht) and pyromellitic (pyr) acid were synthesized by ligand exchange reaction. The complexes were characterized by elemental and TG/DSC analysis, FTIR and diffuse reflectance UV–Vis–NIR spectroscopy and magnetic susceptibility measurements. Based on the analytical and spectral data, the formulae of the complexes were $\{[\text{Fe}_4(\text{bipy})_2(\text{H}_2\text{O})_2(\text{OH})_6(\text{pht})_3]\cdot 2\text{H}_2\text{O}\}_n$ (**1**), $\{[\text{Fe}_4(\text{bipy})_2(\text{Hipt})_2(\text{ipht})_2(\text{OH})_6]\cdot 4\text{H}_2\text{O}\}_n$ (**2**), $\{[\text{Fe}_4(\text{bipy})_2(\text{Htpht})_2(\text{OH})_6(\text{tpht})_2]\cdot 4\text{H}_2\text{O}\}_n$ (**3**) and $\{[\text{Fe}_4(\text{bipy})(\text{H}_2\text{O})_8(\text{OH})_4(\text{pyr})_2]\cdot \text{H}_2\text{O}\}_n$ (**4**). All complexes were red brown and low-spin with a distorted octahedral geometry with FeO_6 or FeN_2O_4 chromophores. The polycarboxylato ligands played a bridging role in all cases, whereas monodentate COO groups were present in **2** and **3**, while bridging and chelate COO groups were established in **1** and **4**. The thermal behaviours of **1–4** were investigated in detail and the molar dehydration enthalpies were calculated. According to the all those results, the structural formulae of complexes **1–4** were proposed.

Keywords: mixed ligand complexes; iron(III); 2,2'-bipyridine; polycarboxylato ligands; $\text{Fe}_2(\text{OH})^{4+}$ dimer.

INTRODUCTION

The growing interest in the field of mixed ligand complexes arises from the high structural tunability of these compounds, which directly impacts their magnetic, electrical, optical and catalytic properties. The variety of individual

* Corresponding author. E-mail: nikola.tasic@imsi.bg.ac.rs

Serbian Chemical Society member.

doi: 10.2298/JSC131028005T

building blocks and coordination modes of aromatic polycarboxylates provides a wide range of potentially supramolecular architectures and, consequently, many practical applications. Hitherto, transition metal complexes with polycarboxylato ligands have been utilized in adsorptive hydrogen storage, gas separation, catalysis, and sensitization in dye-solar cells or sensors.^{1–7}

In the past few decades, special interest has been developed towards the implementation of aromatic polycarboxylato ligands as building units, which combined with transition metals and *N,N*-ligands, result in one-, two- or three-dimensional complexes based on covalent bonds, as well as on hydrogen bonding and non-covalent π – π interactions. The most frequently used aromatic polycarboxylato ligands are the dianions of phthalic ($H_2\text{pht}$), isophthalic ($H_2\text{iplt}$) and terephthalic ($H_2\text{tpht}$) acid, together with the tetra-anion of pyromellitic acid ($H_4\text{pyr}$), which usually have a bridging role using numerous donor O atoms from COO groups. A great number of different coordination modes of these polycarboxylates in a variety of transition metal complexes is well understood and explained elsewhere.^{8–18}

The iron(III) ion has been rarely utilized as the metal centre within mixed ligand complexes containing aromatic polycarboxylato and diamine ligands. To the best of our knowledge, there are only two reported crystal structures of this kind. One of them, $[\text{Fe}_2(\text{OH})_2(\text{phen})_2(\text{pyr})]_n$, where phen is 1,10-phenanthroline, is a two-dimensional polymer.¹⁹ The pyr^{4-} ion bridges two Fe(III) ions and it is coordinated by all four COO groups acting as bis-monodentate and bis-chelate ligands. The distorted octahedral environment of the Fe(III) ion consists of three O atoms from two pyr^{4-} ligands, two N atoms from phen and one OH^- group. In the second reported compound, $[\text{Fe}_2(\text{bipy})_2(\text{H}_2\text{O})_2(\text{H}_2\text{pyr})(\text{pyr})]_n$, where bipy is 2,2'-bipyridine,²⁰ the coordination polyhedron of Fe(III) ion is also a distorted octahedron comprising two N atoms from chelate bipy, one O atom from coordinated H_2O , two O atoms from monodentate COO groups of pyr^{4-} and one O atom from $\text{H}_2\text{pyr}^{2-}$. The binuclear units built zig-zag chains, which are further connected in layers and finally form a three-dimensional crystal packing governed by numerous hydrogen bonds.

On the other hand, the hydrolytic behaviour of Fe(III) ions in aqueous solution is much more investigated, and represents solid ground for further research and implementation in the synthesis of mixed ligand Fe(III) complexes. Absorption spectroscopy of different Fe(III) salts in aqueous solutions, over a wide range of concentrations and pH values, revealed that the Fe(III) ions are subjected to hydrolysis and polymerization reactions, leading to the formation of compounds with Fe(OH)^{2+} , Fe(OH)_2^+ or $\text{Fe}_2(\text{OH})_2^{4+}$ as predominant species,^{21–25} and eventually to hydroxido-bridged complexes, such as $[\text{Fe}_2(\text{C}_4\text{O}_4)_2(\text{H}_2\text{O})_4(\text{OH})_2 \cdot 2\text{H}_2\text{O}]^{26}$ $[\text{Fe}_6\text{O}_2(\text{C}_7\text{H}_5\text{O}_2)_{10}(\text{hedmp})_2(\text{OH})_2 \cdot 3\text{CH}_3\text{CN}$, where hedmp is 2-(hydroxyethyl)-3,5-dimethylpyrazole²⁷ and $[\text{Fe}(\text{barbital})(\text{H}_2\text{O})_2(\text{OH})]^{28}$.

In this work, the possibilities of implementing Fe(III) ions as metal centres, starting from Fe(III) nitrate, bipy as diamine ligand and different aromatic polycarboxylates: pht, ipht, tpht and pyr, were investigated. Such compounds should be comparable to the already known mixed ligand Co(II), Ni(II) and Cu(II) complexes of similar composition.^{12,13,29} In the present study, four novel Fe(III) complexes with μ -hydroxido and μ -carboxylato bridges were synthesized by ligand exchange reaction and characterized by elemental and TG/DSC analysis, FTIR and diffuse reflectance UV–Vis–NIR spectroscopy and magnetic susceptibility measurements.

EXPERIMENTAL

Materials

With the exception of 2,2'-bipyridine, which was of *purum* quality, the other reagents were of analytical grade and were used as purchased.

Preparation of the complexes

The complexes were prepared according to the following procedure: a solution of $\text{Fe}(\text{NO}_3)_3 \cdot 6\text{H}_2\text{O}$ (0.01 mol for complexes with pht, ipht and tpht, or 0.02 mol for complex with pyr) in H_2O (200 mL) and a solution of bipy (0.005 mol) in EtOH (15 mL) were first mixed. Then, a dilute solution of $\text{Na}_2\text{pht}/\text{Na}_2\text{ipht}/\text{Na}_2\text{tpht}/\text{Na}_4\text{pyr}$ (0.015 mol) in H_2O (75 mL) was added dropwise at room temperature over about 1.5 h under vigorous magnetic stirring. During this period, the pH value of the solution increased from 2.0 to 3.0. After standing for several days, the formed precipitates were filtered off, washed several times with H_2O , EtOH, and Et_2O and dried at room temperature.

Characterization of the complexes

Elemental analysis was realised by standard analytical micro-methods. The Fourier-transformed infrared spectra were recorded on a Bomem MB-100, Hartmann Braun FTIR spectrophotometer, using KBr pellets, in the region $4000 - 400 \text{ cm}^{-1}$. The diffuse reflectance UV–Vis–NIR spectra, in the region of 200–1400 nm, were taken on a UV-2600 Shimadzu spectrophotometer with an integrating sphere, using BaSO_4 as an internal standard. The recorded data were transformed using the Kubelka–Munk function in order to obtain absorption spectra.^{30–32} The thermal behaviour of the complexes was investigated from room temperature up to 1050 °C using an SDT Q600 TGA/DSC instrument (TA instruments), at a heating rate of $20 \text{ }^{\circ}\text{C min}^{-1}$ under a nitrogen atmosphere (flow rate: $100 \text{ cm}^3 \text{ min}^{-1}$). The magnetic susceptibility measurements were performed at room temperature on an MSB-MK1 magnetic susceptibility balance (Sherwood Scientific Ltd., Cambridge, UK). The data were corrected for diamagnetic susceptibilities.

RESULTS AND DISCUSSION

All complexes were prepared as microcrystalline products from dilute solutions by ligand exchange reactions. The empirical formulae of the complexes based on analytical and spectral data were: $\text{Fe}_4(\text{bipy})_2(\text{OH})_6(\text{pht})_3 \cdot 4\text{H}_2\text{O}$ (**1**), $\text{Fe}_4(\text{bipy})_2(\text{Hipht})_2(\text{ipht})_2(\text{OH})_6 \cdot 4\text{H}_2\text{O}$ (**2**), $\text{Fe}_4(\text{bipy})_2(\text{Htpht})_2(\text{OH})_6(\text{tpht})_2 \cdot 4\text{H}_2\text{O}$ (**3**) and $\text{Fe}_4(\text{bipy})(\text{OH})_4(\text{pyr})_2 \cdot 9\text{H}_2\text{O}$ (**4**). As seen from the formulae, all the obtained compounds were hydrated hydroxido-carboxylato complexes with tetra-

nuclear building units. The mole ratio Fe(III):bipy was 2:1 for **1–3**, and 4:1 for **4**, meaning that the initial ratios of reagents were preserved in the products. In addition to the fully deprotonated polycarboxylates present in all cases, protonated dicarboxylates, H_{ipht} and H_{tphpt}, were found in **2** and **3**. Moreover, complexes **2** and **3** had identical empirical formulae with the only difference being in the polycarboxylato ligand. All complexes contained OH groups, indicating the formation of μ -hydroxido species typical for Fe(III) compounds.^{21–25}

The analytical data of reported complexes are as follows:

*Fe*₄(bipy)₂(OH)₆(pht)₃·4H₂O (**1**). Yield: 51.6 %; M.W.: 1202.22 g mol⁻¹; Anal. Calcd.: C, 43.96; H, 3.52; N, 4.66; H₂O, 5.99 %. Found: C, 44.16; H, 3.35; N, 4.67; H₂O, 5.90 %.

*Fe*₄(bipy)₂(H_{ipht})₂(ipht)₂(OH)₆·4H₂O (**2**). Yield: 54.2 %; M.W.: 1368.35 g mol⁻¹; Anal. Calcd.: C, 45.64; H, 3.54; N, 4.09; H₂O, 5.27 %. Found: C, 44.95; H, 3.37; N, 3.90; H₂O, 5.90 %.

*Fe*₄(bipy)₂(H_{tphpt})₂(OH)₆(tpht)₂·4H₂O (**3**). Yield: 57.8 %; M.W.: 1368.35 g mol⁻¹; Anal. Calcd.: C, 45.64; H, 3.54; N, 4.09; H₂O, 5.27 %. Found: C, 45.24; H, 3.13; N, 4.03; H₂O, 5.27 %.

*Fe*₄(bipy)(OH)₄(pyr)₂·9H₂O (**4**). Yield: 63.6 %; M.W.: 1109.98 g mol⁻¹; Anal. Calcd.: C, 32.46; H, 3.09; N, 2.52; H₂O, 14.61 %. Found: C, 32.20; H, 2.96; N, 2.74; H₂O, 15.14 %.

The total water content was obtained from TG/DSC analysis.

The magnetic moments, calculated from susceptibility measurements at room temperature (Table I), are in accordance with the values reported for low-spin Fe(III) complexes, which are expected to be in the range 2.0–2.5 μ _B, due to a considerable orbital contribution.³³ Although the complexes exhibited a noticeable difference in shade, all were red–brown coloured, which generally corresponds to other known low-spin Fe(III) complexes with octahedral or distorted octahedral geometry.^{33,34} Compounds **2** and **3** were insoluble in water, EtOH and acetone, **1** was partially soluble in H₂O but insoluble in EtOH and acetone; **4** was to some extent soluble in EtOH, but insoluble in H₂O and acetone. Considering their solubility, complexes **1–4** are probably polymeric.

TABLE I. Magnetic moments and selected FTIR spectral data for **1–4**

Complex	$\mu_{\text{eff}} / \mu_{\text{B}}$	$\nu_{\text{as}} / \text{cm}^{-1}$	ν_s / cm^{-1}	$\Delta\nu / \text{cm}^{-1}$	$\Delta\nu_i / \text{cm}^{-1}$
1	2.59	1566	1410	156	157
2	2.38	1588	1385	203	176
3	2.67	1574	1385	189	173
4	2.21	1583	1385	198	193

The presence of OH groups, water molecules, diamine and benzenepoly-carboxylato ligands were confirmed in detail from the FTIR spectra (Fig. 1). Broad O–H stretching vibrations in the region of 3420–3060 cm⁻¹ correspond to

coordinated or uncoordinated water molecules. A weak shoulder at $\sim 3570\text{ cm}^{-1}$ could be assigned to the bridging OH stretch²² in the FTIR spectra of all compounds. Since the shape and the position of the $\nu(\text{OH})$ bands are similar in the spectra of **1–3**, it can be concluded that the number of water molecules in these complexes was the same or very similar. The extremely broad band centred at $\sim 3420\text{ cm}^{-1}$ in spectrum of **4** indicates a larger number of water molecules. Such bands are characteristic for pyr-containing compounds with numerous and short hydrogen bonds.³⁵ Additional confirmation for these conclusions was obtained from the TG analysis (*vide infra*).

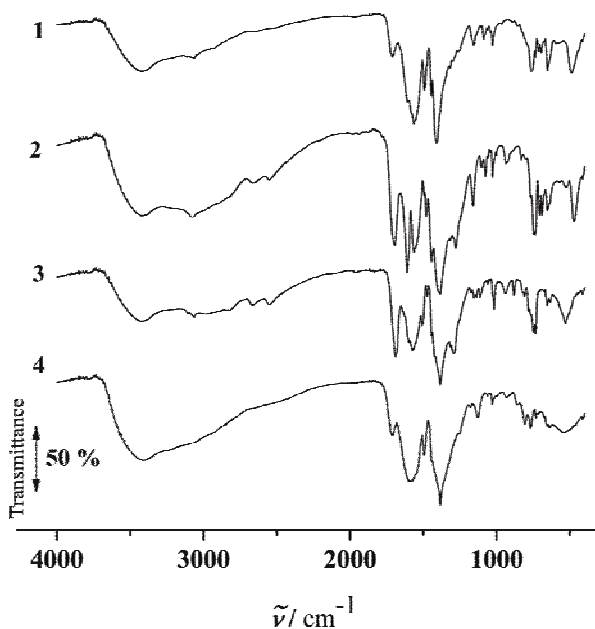


Fig. 1. FTIR spectra of **1–4**.

Characteristic vibrations of the aromatic nuclei: $\nu(\text{C}=\text{C})$, $\nu(\text{C}=\text{N})$ and $\nu(\text{C}-\text{H})$, found in the $1610\text{--}1600$, $1445\text{--}1440$ and $768\text{--}735\text{ cm}^{-1}$ regions, respectively, verify the coordination of the bipy ligand in all the synthesized complexes. The presence of coordinated aromatic polycarboxylato ligands caused the appearance of two very intense bands, due to the asymmetrical (ν_{as}) and symmetrical (ν_{s}) COO vibrations, which are listed in Table I. The difference between these vibrations, $\Delta\nu$, when compared with the “purely ionic” value, $\Delta\nu_i$, for alkaline metal salts Na₂pht (this study), K₂ipht,³⁶ K₂tpht³⁷ and Na₄pyr (this study), predicts the coordination mode of COO groups.³⁸ The significant difference between $\Delta\nu$ and $\Delta\nu_i$ for **2** and **3** suggests a monodentate coordination mode of the COO groups. On the other hand, the small difference between $\Delta\nu$ and $\Delta\nu_i$

indicates a combination of chelate and/or bridging COO groups, such as in **1** and **4**. Besides the $\nu_{as}(\text{COO})$ and $\nu_s(\text{COO})$ vibrations in the FTIR spectra of **2** and **3**, additional pairs of intense bands at 1697 and 1281 cm^{-1} for **2**, and 1690 and 1288 cm^{-1} for **3** confirm the presence of the protonated species Hipt^+ and Htpht^- .³⁸

Close observation of the region between 1000 and 800 cm^{-1} , shown in Fig. 2, provided information about hydrolysis and polymerization tendency of the Fe(III) ions. The asymmetric bands at 858–831 cm^{-1} could be attributed to the Fe–O–Fe unit, while the bands at 962–932 cm^{-1} refer to OH bridging deformation in an $[\text{Fe}-(\text{OH})_2-\text{Fe}]^{4+}$ entity.²²

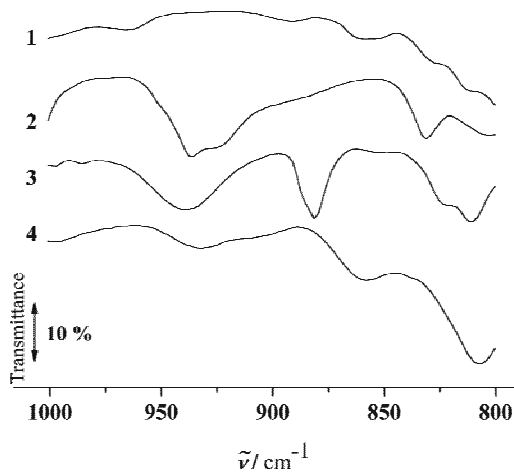
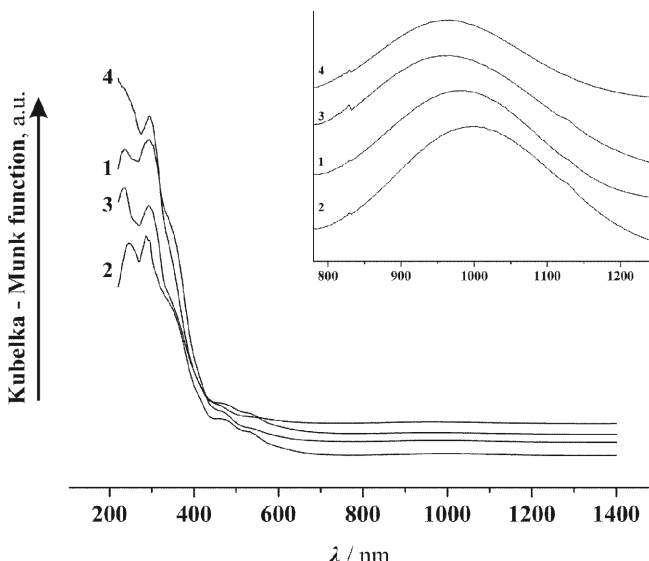


Fig. 2. FTIR spectra of **1–4** in the region 1000–800 cm^{-1} .

Flynn²¹ conducted extensive research regarding the hydrolysis of inorganic Fe(III) salts and established a correlation between the found $\text{OH}^-/\text{Fe}^{3+}$ mole ratio and the pH value of aqueous $\text{Fe}(\text{NO}_3)_3$ solutions. For the mole ratio $\text{OH}^-/\text{Fe}^{3+}$ between 0.5 and 2.5, the pH values of fresh 0.1 and 0.01 mol dm^{-3} solutions were 1.9–2.4 and 2.3–2.8, respectively. Since the initial pH values were ~2.0 in the present case, it could be concluded that the corresponding $\text{OH}^-/\text{Fe}^{3+}$ ratio was within the reported interval 0.5–2.5. This leads to the assumption that during the synthesis of **1–4**, the dominant μ -hydroxido species might be $\text{Fe}_2(\text{OH})_2^{4+}$, *i.e.*, hydroxido-bridged $\text{Fe}(\text{OH})_2^{2+}$ dimers. The confirmation was obtained by the results of UV–Vis–NIR spectroscopic measurements, shown in Fig. 3. All spectra exhibited very prominent peaks at ~235 and ~294 nm and several shoulders at higher wavelengths, which could be attributed to the presence of Fe(III), $\text{Fe}(\text{OH})_2^{2+}$ and $\text{Fe}_2(\text{OH})_2^{4+}$ species.^{25,39} In addition, ${}^4\text{T}_{1g} \rightarrow {}^6\text{A}_{1g}$ energy transitions characteristic for a distorted octahedral environment of low-spin Fe(III) complexes⁴⁰ and the FeO_6 or FeN_2O_4 chromophore⁴¹ were found as weak maxima in the range 956–999 nm (inset in Fig. 3).

Fig. 3. UV-Vis-NIR spectra of **1–4**.

Thermal properties of synthesized complexes were investigated by TG/DSC analysis (Fig. 4). The first significant weight loss corresponded to the dehydration (the H₂O content is listed above), which is a single step process in all four cases, and it was not possible to distinguish between coordinated and uncoordinated water molecules. As seen from the initial, $T_{\text{deh},i}$, and final, $T_{\text{deh},f}$, dehydration temperatures (Table II), complexes **1–3** were easily dehydrated with $T_{\text{deh},f}$ not exceeding 144 °C. In the case of **4**, DSC peak maximum, T_{\max} , corresponding to dehydration, as well as $T_{\text{deh},f}$ were higher in comparison to those for **1–3**, very likely due to the nine H₂O molecules within the formula. According to the DSC curves, the molar dehydration enthalpies, $\Delta_{\text{deh}}H^\circ_m$, for **1–4** were calculated by measuring the area under the peaks. The values $\Delta_{\text{deh}}H^\circ_m$, listed in Table II, varied from 143 to 441 kJ mol⁻¹, as a consequence of the different number of H₂O molecules in the complexes.

Further decomposition of the anhydrous compounds occurred in several not well-separated steps. In the case of **1**, the removal of water was followed by three overlapped steps, with an overall mass loss of 65.9 %, ending at 519 °C, and one additional loss of 12.0 %, ending at 661 °C. These steps could be attributed to the consecutive removal of bipy, pht and OH groups, respectively. In the cases of **2–4**, the thermal decomposition had similar pattern. After the dehydration, the next mass loss corresponded to the elimination of bipy followed by the removal of the polycarboxylato ligand, ending at 524–565 °C, and a final step of about 13 %, after which OH groups were assumed to have been removed. The only noticeable difference between **1** and **2–4** was that the TG curve for **1** dropped suddenly at about

620 °C, which was accompanied by a sharp endothermic DSC maximum, while the analogous processes for **2–4** were slower with broader DSC peaks (Fig. 4).

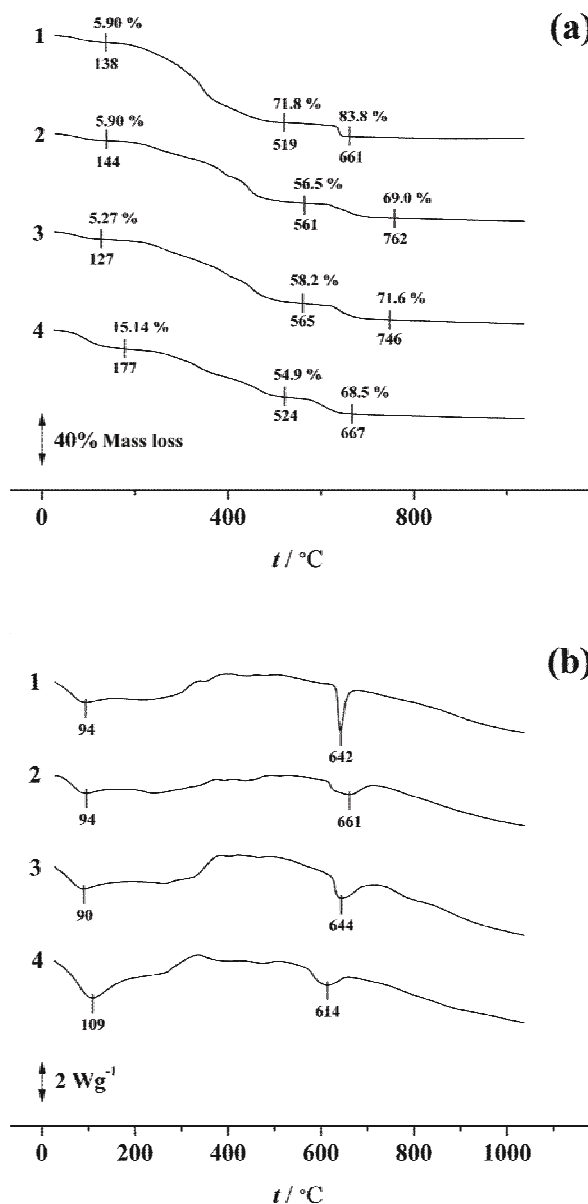


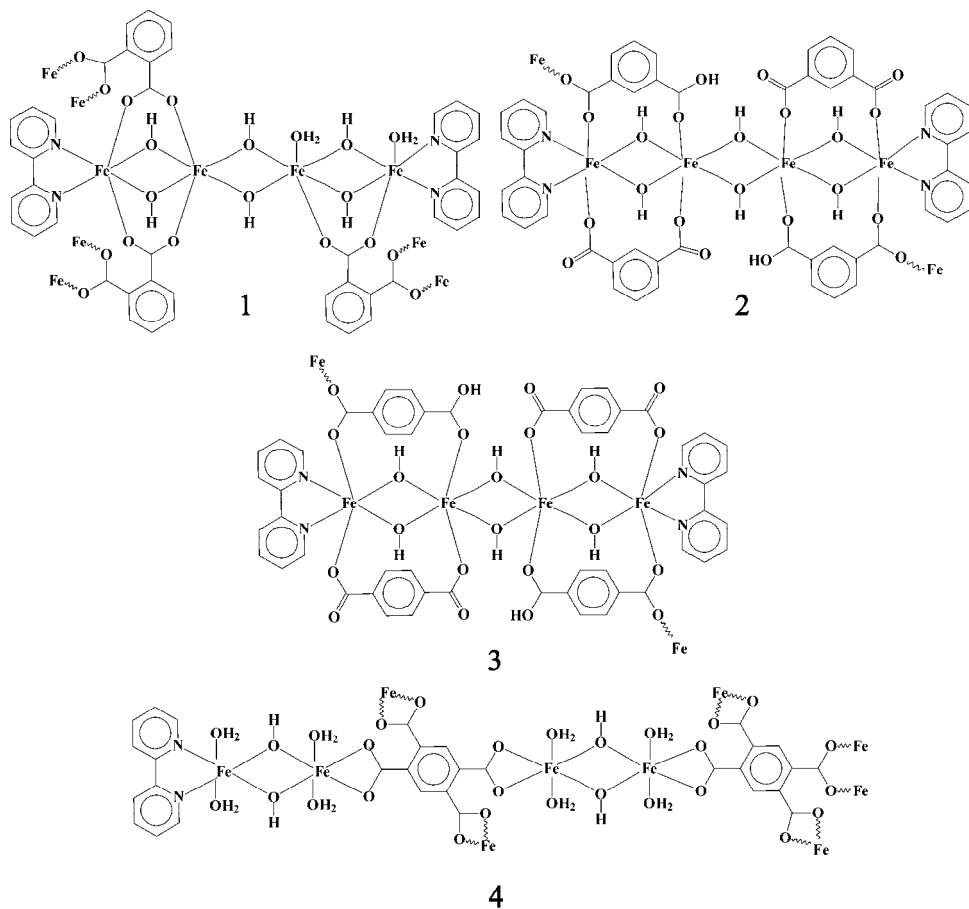
Fig. 4. TG (a) and DSC (b) curves of **1–4**.

Although the final temperature of the decomposition process was insufficient to form pure ferrimagnetic Fe_2O_3 or Fe_3O_4 ,⁴² the black residue exhibited magnetic interactions at room temperature.

TABLE II. Extracted data from the TG and DSC curves

Complex	$T_{\text{deh},i}$ / °C	$T_{\text{deh},f}$ / °C	T_{max} / °C	$\Delta_{\text{deh}}H^\circ_m$ / kJ mol ⁻¹
1	37	138	94	143
2	45	144	94	167
3	35	127	90	170
4	47	177	109	441

Based on the above described analytical and spectral data, and the results of TG/DSC analysis and magnetic measurements, the following structural formulae for complexes **1–4** were proposed: $\{[\text{Fe}_4(\text{bipy})_2(\text{H}_2\text{O})_2(\text{OH})_6(\text{pht})_3]\cdot 2\text{H}_2\text{O}\}_n$ (**1**), $\{[\text{Fe}_4(\text{bipy})_2(\text{Hipht})_2(\text{iplt})_2(\text{OH})_6]\cdot 4\text{H}_2\text{O}\}_n$ (**2**), $\{[\text{Fe}_4(\text{bipy})_2(\text{Htpht})_2(\text{OH})_6(\text{tpht})_2]\cdot 4\text{H}_2\text{O}\}_n$ (**3**) and $\{[\text{Fe}_4(\text{bipy})(\text{H}_2\text{O})_8(\text{OH})_4(\text{pyr})_2]\cdot \text{H}_2\text{O}\}_n$ (**4**), which are shown in Fig. 5.

Fig. 5. Structural formulae of **1–4** (uncoordinated water molecules are not shown).

CONCLUSIONS

Four μ -hydroxido and μ -carboxylato mixed ligand iron(III) complexes, *i.e.*, $\{[Fe_4(bipy)_2(H_2O)_2(OH)_6(pht)_3] \cdot 2H_2O\}_n$ (**1**), $\{[Fe_4(bipy)_2(Hipht)_2(ipht)_2(OH)_6] \cdot 4H_2O\}_n$ (**2**), $\{[Fe_4(bipy)_2(Htpht)_2(OH)_6(tpht)_2] \cdot 4H_2O\}_n$ (**3**) and $\{[Fe_4(bipy)(H_2O)_8(OH)_4(pyr)_2] \cdot H_2O\}_n$ (**4**), were synthesized and characterized. All complexes are polymeric with tetranuclear units, red–brown coloured and low-spin, without noticeable magnetic interactions at room temperature. A distorted octahedral geometry was proposed in all cases. The polycarboxylato ligands play a bridging role in all compounds; while monodentate COO groups were present in **2** and **3**, bridging and chelate COO groups were found in **1** and **4**. The presence of $Fe_2(OH)_2^{4+}$ dimers in **1–4** was confirmed by UV–Vis–NIR spectroscopic measurements. The dehydration and decomposition of the anhydrous compounds were discussed in detail and the calculated molar dehydration enthalpies were in the range of 143–441 kJ mol^{−1}. Furthermore, the structural formulae of the complexes **1–4** were proposed. Attempts to obtain the compounds **1–4** in the single crystal form suitable for X-ray structure analysis are in progress; this could confirm the supposed structural formulae of the complexes.

Acknowledgements. This study was financially supported by the Ministry of Education, Science and Technological Development of the Republic of Serbia (Project No. III45007).

ИЗВОД

**СИНТЕЗА И КАРАКТЕРИЗАЦИЈА ГВОЖЂЕ(III)-КОМПЛЕКСА СА
 μ -ХИДРОКСИДО И μ -ПОЛИКАРБОКСИЛАТО МОСТОВИМА И 2,2'-БИПИРИДИНОМ**
 НИКОЛА ТАСИЋ¹, ЈЕЛЕНА РОГАН², ДЕЈАН ПОЛЕТИ², ЛИДИЈА РАДОВАНОВИЋ² И ГОРАН БРАНКОВИЋ¹

¹Одсек за науку о материјалима, Институт за мултидисциплинарна истраживања, Универзитет у Београду, Кнеза Вишеслава 1, 11030 Београд и ²Кафедра за оштру и неорганску хемију, Технолошко–мешовити факултет, Универзитет у Београду, Карнејевића 4, 11000 Београд

Реакцијом измене лиганада синтетисана су четири нова полимерна комплекса гвожђа(III) са 2,2'-бипирдином (bipy) и различитим ароматичним поликарбоксилатним лигандима, као што су анјони фталне (pht), изофталне (ipht), терефталне (tpht) и пиромелитне (pyr) киселине. Комплекси су окарактерисани елементарном и TG/DSC анализом, FTIR и дифузиона–рефлексионом UV–Vis–NIR спектроскопијом, као и магнетним мерењима. На основу аналитичких и спектралних података, утврђене су следеће формуле комплекса: $\{[Fe_4(bipy)_2(H_2O)_2(OH)_6(pht)_3] \cdot 2H_2O\}_n$ (**1**), $\{[Fe_4(bipy)_2(Hipht)_2(ipht)_2(OH)_6] \cdot 4H_2O\}_n$ (**2**), $\{[Fe_4(bipy)_2(Htpht)_2(OH)_6(tpht)_2] \cdot 4H_2O\}_n$ (**3**) и $\{[Fe_4(bipy)(H_2O)_8(OH)_4(pyr)_2] \cdot H_2O\}_n$ (**4**). Сви комплекси су црвеномрке боје и нискоспински са деформисаном октаедарском геометријом и хромофором типа FeO_6 или FeN_2O_4 . Поликарбоксилатни лиганди имају мостовну улогу код свих једињења, међутим, док код **2** и **3** постоје монодентатне COO^- -групе, код **1** и **4** нађене су мостовне или хелатне COO^- -групе. Детаљно је испитано термичко понашање комплекса **1–4** и израчунате су моларне енталпије дехидратације. На основу свих добијених резултата, предложене су структурне формуле комплекса **1–4**.

(Примљено 28. октобра 2013, ревидирано 10. јануара, прихваћено 17. јануара 2014)

REFERENCES

1. A. S. Polo, M. K. Itokazu, M. Y. M. Iha, *Coord. Chem. Rev.* **248** (2004) 1343
2. S. Qiu, G. Zhu, *Coord. Chem. Rev.* **253** (2009) 2891
3. S. M. Luzan, H. Jung, H. Chun, A. V. Talyzin, *Int. J. Hydrogen Energy* **34** (2009) 9754
4. S. Ferrere, B. A. Gregg, *J. Am. Chem. Soc.* **120** (1998) 843
5. S. Ferrere, *Chem. Mater.* **12** (2000) 1083
6. S. L. James, *Chem. Soc. Rev.* **32** (2003) 276
7. J.-R. Li, Y. Ma, M. C. McCarthy, J. Sculley, J. Yu, H.-K. Jeong, P. B. Balbuena, H.-C. Zhou, *Coord. Chem. Rev.* **255** (2011) 1791
8. E. G. Bakalbassis, A. Terzis, *Inorg. Chim. Acta* **218** (1994) 167
9. D. Poletti, Lj. Karanović, G. A. Bogdanović, A. Spasojević-de Biré, *Acta Crystallogr., C* **55** (1999) 2061 and references therein
10. F. Luo, J.-M. Zheng, G. J. Long, *Cryst. Growth Des.* **9** (2009) 1271
11. W.-Z. Shen, X.-Y. Chen, P. Cheng, S.-P. Yan, B. Zhai, D.-Z. Liao, Z.-H. Jiang, *Eur. J. Inorg. Chem.* (2005) 2297
12. J. Rogan, D. Poletti, Lj. Karanović, G. Bogdanović, A. Spasojević-de Biré, D. M. Petrović, *Polyhedron* **19** (2000) 1415
13. J. Rogan, D. Poletti, Lj. Karanović, Z. Jagličić, *J. Mol. Struct.* **985** (2011) 371 and references therein
14. Lj. Karanović, D. Poletti, J. Rogan, G. A. Bogdanović, A. Spasojević-de Biré, *Acta Crystallogr., Sect. C: Cryst. Struct. Commun.* **58** (2002) m275
15. J. Y. Baeg, S. W. Lee, *Inorg. Chem. Commun.* **6** (2003) 313
16. E. Bakalbassis, P. Bergerat, O. Kahn, S. Jeannin, Y. Jeannin, Y. Dromzee, M. Guillot, *Inorg. Chem.* **31** (1992) 625
17. J. Rogan, D. Poletti, Lj. Karanović, *Z. Anorg. Allg. Chem.* **632** (2006) 133
18. A. M. Atria, G. Corsini, L. Gonzalez, M. T. Garland, R. Baggio, *Acta Crystallogr., C* **65** (2009) m241
19. D.-Q. Chu, J.-Q. Xu, X.-B. Cui, L.-M. Duan, T.-G. Wang, A.-Q. Tang, Y. Xing, Y.-H. Lin, H.-Q. Jia, *Mendeleev Commun.* **11** (2001) 66
20. Z. Shi, L. Li, S. Niu, J. Jin, Y. Chi, L. Zhang, J. Liu, Y. Xing, *Inorg. Chim. Acta* **368** (2011) 101
21. C. M. Flynn Jr., *Chem. Rev.* **84** (1984) 31 and references therein
22. L. Borer, L. Thalken, C. Ceccarelli, M. Glick, J. H. Zhang, W. M. Reiff, *Inorg. Chem.* **22** (1983) 1719
23. G. Lente, I. Fabian, *Inorg. Chem.* **38** (1999) 603
24. G. Lente, M. E. A. Magalhaes, I. Fabian, *Inorg. Chem.* **39** (2000) 1950
25. G. Lente, I. Fabian, *React. Kinet. Catal. Lett.* **73** (2001) 117
26. J. Carranza, J. Sletten, F. Lloret, M. Julve, *Inorg. Chim. Acta* **371** (2011) 13
27. R. Murugavel, N. Gogoi, R. Howlader, R. Clerac, *Inorg. Chim. Acta* **363** (2010) 3004
28. M. S. Masoud, A. M. Ramadan, G. M. El-Ashry, *Thermochim. Acta* **551** (2013) 164
29. J. Rogan, D. Poletti, Lj. Karanović, *J. Serb. Chem. Soc.* **69** (2004) 353
30. P. Kubelka, F. Munk, *Z. Tech. Phys.* **12** (1931) 593
31. P. Kubelka, *J. Opt. Soc. Am.* **38** (1948) 448
32. M. P. Fuller, P. R. Griffiths, *Anal. Chem.* **50** (1978) 1906
33. F. A. Cotton, G. Wilkinson, *Advanced Inorganic Chemistry*, 5th ed., Wiley-Interscience, New York, 1988, p. 720
34. N. N. Greenwood, A. Earnshaw, *Chemistry of the Elements*, 2nd ed., Butterworth-Heinemann, 1997, p. 1090

35. D. C. Luehrs, B. C. Cornilsen, C. B. Lover, T. L. Niels, *Inorg. Chim. Acta* **145** (1988) 81
36. J. F. Arenas, J. I. Marcos, *Spectrochim. Acta A* **35** (1979) 355
37. E. G. Bakalbassis, J. Mrozinski, C. A. Tsipis, *Inorg. Chem.* **25** (1986) 3684
38. a) J. F. Arenas, J. I. Marcos, *Spectrochim. Acta A* **36** (1980) 1075; b) G. B. Deacon, R. J. Phillips, *Coord. Chem. Rev.* **33** (1980) 227
39. C. F. Baes Jr., R. E. Mesmer, *The hydrolysis of cations*, Wiley–Interscience, New York, 1976, p. 232
40. A. B. P. Lever, *Inorganic Chemistry*, 2nd ed., Elsevier, Amsterdam, 1984, p. 452
41. R. Meier, M. Molinier, C. Anson, A. K. Powell, B. Kallies, R. van Eldik, *Dalton Trans.* (2006) 5506
42. P. S. Bassi, B. S. Randhawa, G. K. Bilaspuri, *J. Therm. Anal.* **31** (1986) 1007.



Synthesis, characterization and cytotoxicity of mixed ligand Mn(II), Co(II) and Ni(II) complexes

SOUAD A. OSMAN¹, HANAN A. MOUSA², HISHAM ABDALLAH A. YOSEF¹,
TAGHRID S. HAFEZ¹, ABDALLAH A. EL-SAWY³, MOHAMED M. ABDALLAH⁴
and ASHRAF S. HASSAN^{1*}

¹Department of Organometallic and Organometalloid Chemistry, National Research Centre,
El-Behoos Street, Dokki, P. O. Box 12622, Cairo, Egypt, ²Department of Inorganic
Chemistry, National Research Centre, El-Behoos Street, Dokki, P. O. Box 12622, Cairo,
Egypt, ³Chemistry Department, Faculty of Science, Benha University, Benha, Egypt and
⁴Univet Pharmaceuticals Ltd, Balteem, Egypt

(Received 13 August, revised 31 October, accepted 15 November 2013)

Abstract: Complexes of the type [ML'L(OH)(H₂O)], where M = Ni(II), Co(II) or Mn(II), L' = isatin and HL = 3-(2-phenylhydrazone)acetylacetone, 3-(2-(4-chlorophenyl)hydrazone)acetylacetone or 3-(2-(4-bromophenyl)hydrazone)-acetylacetone, were synthesized by equimolar reaction of a metal(II) chloride with isatin and a 3-(2-arylhydrazone)acetylacetone. The resulting complexes were characterized by elemental analyses, molar conductivity, spectral data (IR and mass spectrometry) and magnetic moments. Furthermore, the ligands and their metal complexes were screened for their cytotoxicity against different human cancer cell lines using the sulforhodamine B (SRB) assay. The results showed that most of the mixed ligand metal complexes have high cytotoxicity in comparison with the reference drugs used.

Keywords: 3-(2-arylhydrazone)acetylacetone; isatin; transition metals; mixed ligands; cytotoxicity.

INTRODUCTION

One of the main goals for research chemists and pharmacologists is the synthesis of novel bioactive compounds for the development of better drugs to fight diseases. Thus, coordination chemistry has developed very rapidly mainly in the last 15 years since many ligands of no or low biological activity become more active when transferred to their metal complexes^{1,2} and some drugs show increased activity when administered as metal complexes.^{3–5} In addition, complexes containing heterocyclic ligands having nitrogen and/or sulfur have inc-

*Corresponding author. E-mail: Ashraf_salmoon@yahoo.com
doi: 10.2298/JSC130813134O

reased biological activities compared to the original ligands.^{6,7} Recently, there is an increasing interest in the synthesis of mixed ligand metal complexes due to their biological significance. These complexes play important roles in biological processes since enzymes are known to be activated by metal ions.^{8,9} Moreover, they have wide antituberculosis, antifungal,¹⁰ antibacterial¹¹ and antitumor^{12,13} pharmacological activities.

A literature survey reveals that isatin (indole-2,3-dione) and its derivatives shows a wide range of antimicrobial,¹⁴ anticonvulsant,¹⁵ anticancer^{16,17} and anti-HIV activities.¹⁸ On the other hand, arylhydrazone-1,3-diketone derivatives have been widely used as intermediates in the preparation of a large number of biologically important heterocyclic compounds.^{19–21}

In view of these facts and continuing our interest in the synthesis of compounds with promising biological activities,^{22,23} Ni(II), Co(II) and Mn(II) complexes of 3-(2-arylhydrazone)acetylacetone with isatin were prepared and characterized by IR and UV–Vis spectroscopy, elemental analyses, molar conductivity and magnetic susceptibility measurements. The study was extended to screen the ligands and their metal complexes against different human cancer cell lines.

EXPERIMENTAL

Chemistry

All melting points were measured on a Gallenkamp melting point apparatus and are uncorrected. The IR spectra were recorded (KBr disk) on a Perkin-Elmer 1650 FT-IR instrument. The ¹H-NMR (500 MHz) spectra were recorded on a Varian 500 MHz spectrometer in DMSO-*d*₆ using TMS as an internal standard. The FAB mass spectra of the complexes were recorded on a JEOL JMS/AX-500 mass spectrometer. Elemental analyses were obtained from the Micro Analytical Data Center at Cairo University, Egypt. The magnetic susceptibilities were measured at 20 °C by the Gouy method at the Faculty of Science, Cairo University. The electronic absorption spectra were recorded on a PG Instruments Ltd., +80+ automatic UV–Vis spectrophotometer in DMSO. The molar conductance values of solutions of the metal complexes in DMF (10⁻³ mol L⁻¹) were measured using Metrohem 660 conductivity meter.

Acetylacetone, *p*-chloroaniline, *p*-bromoaniline, aniline, sodium acetate, methanol and hydrochloric acid were of Merck AR grade, Germany. Isatin was supplied by Riedel de Haën AG, Germany. The employed NiCl₂·6H₂O, CoCl₂·6H₂O and MnCl₂·4H₂O salts (Fluka, Germany) were of AR grade.

Preparation of 3-(arylhydrazone)acetylacetones

The 3-(arylhydrazone)acetylacetone derivatives (HL) were prepared by coupling acetylacetone with different diazonium salts. Thus, a solution of acetylacetone (0.01 mol) and sodium acetate (5 g) in ethanol (50 mL) was cooled to 0–5 °C and then the diazonium salt (0.01 mol) was added under stirring. The reaction was allowed to proceed at 0–5 °C for 30 min. The 3-(arylhydrazone)acetylacetone derivatives were precipitated and collected by filtration, washed with cold deionized water and recrystallized from ethanol.²⁴

Preparation of the complexes 1–9

A solution of the metal chloride (3.4 mmol) in a minimum amount of water was added to a hot solution of the mixed ligand (3.4 mmol) in methanol, whereby a clear solution was obtained. The pH was increased from 6.0 to 8.0 with dilute NaOH solution. The mixture was refluxed under stirring for 6 h. The formed complex was filtered off, washed several times with hot methanol and dried under reduced pressure.

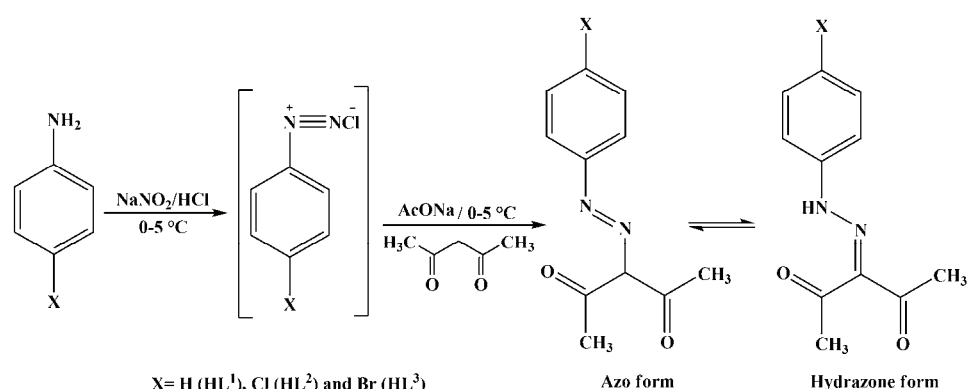
Biological experiments

In vitro cytotoxicity screening. The tested compounds were subjected to *in vitro* disease-oriented primary antitumor screening. Different tumor cell lines were utilized. The human tumor cell lines of the cancer screening panel were grown in RPMI 1640 medium containing 5 % fetal bovine serum and 2 mM L-glutamine. In a typical screening experiment, 100 µL of cells were inoculated into 96-well microtiter plates at plating densities ranging from 5000 to 40000 cells well⁻¹, depending on the doubling time of the individual cell lines. After cell inoculation, the microtiter plates were incubated at 37 °C, 5 % CO₂, 95 % air and 100 % relative humidity for 24 h prior to the addition of the experimental drugs. After 24 h, two plates of each cell line were also fixed *in situ* with trichloroacetic acid (TCA) to represent a measurement of the cell population for each cell line at the time of drug addition (T_0). Experimental drugs were solubilized in DMSO at 400-fold of the desired final maximum test concentration and stored frozen prior to use. At the time of drug addition, an aliquot of frozen concentrate was thawed and diluted to 2-times the desired final maximum test concentration with complete medium containing 50 µg ml⁻¹ gentamicin. Four additional 10-fold or 0.5log serial dilutions were made to provide a total of five drug concentrations plus a control. Aliquots of 100 µL of these different drug dilutions were added to the appropriate microtiter wells already containing 100 µL of medium, resulting in the required final drug concentrations. Following drug addition, the plates were incubated for an additional 48 h at 37 °C, 5 % CO₂, 95 % air and 100 % relative humidity. For adherent cells, the assay was terminated by the addition of cold TCA. The cells were fixed *in situ* by the gentle addition of 50 µL of cold 50 % (w/V) TCA (final concentration, 10 % TCA) and incubated for 60 min at 4 °C. The supernatant layer was discarded and the plates were washed five times with tap water and air-dried. Sulforhodamine B (SRB) solution (100 µL) at 0.4 % (w/V) in 1 % acetic acid was added to each well and the plates were incubated for 10 min at room temperature. After staining, the unbound dye was removed by washing five times with 1 % acetic acid and the plates were air dried. The bound stain was subsequently solubilized with 10 mM Trizma® base and the absorbance was read on an automated plate reader at a wavelength of 515 nm. For suspension cells, the methodology was the same except that the assay was terminated by fixing the settled cells at the bottom of the wells by gently adding 50 µL of 80 % TCA (final concentration, 16 % TCA). The parameter IC_{50} which is the concentration of the drugs inducing a 50% inhibition of cell growth of treated cells when compared to the growth of control cells.^{25–27}

RESULTS AND DISCUSSION

Chemistry

The ligands. The 3-(arylhydrazono)acetylacetone derivatives (HL) are prepared *via* coupling between diazotized aromatic amine derivatives and acetylacetone in a 1:1 molar ratio according to Scheme 1.²⁴ The structures of these ligands were confirmed by elemental analyses and their spectral data (IR and ¹H-NMR), which are discussed later with their metal complexes.



Scheme 1. Synthesis of 3-(arylhydrazone)acetylacetone derivatives (HL).

The complexes. Reactions of the hydrated metal(II) chloride with 3-(arylhydrazone)acetylacetone and isatin in equimolar ratios resulted in formation of the complexes **1–9**, shown in Scheme 2.

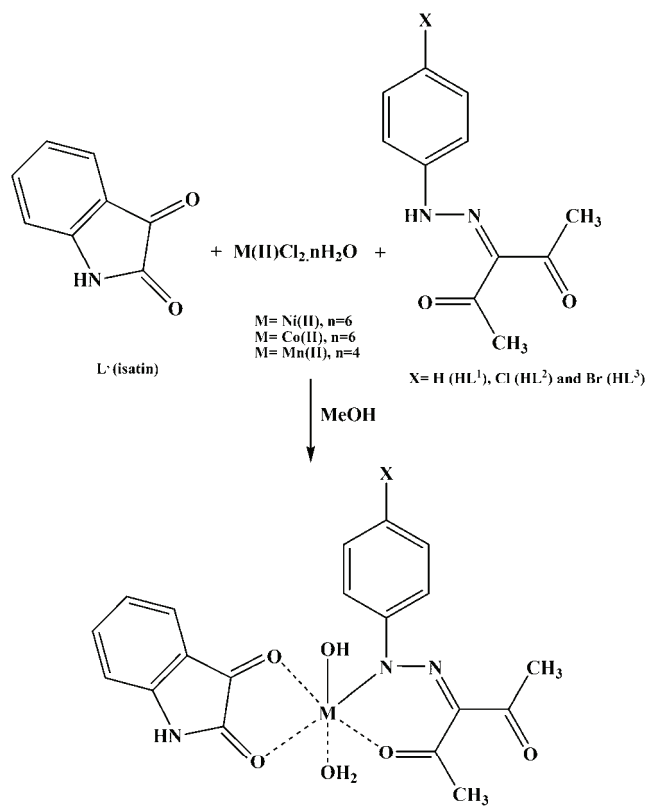
The physical, analytic and spectral data for the ligand and their metal complexes are given in the Supplementary material to this paper.

Infrared spectra of the ligands and their complexes

In the infrared spectra of the ligands (HL¹, HL² and HL³), the broad band in the range 3428–3086 cm^{−1} indicates the existence of strong intramolecular hydrogen bonding.²⁸ Furthermore, there are two strong bands at 1673 and 1623 cm^{−1} assignable to $\nu(\text{C}=\text{O}$, free) and $\nu(\text{C}=\text{O}$, hydrogen bonded), respectively. The $\nu(\text{C}=\text{N})$ band appears at 1593 cm^{−1}, which remains almost unaffected in the spectra of all the complexes suggesting that the nitrogen atom is not involved in the coordination, while the $\nu(\text{C}=\text{O})$ band at 1623 cm^{−1} is shifted to lower frequencies in the spectra of the complexes, suggesting that this oxygen atom is involved in the coordination, while the carbonyl group at \approx 1673 cm^{−1} remains almost unchanged in the spectra. The prominent band present at \approx 1518 cm^{−1} of the ligands is due to $\delta(\text{N}-\text{H})$ vibrations, which disappears in the spectra of all the complexes because of the replacement of the hydrazone NH proton with a metal ion. The infrared spectrum of isatin (L') shows a band at 3191 due to $\nu(\text{N}-\text{H})$ and two $\nu(\text{C}=\text{O})$ group absorptions at 1745 and 1731 cm^{−1}. The IR spectra of the complexes show that the two carbonyl groups of isatin ligand are shifted to lower frequency, suggesting that both groups are involved in the coordination, while $\nu(\text{N}-\text{H})$ at 3191 cm^{−1} is not changed, indicating that the (N-H) group is not involved in the coordination.

Conclusive evidence of bonding was also given by the observation that new bands in the spectra of all metal complexes **1–9** appear in the low frequency regions at 493–438 and 584–540 cm^{−1} characteristic of $\nu(\text{M}-\text{O})$ and $\nu(\text{M}-\text{N})$

stretching vibrations, respectively.²⁹ Furthermore, the observed broad band at 3550 cm⁻¹ in all complexes were attributed to the OH group and the OH stretching vibrations of lattice water molecules.¹⁰



Complexes	M(II)	X	Complexes	M(II)	X
1	Ni	H	6	Mn	Cl
2	Co	H	7	Ni	Br
3	Mn	H	8	Co	Br
4	Ni	Cl	9	Mn	Br
5	Co	Cl			

Scheme 2. Synthesis of mixed ligand complexes of the type [ML'L(OH)(H₂O)].

Nuclear magnetic resonance of the ligands

The ¹H-NMR spectrum of HL revealed a single proton at $\delta \approx 14.02$ ppm due to the N–H···O=C group.^{30,31} The ¹H-NMR spectrum of HL² is illustrated in Fig. S-1 of the Supplementary material to this paper.

Mass spectra of the complexes

The molecular ion peaks in the mass spectra of some complexes were used to confirm the molecular formula. Thus, the mass spectra of the Ni(II) complexes confirmed the molecular formulas, *e.g.*, $[NiL'L^1(OH)(H_2O)]$ and $[NiL'L^3(OH)(H_2O)]$ confirmed $C_{19}H_{19}N_3NiO_6$ and $C_{19}H_{18}BrN_3NiO_6$, respectively. Similarly, the mass spectra of the Co(II) complexes confirmed the molecular formulas, *e.g.*, $[CoL'L^2(OH)(H_2O)]$ and $[CoL'L^3(OH)(H_2O)]$ confirmed the molecular formulas $C_{19}H_{18}ClCoN_3O_6$ and $C_{19}H_{18}BrCoN_3O_6$, respectively. Moreover, the mass spectrum of the Mn(II) complex, *e.g.*, $[MnL'L^3(OH)(H_2O)]$ confirmed the molecular formula $C_{19}H_{18}BrMnN_3O_6$.

Electronic spectra and magnetic moments

The UV-visible spectra of the free ligands HL^1 , HL^2 , HL^3 and L' showed absorption bands at 292–297 and 418–440 nm due to $\pi\rightarrow\pi^*$ and $n\rightarrow\pi^*$ transitions, respectively. These bands were blue- or red-shifted in the spectra of the complexes due to coordination in the ligands.

The Mn(II) complexes **3**, **6** and **9** exhibited two weak bands at 618–622 and 520–526 nm which were attributed to $^6A_{1g}\rightarrow ^4T_{1g}(^4G)$ and $^6A_{1g}\rightarrow ^4T_{2g}(^4G)$ transitions, respectively. These absorptions are consistent with an octahedral geometry around the Mn(II) atom. The magnetic moment values of the Mn(II) complexes were in the range of 5.82–5.90 μ_B , corresponding to five unpaired electrons, which is also indicative of octahedral geometry.³³

The electronic spectra of the Co(II) complexes **5** and **8** showed two d-d transitions in the ranges 654–661 and 540–548 nm due to the $^4T_{1g}(F)\rightarrow ^4A_{2g}(F)$ and $^4T_{1g}(F)\rightarrow ^4A_{2g}(p)$ transitions, respectively, indicating an octahedral configuration around the Co(II) atom. The $^4T_{2g}(F)\rightarrow ^4T_{1g}(F)$ transition (1237–1242 nm) would be observed in the near IR region. This region was out the range of the employed spectrophotometer.³⁴ The μ_{eff} values for the Co(II) complexes were in the range 4.87–4.94 μ_B , which are similar to those reported for octahedral Co(II).³⁵

The Ni(II) complexes **1**, **4** and **7** exhibited two absorption bands in the ranges 963–988 and 572–581 nm, which are assigned to $^3A_{2g}(F)\rightarrow ^3T_{2g}(F)$ and $^3A_{2g}(F)\rightarrow ^3T_{1g}(F)$ transitions, respectively. However, the absorption bands at 420–422 nm due to $^3A_{2g}(F)\rightarrow ^3T_{1g}(p)$ was overlapped with the ligand absorption bands. The spectra of these complexes support an octahedral stereochemistry around the Ni(II) atom. The room temperature magnetic moment values of the Ni(II) complexes were 3.17–3.20 μ_B , which are in the normal range observed for octahedral Ni(II) complexes.³⁶

Molar conductance measurements

The molar conductivities of 10^{-3} mol L⁻¹ solutions of the complexes in DMF were measured at room temperature. The results were in the range 22.1–11.6 Ω⁻¹ cm² mol⁻¹, indicating that all the metal complexes had molar conductance values in the range characteristic for non-electrolytes.³⁷

Biological activity

In vitro cytotoxicity screening. The cytotoxicities of the mixed ligand complexes [ML'L(OH)(H₂O)], the ligands HL¹–HL³ and L' were determined using the SRB assay on different human cancer cell lines including: cervical carcinoma (KB), ovarian carcinoma (SK OV-3), CNS cancer (SF-268), non-small cell lung cancer (NCI H460), colon adenocarcinoma (RKOP 27) (Table I), anti-leukemia (HL60, U937, K562), melanoma (G361, SK-MEL-28) and neuroblastoma (GOTO, NB-1) (Table II). The cytotoxic effect of the ligands and their metal complexes [ML'L(OH)(H₂O)] on the cell lines HeLa (cervical), MCF-7 (breast), HT1080 (fibrosarcoma) and HepG2 (liver) were also tested (Table III). The results are expressed as the IC_{50} , which is the concentration of a drug that causes a 50 % reduction in the proliferation of cancer cells when compared to the growth of the control cells.

TABLE I. Cytotoxicity (IC_{50} / nM, the concentration required for 50 % inhibition of cell growth) of the ligands and the mixed ligand complexes determined by using SRB assay on different human cancer cell lines; the values for most potent compound are marked by “*”

The ligands and their metal complexes	Cell line				
	KB	SK OV-3	SF-268	NCI H460	RKOP27
L'	4.40	5.40	4.50	0.65	7.50
HL ¹	6.70	5.46	0.35*	0.89	2.30*
1	0.32*	3.20	0.55	0.44	4.30
2	4.40	3.40	3.50	0.40*	5.50
3	5.60	6.70	0.43	0.56	7.60
HL ²	9.80	8.80	9.90	0.68	4.50
4	0.55	0.55*	5.60	0.66	7.80
5	0.45	8.80	0.50	0.43	8.80
6	0.45	7.60	0.40	0.67	6.40
HL ³	0.65	0.67	4.50	0.87	4.80
7	8.00	7.70	0.75	0.57	4.30
8	0.67	5.60	0.65	0.43	4.50
9	0.90	0.89	0.85	0.84	2.30*
Fluorouracil	4.46	—	—	—	—
Doxorubicin	—	4.16	—	—	—
Cytarabine	—	—	7.68	—	—
Gemcitabine HCl	—	—	—	2.13	—
Capecitabine	—	—	—	—	4.33

TABLE II. Cytotoxicity (IC_{50} / nM, the concentration required for 50 % inhibition of cell growth) of the ligands and the mixed ligand complexes determined by using SRB assay on different human cancer cell lines; the values for most potent compound are marked by “*”

The ligands and their metal complexes	Cell line						
	Leukemia			Melanoma		Neuroblastoma	
	HL60	U937	K562	G361	SK-MEL-28	GOTO	NB-1
L'	8.00	6.80	3.70	0.43*	5.00	0.65	4.80
HL ¹	6.50	7.70	0.87	0.87	4.00	3.00	3.60
1	0.75	9.00	0.60	0.57	4.00	6.80	9.87
2	5.30	5.40	5.40	0.77	5.00	5.87	3.00
3	3.40	7.30	0.60	0.88	1.00*	7.60	4.00
HL ²	6.00	8.70	9.00	0.50	8.00	7.50	2.30
4	0.44	0.65	6.00	8.80	4.00	0.57	0.70
5	0.56	3.50	0.68	0.64	6.00	0.68	0.69
6	0.32*	6.00	0.90	0.59	8.00	0.67	0.56
HL ³	0.67	0.43*	6.40	0.54	7.00	4.70	0.36*
7	8.00	6.30	0.40*	0.70	8.00	0.50	7.60
8	0.33	8.00	0.50	0.70	7.00	0.34*	9.00
9	0.80	0.79	8.00	0.60	8.00	0.56	0.65
Doxorubicin	1.13	4.45	6.66	—	—	4.73	5.15
Aldesleukin	—	—	—	6.66	3.45	—	—

TABLE III. Cytotoxicity (IC_{50} / nM, the concentration required for 50 % inhibition of cell growth) of the ligands and the mixed ligand complexes determined by using SRB assay on different human cancer cell lines; the values for most potent compound are marked by “*”

The ligands and their metal complexes	Cell line			
	HeLa (cervical)	MCF-7 (breast)	HT1080 (fibrosarcoma)	HepG2 (liver)
L'	0.449	3.650	7.86	2.30
HL ¹	9.860	0.790	0.45	0.64
1	0.009*	9.600	0.09*	0.80
2	7.680	8.400	8.69	0.79
3	0.897	4.587	0.54	0.47
HL ²	6.600	7.600	5.80	3.64
4	0.780	0.900	3.65	0.77
5	5.640	4.970	0.99	0.91
6	0.600	0.764	0.87	0.89
HL ³	0.960	5.800	2.50	0.54*
7	6.500	9.600	0.86	8.50
8	0.770	4.600	7.00	0.79
9	0.444	0.760*	0.59	6.50
Tamoxifen	0.114	0.155	1.16	1.31

Screening the cytotoxicity of the mixed ligand complexes [ML'L(OH)(H₂O)] and the ligands HL¹, HL², HL³ and L' on cervical carcinoma (KB), where 5-fluorouracil was used as a standard drug ($IC_{50} = 4.46$ nM), shows that the complexes **1**, **4**, **5**, **6**, **8**, and **9**, and the ligand HL³ were more potent than the standard drug.

In the case of the ovarian carcinoma (SK OV-3) cell line, the tested complexes **4** and **9** and the ligand HL³ (IC_{50} = 0.55, 0.89 and 0.67 nM, respectively) were found to be more potent than the standard drug doxorubicin (IC_{50} = 4.16 nM).

Studying the cytotoxicity of the tested complexes and the ligands on the CNS cancer (SF-268) cell line using cytarabine (IC_{50} = 7.68 nM) as a standard drug, reveals that all the tested complexes and the ligands except HL² (IC_{50} = 9.90 nM) were more potent than the standard drug.

In the case of the non-small cell lung cancer (NCI H460) cell line, all of the tested complexes and the ligands were found to be more potent than the standard drug gencitabine hydrochloride (IC_{50} = 2.13 nM).

In the case of the colon adenocarcinoma (RKOP 27) cell line, the ligand HL¹ and the complex **9** (IC_{50} = 2.30 nM) were found to be more potent than the standard drug capecitabine (IC_{50} = 4.33 nM).

The study of the cytotoxicity on the leukemia (HL60) cell line indicated that the ligands L', HL¹, HL² and the complexes **2**, **3** and **7** were less potent compounds than doxorubicin (IC_{50} = 1.13 nM).

In the case of the leukemia (U937) cell line, the ligand HL³ (IC_{50} = 0.43 nM) was the most potent, while complex **1** (IC_{50} = 9.00 nM) was the least bioactive.

In the case of the leukemia (K562) cell line, the tested complexes and the ligands, except ligand HL² and complex **9**, were more active than the standard drug doxorubicin (IC_{50} = 6.66 nM); the ligand HL³ and complex **4** had activity comparable to that of doxorubicin.

On estimation of the cytotoxicity on the melanoma (G361) cell line, the tested complexes and the ligands, except complex **4** (IC_{50} = 8.80 nM) were more active than the standard drug aldesleukin (IC_{50} = 6.66 nM).

In the case of the melanoma (SK-MEL-28) cell line, the tested complexes and the ligands were less active than the standard drug Aldesleukin (IC_{50} = 3.45 nM), except complex **3** that was more active (IC_{50} = 1.00 nM).

Cytotoxicity of the tested complexes and the ligands on neuroblastoma (GOTO) cell line showed that complex **8** was the most potent (IC_{50} = 0.34 nM) and more active than the standard drug doxorubicin (IC_{50} = 4.73 nM).

In the case of the neuroblastoma (NB-1) cell line, complex **2** was less active than the standard drug doxorubicin (IC_{50} = 5.15 nM), while ligand HL³ (IC_{50} = 0.36 nM) was the most active.

The cytotoxicity of the tested complexes and the ligands on the HeLa (cervical) cell line showed that complex **1** (IC_{50} = 0.009 nM) was the most potent and more active than the standard drug tamoxifen (IC_{50} = 0.114 nM).

In the case of the MCF-7 (breast) cell line, the standard drug tamoxifen (IC_{50} = 0.155 nM) was more active than all the other tested complexes and ligands.

In the case of the HT1080 (fibrosarcoma) cell line, complex **1** ($IC_{50} = 0.09$ nM) was the most potent and complex **2** ($IC_{50} = 8.69$ nM) was found to be less potent than tamoxifen ($IC_{50} = 1.16$ nM).

The cytotoxicity of the tested complexes and the ligands on the HepG2 (liver) cell line shows that the complexes **1–6** and **8**, and the ligands HL³ and HL¹ were more active than the standard drug tamoxifen ($IC_{50} = 1.16$ nM), whereby complex **3** ($IC_{50} = 0.47$ nM) was the most promising one.

CONCLUSIONS

Ni(II), Co(II) and Mn(II) complexes of 3-(2-arylhydrazono)acetylacetone (HL) and isatin (L') were synthesized. The ligands (L' and HL¹–HL³) act as bidentate molecules, whereby L' was coordinated through two oxygen atoms while the 3-(2-arylhydrazono)acetylacetones were coordinated by oxygen and nitrogen atoms. The prepared complexes **1–9**, which were non-electrolytes, have octahedral geometry with the general structural formula [ML'L(OH)(H₂O)]. The cytotoxicity results of the ligands and their complexes **1–9** against different human cancer cell lines indicated that most of the complexes exhibited high cytotoxicity at very low concentrations in comparison with the reference drugs considered.

SUPPLEMENTARY MATERIAL

Physical, analytic and spectral data of the ligands and complexes are available electronically at <http://www.shd.org.rs/JSCS/>, or from the corresponding author on request.

ИЗВОД

СИНТЕЗА, КАРАКТЕРИЗАЦИЈА И ЦИТОТОКСИЧНА АКТИВНОСТ КОМПЛЕКСА МАНГАНА(II), КОБАЛТА(II) И НИКЛА(II) СА МЕШОВИТИМ ЛИГАНДИМА

SOUAD A. OSMAN¹, HANAN A. MOUSA², HISHAM ABDALLAH A. YOSEF¹, TAGHRID S. HAFEZ¹, ABDALLAH A. EL-SAWY³, MOHAMED M. ABDALLAH⁴ и ASHRAF S. HASSAN¹

¹Department of Organometallic and Organometalloid Chemistry, National Research Centre, El-Behoos Street, Dokki, P. O Box 12622, Cairo, Egypt, ²Department of Inorganic Chemistry, National Research Centre, El-Behoos Street, Dokki, P. O. Box 12622, Cairo, Egypt, ³Chemistry Department, Faculty of Science, Benha University, Benha, Egypt и ⁴Univet Pharmaceuticals Ltd, Balteem, Egypt

У реакцијама одговарајућег метал(II)-хлорида са изатином и 3-(2-арилхидразоно)акетилацетоном синтетизовани су комплекси опште формуле [ML'L(OH)(H₂O)] (где је M = Ni(II), Co(II) или Mn(II), L' = изатин и HL = 3-(2-фенилхидразоно)акетилацетон, 3-(2-(4-хлорфенил)хидразоно)акетилацетон или 3-(2-(4-бромфенил)хидразоно)акетилацетон). Комплекси су охарактерисани применом елементалне микронализе, спектроскопских метода (IR спектроскопија и масена спектрометрија) и мерењем моларне проводљивости и магнетног момента. Испитивана је цитотоксична активност лиганда и комплекса на различитим туморским ћелијским линијама применом SRB теста. Добијени резултати су показали да већина комплекса показује већу цитотоксичну активност у поређењу са стандардним лековима.

(Примљено 13. августа, ревидирано 31. октобра, прихваћено 15. новембра 2013)

REFERENCES

- A. S. Abd-El-All, A. A. Labib, H. A. Mousa, F. A. Bassyouni, K. H. Hegab, M. A. El-Hashash, S. R. Atta-Allah, W. H. AbdEl-Hady, S. A. M. Osman, *J. Appl. Sci. Res.* **9** (2013) 469
- E. A. Elzahany, K. H. Hegab, S. K. H. Khalil, N. S. Youssef, *Aust. J. Basic Appl. Sci.* **2** (2008) 210
- A. Furst, R. A. Haro, *Prog. Exp. Tumor Res.* **12** (1969) 102
- D. R. Williams, *Chem. Rev.* **72** (1972) 203
- M. J. M. Campbell, *Coord. Chem. Rev.* **15** (1975) 279
- M. A. Ali, S. E. Livingstone, *Coord. Chem. Rev.* **13** (1974) 101
- K. Severin, R. Bergs, W. Beck, *Angew. Chem. Int. Ed.* **37** (1998) 1634
- A. S. Mildvan, J. S. Leigh, M. Cohn, *Biochemistry* **6** (1967) 1805
- A. S. Mildvan, M. C. Scrutton, M. F. Utter, *J. Biol. Chem.* **241** (1966) 3488
- G. J. Kharadi, J. R. Patel, B. Z. Dholakiya, *Appl. Organomet. Chem.* **24** (2010) 821
- P. K. Panchal, D. H. Patel, M. N. Patel, *Synth. React. Inorg. Met.-Org. Chem.* **34** (2004) 1223
- F. Arjmand, M. Muddassir, R. H. Khan, *Eur. J. Med. Chem.* **45** (2010) 3549
- N. Raman, R. Jeyamurugan, R. Senthilkumar, B. Rajk Kapoor, S. G. Franzblau, *Eur. J. Med. Chem.* **45** (2010) 5438
- S. N. Pandeya, S. Smitha, M. Jyoti, S. K. Sridhar, *Acta Pharm. (Zagreb, Croatia)* **55** (2005) 27
- S. N. Pandeya, A. S. Raja, J. P. Stables, *J. Pharm. Pharm. Sci.* **5** (2002) 266
- V. R. Solomon, C. Hu, H. Lee, *Bioorg. Med. Chem.* **17** (2009) 7585
- K. L. Vine, J. M. Locke, M. Ranson, S. G. Pyne, J. B. Bremner, *Bioorg. Med. Chem.* **15** (2007) 931
- T. R. Bal, B. Anand, P. Yogeeshwari, D. Sriram, *Bioorg. Med. Chem. Lett.* **15** (2005) 4451
- I. V. Kravtsov, P. A. Belyakov, S. V. Baranin, V. A. Dorokhov, *Russ. Chem. Bull. Int. Ed.* **56** (2007) 1561
- P. K. Sharma, S. Kumar, P. Kumar, P. Kaushik, D. Kaushik, Y. Dhingra, K. R. Aneja, *Eur. J. Med. Chem.* **45** (2010) 2650
- M. George, M. Jolocam, B. Odongkara, H. Twinomuhwezi, G. B. Mpango, *Res. J. Chem. Sci.* **1** (2011) 102
- S. A. Osman, H. A. A. Yosef, T. S. Hafez, A. A. El-Sawy, H. A. Mousa, A. S. Hassan, *Aust. J. Basic Appl. Sci.* **6** (2012) 852
- T. S. Hafez, S. A. Osman, H. A. A. Yosef, A. S. Abd El-All, A. S. Hassan, A. A. El-Sawy, M. M. Abdallah, M. Youns, *Sci. Pharm.* **81** (2013) 339
- a) M. H. Helal, G. H. Elgemeie, M. A. El-Kashouti, M. M. ElMolla, H. S. Elsayad, K. A. Ahmed, *Pigm. Resin Technol.* **37** (2008) 234; b) D. Mijin, G. Uscumlić, N. Perisic-Janjić, I. Trkulja, M. Radetić, P. Jovancić, *J. Serb. Chem. Soc.* **71** (2006) 435; c) K. T. Mahmudov, A. M. Maharramov, R. A. Aliyeva, I. A. Aliyev, R. K. Askerov, R. Batmaz, M. N. Kopylovich, A. J. L. Pomeiro, *J. Photochem. Photobiol., A* **219** (2011) 159
- M. R. Grever, S. A. Schepartz, B. A. Chabner, *Sem. Oncol.* **19** (1992) 622
- M. R. Boyd, K. D. Paull, *Drug Dev. Res.* **34** (1995) 91
- A. Monks, D. Scudiero, P. Skehan, R. Shoemaker, K. Paull, D. Vistica, C. Hose, J. Langley, P. Cronise, A. Vaigro-Wolff, M. Gray-Goodrich, H. Campbell, J. Mayo, M. Boyd, *J. Natl. Cancer Inst.* **83** (1991) 757
- K. Krishnankutty, M. B. Ummathur, P. Ummer, *J. Serb. Chem. Soc.* **74** (2009) 1273
- P. B. Pansuriya, M. N. Patel, *Appl. Organomet. Chem.* **21** (2007) 739

30. A. Mitchell, D. C. Nonhebel, *Tetrahedron* **35** (1979) 2013
31. A. Lyčka, J. Jirman, A. Cee, *Magn. Reson. Chem.* **28** (1990) 408
32. A. G. Evans, J. C. Evans, B. A. El-Shetary, C. C. Rowlands, P. H. Morgan, *J Coord. Chem.* **9** (1979) 19
33. A. Katiyar, V. P. Singh, *J. Coord. Chem.* **61** (2008) 3200
34. B. K. Singh, P. Mishra, B. S. Garg, *Spectrochim. Acta, A* **69** (2008) 880
35. Z. H. Abd El-Wahab, *Spectrochim. Acta, A* **67** (2007) 25
36. E. K. Efthimiadou, Y. Sanakis, N. Katsaros, A. Karaliota, G. Psomas, *Polyhedron* **26** (2007) 1148
37. K. D. A. Domopoulou, M. A. Demertzis, A. Papageorgiou, *J. Inorg. Biochem.* **68** (1997) 147.



SUPPLEMENTARY MATERIAL TO
**Synthesis, characterization and cytotoxicity of mixed ligand
Mn(II), Co(II) and Ni(II) complexes**

SOUAD A. OSMAN¹, HANAN A. MOUSA², HISHAM ABDALLAH A. YOSEF¹,
TAGHRID S. HAFEZ¹, ABDALLAH A. EL-SAWY³, MOHAMED M. ABDALLAH⁴
and ASHRAF S. HASSAN^{1*}

¹Department of Organometallic and Organometalloid Chemistry, National Research Centre,
El-Behoos Street, Dokki, P. O. Box 12622, Cairo, Egypt, ²Department of Inorganic
Chemistry, National Research Centre, El-Behoos Street, Dokki, P. O. Box 12622, Cairo,
Egypt, ³Chemistry Department, Faculty of Science, Benha University, Benha, Egypt and
⁴Univet Pharmaceuticals Ltd, Balteem, Egypt

J. Serb. Chem. Soc. 79 (8) (2014) 953–964

PHYSICAL, ANALYTIC AND SPECTRAL DATA FOR THE LIGANDS

3-(2-Phenylhydrazone)acetylacetone (HL^1). Yield: 86 %; Yellow needles;
m.p.: 86–87 °C; Anal. Calcd. for $C_{11}H_{12}N_2O_2$ (FW: 204.23): C, 64.69; H, 5.92;
N, 13.72 %. Found: C, 64.50; H, 6.10; N, 13.65 %; IR (KBr, cm^{-1}): 3430–3092
(N–H···O=C, hydrogen bonded), 1673 (C=O, free), 1623 (C=O, hydrogen
bonded), 1593 (C=N), 1518 (N–H); ^1H -NMR (500 MHz, DMSO- d_6 , δ / ppm)
2.36 (3H, s, CH_3CO free), 2.43 (3H, s, CH_3CO hydrogen bonded), 7.16 (1H, t,
 J = 8.5 Hz, aromatic), 7.27 (2H, t, J = 8.5 Hz, aromatic), 7.52 (2H, d, J = 8.5 Hz,
aromatic), 14.02 (1H, s, D_2O exchangeable, NH).

3-(2-(4-Chlorophenyl)hydrazone)acetylacetone (HL^2). Yield: 86 %;
Yellow needles; m.p.: 147–148 °C; Anal. Calcd. for $C_{11}H_{11}\text{ClN}_2O_2$ (FW:
238.67): C, 55.36; H, 4.65; N, 11.74 %. Found: C, 55.50; H, 4.52; N, 11.80 %; IR
(KBr, cm^{-1}): 3432–3094 (N–H···O=C, hydrogen bonded), 1667 (C=O, free),
1625 (C=O, hydrogen bonded), 1589 (C=N), 1519 (N–H); ^1H -NMR (500
MHz, DMSO- d_6 , δ / ppm) 2.37 (3H, s, CH_3CO free), 2.42 (3H, s, CH_3CO
hydrogen bonded), 7.43 (2H, d, J = 8.4 Hz, aromatic), 7.57 (2H, d, J = 8.4 Hz,
aromatic), 13.81 (1H, s, D_2O exchangeable, NH).

3-(2-(4-Bromophenyl)hydrazone)acetylacetone (HL^3). Yield 86 %; Yellow
needles; m.p.: 141–142 °C; Anal. Calcd. for $C_{11}H_{11}\text{BrN}_2O_2$ (FW: 283.12): C,
46.66; H, 3.92; N, 9.89 %. Found: C, 46.50; H, 4.10; N, 10.00 %; IR (KBr, cm^{-1}):
3422–3073 (N–H···O=C, hydrogen bonded), 1667 (C=O, free), 1623 (C=O,
hydrogen bonded), 1585 (C=N), 1513 (N–H); ^1H -NMR (500 MHz, DMSO- d_6 ,

*Corresponding author. E-mail: Ashraf_salmoon@yahoo.com

δ / ppm) 2.37 (3H, s, CH₃CO free), 2.42 (3H, s, CH₃CO hydrogen bonded), 7.50 (2H, d, *J* = 9.15 Hz, aromatic), 7.56 (2H, d, *J* = 9.15 Hz, aromatic), 13.75 (1H, s, D₂O exchangeable, NH).

Isatin (L'). IR (KBr, cm⁻¹): 3191 (N–H), 1745 (C=O), 1731 (C=O); ¹H-NMR (500 MHz, DMSO-*d*₆, δ / ppm): 6.88 (1H, d, *J* = 7.7 Hz, aromatic), 7.03 (1H, t, *J* = 7.7 Hz, aromatic), 7.46 (1H, d, *J* = 7.7 Hz, aromatic), 7.54 (1H, t, *J* = 7.7 Hz, aromatic), 10.98 (1H, s, D₂O exchangeable, NH).

PHYSICAL, ANALYTIC AND SPECTRAL DATA FOR THE COMPLEXES

[NiL'L'(OH)(H₂O)] (**1**). Yield 50 %; Greenish yellow; m.p.: 215–218 °C; Anal. Calcd. for C₁₉H₁₉N₃NiO₆ (FW: 444.06): C, 51.39; H, 4.31; N, 9.46 %. Found: C, 51.50; H, 4.25; N, 9.55 %; IR (KBr, cm⁻¹): 3522 (O–H), 3181 (N–H, L'), 1717 (C=O, L'), 1709 (C=O, L'), 1667 (C=O free, L¹), 1600 (C=O coordinated, L¹), 1590 (C=N, L¹), 583 (Ni–N), 493 (Ni–O); UV–Vis (DMSO) (λ_{max} / nm): 963, 576, 420; magnetic moment ($\mu_{\text{eff}} / \mu_{\text{B}}$): 3.17; molar conductivity (DMF, *c* / 10⁻³ mol L⁻¹, $A_{\text{m}} / \Omega^{-1} \text{cm}^2 \text{mol}^{-1}$): 11.6.

[CoL'L'(OH)(H₂O)] (**2**). Yield 53 %; Dark green; m.p.: 209–211 °C; Anal. Calcd. for C₁₉H₁₉CoN₃O₆ (FW: 444.30): C, 51.36; H, 4.31; N, 9.46 %. Found: C, 51.55; H, 4.25; N, 9.55 %; IR (KBr, cm⁻¹): 3580 (O–H), 3183 (N–H, L'), 1715 (C=O, L'), 1707 (C=O, L'), 1669 (C=O free, L¹), 1602 (C=O coordinated, L¹), 1591 (C=N, L¹), 584 (Co–N), 491 (Co–O); UV–Vis (DMSO) (λ_{max} / nm): 654, 540 nm; magnetic moment ($\mu_{\text{eff}} / \mu_{\text{B}}$): 4.92; molar conductivity (DMF, *c* / 10⁻³ mol L⁻¹, $A_{\text{m}} / \Omega^{-1} \text{cm}^2 \text{mol}^{-1}$): 12.8.

[MnL'L'(OH)(H₂O)] (**3**). Yield 45 %; Green; m.p. 210–212 °C; Anal. Calcd. for C₁₉H₁₉MnN₃O₆ (FW: 440.31): C, 51.83; H, 4.35; N, 9.54 %. Found: C, 51.70; H, 4.40; N, 9.47 %; IR (KBr, cm⁻¹): 3544 (O–H), 3182 (N–H, L'), 1719 (C=O, L'), 1711 (C=O, L'), 1661 (C=O free, L¹), 1605 (C=O coordinated, L¹), 1590 (C=N, L¹), 540 (Mn–N), 487 (Mn–O); UV–Vis. (DMSO) (λ_{max} / nm): 752, 618, 520 nm; magnetic moment ($\mu_{\text{eff}} / \mu_{\text{B}}$): 5.82; molar conductivity (DMF, *c* / 10⁻³ mol L⁻¹, $A_{\text{m}} / \Omega^{-1} \text{cm}^2 \text{mol}^{-1}$): 15.4.

[NiL'L²(OH)(H₂O)] (**4**). Yield 60 %; Greenish yellow; m.p.: 217–220 °C; Anal. Calcd. for C₁₉H₁₈CIN₃NiO₆ (FW: 478.51): C, 47.69; H, 3.79; N, 8.78 %. Found: C, 47.50; H, 3.70; N, 8.70 %; IR (KBr, cm⁻¹): 3565 (O–H), 3180 (N–H, L'), 1715 (C=O, L'), 1707 (C=O, L'), 1661 (C=O free, L²), 1605 (C=O coordinated, L²), 1585 (C=N, L²), 579 (Ni–N), 448 (Ni–O); UV–Vis (DMSO) (λ_{max} / nm): 988, 581, 422 nm; magnetic moment ($\mu_{\text{eff}} / \mu_{\text{B}}$): 3.20; molar conductivity (DMF, *c* / 10⁻³ mol L⁻¹, $A_{\text{m}} / \Omega^{-1} \text{cm}^2 \text{mol}^{-1}$): 20.5.

[CoL'L²(OH)(H₂O)] (**5**). Yield 58 %; Dark green; m.p.: 207–209 °C; Anal. Calcd. for C₁₉H₁₈ClCoN₃O₆ (FW: 478.75): C, 47.67; H, 3.79; N, 8.78 %. Found: C, 47.50; H, 3.85; N, 8.70 %; IR (KBr, cm⁻¹): 3553 (O–H), 3186 (N–H, L'), 1716 (C=O, L'), 1708 (C=O, L'), 1662 (C=O free, L²), 1602 (C=O coordinated,

L^2), 1584 (C=N, L^2), 572 (Co–N), 438 (Co–O); UV–Vis (DMSO) (λ_{\max} / nm): 661, 548 nm; magnetic moment (μ_{eff} / B.M.): 4.94; molar conductivity (DMF, $c / 10^{-3}$ mol L $^{-1}$, $A_m / \Omega^{-1} \text{cm}^2 \text{mol}^{-1}$): 22.1.

$[MnL'L^2(OH)(H_2O)]$ (6). Yield 55 %; Greenish yellow; m.p.: 216–219 °C; Anal. Calcd. for $C_{19}H_{18}ClMnN_3O_6$ (FW: 474.75): C, 48.07; H, 3.82; N, 8.85 %. Found: C, 48.20; H, 3.75; N, 8.80 %; IR (KBr, cm $^{-1}$): 3550 (O–H), 3183 (N–H, L'), 1718 (C=O, L'), 1710 (C=O, L'), 1661 (C=O free, L^2), 1605 (C=O coordinated, L^2), 1580 (C=N, L^2), 569 (Mn–N), 444 (Mn–O); UV–Vis (DMSO) (λ_{\max} / nm): 758, 622, 526 nm; magnetic moment (μ_{eff} / μ_B): 5.90; molar conductivity (DMF, $c / 10^{-3}$ mol L $^{-1}$, $A_m / \Omega^{-1} \text{cm}^2 \text{mol}^{-1}$): 19.8.

$[NiL'L^3(OH)(H_2O)]$ (7). Yield 53 %; Greenish yellow; m.p.: 223–226 °C; Anal. Calcd. for $C_{19}H_{18}BrN_3NiO_6$ (FW: 522.96): C, 43.64; H, 3.47; N, 8.04 %. Found: C, 43.50; H, 3.55; N, 8.00 %; IR (KBr, cm $^{-1}$): 3575 (O–H), 3184 (N–H, L'), 1722 (C=O, L'), 1711 (C=O, L'), 1660 (C=O free, L^3), 1600 (C=O coordinated, L^3), 1580 (C=N, L^3), 578 (Ni–N), 447 (Ni–O); UV–Vis (DMSO) (λ_{\max} / nm): 979, 572, 420 nm; magnetic moment (μ_{eff} / μ_B): 3.19; molar conductivity (DMF, $c / 10^{-3}$ mol L $^{-1}$, $A_m / \Omega^{-1} \text{cm}^2 \text{mol}^{-1}$): 18.7.

$[CoL'L^3(OH)(H_2O)]$ (8). Yield: 51 %; Greenish yellow; m.p.: 212–215 °C; Anal. Calcd. for $C_{19}H_{18}BrCoN_3O_6$ (FW: 523.20): C, 43.62; H, 3.47; N, 8.03 %. Found: C, 43.80; H, 3.40; N, 8.10 %; IR (KBr, cm $^{-1}$) 3535 (O–H), 3184 (N–H, L'), 1719 (C=O, L'), 1707 (C=O, L'), 1662 (C=O free, L^3), 1601 (C=O coordinated, L^3), 1582 (C=N, L^3), 584 (Co–N), 481 (Co–O); UV–Vis (λ_{\max} / nm): 659, 544 nm; magnetic moment (μ_{eff} / μ_B): 4.87; molar conductivity (DMF, $c / 10^{-3}$ mol L $^{-1}$, $A_m / \Omega^{-1} \text{cm}^2 \text{mol}^{-1}$): 16.9.

$[MnL'L^3(OH)(H_2O)]$ (9). Yield: 45 %; Green; m.p.: 215–218 °C; Anal. Calcd. for $C_{19}H_{18}BrMnN_3O_6$ (FW: 519.20): C, 43.95; H, 3.49; N, 8.09 %. Found: C, 44.10; H, 3.40; N, 8.15 %; IR (KBr, cm $^{-1}$): 3545 (O–H), 3182 (N–H, L'), 1721 (C=O, L'), 1712 (C=O, L'), 1661 (C=O free, L^3), 1602 (C=O coordinated, L^3), 1582 (C=N, L^3), 571 (Mn–N), 472 (Mn–O); UV–Vis (DMSO) (λ_{\max} / nm): 755, 621, 524 nm; magnetic moment (μ_{eff} / μ_B): 5.87; molar conductivity (DMF, $c / 10^{-3}$ mol L $^{-1}$, $A_m / \Omega^{-1} \text{cm}^2 \text{mol}^{-1}$): 17.3.

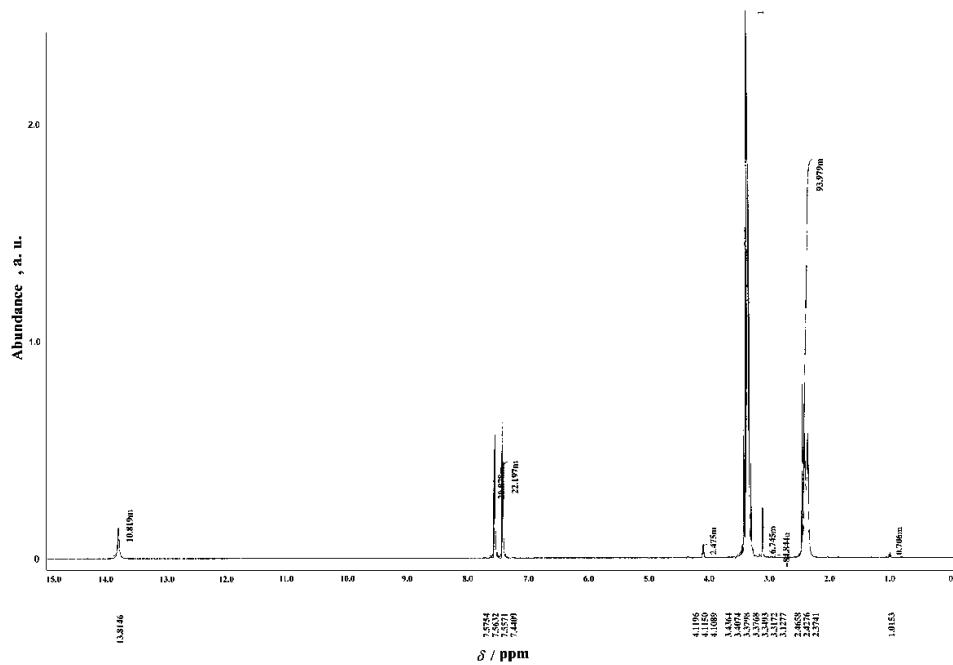
NMR SPECTRA OF HL^2 

Fig. S-1. The ${}^1\text{H}$ -NMR spectrum of 3-(2-(4-chlorophenyl)hydrazone)acetylacetone (HL^2).



QSPR study on the gas/particle partition coefficient of polychlorinated biphenyls using the molecular distance-edge vector index

LONG JIAO^{1,2*}, XIAOFEI WANG¹, HUA LI² and YUNXIA WANG²

¹College of Chemistry and Chemical Engineering, Xi'an Shiyou University, Xi'an 710065, P. R. China and ²College of Chemistry and Materials Science, Northwest University, Xi'an 710069, P. R. China

(Received 27 November, accepted 12 December 2013)

Abstract: The quantitative structure property relationship (QSPR) for the gas/particle partition coefficient, K_p , of polychlorinated biphenyls (PCBs) was investigated. Molecular distance-edge vector (MDEV) index was used as the structural descriptor of the PCBs. The quantitative relationship between the MDEV index and $\log K_p$ was modeled by multivariate linear regression (MLR) and artificial neural network (ANN), respectively. The leave-one-out cross validation and external validation were performed to assess the prediction ability of the developed models. When the MLR method was used, the root mean square relative error (*RMSRE*) of the prediction for the leave-one-out cross validation and external validation were 4.72 and 8.62, respectively. When the ANN method was employed, the prediction *RMSRE* of the leave-one-out cross validation and the external validation were 3.87 and 7.47, respectively. It was demonstrated that the developed models are practicable for predicting the K_p of PCBs. The MDEV index was shown to be quantitatively related to the K_p of PCBs.

Keywords: QSPR; PCBs; gas/particle partition coefficient; molecular distance-edge vector index; artificial neural network.

INTRODUCTION

Polychlorinated biphenyls (PCBs) are a group of poly halogenated organic compounds that are persistent organic pollutants. They have gained much attention due to their environmental persistence, high toxicity, tendency to bioaccumulate through the food chain, and risk to human health.^{1–3} PCBs are used in various industrial applications as organic diluents, plasticizers, and paint additives, etc. It is estimated that hundreds of million of kilograms of PCBs have

*Corresponding author. E-mail: mop@xsysu.edu.cn
doi: 10.2298/JSC130611152J

been released into the environment due to inappropriate disposal practices and accidental releases.⁴ Although the production and use of PCBs have been banned in most countries, PCBs have already become ubiquitous pollutants in all environmental compartments, including water, air, vegetation, soil and animals, worldwide.⁵ A total of 209 theoretical PCBs exist and approximately 150 have been found in the environment.⁶ Being semi-volatile organic compounds, PCBs in the atmosphere are simultaneously present in the gas and particle phase. The gas/particle partition behavior of PCBs in the atmosphere may affect their fate, transport and transformation in the atmosphere. Thus, a quantitative study on gas/particle partition coefficient, K_p , which is a parameter for describing the gas/particle partition behavior of PCBs, is useful for an understanding of the environment fate, transport, and transformation of PCBs.^{7–9} Many studies focusing on the gas/particle partition coefficient of PCBs have been reported and several methods for determining the K_p of PCBs were proposed.^{7–12} However, the experimental determination of K_p is still difficult due to the complexity of the analytical methods and the high cost of experiments.¹³ Therefore, attention has been paid to the quantitative structure–property relationship (QSPR) method, which is fast, easy-to-use and cost-effective, for a preliminary assessment and the estimation of K_p of PCBs. Thus, a QSPR model for the K_p of PCBs based on quantum chemical descriptors was recently studied by Wei *et al.*¹³ However, it is also time-consuming and complicated to develop a QSPR model based on quantum chemical descriptors, because the calculation and selection of the structural descriptors, which are always time-consuming and complicated, are still necessary to establish the model. Obviously, it is still worthwhile to develop an easy-to-use QSPR model for the K_p of PCBs. The topological index is a structural descriptor that has frequently been used in the field of QSPR research. It can efficiently describe the structure of molecules without the need for detailed molecular orbital calculations. This is useful because, despite its mathematical simplicity, it is able to differentiate molecules with different structures.¹⁴ Thus, the aim of the present study was to develop a QSPR model for the K_p of PCBs based on the topological index. The molecular distance-edge vector (MDEV) index, which has not gained sufficient attention in QSPR research although having been used in a few QSPR studies,^{15–17} was introduced and employed as the structural descriptor of PCBs. Multivariate linear regression (MLR) and artificial neural network (ANN) methods were applied in the modeling of the quantitative relationship between the MDEV index and $\log K_p$ of PCBs.

CALCULATION AND EXPERIMENTAL

Data set

The MDEV index was calculated according to the approach presented later. The calculated MDEV indexes for the PCBs are listed in Table I. The experimental $\log K_p$ values of the 41 PCBs listed in Table II were taken from the literature.¹³

TABLE I. Values of the MDEV index of the investigated PCBs

Group	No.	PCB	μ_1	μ_2
I	1	2,4'	0.0204	2.1510
	2	2,3,4'	0.1471	3.2140
	3	2,2',3,3'	0.3382	4.3470
	4	2,2',3,5'	0.2671	4.3470
	5	2,2',4,5'	0.2063	4.3250
	6	2,3',4,4'	0.2498	4.2540
	7	2,3',4',5	0.2353	4.2760
	8	2,4,4',5	0.2498	4.2540
	9	2,2',3,4,5'	0.6143	5.3870
	10	2,2',4,4',5	0.4127	5.3650
	11	2,2',4',5,5'	0.4056	5.3870
	12	2,3,3',4',6	0.4571	5.3650
	13	2,2',3,3',4,4'	0.7698	6.4270
	14	2,2',3,4,4',5'	0.6987	6.4270
	15	2,2',3,3',4,4',5	1.0470	7.4900
	16	2,2',3,4,4',5,5'	0.9761	7.4900
II	17	2,3'	0.0278	2.1740
	18	2,2',4	0.1229	3.2620
	19	2,2',5	0.1078	3.2850
	20	2,3',4'	0.1059	3.2140
	21	2,4,4'	0.0953	3.1910
	22	2,4',5	0.0760	3.2140
	23	3,4,4'	0.1391	3.1430
	24	2,2',5,5'	0.1960	4.3470
	25	3,3',4,4'	0.2862	4.2050
	26	2,2',3,4',5'	0.4767	5.3870
	27	2,2',3,5',6	0.4374	5.4580
	28	2,3,3',4,4'	0.5080	5.3160
	29	2,3',4,4',5	0.4369	5.3160
	30	2,3',4',4',5'	0.4668	5.3160
	31	2,2',3,4',5',6	0.6674	6.4980
	32	2,2',4,4',5,5'	0.5790	6.4270
	33	2,2',3,5,5',6	0.6991	6.5210
	34	2,3,3',4,4',6	0.7212	6.3650
	35	2,2',3,3',4,5,6'	0.7806	6.4980
	36	2,2',3,3',4,5',6'	1.0160	7.5610
	37	2,2',3,4,4',5',6	0.9519	7.5380
	38	2,2',3,4',5,5',6	0.9375	7.5610
	39	2,3,3',4,4',5,5'	1.0150	7.3790
	40	2,2',3,3',4,4',5,5'	1.3450	8.5520
	41	2,2',3,3',4,4',6	1.0230	7.5383

The root mean square relative error (*RMSRE*) was used to indicate the prediction performance of the obtained QSPR model. The *RMSRE* is defined as follows:

$$RMSRE = \sqrt{\frac{\sum (RE_i)^2}{n}} \quad (1)$$

where RE_i is the relative error of the i^{th} sample and n is the number of samples.

TABLE II. Experimental and predicted $\log K_p$ values of the investigated PCBs

Group	No.	Experimental $\log K_p$	Predicted $\log K_p$	Relative error, %
I	1	-4.60	-4.44	-3.39
	2	-4.03	-4.13	2.53
	3	-3.72	-3.64	-2.03
	4	-3.80	-3.67	-3.39
	5	-3.89	-3.68	-5.41
	6	-3.58	-3.73	4.23
	7	-3.54	-3.72	5.16
	8	-3.63	-3.71	2.21
	9	-3.26	-3.18	-2.49
	10	-3.35	-3.30	-1.38
	11	-3.39	-3.28	-3.28
	12	-3.19	-3.27	2.43
	13	-2.67	-2.79	4.37
	14	-2.79	-2.80	0.36
	15	-2.29	-2.28	-0.49
	16	-2.36	-2.32	-1.69
II	17	-4.45	-4.43	-0.55
	18	-4.27	-4.10	-3.91
	19	-4.35	-4.10	-5.66
	20	-4.03	-4.08	1.27
	21	-4.09	-4.09	0.10
	22	-4.10	-4.10	-0.03
	23	-3.84	-4.07	6.02
	24	-3.88	-3.74	-3.72
	25	-3.10	-3.69	18.90
	26	-3.29	-3.25	-1.17
	27	-3.74	-3.27	-12.69
	28	-3.16	-3.24	2.62
	29	-3.05	-3.28	7.45
	30	-3.25	-3.27	0.51
	31	-2.85	-2.81	-1.40
	32	-2.88	-2.88	0.08
	33	-2.97	-2.79	-6.23
	34	-2.84	-2.82	-0.82
	35	-2.47	-2.74	10.90
	36	-2.57	-2.30	-10.58
	37	-2.50	-2.34	-6.21
	38	-2.63	-2.35	-10.77
	39	-2.04	-2.31	13.31
	40	-1.85	-1.82	-1.42
	41	-2.06	-2.26	9.91

MDEV index

For calculating the MDEV index of a molecule, each non-hydrogen atom is regarded as a point and each chemical bond is regarded as an edge. The whole molecule is regarded as a geometric graph. When dealing with PCBs, the molecular structure of PCBs can be encoded by the MDEV index of chlorine atoms and benzene rings. If the relative electronegativity of each chlorine atom and benzene ring is defined as 1, the *MDEV* index can be defined follows:

$$M_{kl} = \sum_{j \geq i} \left(\frac{1}{d_{ik,jl}^2} \right) \quad k, l = 1, 2 \text{ and } l \geq k \quad (2)$$

where k and l denote the type of an atom ($k = 1$ or $l = 1$ denotes a chlorine atom, and $k = 2$ or $l = 2$ denotes a benzene ring). In addition, i and j are the coding number of a chlorine atom or benzene ring in the molecular skeleton graph. Moreover, i and j belong to the k^{th} and l^{th} type, respectively. The term $d_{ik,jl}$ expresses the shortest relative distance between the i^{th} and j^{th} atom. For example, $d_{i1,j1}$ is the nearest relative distance between the i^{th} and j^{th} chlorine atom. The relative bond length between the two adjacent non-hydrogen atoms is defined as $d = 1$. According to Eq. (2), there are three elements, M_{11} , M_{12} and M_{22} in the MDEV index for a PCB molecule. The three elements are usually noted as μ_1 , μ_2 and μ_3 , respectively. For example, the MDEV index of 2,2',3,5'-PCB should be calculated as follows:

$$\begin{aligned} \mu_1 &= M_{11} = \left(\frac{1}{3} \right)^2 + \left(\frac{1}{5} \right)^2 + \left(\frac{1}{6} \right)^2 + \left(\frac{1}{6} \right)^2 + \left(\frac{1}{7} \right)^2 + \left(\frac{1}{5} \right)^2 = 0.6271 \\ \mu_2 &= M_{12} = \left(\frac{1}{1} \right)^2 + \left(\frac{1}{3} \right)^2 + \left(\frac{1}{1} \right)^2 + \left(\frac{1}{3} \right)^2 + \left(\frac{1}{1} \right)^2 + \left(\frac{1}{4} \right)^2 + \left(\frac{1}{1} \right)^2 + \left(\frac{1}{4} \right)^2 = 4.3472 \\ \mu_3 &= M_{22} = \left(\frac{1}{1} \right)^2 = 1 \end{aligned} \quad (3)$$

Obviously, the M_{22} value of every PCB is 1. Thus, μ_1 and μ_2 are used to describe the structure of PCBs.

Artificial neural networks

As the theory of ANN has been described in detail by many introductory articles,¹⁸⁻²⁸ only a brief outline of an ANN is presented here.

An ANN is a multivariate calibration method capable of modeling complex functions. Its basic processing unit is the neuron (node). An ANN comprises a number of neurons organized in different layers. A linear artificial neural network (L-ANN),²⁴⁻²⁸ which is usually used to develop a linear model, is a neural network having no hidden layers, but an output layer with fully linear neurons (that is, linear neurons with a linear activation function). In an L-ANN, the neurons between the input and output layers fully connect, while the neurons in the same layer do not. The basic architecture of an L-ANN is presented in Fig. 1.

In Fig. 1, x_i ($i = 1, 2, \dots, n$), y_j ($j = 1, 2, \dots, m$) and w_{ij} are the input variables, output variables and the element of connection weight matrix \mathbf{W} , respectively. b_j is the bias vector, which corresponds to the thresholds. The symbol $f_{\text{act}}(\mathbf{x})$ denotes the activation function. Prior to the training procedure, the input and output variables require normalization. When the network is executed, it effectively multiplies the input variables by the weights matrix, and then adds the bias vector. Hence, the postsynaptic potential (PSP) function of the neuron could be described as follows:

$$v_j = \sum_{i=1}^n x_i \mathbf{W}_{ij} + b_j \quad (4)$$

Routinely, the activation function used in an L-ANN is a linear function described as:

$$y_j = v_j \quad (5)$$

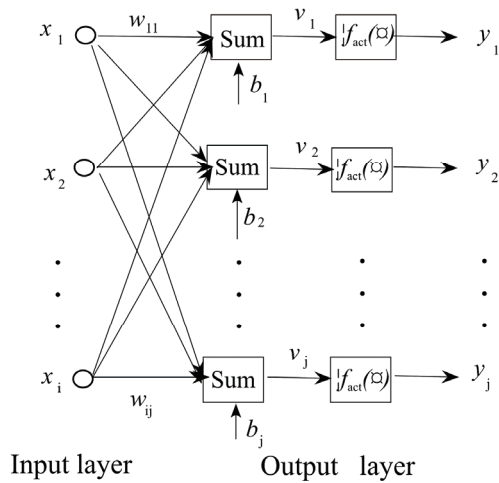


Fig. 1. The architecture of the linear artificial neural network.

As there are no non-linear functions and hidden neurons in the network, an L-ANN is ideal for dealing with linear problems. Actually, training a linear network means finding the optimal setting for the weight matrix \mathbf{W} to minimize the root mean squared error of the calibration set. In order to achieve this aim, the known samples are generally divided into two parts: a training set and a verification set. The network is trained using the training set, but is also tested after each epoch using the verification set. The training should be stopped once deterioration in the verification error is observed. Overfitting and overlearning can be effectively avoided in this way. Although the verification set is used to identify the best network, actually, training algorithms do not use the verification set to adjust network weights. A standard pseudo-inverse linear optimization algorithm²⁴ is usually employed to train the network. This algorithm uses the singular value decomposition technique to calculate the pseudo-inverse of the matrix required to set the weights in a linear output layer, to find the least mean squared solution. Essentially, it guarantees the optimal setting for the weights in a linear layer is found.

The main difference between MLR and L-ANN is the optimization algorithm. In MLR, the aim of least square algorithm is to minimize the sum of squared residuals of the training set. As for L-ANN, the aim of training algorithm is to minimize the root mean squared error of verification set.²⁴ Thus, the prediction ability of L-ANN is usually superior to that of MLR.

In this study, a 2-1 L-ANN (*i.e.*, a network with 2 input variables and 1 output variable) was used to establish the calibration model. The used activation function is presented in Eq. (5). The MDEV index and $\log K_p$ were used as the input and output variables, respectively. Prior to the training procedure, the input and output values were normalized.

Leave-one-out cross validation

The leave-one-out cross validation²⁹ is a commonly used algorithm for estimating the predictive performance of a multivariable calibration model. Usually, practical calibration experiments must be based on a limited set of available samples. The idea behind the leave-one-out cross validation algorithm is to predict the property value of each sample in turn with the calibration model that was developed with the other samples. When applying the algorithm to a dataset with n samples, the calibration modeling is performed n times, each time using $(n-1)$ samples for modeling and one sample for testing. Thus, the procedure of leave-one-out cross validation can be divided into n segment. In each segment i ($i = 1, \dots, n$), there are three steps: 1) taking sample i out as temporary "test set", which was not used to develop the calibration model, 2) developing the calibration model with the remaining $(n-1)$ samples and 3) testing the developed model with sample i , calculating and storing the prediction error of the sample.

External validation

External validation^{25,30,31} is a conventional approach that is usually used to assess the predictive ability of a calibration model. When using the approach, all the available samples are split into two subsets: a calibration set, which is used to establish the prediction model, and a test set, which is employed to verify the reliability of the established model. Usually, the samples in calibration set and test set are randomly selected from the working dataset.

Software

All data processing was realized with subroutines developed under Matlab (Ver. 7.0). The computation was performed on a personal computer equipped with a Core2 T9400 processor.

RESULTS AND DISCUSSION

First, the values of the MDEV index for the PCBs were calculated according to the method presented in the Calculation and Experimental section and the results are listed in Table I. The MDEV index of different PCB molecules are different, which confirms that the MDEV index can describe the structural differences among these molecules. Thus, it is reasonable to employ MDEV index as structural descriptor for developing QSPR models of PCBs.

Then the two QSPR models (the MLR and L-ANN models) were developed and investigated.

MLR model

Generally, a simple model should always be chosen in preference to a complex model, unless the latter fits the data better. Thus, the MLR model was first investigated to determine whether it could describe adequately the quantitative relationship between the MDEV indexes and $\log K_p$ values of the PCBs. The MDEV index was used as the independent variable and the $\log K_p$ value as the dependent variable to develop the model. In order to assess the predictive ability of the developed QSPR model, two validation methods, the leave-one-out cross validation and external validation, were performed. The 41 PCBs for which their

$\log K_p$ value is known were randomly divided into two groups: Group I, which comprised 20 PCBs and Group II, which comprised 21 PCBs.

Then, the leave-one-out cross validation was applied to Group I and the results are presented in Table II, from which it could be seen that the predicted $\log K_p$ were in agreement with the experimental values. For all the 20 compounds, the obtained $RMSRE$ was 4.72. Moreover, the predicted $\log K_p$ values were plotted vs. the corresponding experimental ones (shown in Fig. 2a) and the plot exhibited a linear relationship ($y = 0.9592x - 0.1314$ with $R^2 = 0.9519$). Subsequently, external validation was performed to assess further the predictive ability of the MLR model. In this procedure, the calibration model was developed by using all the 20 compounds in Group I. The obtained regression equation is $\log K_p = 0.883\mu_1 + 0.244\mu_2 - 5.056$. The R^2 , standard error of the estimate and F values of the regression model were 0.9636, 0.1501 and 225.0, respectively. Then, the $\log K_p$ values of the PCBs in Group II were predicted by the obtained model. The prediction results are also given in Table II, from which it can be seen that the predicted $\log K_p$ values were still in agreement with the experimental $\log K_p$. For the 21 compounds, the prediction $RMSRE$ was 8.62. The plot of the predicted $\log K_p$ vs. the experimental values (Fig. 2a) exhibited a linear relationship ($y = 0.9649x - 0.2291$ with $R^2 = 0.9038$).

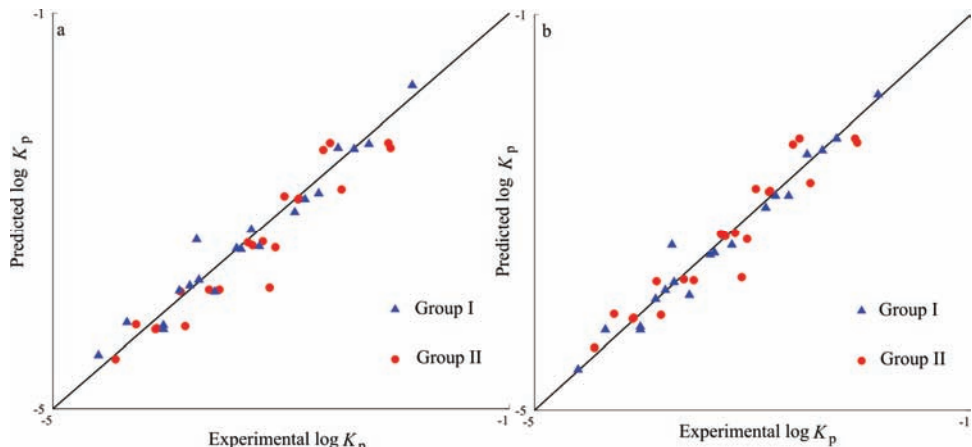


Fig. 2. Experimental $\log K_p$ vs. predicted $\log K_p$ values, a) MLR and b) L-ANN.

The result of the leave-one-out cross validation and external validation demonstrates that the values of MDEV index of the investigated PCBs are quantitatively related to their $\log K_p$ values. MLR was shown to be practicable for modeling the quantitative relationship between the MDEV index and $\log K_p$ value of PCBs. Obviously, a linear QSPR model based on MDEV index could be used to predict the $\log K_p$ of other PCBs.

Thus, an MLR model was developed using the 41 samples listed in Table II. The obtained regression equation was $\log K_p = 1.046\mu_1 + 0.196\mu_2 - 4.825$. The R^2 , standard error of the estimate and F values of the regression model were 0.9282, 0.1958 and 245.5, respectively.

L-ANN model

Besides MLR, an L-ANN, which is the simplest artificial neural network, is a commonly used linear calibration method in QSPR studies. Thus, we investigate whether a better model can be established by using L-ANN. Leave-one-out cross validation and external validation were carried out to assess the predictive ability of the developed model.

Group I was still used to accomplish leave-one-out cross validation. In each run of the ANN, the verification set comprised four randomly selected samples, and the learning rate and momentum were set as 0.6 and 0.3, respectively. The results are presented in Table II, from which it could be seen that the predicted $\log K_p$ values were in good agreement with the corresponding experimental ones. For all the 20 compounds, the obtained *RMSRE* was 3.87. Moreover, the predicted $\log K_p$ values were plotted *vs.* the experimental ones (Fig. 2b) and the plot exhibited a linear relationship ($y = 0.9511x - 0.1613$ with $R^2 = 0.9725$). Then, all the 41 samples listed in Table II were used to accomplish an external validation. The L-ANN model was trained using the 20 samples of Group I. In the training procedure, the verification set comprises four randomly selected samples, and the learning rate and momentum was set as 0.6 and 0.3, respectively. The results of the external validation are given in Table II, from which it could be seen that the predicted $\log K_p$ values were in good agreement with the experimental ones. For the 21 compounds, the prediction *RMSRE* was 7.47. The plot of the predicted $\log K_p$ values *vs.* the experimental ones (Fig. 2b) showed a linear relationship ($y = 0.9574x - 0.1435$ with $R^2 = 0.9136$). Obviously, the prediction accuracy of L-ANN model was slightly higher than that of the MLR model. Hence, using the L-ANN model would be slightly better than the MLR model for the prediction of the $\log K_p$ values of PCBs. Thus, it was demonstrated that the L-ANN technique is a practicable and promising method for modeling the quantitative relationship between the values of the MDEV index and the $\log K_p$ values of PCBs.

Thus, an L-ANN model was developed using the 41 samples listed in Table II as the calibration set. In the training procedure, the verification set comprised eight randomly selected samples, and the learning rate and momentum was set as 0.6 and 0.3, respectively. Wei *et al.*¹³ predicted the $\log K_p$ values of the PCBs using a quantum chemistry QSPR model. A comparison of the present result with theirs showed no significant difference between the two sets of predicted results. Thus, the models developed within the present study should provide a reasonable method for the prediction of the $\log K_p$ value of PCBs. Compared with quantum chemical descriptors, the MDEV index is easier to generate. Obviously, the

development of QSPR models based on the MDEV index is a simple and easy-to-use method for predicting the $\log K_p$ values of PCBs.

CONCLUSIONS

QSPR models for predicting the gas/particle partition coefficient of PCBs were investigated. The MDEV index was used as the structural descriptor of the PCBs. Both a MLR and an L-ANN model were investigated. The predictive ability of the developed models was assessed by the leave-one-out cross validation and by external validation. The results indicate that both the MLR and the L-ANN models are practicable for predicting the $\log K_p$ values of PCBs. It is demonstrated that the values of the MDEV index of PCBs are quantitatively related to the $\log K_p$ values of PCBs. MDEV index can be generated easier than quantum chemical descriptors. Accordingly, using MDEV index as structural descriptor is more convenient than using a quantum chemical descriptor when developing a QSPR model for the K_p of PCBs. In addition, the result demonstrated that both the MLR and L-ANN models are practicable for modeling the quantitative relationship between the MDEV index and $\log K_p$ of PCBs. Therefore, the proposed method should be easy-to-use and practicable for the prediction of the $\log K_p$ values of PCBs.

Acknowledgments. The work was supported by the National Natural Science Foundation of China, Nos. 21305108 and 20975081, the project supported by Natural Science Basic Research Plan in Shaanxi Province of China (Program No. 2014JM2039) and the Innovative Research Team of Xi'an Shiyou University.

ИЗВОД

QSPR СТУДИЈА ПОДЕОНОГ КОЕФИЦИЈЕНТА ГАС/ЧЕСТИЦА ПОЛИХЛОРОВАНИХ БИФЕНИЛА ПРИМЕНОМ ВЕКТОРСКОГ ИНДЕКСА РАСТОЈАЊЕ-ГРАНА

LONG JIAO^{1,2}, XIAOFEI WANG¹, HUA LI² и YUNXIA WANG²

¹*Xi'an Shiyou University, Xi'an, China* и ²*Northwest University, Xi'an, China*

Истраживане су QSPR релације за подеони кофицијент гас/честица, K_p , за полихлороване бифениле (PCB). Као структурни дескриптор коришћен је векторски индекс растојање-грана (MDEV индекс). Квантитативна релација између MDEV индекса и $\log K_p$ моделована је методом мултиваријантне линеарне регресије и неуронским мрежама. Показано је да се модел који је развијен може употребити за предвиђање K_p вредности код PCBs. Постоји квантитативна веза између MDEV индекса и K_p за PCBs.

(Примљено 27. Новембра, прихваћено 12.децембра 2013)

REFERENCES

- Environmental protection agency of United States, *Persistent organic pollutants*, <http://www.epa.gov/international/toxics/pop.pdf> (accessed 26 January 2013)
- M. S. El-Shahawi, A. Hamza, A. S. Bashammakh, W. T. Al-Saggaf, *Talanta* **80** (2010) 1587
- S. Jensen, A. G. Johnels, M. Olsson, G. Otterlind, *Nature* **224** (1969) 247

4. X. Y. Han, Z. Y. Wang, Z. C. Zhai, L. S. Wang, *QSAR Comb. Sci.* **25** (2006) 333
5. M. Mandalakis, M. Tsapakis, A. Tsoga, E. G. Stephanou, *Atmos. Environ.* **36** (2002) 4023
6. B. G. Hansen, A. B. Paya-Perez, M. Rahman, B. R. Larsen, *Chemosphere* **39** (1999) 2209
7. J. He, R. Balasubramanian, *Atmos. Environ.* **43** (2009) 4375
8. R. L. Falconer, T. Harner, *Atmos. Environ.* **34** (2000) 4043
9. M. Simick, T. Franz, H. X. Zhang, S. J. Eisenreich, *Environ. Sci. Technol.* **32** (1998) 251
10. T. Harner, T. F. Bidleman, *Environ. Sci. Technol.* **32** (1998) 1494
11. H. G. Yeo, M. Choi, M. Y. Chun, Y. Sunwoo, *Atmos. Environ.* **37** (2003) 3561
12. K. S. Kim, S. Masunaga, *Environ. Pollut.* **138** (2005) 290
13. B. N. Wei, S. D. Xie, M. Yu, L. Wu, *Chemosphere* **66** (2007) 1807
14. I. Gutman, J. Tosovic, *J. Serb. Chem. Soc.* **78** (2013) 805
15. H. H. Liu, X. Xiao, J. Qin, Y. M. Liu, *J. Chongqing Inst. Tech.* **19** (2005) 67 (in Chinese)
16. S. S. Liu, H. L. Liu, Z. N. Xia, C. Z. Cao, Z. L. Li, *J. Chem. Inf. Comput. Sci.* **39** (1999) 951
17. C. S. Yin, W. M. Guo, T. Lin, S. S. Liu, R. Q. Fu, Z. X. Pan, L. S. Wang, *J. Chin. Chem. Soc.* **48** (2001) 739
18. M. Jalali-Heravi, M. Asadollahi-Baboli, P. Shahbazikhah, *Euro. J. Med. Chem.* **43** (2008) 548
19. L. Jiao, *Chemosphere* **80** (2010) 671
20. M. H. Fatemi, Z. G. Chahi, *SAR QSAR Environ. Res.* **23** (2012) 155
21. R. Smiljanić, D. Lazić, M. Gligorić, M. Jotanović, Z. Živković, I. Mihajlović, *J. Serb. Chem. Soc.* **76** (2011) 1163
22. X. J. Yao, A. Panaye, J. P. Doucet, H. F. Chen, R. S. Zhang, B. T. Fan, M. C. Liu, Z. D. Hu, *Anal. Chim. Acta* **535** (2005) 259
23. M. Fatemi, Z. Ghorbannezhad, *J. Serb. Chem. Soc.* **76** (2011) 1003
24. Statsoft, *Model extremely complex functions neural networks*, <http://www.statsoft.com/textbook/neural-networks> (accessed 26 January 2013)
25. L. Jiao, H. Li, *Chemometr. Intell. Lab. Syst.* **103** (2010) 90
26. Y. X. Zhang, H. Li, A. X. Hou, J. Havel, *Chemometr. Intell. Lab. Syst.* **82** (2006) 165
27. C. S. Yin, Y. Shen, S. S. Liu, Q. S. Yin, W. M. Guo, Z. X. Pan, *Comput. Chem.* **25** (2001) 239
28. W. J. Zhang, X. Q. Zhong, G. H. Liu, *Stoch. Environ. Res. Risk A* **22** (2008) 207
29. H. A. Martens, P. Dardenne, *Chemometr. Intell. Lab. Syst.* **44** (1998) 99
30. E. Kolossov, R. Stanforth, *SAR QSAR Environ. Res.* **18** (2007) 89
31. P. Gramatica, *QSAR Comb. Sci.* **26** (2007) 694.



Fenton-like oxidation of an azo dye using mesoporous Fe/TiO₂ catalysts prepared by a microwave-assisted hydrothermal process

JELENA NEŠIĆ^{1*}, DRAGAN D. MANOJLOVIĆ^{2#}, MILICA JOVIĆ^{1#}, BILJANA P. DOJČINOVIC³, PREDRAG J. VULIĆ⁴, JUGOSLAV KRSTIĆ⁵
and GORAN M. ROGLIĆ^{2***}

¹Innovation Center of the Faculty of Chemistry, University of Belgrade, Studentski trg 12, 11000 Belgrade, Serbia, ²Faculty of Chemistry, University of Belgrade, Studentski trg 12, Belgrade, Serbia, ³Institute of Chemistry, Technology and Metallurgy, Center of Chemistry, University of Belgrade, Njegoševa 12, 11000 Belgrade, Serbia, ⁴Laboratory of Crystallography, Faculty of Mining and Geology, University of Belgrade, Đušina 7, 11000 Belgrade, Serbia and ⁵Institute of Chemistry, Technology and Metallurgy, Department of Catalysis and Chemical Engineering, University of Belgrade, Njegoševa 12, 11000 Belgrade, Serbia

(Received 1 October, revised 20 November, accepted 21 November 2013)

Abstract: Fe-doped TiO₂ photocatalysts with different contents of Fe (0.5, 1.6, 3.4 and 6.4 %) were synthesized by a microwave-hydrothermal method and characterized by X-ray diffraction analysis, N₂ physisorption at 77 K and UV–Vis spectrometry. The characterization showed that the Fe ions were highly dispersed in the TiO₂ lattice. It was found that all the synthesized catalysts had a mesoporous structure and that Fe-doping increased the BET surface area. The UV–Vis study showed that the absorption spectra were shifted to longer wavelengths (red shift) with increasing dopant concentration. The photocatalytic activity of the samples was evaluated by the decolorization of the textile dye Reactive Blue 52 (RB) in aqueous solutions under sun-like radiation in the presence of H₂O₂ (a heterogeneous photo-Fenton process). The photocatalyst with 3.4 % Fe was found to be the most efficient in the presence of H₂O₂. The effect of the initial pH of the dye solution was assessed and dissolution of iron ions was studied as a function of pH value. It was concluded that decolorization was more favorable in acidic pH, and that at pH values >4, the release of Fe ions into the solution was negligible. Photocatalytic degradation of 4-chlorophenol (4-CP) was investigated under the optimal conditions and it was shown that the catalyst was capable of degrading colorless pollutants.

Keywords: Fe/TiO₂; heterogeneous photo-Fenton; Reactive Blue 52; 4-chlorophenol.

Corresponding authors. E-mail: (*)jelenanesic@chem.bg.ac.rs; (**)groglic@chem.bg.ac.rs

Serbian Chemical Society member.

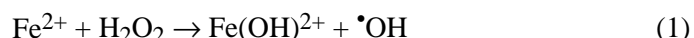
doi: 10.2298/JSC131001143N

INTRODUCTION

Dye pollution from textile plants is a source of environmental concern the world over. These effluents are toxic and mostly non-biodegradable. Moreover, they absorb and scatter sunlight and thus, affect aquatic ecosystems. Most of the dye molecules are resistant to destruction by conventional methods for water treatment (coagulation, carbon adsorption, reverse osmosis, ultrafiltration and biological treatments).¹ In the last decades, advanced oxidation processes (AOPs) appear to be a promising alternative for the degradation of organic pollutants. These processes are based on the generation of very reactive species, such as hydroxyl ($\cdot\text{OH}$) and hydroperoxyl ($\text{HO}_2\cdot$) radicals, and complete mineralization of the target pollutant species is achieved.²

Among the advanced oxidation processes, titanium dioxide (TiO_2) offers a great potential as a photocatalytic material for detoxifying wastewater. TiO_2 has the advantage of being non-toxic and stable in aqueous solutions. Furthermore, photo-assisted processes are inexpensive and do not require special conditions. They are open-atmospheric systems that can operate at room temperature, utilizing natural solar light as an energy source.

In addition, the photo-Fenton oxidation is a very efficient system for the degradation of pollutants. This method involves the catalytic decomposition of H_2O_2 in the presence of ferrous ions, resulting in the generation of hydroxyl radicals. The formation of hydroxyl radicals and the regeneration of Fe^{2+} by photo-reduction from Fe^{3+} can be represented by the following reactions:³



Both of these processes suffer from limitations. TiO_2 has wide bandgap (3.2 eV), which means it can utilize only $\approx 5\%$ of the solar spectrum, all in the UV region.⁴ This problem is partially overcome by doping with different species, such as: iron,^{5–7} nitrogen–sulfur,⁸ silver,^{9,10} molybdenum¹¹ and lanthanum,¹² which enables the reactions to be induced not only with UV, but also with visible light. The homogenous photo-Fenton system requires a pH of ≈ 3 , in order to avoid the formation of insoluble Fe(OH)_3 , and the after treatment separation of the dissolved iron ions.¹³

In order to overcome these problems, a combination of these two processes could be used and the advantage of potential synergistic effects taken. A heterogeneous catalyst of this type would enable operation over a wide pH range, a TiO_2 and Fenton reagent combination would enhance visible-light absorption and the removal of sludge containing Fe ions would not be necessary, which would reduce the costs of treatment.^{14,15}

The aim of this research was to prepare Fe/TiO_2 materials with different contents of Fe by a microwave-assisted, hydrothermal method and investigate

their applicability as heterogeneous photo-Fenton catalysts for the decolorization of the textile dye Reactive Blue 52 (RB) in aqueous solutions under sun-like radiation in the presence of H₂O₂. The effects of different Fe contents and initial pH values of the dye solution on the decolorization efficiency were assessed. The dissolution of iron ions was studied in dependence on the experimental conditions, because it is a common phenomenon during heterogeneous photo-Fenton oxidation, which increases the contribution of the homogeneous photo-Fenton process. In addition, the degradation of 4-chlorophenol (4-CP) was investigated to show that the studied catalyst was also able to degrade colorless pollutants and that the excitation of the dye molecule is not the only mechanism, but also the production of reactive oxygen species is operative.

EXPERIMENTAL

Materials

Titanium tetrachloride, TiCl₄ (Fluka 98 %), ammonium hydroxide, NH₄OH (Sigma–Aldrich 25 %), iron(III) chloride, FeCl₃ (Merck), hydrogen peroxide, H₂O₂ (Sigma–Aldrich 30%) and 4-chlorophenol (Sigma–Aldrich) were used as received. The azo dye Reactive Blue 52 (RB) was obtained from Clariant (Switzerland) and used without further purification; the molecular structure of RB is shown in Fig. 1. All solutions were prepared with deionized water.

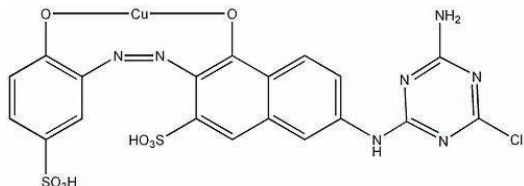


Fig. 1. Structural formula of Reactive Blue 52.

Preparation of catalysts

All the catalysts were prepared using the microwave-hydrothermal method. TiCl₄ was added to icy water containing the required amount of the iron salt (TiCl₄:H₂O (V/V) ratio 1:10) Then, the precipitation was induced by the slow addition of NH₄OH (25 %) solution under constant stirring at room temperature until the reaction mixture attained a pH between 7 and 8. The suspension was transferred into a Teflon® microwave closed vessels (digestion system ETHOS One Milestone, equipped with a High Pressure Rotor SK-10, Italy), sealed and heated by microwave irradiation, whereby the maximum temperature of 150 °C was attained in 10 min, and then kept at this temperature for a further 15 min more for hydrothermal treatment. The resulting product was separated by centrifugation and washed repeatedly with deionized water until the precipitate becomes free of chloride ion (confirmed by the AgNO₃ test). Finally, it was dried at 80 °C for 5 h and then calcined at 500 °C for 10 h.

Characterization

The content of Fe in the synthesized samples was determined by the inductively coupled plasma-optical emission spectroscopy (ICP–OES) technique (Thermo Scientific iCAP 6500 Duo ICP spectrometer, UK). Samples were prepared by microwave digestion using an Ethos

One microwave system (Advanced Microwave Digestion System, Milestone, Italy). Each sample (0.1 g) was mixed with 5 mL of sulfuric acid (H_2SO_4 , 98 %), 2 mL of nitric acid (HNO_3 , 65 %) and 1 mL of hydrofluoric acid (HF, 50 %), all analytical grade reagents from Carlo Erba, transferred into a microwave digestion vessel and microwave heated. The maximum temperature of 220 °C was reached after 15 min and then this temperature kept constant for a further 20 min. The concentrations of Fe in the prepared powders are expressed in terms of mass weight percent.

Powder X-ray diffraction (XRPD) analysis was used for the identification of the crystalline phases, a quantitative phase analysis and an estimation of the crystallite size and strain. The XRPD patterns were collected on a Philips diffractometer (PW1710) employing $CuK_{\alpha 1,2}$ radiation. Step scanning was performed within the 2θ range from 20 to 100° with a step size of 0.080° and a fixed counting time of 5 s per step. The XRPD patterns were used to refine crystallographic structure and microstructural parameters using the procedure implemented in the FullProf computer program.¹⁶

Adsorption–desorption isotherms were obtained by nitrogen adsorption at 77 K using a Sorptomatic 1990 Thermo Finnigan device. Prior to adsorption, the samples were outgassed for 1 h at room temperature under vacuum and additionally for 16 h at 110 °C at the same residual pressure. The specific surface areas of the samples (S_{BET}) were calculated by applying the Brunauer–Emmet–Teller (BET) Equation, from the linear part of the adsorption isotherm.¹⁷ The total pore volumes (V_{tot}) were obtained from the N_2 adsorption, expressed in liquid form, by application of the Gurvitsch rule.¹⁸ The micropore volumes (V_{mic}) were estimated according to the Dubinin–Radushkevich method.¹⁹ The mesopore volumes (V_{mes}) were estimated according to the Barrett, Joyner and Halenda method from the desorption branch of the isotherms.²⁰

The UV–Vis diffuse reflectance spectra (DRS) were recorded on an Evolution 600 UV–Vis spectrophotometer (Thermo Scientific), equipped with a DRA-EV-600 diffuse reflectance accessory.

Photodegradation procedure

A typical photocatalytic experiment was performed in a cylindrical photochemical reactor, with a water circulation arrangement to maintain the temperature in the range 22±1 °C. An Osram Ultra-Vitalux lamp (300 W) with a sun-like radiation spectrum was used as the light source. The distance between the lamp and the sample was 25 cm. Appropriate amounts of Fe/TiO₂ were added into 100 mL of RB solution and stirred in the dark for 1 h before illumination, to ensure the establishment of the adsorption–desorption equilibrium between the photocatalyst and RB. The pH was adjusted by the addition of H_2SO_4 or NaOH using a pH monitor (Microcomputer pH-vision 6071, JENCO Electronics Ltd., Taiwan). Concentration changes of the RB were monitored according to the decreasing intensity of the absorption peak at 615 nm. Absorption spectra of RB were recorded on a double-beam UV–Vis spectrophotometer (Cintra 10 UV–Visible spectrometer, Australia), at a fixed slit width (1 nm), using 1 cm quartz cell. The decolorization efficiency was calculated from the relation:

$$\text{Decolorization} = \frac{(A_0 - A)}{A_0} \times 100$$

where A_0 and A are the absorbance at the maximum absorption wavelength (λ_{max}) of the initial dye solution and after the treatment, respectively.

Degradation of 4-chlorophenol was monitored by high-performance liquid chromatography with photodiode array detection (HPLC-DAD). The HPLC analysis was performed

using Dionex UltiMate 3000 chromatograph. A Hypersil Gold C8 column (150 mm×3 mm, 3 µm) at 40 °C was used. The mobile phases were water as component A and acetonitrile as component B (both HPLC grade, Sigma–Aldrich). The compounds were eluted at flow rate of 1.0 ml min⁻¹. The injection volume was 10 µl and the detector was set at 280 nm. The gradient elution was as follows: 30–80 % B in 20 min. The data analyses were realized using a computer equipped with the Chromeleon 6.8 program (ThermoFisher Scientific, Bremen, Germany).

RESULTS AND DISCUSSION

X-Ray diffraction analysis of photocatalysts

The diffraction patterns of four Fe/TiO₂ catalysts are shown in Fig. 2. It can be seen that only the anatase phase (JCPDS card 78-2486) was present up to a Fe content of 6.4 %, when the presence of broad low-intensity diffraction peak at $2\theta \approx 32.5^\circ$ for 6.4Fe/TiO₂ could be ascribed to the pseudobrookite (Fe₂TiO₅) phase (JCPDS card 29-1360). The pseudobrookite content in this sample was determined to be 3 %. This is formed because Fe³⁺ substitute Ti⁴⁺ in the TiO₂ lattice. This can occur because the radii of Ti⁴⁺ and Fe³⁺ are similar (0.69 and

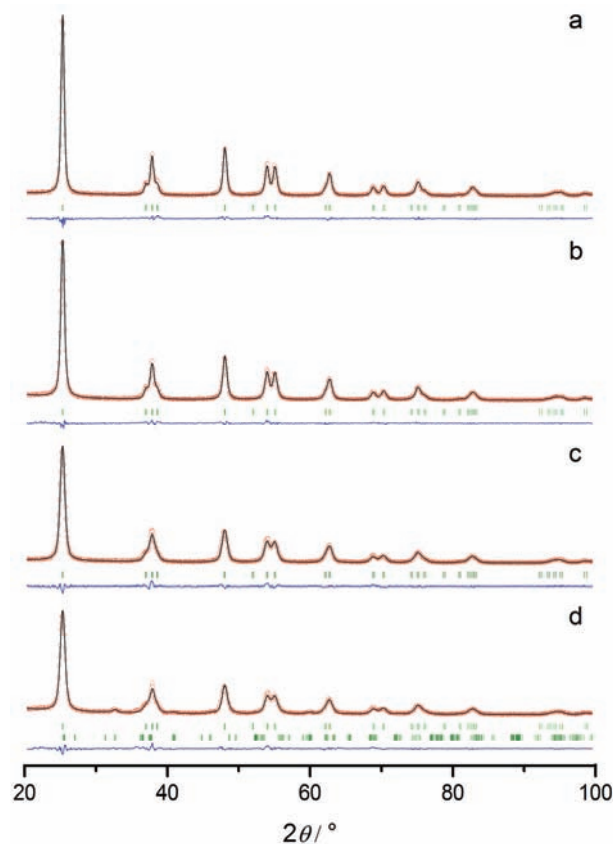


Fig. 2. The final Rietveld refinement plots of the samples: a) 0.5Fe/TiO₂; b) 1.6Fe/TiO₂; c) 3.4Fe/TiO₂; d) 6.4Fe/TiO₂. The observed data are represented by circles and the calculated data by a continuous line. The Bragg positions are denoted by vertical ticks and the difference curve is shown at the bottom.

0.64 nm for Ti^{4+} and Fe^{3+} , respectively²¹) and the electronegativities of both ions are reasonably close (Fe^{3+} : 1.96,²¹ Ti^{4+} : 1.5²²). No peaks due to Fe-oxide phase were observed in any of the samples; the Fe^{3+} were highly dispersed in the TiO_2 lattice.

Structure refinements were performed by the Rietveld method. The final Rietveld refinement plots of the samples are presented in Fig. 2, while the main results of the refinement are listed in Table I. The obtained values for the unit cell parameters of anatase show that the value of the parameter a varied around its reference value ($a_0 = 3.78479(3)$ Å), while the value of the c parameter was slightly smaller than the reference one ($c_0 = 9.51237(12)$ Å) in all the samples. The obtained average crystallite size slightly decreased with increasing content of Fe. The radius of the Fe^{3+} is smaller than that of Ti^{4+} ; hence, the doping of Fe made the cell parameter smaller than that of pure anatase.²³

Low values of agreement factors between the model, both structure and microstructure, and XRD data (Table I) indicate the high accuracy of the obtained results.

TABLE I. The results of the Rietveld analyses of the anatase phase (unit cell parameters, microstructure parameters and refinement residuals)

Sample	Unit cell parameters		Microstructure parameters		Rietveld refinement residuals				
	a / Å	c / Å	Average size Å	Average strain $\times 10^{-3}$	R_p	R_{wp}	R_{exp}	χ^2	R_B
0.5Fe/TiO ₂	3.7854(2)	9.5049(6)	163	20	7.5	9.9	8.5	1.37	2.77
1.6Fe/TiO ₂	3.7858(2)	9.5039(7)	128	16	7.4	9.9	8.4	1.39	1.95
3.4Fe/TiO ₂	3.7884(3)	9.5040(10)	97	15	8.9	11.1	8.9	1.54	2.58
6.4Fe/TiO ₂	3.7881(4)	9.4958(13)	94	15	9.7	12.1	9.3	1.69	2.34

Nitrogen physisorption

Information about specific surface areas and the pore volumes of the catalysts are summarized in Table II. The isotherms of all the synthesized materials presented in Fig. 3 could be interpreted²⁴ as type IV, which is typical for mesoporous materials, with an H2-type hysteresis loop, indicating the presence of pore networks. It could be seen that the position of the condensation branches on the pressure axis, the specific surface area and the pore volume were dependent on the Fe content. The introduction of the Fe ions causes an increase in specific surface area and a decrease in the pore volume. The origin of increase in the specific surface area could be explained in two ways: the reorganization of the pore system through the entrance of small particles into the pore system or the formation of a new phase, which has a higher specific surface area. The reorganization of the pore would also lead to preservation or reduction of the pore volume. From the results for V_{mic} , V_{meso} and V_{tot} given in Table II, it is clear this is

the case for synthesized Fe/TiO₂ catalysts. Fe species are not located on the outer side of the TiO₂ particles as a separate oxide phase. This statement was also confirmed by the XRD results, that Fe ions are highly dispersed in the TiO₂ lattice.

TABLE II. Textural and structural properties of the Fe/TiO₂ samples

Sample	Content of Fe, mass %	S_{BET} / m ² g ⁻¹	V_{tot} / cm ³ g ⁻¹	V_{mic} / cm ³ g ⁻¹	V_{meso} / cm ³ g ⁻¹
0.5Fe/TiO ₂	0.47	72.4	0.252	0.021	0.2189
1.6Fe/TiO ₂	1.60	93.5	0.261	0.027	0.232
3.4Fe/TiO ₂	3.42	83.7	0.250	0.028	0.191
6.4Fe/TiO ₂	6.41	123.1	0.257	0.037	0.189

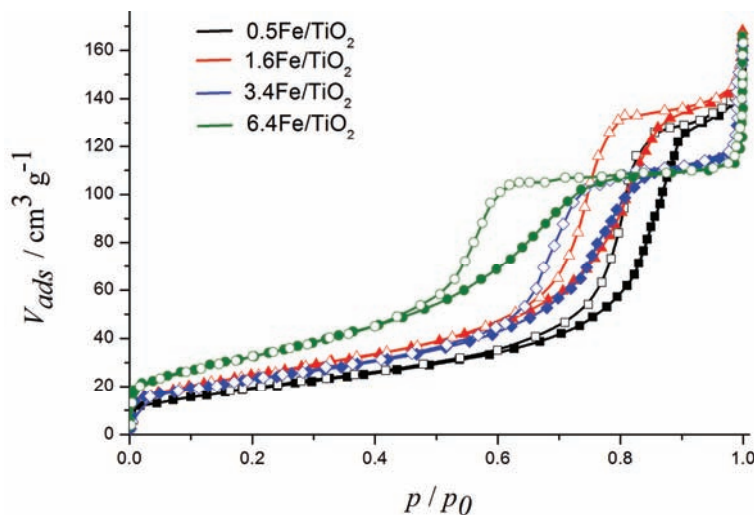


Fig. 3. Nitrogen physisorption isotherms of Fe/TiO₂ at 77 K. The empty symbols represent adsorption points and the filled symbols represent desorption points.

UV-Vis diffuse reflectance spectra

The UV-Vis diffuse reflectance spectra of synthesized samples are shown in Fig. 4. It could be seen that with increasing Fe content, the photocatalyst response shifted to higher wavelengths, which was accompanied by changes in color from pale yellow to reddish brown. The absorptions in the visible region may be induced by two factors. One is the excitation of 3d electrons of Fe³⁺ to the TiO₂ conduction band (charge transfer transition) at 415 nm.²⁵ The other can be ascribed to the d-d transitions $^2T_{2g} \rightarrow ^2A_{2g}$ and $^2T_{1g}$ of Fe³⁺ or to the charge transfer transition between iron ions ($Fe^{3+} + Fe^{3+} \rightarrow Fe^{4+} + Fe^{2+}$) at 500 nm.^{26,27} These results are in agreement with the XRD and nitrogen physisorption results and confirmed that the Fe ions were incorporated into the lattice of TiO₂, thus altering its crystal and electronic structures.

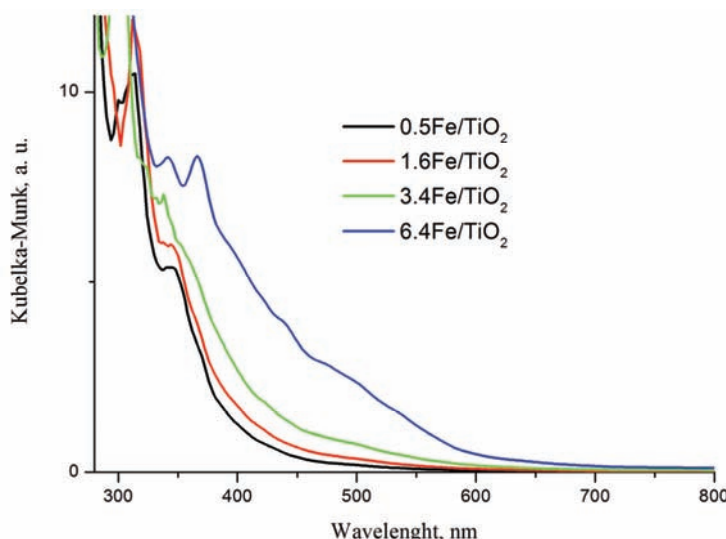


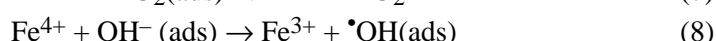
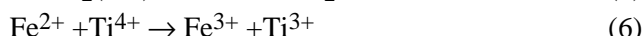
Fig. 4. Diffuse reflectance spectra of Fe/TiO_2 powders, plotted as the Kubelka–Munk function (F) of the reflectance (R).

Decolorization of RB

The efficiencies of different AOPs in the degradation of RB are shown in Fig. 5, from which it could be seen that the efficiency of direct photolysis under sun-like irradiation was very small. The dye removal efficiency with only H_2O_2 was much higher when H_2O_2 was applied in combination with illumination. This could be explained by the generation of highly reactive $\cdot\text{OH}$ by direct photolysis of the added H_2O_2 .²⁸ As the photolysis wavelength range of H_2O_2 is between 200 and 350 nm and since the employed lamp is active in the UV-B and UV-A regions, this reaction was possible.

In order to examine whether the presence of Fe in the Fe/TiO_2 samples influences the efficiency of photocatalytic degradation of RB, the efficiency of 3.4Fe/TiO₂ was compared with that of the pure TiO₂. The degradation efficiency of 3.4Fe/TiO₂ was higher, which indicates that the addition of Fe contributes to the catalytic activity. The beneficial effect of Fe ions could be explained by considering the efficient separation of the photo-excited electrons and holes.²⁹ Since the energy level for $\text{Fe}^{3+}/\text{Fe}^{4+}$ is above the valence band edge of anatase TiO_2 , Fe^{3+} could act as photogenerated hole traps (Eq.(3)). Fe^{3+} could also serve as photogenerated electron traps, as the energy level for $\text{Fe}^{3+}/\text{Fe}^{2+}$ is below the conduction band edge of TiO_2 (Eq. (4)). Thus, Fe^{3+} could act as both electron and hole traps, whereby Fe^{2+} and Fe^{4+} are generated, respectively. The Fe^{2+} could be oxidized to Fe^{3+} by transferring electrons to absorbed O_2 on the surface of TiO_2 (Eq. (5)) or to a neighboring surface Ti^{4+} (Eq. (6)), thereby leading to interfacial electron transfer (Eq. (7)). The trapped holes in Fe^{4+} could migrate to surface

adsorbed hydroxyl ions (Eq. (8)) to produce hydroxyl radicals. As a result, the introduction of Fe ions reduces electron–hole recombination rate and improves the photoactivity:⁵



As can be seen in Fig. 5, the presence of H_2O_2 increased the photocatalytic efficiency of the TiO_2 , which could be explained by the electron-acceptor role of H_2O_2 . With the 3.4Fe/TiO₂ catalyst, the presence of H_2O_2 increased the efficiency to a high extent. This means that H_2O_2 in addition to its electron-acceptor role also participates in the heterogeneous photo-Fenton process.

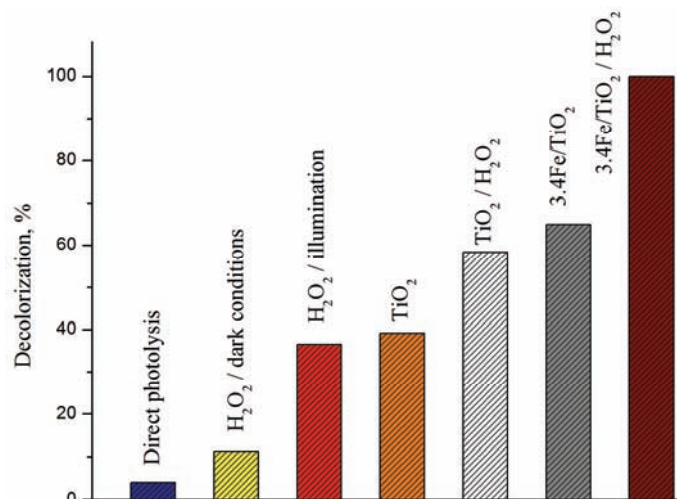


Fig. 5. Decolorization of RB using different AOPs. Operating conditions: $[\text{RB}]_0 = 60 \text{ mg dm}^{-3}$, $[\text{H}_2\text{O}_2]_0 = 20 \text{ mM}$, photocatalysts, 0.5 g dm^{-3} , pH 4 and time = 60 min.

Effect of Fe content

The influence of the doping concentration on the photocatalytic efficiency of the Fenton-like process was examined and the results are presented in Fig. 6. It could be seen that the optimal amount of Fe doping was 3.4 %, as this level of doping led to the complete elimination of RB within 60 min. Hence, all the other investigations were performed using the 3.4Fe/TiO₂ catalyst. It could be noticed that a further increase in the Fe content led to a decrease in the photoactivity. An explanation about the beneficial effect of Fe ions was given above. Thus, Fe^{3+}

act as both electron and hole traps, but they can also act as recombination centers for photogenerated electrons. When the dopant concentration is too high, the recombination will compete with the redox processes because the distance between trap sites is shorter. These trapped e^- or h^+ might recombine before migrating to the surface, resulting in a lower photocatalytic activity, because all the reactions occur only on the surface.³⁰

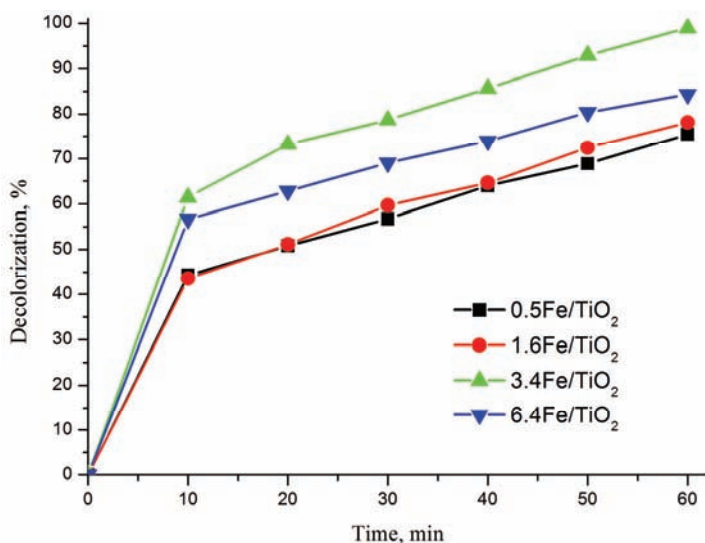


Fig. 6. Effect of Fe content in Fe/TiO_2 on the RB decolorization. Operating conditions: $[\text{RB}]_0 = 60 \text{ mg dm}^{-3}$, $[\text{H}_2\text{O}_2]_0 = 20 \text{ mM}$, photocatalysts, 0.5 g dm^{-3} and pH 4.

The adsorption properties of Fe/TiO_2 catalysts are shown in Fig. 7. The adsorption capacity of the powders increased with increasing Fe ion doping. The factors leading to the enhanced adsorption capacity involve changes in the physical properties owing to doping. In the present case, it was the larger specific surface area that enabled better adsorption of RB. Thus, the largest specific surface area and the highest content of Fe ions with H_2O_2 in Fenton-like process gave reasons to expect that the $6.4\text{Fe}/\text{TiO}_2$ catalyst would be the most efficient. Figures 6 and 7 illustrate that the photocatalytic activity did not follow the changes of the adsorption ability. Although adsorption is a prerequisite for the photocatalytic process, it is not obligatory that large adsorption abilities stimulate a faster degradation of the pollutant. An increase in photoactivity with increasing adsorption could be observed up to a certain amount of dopant but a decrease thereafter. This indicates that some other factors influence the degradation efficiency, *i.e.*, at higher contents, Fe^{3+} play the role of recombination sites and this effect dominates.

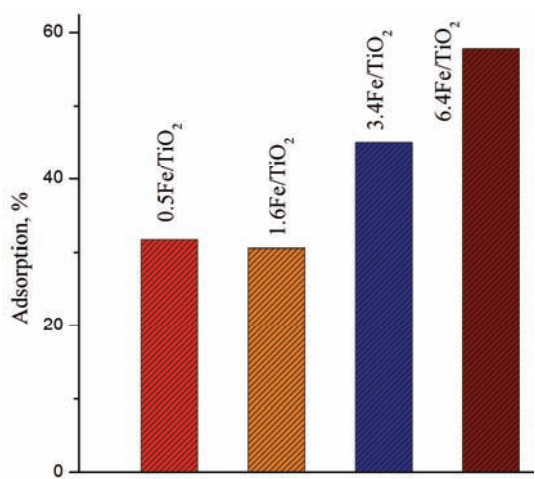


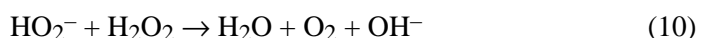
Fig. 7. Sorption ability of the Fe/TiO₂ catalysts. Operating conditions: [RB]₀ = 60 mg dm⁻³, photocatalysts, 0.5 g dm⁻³, pH 4 and time = 60 min.

Effect of the initial pH

The pH plays an important role in the photocatalytic degradation of various pollutants.^{31,32} The effect of pH on the kinetics of RB removal by the 3.4Fe/TiO₂ photocatalyst is presented in Fig. 8, which clearly indicates that the pH value had a great effect on the photocatalytic efficiency. It could be seen that the efficiency decreased with increasing pH value. This could be explained by the fact that the higher values of pH favor the dissociation of H₂O₂ to form HO₂⁻, as shown in Eq. (9):



HO₂⁻ reacts with a non-dissociated molecule of H₂O₂ according to Eq. (10), which leads to oxygen and water, instead of hydroxyl radicals.



At pH > 7, the ionic dissociation of H₂O₂ is the predominant process, hence, no experiments under alkaline conditions were performed.³³ In addition, a possible cause of such behavior could be the fact that the oxidation potential of •OH decreases with increasing pH.³⁴

The best results were obtained at a pH value of 3. The inset of Fig. 8 shows the leaching of iron after the photocatalytic process. The leaching of Fe ions was enhanced at pH 3; hence, in this case, the homogeneous photo-Fenton process contributed to the overall photodegradation. Since the efficiency was the same after 60 min at pH 4, only with different kinetics, and the detected concentration of Fe ions was only 24 µg dm⁻³, this pH value was chosen as the optimum for the further experiments. Fe leaching to such a low extent does not have a significant influence on the photodegradation.

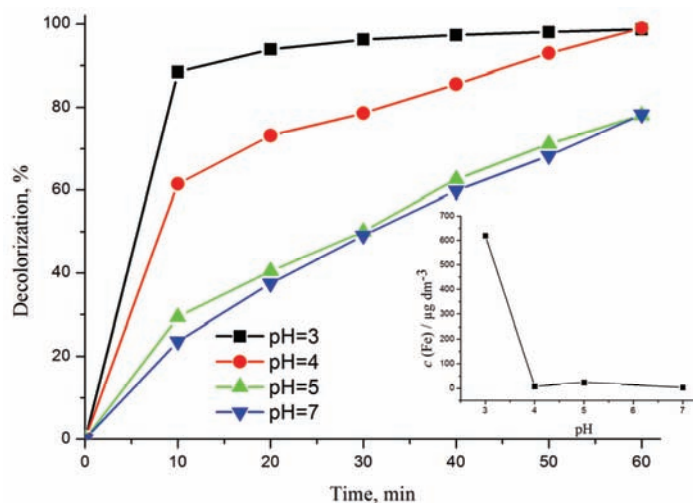


Fig. 8. Effect of solution pH on the RB decolorization in the presence of 3.4Fe/TiO₂. The inset shows the effect of the initial pH on the leaching of iron. Operating conditions: [RB]₀ = 60 mg dm⁻³ [H₂O₂]₀ = 20 mM and photocatalyst, 0.5 g dm⁻³.

One additional possible reason of such dependence on the pH value is the influence of adsorption and the results are presented in Fig. 9. A strong electrostatic attraction between dye and the surface exists when the Fe/TiO₂ surface is positively charged and the dye is negatively charged. At lower pH values, the conditions for sorption were optimal.

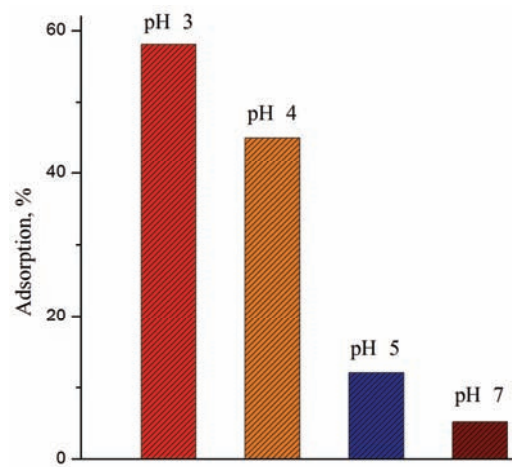


Fig. 9. Sorption ability of the 3.4Fe/TiO₂ catalyst at different pH values. Operating conditions: [RB]₀ = 60 mg dm⁻³, photocatalyst, 0.5 g dm⁻³ and time = 60 min.

Degradation of a colorless pollutant

When the compound used as model pollutant absorbs in the visible region, such as the azo dye in the present study, the dye rather than the TiO₂ particles is

excited by visible light. After excitation, the electrons from the dye molecule are injected into the TiO_2 conduction band. The TiO_2 acts only as an electron transfer mediator in this reaction.³⁵ Thus, an experiment with 4-CP was performed to prove that the studied catalyst is capable of degrading colorless pollutants and to produce reactive oxygen species, meaning that excitation of the dye molecule is not the only mechanism. The results are shown in Fig. 10, from which it can be seen that after just 10 min of the treatment, the 4-CP peak with a retention time of about 10 min had almost disappeared. Three additional peaks of degradation products with retention times of 6.8, 2.9 and 1 min appeared. In Fig. 10c, after 20 min of the treatment, a further decrease in the intensity of the peaks, indicating further degradation, could be observed.

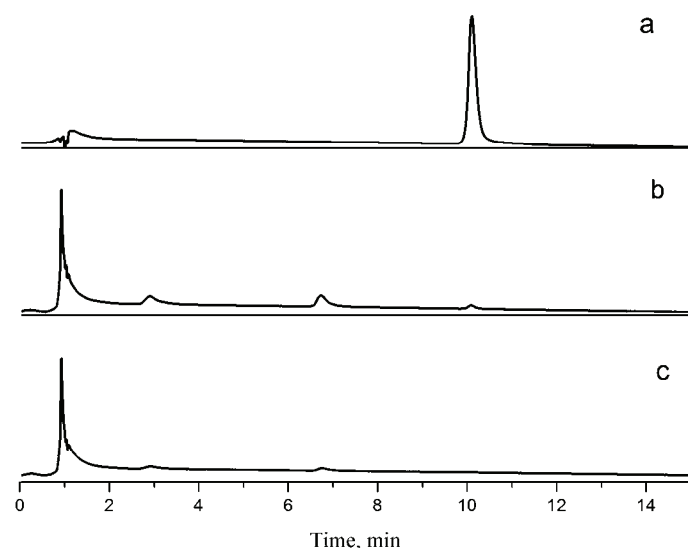


Fig. 10. Chromatograms of 4-CP degraded by the 3.4Fe/TiO₂ catalyst at different times:
a) 0; b) 10 and c) 20 min. Operating conditions: [4-CP]₀ = 100 mg dm⁻³, [H₂O₂]₀ = 20 mM,
photocatalyst, 0.5 g dm⁻³ and pH 4.

CONCLUSIONS

Fe/TiO_2 photocatalysts with different contents of Fe (0.5, 1.6, 3.4 and 6.4 %) were successfully prepared by the microwave-hydrothermal method. The XRD results showed that the Fe^{3+} were highly dispersed in the TiO_2 lattice. The Fe doping influenced the textural characteristics of the synthesized photocatalysts, increasing the specific surface area, which is the critical parameter for the enhancement of photocatalytic activity. Furthermore, Fe doping played a role in extending the light absorption into the visible region. $\text{Fe}-\text{TiO}_2$ can efficiently catalyze the degradation of RB under sun-like irradiation in the presence of H₂O₂. The photocatalyst 3.4Fe/TiO₂ was found to be the most efficient with

H_2O_2 . The results indicate that the pH value had a great effect on the photo-catalytic efficiency. The decolorization of RB by the 3.4Fe/TiO₂/H₂O₂ process was more favorable at acidic pH values. With pH > 4, the release of Fe ions into the solution was negligible in the heterogeneous photo-Fenton process.

Under the optimal experimental conditions, the catalyst was able to degrade even a colorless pollutant. Therefore, it could be considered a good candidate for wastewaters remediation purposes.

Acknowledgements. This work is supported by the Ministry of Education, Science and Technological Development of the Republic of Serbia (Contracts No. 172030 and 172035).

ИЗВОД

ФЕНТОНОВА ОКСИДАЦИЈА АЗО БОЈЕ ПОМОЋУ МЕЗОПОРОЗНОГ Fe/TiO₂ ПРИПРЕМЉЕНОГ ХИДРОТЕРМАЛНОМ МЕТОДОМ ПОТПОМОГНУТОМ МИКРОТАЛАСИМА

ЈЕЛЕНА НЕШИЋ¹, ДРАГАН Д. МАНОЛОВИЋ², МИЛИЦА ЈОВИЋ¹, БИЉАНА П. ДОЈЧИНОВИЋ³,
ПРЕДРАГ Ј. ВУЛИЋ⁴, ЈУГОСЛАВ КРСТИЋ⁵ и ГОРАН М. РОГЛИЋ²

¹Иновациони центар Хемијској факултети, Универзитет у Београду, Студентски трг 12, 11000
Београд, ²Хемијски факултет, Универзитет у Београду, Студентски трг 12, 11000 Београд,

³Институција за хемију, технолоџију и мешалуртију, Центар за хемију, Универзитет у Београду,
Његошева 12, 11000 Београд, ⁴Лабораторија за кристалографију, Рударско-геолошки факултет
Универзитета у Београду, Ђушина 7, 11000 Београд и ⁵Институција за хемију, технолоџију и
мешалуртију, Центар за катализу и хемијско инжењерство, Универзитет у Београду,
Његошева 12, 11000 Београд

Fe-допирани TiO₂ фотокатализатори са различитим садржајем гвожђа (0,5, 1,6, 3,4 и 6,4 %) синтетисани су микроталасно-хидротермалном методом и карактерисани помоћу XRD, физисорпције N₂ на 77 K и DRS методом. Карактеризација је показала да су јони гвожђа потпуно дисперговани унутар кристалне решетке TiO₂. Нађено је да сви катализатори имају мезопорозну структуру и да Fe-допирање повећава специфичну површину. UV-Vis спектри показују да се апсорпција помера ка већим таласним дужинама (црвено померање) са повећањем концентрације допанта. Фотокатализичка активност узорака је процењена на основу деколоризације текстилне реактивне боје реактивно плаво 52 (RB) у воденом раствору помоћу лампе са спектром сунчевог зрачења у присуству H₂O₂ (хетерогени фото-Фентонов процес). Фотокатализатор са 3,4 % гвожђа се показао као најефикаснији са H₂O₂. Утицај иницијалне pH вредности је утврђен и испитано је отпуштање јона гвожђа у зависности од pH. Закључено је да је погоднија кисела средина за деколоризацију и да је, када је pH > 4, отпуштање гвожђа у раствор занемарљиво. Испитана је фотокатализичка деградација 4-хлорфенола (4-CP) при оптималним условима и показало се да је дати катализатор способан и за деградације безбојних загађивача.

(Примљено 1. октобра, ревидирано 20 новембра, прихваћено 21. новембра 2013)

REFERENCES

1. M. A. Behnajady, N. Modirshahla, H. Fathi, *J. Hazard. Mater., B* **136** (2006) 816
2. O. Lergini, E. Oliveros, A. M. Braun, *Chem. Rev.* **93** (1993) 671
3. M. S. Lucas, J. A. *Dyes Pigm.* **74** (2007) 622

4. V. Augugliaro, V. Loddo, G. Palmisano, L. Palmisano, *Clean by light irradiation: Practical applications of supported TiO₂*, The Royal Society of Chemistry, Cambridge, UK, 2010, p. 15
5. J. Zhu, F. Chen, J. Zhang, H. Chen, M. Anpo, *J. Photochem. Photobiol., A* **180** (2006) 196
6. M. Zhou, J. Yu, B. Cheng, H. Yu, *Mater. Chem. Phys.* **93** (2005) 159
7. X. H. Wang, J.-G. Li, H. Kamiyama, Y. Moriyoshi, T. Ishigaki, *J. Phys. Chem., B* **110** (2006) 6804
8. J. A. Rengifo-Herrera, E. Mielczarski, J. Mielczarski, N. C. Castillo, J. Kiwi, C. Pulgarin, *Appl. Catal., B* **84** (2008) 448
9. A. Dobosz, A. Sobczynski, *Water Res.* **37** (2003) 1489
10. Z. Xiong, J. Ma, W. J. Ng, T. D. Waite, X. S. Zhao, *Water Res.* **45** (2011) 2095
11. C. Fountzoula, N. Spanos, H. K. Matralis, C. Kordulis, *Appl. Catal., B* **35** (2002) 295
12. J. Nešić, D. D. Manojlović, I. Andelković, B. P. Dojčinović, P. J. Vulić, J. Krstić, G. M. Roglić, *J. Mol. Catal., A* **378** (2013) 67
13. F. Mazille, T. Schoettl, C. Pulgarin, *Appl. Catal., B* **89** (2009) 635
14. F. Mazille, A. Lopez, C. Pulgarin, *Appl. Catal., B* **90** (2009) 321
15. N. Banić, B. Abramović, J. Krstic, D. Šojic, D. Lončarević, Z. Cherkezova-Zheleva, V. Guzsvany, *Appl. Catal., B* **107** (2011) 363
16. J. Rodríguez-Carvajal, *FullProf Suite: Crystallographic tools for Rietveld, profile matching & integrated intensity refinements of X-ray and/or neutron data*. <http://www.ill.eu/sites/fullprof/>
17. S. Brunauer, P. H. Emmett, E. Teller, *J. Am. Chem. Soc.* **60** (1938) 309
18. S. J. Gregg, K. S. W. Sing, *Adsorption, Surface Area and Porosity*, Academic Press, London, 1982, p. 126
19. F. Rouquerol, J. Rouquerol, K. Sing, *Adsorption by powders and porous solids*, Academic Press, London, 1999, p. 111
20. E. P. Barrett, L. G. Joyner, P. P. Halenda, *J. Am. Chem. Soc.* **73** (1951) 373
21. J. Chen, M. Yao, X. Wang, *J. Nanopart. Res.* **10** (2008) 163
22. Y. C. Cao, T. He, Y. Chen, Y. Cao, *J. Phys. Chem., C* **114** (2010) 3627
23. Y. Wang, H. Cheng, Y. Hao, J. Ma, W. Li, S. Cai, *J. Mater. Sci.* **34** (1999) 3721
24. J. Rouquerol, D. Avnir, C. W. Fairbridge, D. H. Everett, J. H. Haynes, N. Pemicone, J. D. F. Ramsay, K. S. W. Sing, K. K. Unger, *Pure Appl. Chem.* **66** (1994) 1739
25. T. Umebayashi, T. Yamaki, H. Itoh, K. Asail, *J. Phys. Chem. Solids* **63** (2002) 1909
26. J. Zhu, W. Zheng, B. He, J. Zhang, M. Anpo, *J. Mol. Catal., A* **216** (2004) 35
27. Y. Jiaguo, X. Quanjun, Z. Minghua, *Appl. Catal., B* **90** (2009) 595
28. J. Mitrović, M. Radović, D. Bojić, T. Andelković, M. Purenović, A. Bojić, *J. Serb. Chem. Soc.* **77** (2012) 465
29. T. Tong, J. Zhang, B. Tian, F. Chen, D. He, *J. Hazard. Mater.* **155** (2008) 572
30. B. Zhao, G. Mele, I. Pio, J. Li, L. Palmisano, G. Vasapollo, *J. Hazard. Mater.* **176** (2010) 569
31. C. Lizama, J. Freer, J. Baeza, H. D. Mansilla, *Catal. Today* **76** (2002) 235
32. S. Sakthivel, B. Neppolian, M. V. Shankar, B. Arabindoo, M. Palanichamy, V. Murugesan, *Sol. Energy Mater. Sol. Cells* **77** (2003) 65
33. M. I. Stefan, A. R. Hoy, J. R. Bolton, *Environ. Sci. Technol.* **30** (1996) 2382
34. H. R. Eisenhauer, *J.-Water Pollut. Control Fed.* **36** (1964) 1116
35. M. A. Fox, M. T. Dulay, *Chem. Rev.* **93** (1993) 341.



Effect of the orientation of the initially formed grains on the final morphology of electrodeposited lead[•]

NEBOJŠA D. NIKOLIĆ^{1#}, KONSTANTIN I. POPOV^{1,2*}, EVICA R. IVANOVIĆ³
and GORAN BRANKOVIĆ^{4#}

¹ICTM – Institute of Electrochemistry, University of Belgrade, Njegoševa 12, P. O. Box 473, 11001 Belgrade, ²Faculty of Technology and Metallurgy, University of Belgrade, Karnegijeva 4, P. O. Box 3503, 11001 Belgrade, ³Faculty of Agriculture, University of Belgrade, Nemanjina 6, Belgrade-Zemun and ⁴Institute for Multidisciplinary Research, University of Belgrade, Kneza Višeslava 1a, Belgrade, Serbia

(Received 11 December 2013, revised 20 January, accepted 21 January 2014)

Abstract: The processes of Pb electrodeposition under diffusion control were examined by scanning electron microscopy (SEM) of the formed crystals. The orientation of grains of hexagonal shape formed in the initial stage of electrodeposition strongly affected the final morphology of the Pb crystals. The formation of Pb crystals of the different shape from the same initial shape was discussed in terms of the effect of orientation of initially formed grains on the type of diffusion control. A spherical diffusion layer was formed around the tip of the hexagonal-shaped grain oriented with its tip towards the bulk solution that led to the formation of elongated crystals in the growth process. On the other hand, a cylindrical type of diffusion was responsible for the growth of hexagonal-shaped grains oriented with the lateral side towards the bulk solution. Pb crystals with well-defined sides parallel to the surface area of the macroelectrode were formed under this type of diffusion.

Keywords: electrodeposition; lead; crystal; spherical diffusion; cylindrical diffusion; scanning electron microscope (SEM).

INTRODUCTION

Thanks to its specific characteristics, such as extremely high reactivity and superconductivity, lead has found an application in many very important technologies.¹ Some of these technologies are related with a production of high purity active material for acid batteries,² for semiconductors,^{3,4} and in the fabrication of electrochromic devices.⁵ Electrodeposition technique is very attractive way to

• In memory of Prof. Dr. John O'M. Bockris.

* Corresponding author. E-mail: kosta@tmf.bg.ac.rs

Serbian Chemical Society member.

doi: 10.2298/JSC131211006N

obtain Pb in the form suitable for application in various technologies. The morphology of electrodeposited Pb, the growth rate, particle size and number density can be easily regulated by the choice and control of parameters such as deposition potential or current density, regime of electrolysis, time, temperature and solution composition.

Lead belongs to the group of normal metals that are characterized by high exchange current density values, low melting points and high overpotentials for hydrogen discharge.^{6,7} Regardless of the type of electrolyte, electrodeposition of lead occurs under mixed ohmic–diffusion or even full ohmic control of the electrodeposition.^{8–11} The ratio of the ohmic to the overall control of the electrodeposition increases with increasing concentration of Pb^{2+} so that the electrodeposition process becomes a full ohmic controlled one at high concentrations of Pb^{2+} .^{8,11}

Regular crystals were the main morphological forms obtained in electrodepositions at overpotentials in the ohmic control region.^{11,12} The shape of these crystals did not depend on the type of electrolyte. On the contrary, the shape of the dendrites formed under the diffusion control was strongly influenced by the type of electrolyte used. Considering the Wranglen definition of a dendrite,¹³ dendrites of the secondary (S) type, constructed from a stalk and primary and secondary branches, were electrodeposited from complex electrolytes, such as acetate⁹ and alkaline¹⁰ electrolytes. Needle-like and dendrites constructed from stalk and only primary branches (the primary (P) type) were formed during electrodepositions from basic (nitrate) electrolytes. In addition to dendrites, irregular crystals of various shapes were also formed during electrodepositions under diffusion control. The aim of this study was to investigate the mechanism of the formation of these irregular Pb crystals.

EXPERIMENTAL

Electrodeposition of lead was performed in an open cell from 0.40 M $\text{Pb}(\text{NO}_3)_2$ in 2.0 M NaNO_3 at room temperature ($22.0 \pm 0.5^\circ\text{C}$). Lead was electrodeposited at overpotentials of 50 and 75 mV, with amounts of the electricity of 0.10 and 0.95 mA h cm^{-2} . Doubly distilled water and analytical grade chemicals were used for the preparation of the solution for electrodeposition of lead. All electrodepositions were performed on vertical cylindrical copper electrodes. The geometric surface areas of the copper electrodes were 0.25 cm^2 for the SEM analyses of the obtained Pb deposits and 0.50 cm^2 for recording the polarization curve. The polarization curve for the electrodeposition of lead was recorded potentiostatically by changing the overpotential in 5 mV steps. In order to obtain a reproducible shape of the polarization curve for this reaction, the following experimental procedure,^{8,14} usual for the recording of the polarization curves of fast electrodeposition processes, was applied. At low overpotentials up to 55 mV (Fig. 1), the values of the current obtained after reaching steady-state values were used for constructing the polarization curves. Since at the overpotentials after the inflection point (55 mV) on the polarization curve in Fig. 1, the current increased dramatically over

time, the values were recorded immediately after setting the selected overpotential values were used.

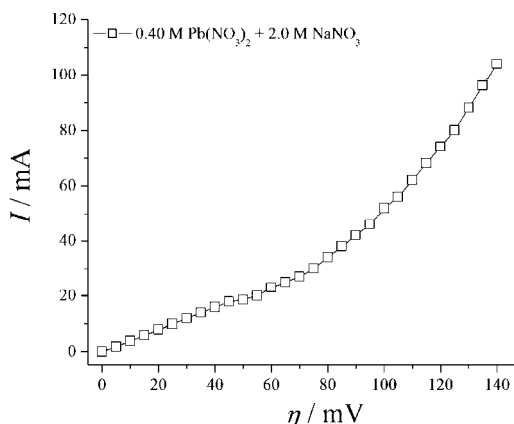


Fig. 1. The polarization curve for lead electrodeposition from 0.40 M $\text{Pb}(\text{NO}_3)_2$ in 2.0 M NaNO_3 . The surface area of working electrode was 0.50 cm^2 .

The reference and counter electrodes were of pure lead. The counter electrode was lead foil with surface area of 0.80 dm^2 and was placed close to the cell walls. The reference electrode was lead wire, the tips of which were positioned at a distance of about 0.2 cm from the surface of the working electrode. The working electrodes were placed in the centre of the cell, at the same location for each experiment.

A Tescan digital scanning electron microscope was used for the examination of the morphology of the Pb deposits.

RESULTS AND DISCUSSION

Polarization curve for Pb electrodeposition from 0.40 M $\text{Pb}(\text{NO}_3)_2$ in 2.0 M NaNO_3 is shown in Fig. 1. The interval of overpotentials between 0 and 45 mV corresponds to ohmic control. The diffusion control commences at an overpotential of 45 mV and the inflection point is observed at 55 mV.

SEM images of the Pb deposits formed during the initial stages of electrodeposition at overpotentials of 50 and 75 mV are shown in Fig. 2a and b, and Fig. 2c and d, respectively. It is necessary to note that both overpotentials corresponded to electrodeposition under diffusion control. At both overpotentials, hexagonal-shaped grains were formed together with numerous other grains of various shapes that showed well-defined crystal planes. Although the shape of the hexagonal grains was the same in both cases, the orientations of these grains were completely different. In the Pb deposit electrodeposited at 50 mV, the hexagonal-shaped grain was oriented with its lateral side towards the bulk solution (Fig. 2a and b). On the other hand, the hexagonal-shaped grain in the Pb deposit electrodeposited at 75 mV was oriented with its tip towards the bulk solution (Fig. 2c and d).

Analysis of Fig. 2 clearly confirms that nucleation did not occur simultaneously over the entire cathode surface, but it was a process extended in time so that

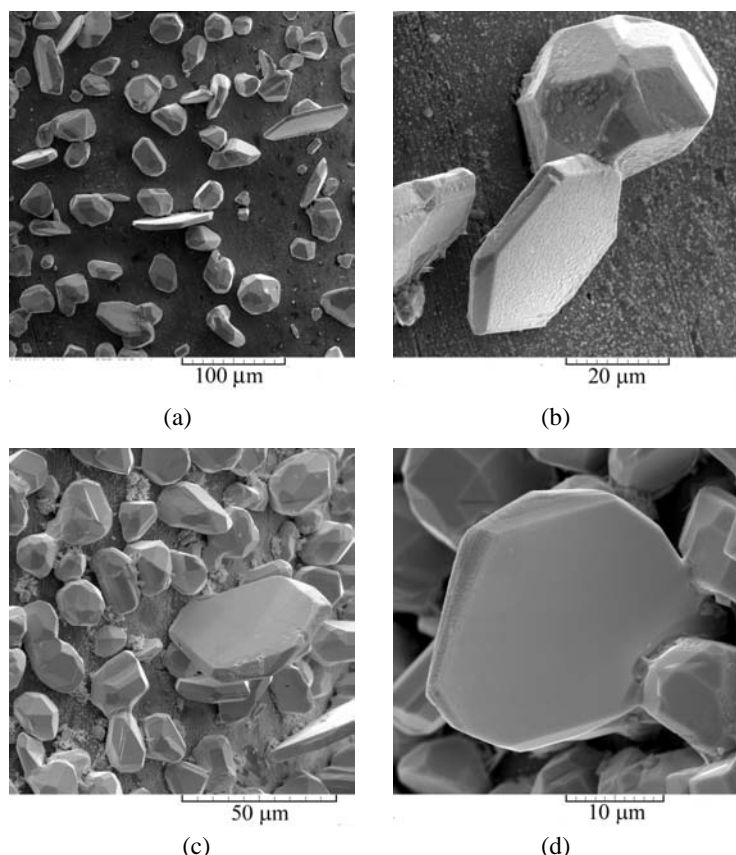


Fig. 2. SEM images of the Pb deposits formed in the initial stages of Pb electrodeposition from 0.40 M $\text{Pb}(\text{NO}_3)_2$ in 2.0 M NaNO_3 at overpotentials of: a) and b) 50 mV, and c) and d) 75 mV. The amount of electricity was $0.10 \text{ mA h cm}^{-2}$.

grains generated earlier may be considerably larger in size than those generated later.¹⁵ In the case of fast electrochemical processes, nucleation exclusion zones around already existing nuclei are formed,^{16,17} as seen from Fig. 2. This process causes a periodicity in the structure of polycrystalline deposit.^{18–20} With increasing the electrodeposition time, due to the current density distribution effect,²¹ further nucleation and growth primarily occurs at these hexagonal-shaped grains. The final forms of the Pb crystals obtained at overpotentials of 50 and 75 mV with an amount of electricity of $0.95 \text{ mA h cm}^{-2}$ are shown in Fig. 3. From Fig. 3, it can be seen that the Pb crystals formed at an overpotential of 50 mV (Fig. 3a and b) were completely different in shape to those formed at 75 mV (Fig. 3c and 3d). The characteristics of the 2D (two-dimensional) Pb crystals formed at 50 mV were well-developed sides parallel to the surface area of the macroelectrode (crystals denoted with A, B, C and D in Fig. 3a and the crystal shown in Fig. 3b).

The 2D crystals obtained at 75 mV were with sharp tips as can be seen from Fig. 3c and d.

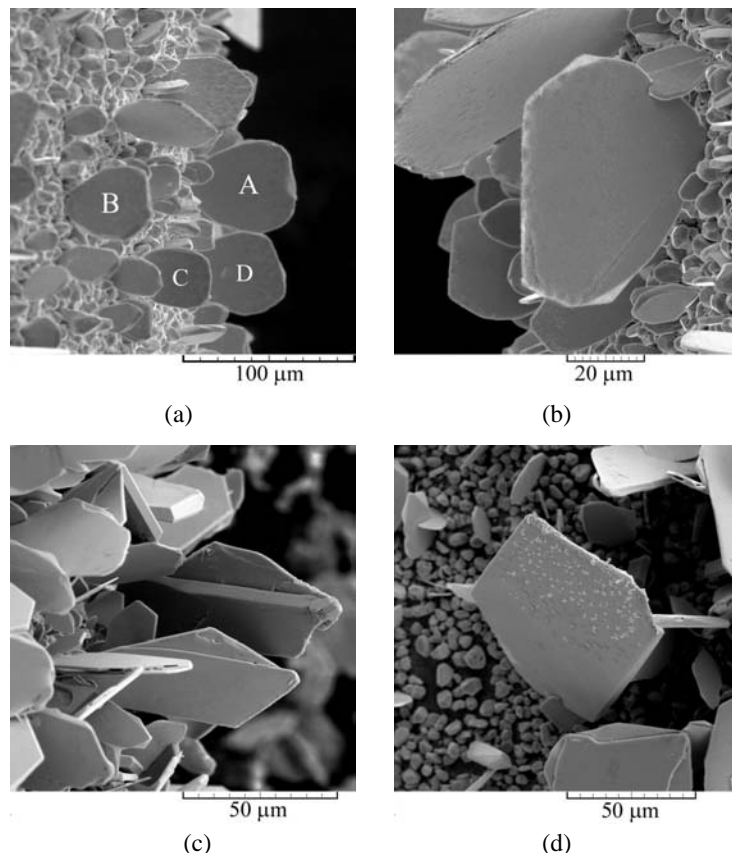


Fig. 3. SEM images showing the shape of crystals formed by electrodeposition processes from 0.40 M $\text{Pb}(\text{NO}_3)_2$ in 2.0 M NaNO_3 with amount of electricity of $0.95 \text{ mA h cm}^{-2}$. The overpotentials of electrodeposition were: a) and b) 50 mV, and c) and d) 75 mV.

Hence, the same shape of Pb grains formed in the initial stage of the electrodeposition (Fig. 2) gave completely different final shapes of the Pb crystals (Fig. 3). Considering that the electrodeposition processes at both overpotentials were under diffusion control, it is very clear that the orientation of the grains formed in the initial stages of electrodeposition played an important, or even crucial, role in the mechanism of the formation of the final forms of the Pb crystals. A schematic presentation of the processes of formation and growth of the crystals in dependence of the orientation of the initially formed grains is given in Fig. 4.

The equation of the cathodic polarization curve for a flat or a large spherical electrode of a massive metal is given by Eq. (1):¹⁵

$$j = \frac{j_0(f_c - f_a)}{1 + \frac{j_0 f_c}{j_L}} \quad (1)$$

where j , j_0 and j_L are the current density, the exchange current density and the limiting diffusion current density, respectively, and:

$$f_c = 10^{\frac{\eta}{b_c}} \quad (2)$$

$$f_a = 10^{-\frac{\eta}{b_a}} \quad (3)$$

where b_c and b_a are the cathodic and anodic Tafel slopes and η is the overpotential. Eqation (1) is modified for use in electrodeposition of metals by taking cathodic current density and overpotential as positive.

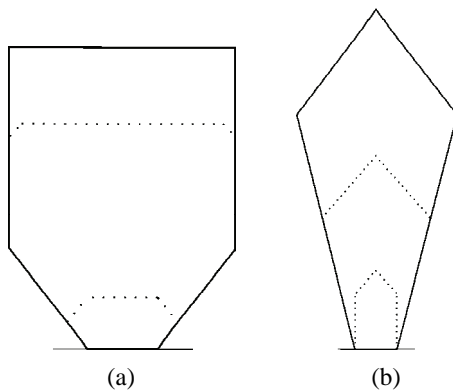


Fig. 4. Time dependent simulation of growth of the differently oriented crystals.

The cathodic limiting diffusion current density for steady-state linear diffusion, j_L , is given by Eq. (4):

$$j_L = \frac{nFDc_0}{\delta} \quad (4)$$

where n is the number of transferred electrons, F is the Faraday constant, D and c_0 are the diffusion coefficient and bulk concentration of the depositing ion, respectively, and δ is the thickness of the diffusion layer of the macroelectrode.

The parallel sides of initially and finally formed Pb crystals (Fig. 3a and b) clearly indicate that the growth of the hexagonal-shaped grains (Fig. 2a and b) can be ascribed to a cylindrical type of diffusion around their top edges. A schematic presentation of a crystal that obeys this type of diffusion is presented in Fig. 5a. The limiting diffusion current density to the cylindrical electrode, $j_{L,c}$ growing inside the diffusion layer of the macroelectrode is given by Eq. (5):^{22,23}

$$j_{L,c} = \frac{nFDc_0}{r \ln \frac{r+d}{r}} \quad (5)$$

where $d = (\pi Dt)^{0.5}$, r is the radius of the flat dendrite precursor and $r \ll l$. Assuming to a first approximation that under steady state conditions d corresponds to thickness of the diffusion layer of the macroelectrode, δ , then the condition $\delta \gg r$ is valid and Eq. (5) can be rewritten in the form:

$$j_{L,c} = \frac{nFDc_0}{r \ln \frac{\delta}{r}} \quad (6)$$

or in the form:

$$j_{L,c} = \frac{j_L}{\frac{r}{\delta} \ln \frac{\delta}{r}} \quad (7)$$

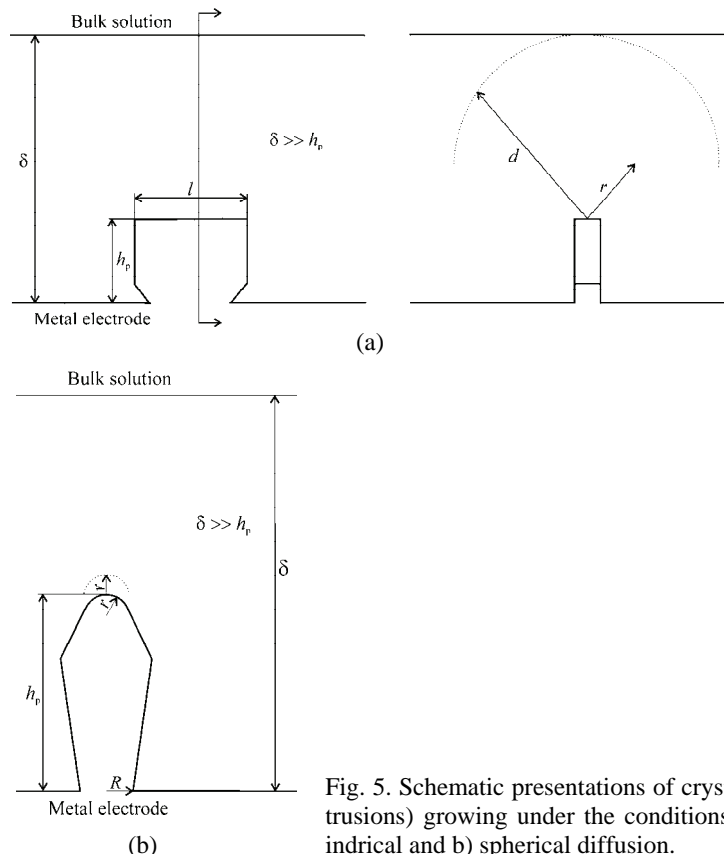


Fig. 5. Schematic presentations of crystals (or protrusions) growing under the conditions of: a) cylindrical and b) spherical diffusion.

In the initial stage of the electrodeposition, the sizes of all grains are similar to each other, and the cylindrical type of diffusion cannot be established due to the overlapping of the diffusion zones. Then, the maximum current density to the surface of grain (top edge) corresponds to the limiting diffusion current density, j_L . Dendritic growth may be expected for:

$$j_L < j_{tip,c} \quad (8)$$

i.e., when the current density under mixed controlled deposition to the tip of the grain, $j_{tip,c}$, becomes larger than the linear limiting diffusion current density.

Substitution of $j_{L,c}$ from Eq. (7) into Eq. (1) instead of j_L gives the equation for the tip current density, $j_{tip,c}$, as:

$$j_{tip,c} = \frac{j_0(f_c - f_a)}{1 + \frac{j_0 f_c}{j_L} \frac{r}{\delta} \ln \frac{\delta}{r}} \quad (9)$$

Relation (8) can then be written in the form:

$$j_L < \frac{j_0(f_c - f_a)}{1 + \frac{j_0 f_c}{j_L} \frac{r}{\delta} \ln \frac{\delta}{r}} \quad (10)$$

If it is assumed that $r \ll \delta$, which is true for the assumed meaning of r and δ , then:

$$\frac{r}{\delta} \ln \frac{\delta}{r} \ll 1$$

and the overpotential function is larger than the j_L/j_0 ratio. Using Eq. (2), it follows that the minimum overpotential at which the growth of a dendrite is possible, η_i , is given by Eq. (11):

$$\eta_i = b_c \log \frac{j_L}{j_0} \quad (11)$$

Hence, initiation of dendritic growth is possible only at overpotentials larger than η_i .

On the other hand, it could be assumed that the condition of spherical diffusion is fulfilled around the tip of a hexagonal-shaped grain oriented normally to the electrode surface, *i.e.*, with the tip towards the bulk of the solution (Fig. 2c and d). A schematic presentation of a crystal buried deep in the diffusion layer of the macroelectrode around the tip of which a spherical diffusion layer is formed is shown in Fig. 5b. The local limiting diffusion current density is larger at the tips of such crystals than the corresponding linear diffusion current density, and for this reason, the tip of a crystal will grow faster than the other parts of a crystal where the conditions of cylindrical diffusion are fulfilled.^{24,25} As a result of this

process, elongated crystals, like those shown in Fig. 3c and d, are formed. Then, the formation of the elongated crystals could be explained in the following way.

At the tip of a hexagonal-shaped grain, the lateral flux cannot be neglected and the situation can be approximated by assuming a spherical diffusion current density, $j_{L,s}$, given by Eq. (12):^{24,25}

$$j_{L,s} = \frac{nFDc^*}{r} \quad (12)$$

where c^* is the concentration of the diffusing species at a distance r from the tip, assuming that around the tip a spherical diffusion layer having a thickness equal to the radius of the protrusion tip is formed.²⁶

If deposition to the macroelectrode is under full diffusion control, the distribution of the concentration, c , inside the linear diffusion layer is given by Eq. (13):²⁷

$$c = c_0 \frac{h}{\delta} \quad (13)$$

where $0 \leq h \leq \delta$. In the present case, it will be:

$$c^* = c_0 \frac{h_p + r}{\delta} \quad (14)$$

and

$$j_{L,s} = j_L \left(1 + \frac{h_p}{r} \right) \quad (15)$$

because of Eqs. (4), (12) and (14), where h_p is height of a protrusion (*i.e.*, crystal in the present case).

Substitution of $j_{L,s}$ from Eq. (15) into Eq. (1) produces for $h_p/r \gg 1$ after rearranging Eq. (16):

$$j_{tip,s} = j_{0,tip} (f_c - f_a) \quad (16)$$

where $j_{tip,s}$ and $j_{0,tip}$ are the current density and the exchange current density at the tip of the protrusion, respectively. Then, the electrodeposition process to the tip of such protrusion inside the diffusion layer of the macroelectrode is an activation-controlled process relative to the surrounding electrolyte, but it is under mixed control relative to the bulk solution. The maximum growth rate at a given overpotential corresponds to activation-controlled deposition, occurring on the tip of a crystal, where spherical diffusion control can be established.

Naturally, the concentration of depositing ions at the tip of crystal, c_{tip} , is given by Eq. (17):

$$c_{\text{tip}} = c_0 \frac{h_p}{\delta} \quad (17)$$

According to Newman,²⁸ the exchange current density at the tip of a protrusion growing inside the diffusion layer of a macroelectrode, $j_{0,\text{tip}}$, is given by Eq. (18):

$$j_{0,\text{tip}} = j_0 \left(\frac{c_{\text{tip}}}{c_0} \right)^\gamma \quad (18)$$

where:

$$\gamma = \frac{d(\log j_0)}{d(\log c_0)} \quad (19)$$

and j_0 corresponds to the exchange current density for a surface concentration, c_0 , equal to the bulk concentration, or:

$$j_{0,\text{tip}} = j_0 \left(\frac{h_p}{\delta} \right)^\gamma \quad (20)$$

because of Eq. (17). Substitution of $j_{0,\text{tip}}$ from Eq. (20) into Eq. (16) produces:

$$j_{\text{tip},s} = j_0 \left(\frac{h_p}{\delta} \right)^\gamma (f_c - f_a) \quad (21)$$

and the minimum overpotential at which dendritic growth is possible is:

$$\eta_i = b_c \log \frac{j_L}{j_0}$$

for $h_p = \delta$ and $f_c \gg f_a$, if the condition for dendritic growth initiation is $j_L < j_{\text{tip},s}$. Hence, both kinds of dendrites can grow at the same deposition overpotential.

In any case, the orientation of the initially formed grains affects the type of diffusion, and hence, the final surface morphology. Orientation of the initially formed grains is not strictly related to the overpotential of the electrodeposition, but to the nucleation processes. However, irregular crystals grown under the conditions of cylindrical diffusion are not found in Pb deposits electrodeposited at overpotentials after the inflection point. The crystals shown in Fig. 3 are not dendrites following the classical definition of a dendrite,¹³ but they behave as dendrites from the electrochemical point of view. This was especially valid for crystals obtained at an overpotential of 75 mV that have sharp tips oriented to the bulk solution. From the electrochemical point of view, a dendrite is defined as an electrode surface protrusion that grows under activation control, while electrodeposition to the macroelectrode is predominantly under diffusion con-

trol.^{15,24,25,27,29,30} Following this definition, the increase of current after the inflection point can be partially ascribed to the activation controlled electrodeposition at the tips of the irregular crystals, and to the strong increase of surface area of the electrode caused by the formation and growth of these forms. In this zone, another two dendritic forms, such as needle-like and fern-like dendrites, are formed with mechanisms of formation somewhat different to those presented in this investigation. The specific mechanism of formation of these types of dendrites will be presented in the future.

It is clear that the irregular crystals shown in Fig. 3 could be considered as microelectrodes situated on the macroelectrodes inside their diffusion layers, as described by Bockris *et al.*^{26,27,31} The majority of current theories concerning the examination of morphology of metal deposits are based on the Barton and Bockris,²⁶ Diggle, Despić and Bockris²⁷ and Despić, Diggle and Bockris³¹ approaches to the examination of metal electrodeposition processes. The Belgrade Electrochemical School also contributed greatly to this field of investigation. This contribution of the Belgrade Electrochemical School to the investigation of the processes of electrochemical deposition, in particular the morphology of electrodeposited metals, was clearly indicated by Bockris.³²

The current theories concerning the electrodeposition of metals are mainly nonspecific dealing with the electrochemical and mass transfer conditions in which some morphological forms of deposits are obtained. This paper is one of the first papers in which specific characteristics of the formation of the determined morphological forms are considered.

CONCLUSIONS

Electrodeposition of lead from 0.40 M Pb(NO₃)₂ in 2.0 M NaNO₃ at overpotentials belonging to diffusion control was investigated. The technique of scanning electron microscopy (SEM) was used for morphological analysis of the obtained Pb deposits. The morphology of the obtained Pb crystals strongly depended on the orientation of hexagonal-shaped grains formed in the initial stage of electrodeposition. The different shapes formed from the same initial shapes were explained by the effect of orientation of initially formed Pb grains on the type of diffusion. A spherical diffusion layer is formed around the tip of hexagonal-shaped grains oriented with the tip towards the bulk solution. On the contrary, orientation of hexagonal-shaped grains with the lateral side towards the bulk solution causes a cylindrical type of diffusion.

Acknowledgement. The work was supported by the Ministry of Education, Science and Technological Development of the Republic of Serbia under the research project: "Electrochemical synthesis and characterization of nanostructured functional materials for application in new technologies" (No. 172046).

И З В О Д
УТИЦАЈ ОРИЈЕНТАЦИЈЕ ПОЧЕТНО ФОРМИРАНИХ ЗРНА НА МОРФОЛОГИЈУ
ЕЛЕКТРОХЕМИЈСКИ ИСТАЛОЖЕНОГ ОЛОВА

НЕБОЈША Д. НИКОЛИЋ¹, КОНСТАНТИН И. ПОПОВ^{1,2}, ЕВИЦА Р. ИВАНОВИЋ³ и ГОРАН БРАНКОВИЋ⁴

¹ИХТМ – Центар за електрохемију, Универзитет у Београду, Његошева 12, Београд, ²Технолошко–металуршки факултет, Универзитет у Београду, Карнејијева 4, Београд, ³Полој privредни факултет, Универзитет у Београду, Немањина 6, Београд–Земун и ⁴Институт за мултидисциплинарна истраживања, Универзитет у Београду, Кнеза Вишеслава 1а, Београд

Процеси електрохемијског таложења олова у условима дифузионе контроле су испитивани анализом добијених кристала техником скенирајуће електронске микроскопије. Оријентација зrna хексагоналног облика формираних у почетној фази електрохемијског таложења је снажно утицала на крајњу морфологију кристала олова. Формирање кристала олова различитог облика од истог почетног облика је дискутовано преко утицаја оријентације почетно формираних зrna на тип дифузионе контроле. Сферични дифузиони слој формира се око врха зrna хексагоналног облика оријентисаног врхом ка дубини раствора, доводећи до формирања издужених кристала током процеса раста. На другој страни, цилиндрични тип дифузије је одговоран за раст хексагонално обликованих зrna оријентисаних бочном страном ка дубини раствора. Кристали олова са добро дефинисаним странама паралелним површини макроелектроде се формирају овим типом дифузије.

(Примљено 11. децембра 2013, ревидирано 20. јануара, прихваћено 21. јануара 2014)

REFERENCES

1. C.-Z. Yao, M. Liu, P. Zhang, X.-H. He, G.-R. Li, W.-X. Zhao, P. Liu, Y.-X. Tong, *Electrochim. Acta* **54** (2008) 247
2. D. Pavlov, *J. Power Sources* **42** (1993) 345
3. B. Rashkova, B. Guel, R. T. Potschke, G. Staikov, W. J. Lorenz, *Electrochim. Acta* **43** (1998) 3021
4. C. Ehlers, U. Konig, G. Staikov, J. W. Schultze, *Electrochim. Acta* **47** (2002) 379
5. C. O. Avellaneda, M. A. Napolitano, E. K. Kaibara, L. O. S. Bulhoes, *Electrochim. Acta* **50** (2005) 1317
6. R. Winand, *Electrochim. Acta* **39** (1994) 1091
7. V. M. Kozlov, L. Peraldo Bicelli, *J. Cryst. Growth* **203** (1999) 255
8. N. D. Nikolić, K. I. Popov, P. M. Živković, G. Branković, *J. Electroanal. Chem.* **691** (2013) 66
9. N. D. Nikolić, Dj. Dj. Vaštag, P. M. Živković, B. Jokić, G. Branković, *Adv. Powder Technol.* **24** (2013) 674
10. N. D. Nikolić, Dj. Dj. Vaštag, V. M. Maksimović, G. Branković, *Trans. Nonferrous Met. Soc. China* **24** (2014) 884
11. N. D. Nikolić, G. Branković, U. Lačnjevac, *J. Solid State Electrochem.* **16** (2012) 2121
12. N. D. Nikolić, V. M. Maksimović, G. Branković, *RSC Adv.* **3** (2013) 7466
13. G. Wranglen, *Electrochim. Acta* **2** (1960) 130
14. N. D. Nikolić, V. M. Maksimović, G. Branković, P. M. Živković, M. G. Pavlović, *J. Serb. Chem. Soc.* **78** (2013) 1387
15. K. I. Popov, S. S. Djokić, B. N. Grgur, *Fundamental aspects of electrometallurgy*, Kluwer Academic/Plenum Publishers, New York, 2002, p.p. 1–305
16. I. Markov, A. Boynov, S. Toshev, *Electrochim. Acta* **18** (1973) 377

17. K. I. Popov, B. N. Grgur, E. R. Stojilković, M. G. Pavlović, N. D. Nikolić, *J. Serb. Chem. Soc.* **62** (1997) 433
18. N. Ya. Kovarskii, A. V. Lisov, *Elektrokhimiya* **20** (1984) 221 (in Russian)
19. N. Ya. Kovarskii, A. V. Lisov, *Elektrokhimiya* **20** (1984) 833 (in Russian)
20. N. Ya. Kovarskii, A. V. Lisov, *Elektrokhimiya* **20** (1984) 452 (in Russian)
21. K. I. Popov, P. M. Živković, N. D. Nikolić, *J. Serb. Chem. Soc.* **76** (2011) 805
22. K. I. Popov, M. I. Čekerevac, *Surf. Technol.* **37** (1989) 435
23. I. M. Epstein, *Elektrokhimiya* **2** (1966) 734 (in Russian)
24. K. I. Popov, N. V. Krstajić, M. I. Čekerevac, in *Modern Aspects of Electrochemistry*, R. E. White, B. E. Conway, J. O'M. Bockris, Eds., Vol. 30, Plenum Press, New York, 1996, p.p. 261–312
25. K. I. Popov, N. D. Nikolić, in *Modern Aspects of Electrochemistry*, S. S. Djokić, Ed., Vol. 54, Springer, Berlin, 2012, p.p. 1–62
26. J. L. Barton, J. O'M. Bockris, *Proc. Roy. Soc., A* **268** (1962) 485
27. J. W. Diggle, A. R. Despić, J. O'M. Bockris, *J. Electrochem. Soc.* **116** (1969) 1503
28. J. S. Newman, *Electrochemical Systems*, Prentice-Hall, Inc. Engelwood Cliffs, NJ, 1973
29. A. R. Despić, K. I. Popov, in *Modern Aspects of Electrochemistry*, B. E. Conway, J. O'M. Bockris, Eds., Vol. 7, Plenum Press, New York, 1972, p.p. 199–313
30. K. I. Popov, P. M. Živković, N. D. Nikolić, in *Modern Aspects of Electrochemistry*, S. S. Djokić, Ed., Vol. 48, Springer, New York, 2010, p.p. 163–213
31. A. R. Despić, J. W. Diggle, J. O'M. Bockris, *J. Electrochem. Soc.* **116** (1969) 507
32. J. O'M. Bockris, A. K. N. Reddy, *Modern Electrochemistry I, Ionics*, Plenum Press, New York and London, 1998, p. 2.



Synthesis of micro–mesopores flower-like γ -Al₂O₃ nano-architectures

MOZAFFAR ABDOLLAHIFAR^{1*}, MOHAMMAD REZA ZAMANI², EHSAN BEIYGIE²
and HOSAIN NEKOUEI³

¹Department of Chemical Engineering, Science and Research Branch, Islamic Azad University, Kermanshah 67131, Iran, ²Young Researchers' Club, Shahreza Branch, Islamic Azad University, Shahreza 86131, Iran and ³Department of Industry, University of Applied Science and Technology, Larestan Branch, Larestan 74311, Iran

(Received 3 September 2013, revised 20 January, accepted 21 January 2014)

Abstract: Micro–mesopores flowerlike γ -Al₂O₃ nano-architectures were synthesized by a thermal decomposition method using synthesized AlOOH (boehmite) as a precursor. After calcination at 500 °C for 5 h, the obtained flower-like γ -Al₂O₃ had a structure similar to that of the AlOOH precursor. X-Ray diffraction (XRD), FTIR, TG, FESEM and TEM techniques were used to characterize morphology and structure of the synthesized samples. The specific surface area (BET), pore volume and pore-size distribution of the products were determined by N₂ adsorption–desorption measurements. The flower-like γ -Al₂O₃ showed a high BET specific surface area of 148 m² g⁻¹ with a total pore volume of 0.59 cm³ g⁻¹.

Keywords: γ -Al₂O₃; micro–mesopores; nano-architecture; flower-like.

INTRODUCTION

Nowadays, materials, such as γ -Al₂O₃, having a crystalline framework, large porosity and high surface area are receiving a great deal of attention. Due to their thermal, chemical and mechanical stability, hydrated alumina or aluminum hydroxides find potential applications as ceramic oxides,¹ adsorbents,² catalysts,³ catalyst supports⁴ and are mainly used as refractory materials,⁵ electrical insulators,⁶ in electronics⁷ and for ceramic membranes.⁸ From another point of view, important usages requiring large tonnages of hydrated alumina or aluminum hydroxides are as fillers in polymer and plastics products and for the production of aluminum chemicals. Particularly, γ -Al₂O₃ is extensively used in catalysis or as an adsorbent due to its high porosity and surface area.^{2,9} The alumina adsorbents and the catalytic performance of alumina-supported catalysts are, however,

*Corresponding author. E-mail: abdollahifar@gmail.com
doi: 10.2298/JSC130903007A

highly dependent on the textural and structural properties of the support and adsorbent, both of which depend on the synthesis procedure.

AlOOH is used as a precursor for γ -Al₂O₃, which is formed through the dehydration of the boehmite form of AlOOH at temperatures in the range 400–700 °C, whereby the produced γ -Al₂O₃ has the same morphology as that of the parent material.¹⁰ Therefore, many efforts have been made to control the morphology of AlOOH. Hitherto, different morphologies of hierarchical AlOOH, such as microspheres consisting of nanosheets,¹¹ nanofibers,¹² nanotubes,¹³ nanorods,¹⁴ nanowires,¹⁰ hollow nanospheres,¹⁵ nano-belts,¹⁶ cantaloupe-like architectures¹⁷ and hollow and self-encapsulated microspheres¹⁸ have been reported. Despite these previous extensive studies, the current knowledge concerning the formation of AlOOH structures of desired morphology for the production of γ -Al₂O₃ is still inadequate.

The hydrothermal route is one of the favorable and attractive methods for the synthesis of nanomaterials and nanostructures of very good quality. The products prepared *via* a hydrothermal route have good dispersity and crystallinity, and do not show macroscopic agglomeration. Moreover, the process conditions are moderate and easily controllable. The objective of the work reported herein, was to synthesize AlOOH by means of a hydrothermal treatment using aluminum nitrate and urea as the starting materials. A flower-like γ -Al₂O₃ nano-architecture was obtained by the thermal decomposition method using the synthesized AlOOH as the precursor.

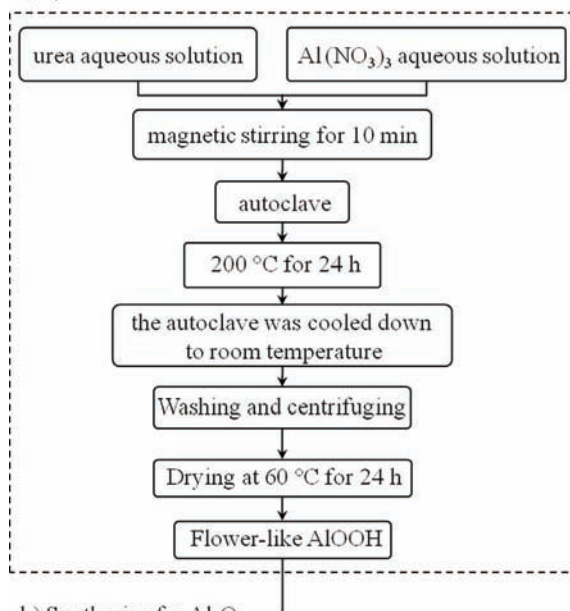
EXPERIMENTAL

All the chemical materials used in the experiments were used without further purification. In a typical procedure, 18.75 g of Al(NO₃)₃·9H₂O (Scharlau, Spain, extra pure) and 6 g of urea, CH₄N₂O (Scharlau, Spain, synthesis grade) were dissolved in 100 and 30 mL of distilled water, respectively, at room temperature in beakers and magnetically stirred to obtain homogeneous solutions A and B, respectively. Then solution B was added to solution A and stirred at room temperature for 15 min before the mixed solution was transferred into a 200 mL Teflon-lined stainless autoclave and heated at 200 °C for several hours under autogenous pressure. After reaching room temperature, the precipitate was filtered, washed three times with distilled water, and finally dried in an oven at 60 °C for 24 h under air to afford a dried sample of boehmite. The flower-like γ -Al₂O₃ was prepared by dehydroxylation of the synthesized boehmite at 500 °C under air for 5 h. A schematic flow chart for the preparation of flower-like γ -Al₂O₃ is presented in Fig. 1.

Thermal analysis of the AlOOH sample was carried out on 10 mg powder sample under air up to 800 °C at a heating rate of 13 °C min⁻¹ using a TG/DTA6300 (SII Nanotechnology, Japan) thermal analyzer that simultaneously provided thermogravimetric analysis (TG), derivative thermal analysis (DTG) and differential thermal analysis (DTA) curves. Fourier transform infrared spectroscopy (FTIR) was performed on RAYLEIGH, model WQF-510 instrument. X-Ray powder diffraction (XRD) analysis was conducted on a Bruker, model B8 Advance X-ray diffractometer with CuK_α radiation. The crystallite size of the particles of the samples were calculated using the Scherrer formula ($d = 0.9\lambda/(B\cos\theta)$, where d , λ , B , and θ are

the crystallite size, CuK α wavelength ($\lambda = 1.54 \text{ \AA}$), full width at half-maximum intensity (FWHM) of the peak in radians and the Bragg diffraction angle, respectively). TEM images of the samples were taken using a PHILIPS model CM30 transmission electron microscope operated at an accelerating voltage of 250 kV. FESEM images were obtained using a HITACHI S-4160 field emission scanning electron microscope. The nitrogen adsorption and desorption isotherms at 77 K were measured using a BEL SORP, MINI II-310 adsorption analyzer after the samples had been degassed under vacuum at 200 °C for 3 h. The original Barrett, Joyner and Halenda (BJH) method¹⁹ was applied for the calculation of the pore size distributions using the adsorption branch of the isotherms and the specific surface areas and pore volumes were determined by the BET method.

a) Synthesis of Flower-like boehmite



b) Synthesis of γ -Al₂O₃

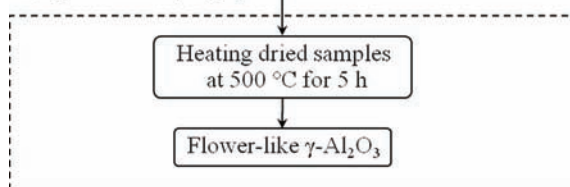


Fig. 1. Schematic flow chart for the preparation of a) AlOOH and b) γ -Al₂O₃.

RESULTS AND DISCUSSIONS

Figure 2 shows the XRD results of AlOOH and γ -Al₂O₃, Fig. 2a and b, respectively. The main diffraction peaks could be indexed within experimental error as the orthorhombic phase of boehmite AlOOH (JCPDS card No. 00-021-1307) and as cubic γ -Al₂O₃ (JCPDS card No. 00-001-1303), respectively. No

evidence could be found for the existence of impurities in the synthesized AlOOH and γ -Al₂O₃. The crystallite sizes calculated from the FWHM of the (120) diffractions for AlOOH and the (211) peaks for γ -Al₂O₃ using the Scherrer equation were found to be 12 and 10 nm, respectively.

Typical FT-IR spectra of the corresponding samples are shown in Fig. 3a and b. Figure 3a shows that all the absorption bands at 3300, 3096, 2098, 1638, 1518, 1390, 1156, 1066, 750, 640 and 492 cm⁻¹ are consistent with the reported

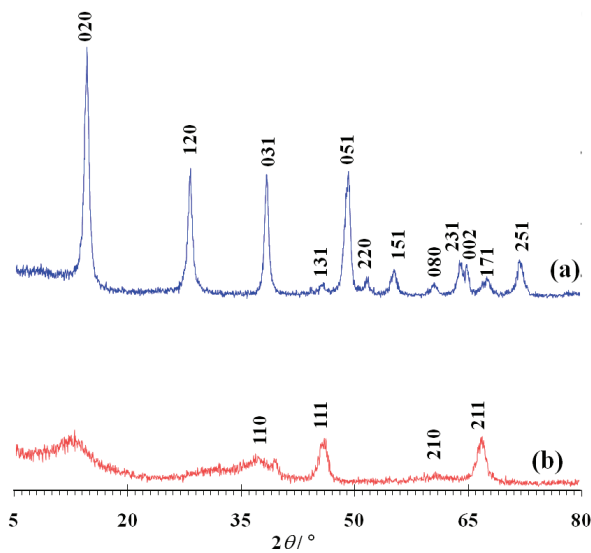


Fig. 2. XRD patterns of a) AlOOH and b) γ -Al₂O₃.

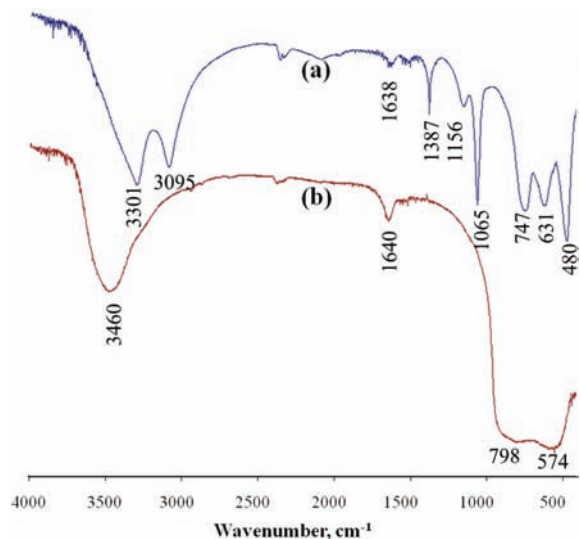


Fig. 3. FTIR spectrum of a) AlOOH and b) γ -Al₂O₃.

values for AlOOH,²⁰ which strongly support the formation of the synthesized sample. In the spectrum of the calcined powder shown in Fig. 3b, the peaks at 606 and 829 cm⁻¹ are assigned to γ -AlO₆ and γ -AlO₄, respectively. Thus, the γ -Al₂O₃ phase contained both octahedral and tetrahedral coordination. The broad band at 3459 cm⁻¹ and the weak band at 1641 cm⁻¹ are due to adsorbed water.²¹

The temperature at which complete decomposition of organics had occurred can be determined by TG/DTA analysis. Thermal analysis data consisting of TG, DTG and DTA curves of the synthesized AlOOH are shown in Fig. 4. The chosen calcination temperature of 500 °C for the conversion of AlOOH into γ -Al₂O₃ was derived from the TG curve. The dehydration of AlOOH appears to occur in four steps. The first step, occurring in the temperature range 25–95 °C and accounting for 1.5 % of the estimated weight loss, may have been due to the loss of physisorbed water. The second step, occurring in the temperature range 95–230 °C with about 1.9 % weight loss, may be due to the loss of chemisorbed water. The third step with a mass loss of about 15.2 % occurred in the temperature range 230–500 °C, which could be ascribed to the conversion of AlOOH into

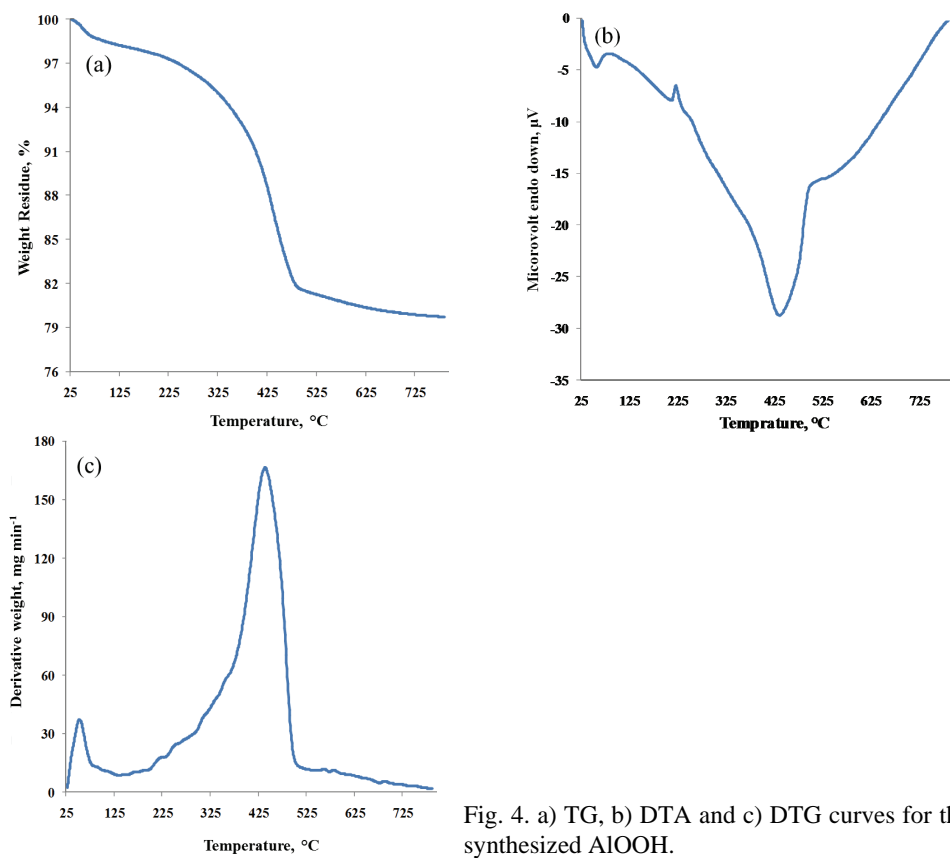


Fig. 4. a) TG, b) DTA and c) DTG curves for the synthesized AlOOH.

γ -Al₂O₃, while the weight loss (1.5 %) at temperatures above 500 °C is associated with the removal of the remaining hydroxyls. The weight losses appeared on the DTA curve as exothermic peaks that refer to several chemical processes, occurring because of thermal degradation of the synthesized AlOOH over the temperature ranges given in Table I.

TABLE I. Thermal data (TG, DTG and DTA) for the synthesized AlOOH; (-):exothermic

Temperature range, °C	DTG max. °C	Mass loss %	DTA °C	Assignment
25–95	54	1.5	58 (-)	Loss of physisorbed water
95–230	215	1.9	222 (-)	Loss of chemisorbed water
230–500	433	15.2	437 (-)	Conversion of alooh into γ -Al ₂ O ₃
Above 500	–	1.5	–	Removal of remaining hydroxyls

The morphology and structure of the as-synthesized products were determined using FESEM and TEM. The FESEM images showing the flower-like nanostructures of AlOOH and γ -Al₂O₃ are presented in Fig. 5. The low-magnification images (Fig. 5a₁) shows that the AlOOH crystallites self-organize into flower-like assemblies. It can be seen from Fig. 5a₁ and b₁ that the morphology of AlOOH was retained after the formation of γ -Al₂O₃ by calcination. According to Fig. 5, several AlOOH and γ -Al₂O₃ nano-flowers appeared to be separate. To examine further the surface morphology of the flowerlike architectures, high-magnification FESEM images of both samples in the top view of the products,

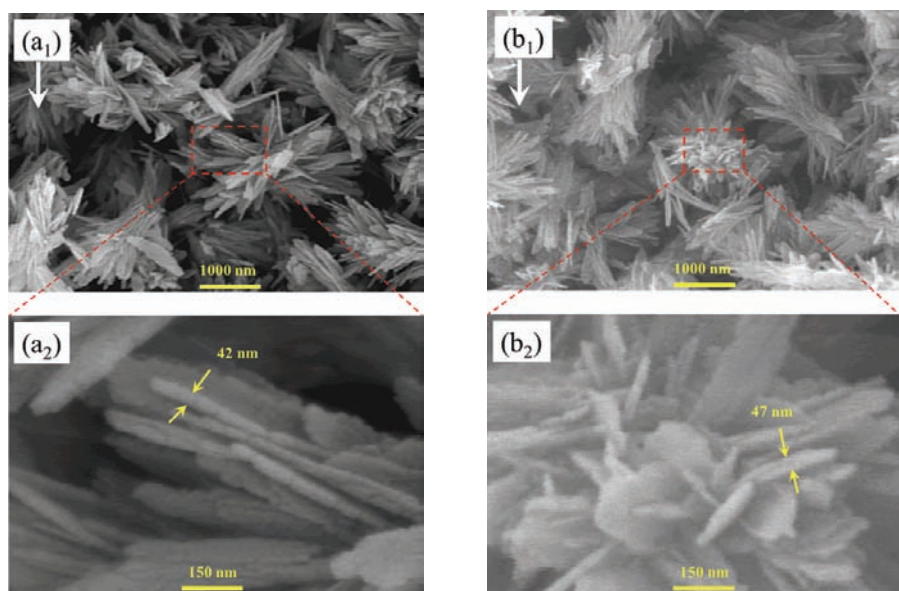


Fig. 5. FESEM images of the flower-like AlOOH (a₁ and a₂) and γ -Al₂O₃ (b₁ and b₂).

which were found to be constructed of several nano-pieces, were recorded, as shown in Figs. 5a₂ and b₂.

The detailed structure of the γ -Al₂O₃ recorded as TEM micrographs is shown in Fig. 6. A low-magnification TEM image of γ -Al₂O₃ is shown in Fig. 6a and b; these might be detached parts from the flower-like nano-architectures or particles that aggregated in one-side flower structures. The nano-pieces were collected together by a center to form a hierarchical flower-like nanostructure. The high-magnification images of the nano-pieces structure of γ -Al₂O₃ could be observed clearly in Fig. 6e and f. In general, the FESEM micrographs are in good agreement with the TEM observations.

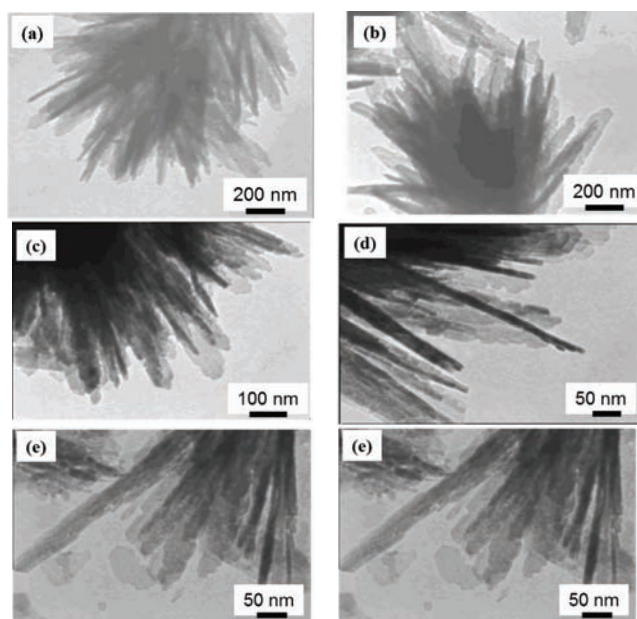


Fig. 6. TEM images of the flower-like γ -Al₂O₃.

The N₂ sorption isotherms of the synthesized AlOOH and γ -Al₂O₃ are illustrated in Fig. 7. The both samples showed a type IV isotherm with H1 + H3 type hysteresis loops, which indicated that these samples had some slit-shaped pores according to the Brunauer, Deming, Deming and Teller (BDDT) classification. This type of isotherm is characteristic for mesoporous samples. As could be seen from the adsorption and desorption curves, it was not a reversible phenomenon that led to the appearance of a hysteresis between the adsorption and desorption curves. The uptake of nitrogen by the both samples proceeded as monolayer–multilayer adsorption followed by capillary condensation, *i.e.*, instantaneous filling of mesopores with adsorbate, in the relative pressure (p/p_0) range of 0.90–0.99. However, the γ -Al₂O₃ showed a steep increase of the adsorption in the p/p_0

range 0.8–0.95, while the AlOOH displayed a gradual increase in the p/p_0 range 0.7–0.96, indicating that the $\gamma\text{-Al}_2\text{O}_3$ had larger mesopores than the AlOOH, as shown in the Table II. Thus, the formation of $\gamma\text{-Al}_2\text{O}_3$ resulted in a higher surface area and pore volume, but with a lower mean pore diameter. The inset of Fig. 7 presents the pore size distribution of the samples derived from the desorption branch of the N_2 adsorption/desorption isotherms. The pore size distribution curves for both samples showed one narrow and two wide distributions that were centered around 1.35, 12 and 26 nm, respectively. It can be seen that the intensity of peaks for the AlOOH were higher than those for $\gamma\text{-Al}_2\text{O}_3$.

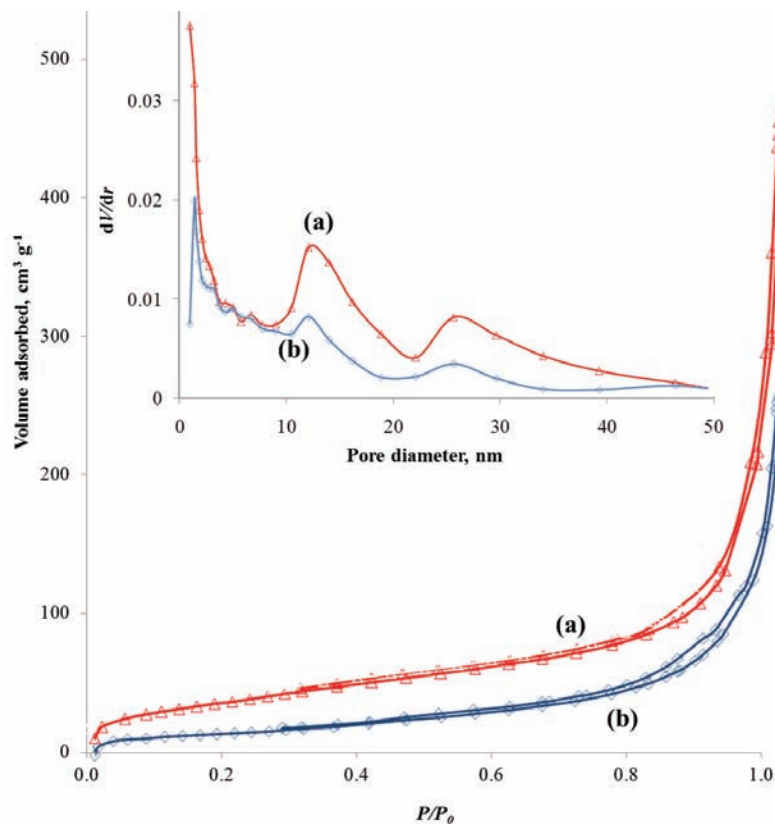


Fig. 7. Nitrogen adsorption/desorption isotherms and pore-size distribution (inset) of
a) AlOOH and b) $\gamma\text{-Al}_2\text{O}_3$.

TABLE II. The textural properties of the samples

Sample	Surface area, m² g⁻¹	Pore volume, cm³ g⁻¹	mean pore diameter, nm
AlOOH	69	0.36	21
$\gamma\text{-Al}_2\text{O}_3$	148	0.59	16

Further details concerning the structural characteristic of the synthesized AlOOH and γ -Al₂O₃, *i.e.*, the micropore volume in the presence of mesopores, are given in the *t*-plots presented in Fig. 8, from which, the contributions of the two different types of pores, namely micropores and mesopores, are obvious.

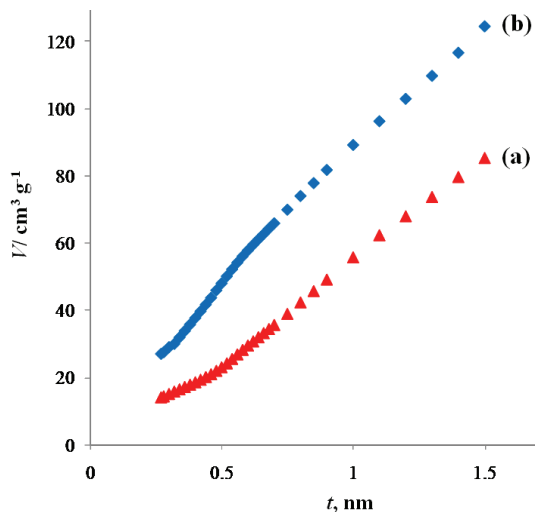


Fig. 8. *t*-Plot curves for a) AlOOH and b) γ -Al₂O₃.

In general, porous materials can contain more than one class of pores, *e.g.*, micropores and mesopores. It is possible to differentiate the contribution of micropores and mesopores to the surface area using the method developed by de Boer *et al.*²² The nitrogen adsorption data can be plotted as a *t*-curve, in which the adsorbed nitrogen volume is presented as a function of the statistical thickness, *t*, of an adsorbed layer on a nonporous surface. If the adsorbent contains mesopores, capillary condensation occurs in each pore when the relative pressure reaches a value that is related to the pore radius by the Kelvin Equation, the *t*-plot therefore shows an upward deviation commencing at the relative pressure at which the finest pores are just being filled and the extrapolated plot passes through the origin. On the other hand, if microporosity exists, the uptake is enhanced in the low-pressure region and a positive intercept is observed that can be assigned to the micropore volume.

CONCLUSIONS

In summary, a micro/mesoporous flower-like γ -Al₂O₃ assembly from nano-pieces with a surface area of 148 m² g⁻¹, a mean pore diameter of 16 nm and a pore volume of 0.59 cm³ g⁻¹ was successfully synthesized by the decomposition of a synthesized AlOOH. The FESEM and TEM micrographs shows that the γ -Al₂O₃ was flower-like and a high-magnification micrograph of the sample showed that the products were constructed of several nano-pieces. The flower-

-like γ -Al₂O₃ is expected to have potential applications in catalysis, adsorption and other fields, due to its large surface area.

Acknowledgement. The support of the Islamic Azad University, Kermanshah Branch is greatly acknowledged.

И З В О Д

СИНТЕЗА МИКРО-МЕЗОПОРОЗНОГ ЦВЕТАСТОГ γ -Al₂O₃ НАНОАРХИТЕКТУРЕ

MOZAFFAR ABDOLLAHIFAR¹, MOHAMMAD REZA ZAMANI², EHSAN BAYGI² и HOSAIN NEKOUEI³

¹Department of Chemical Engineering, Science and Research Branch, Islamic Azad University, Kermanshah 67131, Iran, ²Young Researchers Club, Shahreza Branch, Islamic Azad University, Shahreza 86131, Iran и

³Department of Industry, University of Applied Science and Technology, Larestan Branch, Larestan 74311, Iran

Микро-мезопорозни наноструктурни γ -Al₂O₃ цветног облика добијен је методом термичке разградње синтетизованог AlOOH (бемит) као прекурсора. После калцинисања на температури 500 °C током 5 h, добијен је γ -Al₂O₃ облика цвета са структуром сличном AlOOH прекурсору. XRD, FTIR, TG, FESM и TEM технике коришћене су за карактерисање морфологије и структуре добијених узорака. Специфична површина (BET), запремина и расподела пора одредјиване су адсорпцијом/десорпцијом N₂. Цветаст γ -Al₂O₃ имао је велику специфичну површину- 148 m² g⁻¹, са укупном запремином пора 0,59 cm³ g⁻¹.

(Примљено 23. септембра 2013, ревидирано 20. јануара, прихваћено 21. јануара 2014)

REFERENCES

1. S. A. Hassanzadeh Tabrizi, E. Taheri Nassaj, *Ceram. Int.* **37** (2011) 1251
2. Y. J. O. Asencios, M. R. Sun Kou, *Appl. Surf. Sci.* **258** (2012) 10002
3. A. M. D. A. Cruz, J. Guillaume Eon, *Appl. Catal., A* **167** (1998) 203
4. M. Fattahi, F. Khorasheh, S. Sahebdelfar, F. T. Zangeneh, K. Ganji, M. Saeedizad, *Sci. Iran.* **18** (2011) 1377
5. D. Larson, J. Coppola, D. Hasselman, R. Bradt, *J. Am. Ceram. Soc.* **57** (1974) 417
6. H. Bartzsch, D. Glob, B. Bocher, P. Frach, K. Goedicke, *Surf. Coat. Technol.* **174** (2003) 774
7. J. H. Choi, Y. M. Kim, Y. W. Park, T. H. Park, J. W. Jeong, H. J. Choi, E. H. Song, J. W. Lee, C. H. Kim, B. K. Ju, *Nanotechnology* **21** (2010) 475203
8. M. Moosemiller, C. Hill Jr., M. A. Anderson, *Sep. Sci. Technol.* **24** (1989) 641
9. P. P. Morajkar, J. B. Fernandes, *Catal. Commun.* **11** (2010) 414
10. J. Zhang, S. Wei, J. Lin, J. Luo, S. Liu, H. Song, E. Elawad, X. Ding, J. Gao, S. Qi, *J. Phys. Chem., B* **110** (2006) 21680
11. H. Liang, L. Liu, Z. Yang, Y. Yang, *Cryst. Res. Technol.* **45** (2010) 195
12. K. Mahmoodi, B. Alinejad, *Powder Technol.* **199** (2010) 289
13. L. Qu, C. He, Y. Yang, Y. He, Z. Liu, *Mater. Lett.* **59** (2005) 4034
14. X. Zhang, M. Honkanen, E. Levänen, T. Mäntylä, *J. Cryst. Growth* **310** (2008) 3674
15. D. H. M. Buchold, C. Feldmann, *Nano Lett.* **7** (2007) 3489
16. P. Gao, Y. Xie, Y. Chen, L. Ye, Q. Guo, *J. Cryst. Growth* **285** (2005) 555
17. Y. Feng, W. Lu, L. Zhang, X. Bao, B. Yue, Y. Lv, X. Shang, *Cryst. Growth Des.* **8** (2008) 1426
18. W. Cai, J. Yu, S. Mann, *Microporous Mesoporous Mater.* **122** (2009) 42

19. E. P. Barrett, L. G. Joyner, P. P. Halenda, *J. Am. Chem. Soc.* **61** (1951) 373
20. W. Cai, J. Yu, S. Gu, M. Jaroniec, *Cryst. Growth Des.* **10** (2010) 3977
21. H. S. Potdar, K. W. Jun, J. W. Bae, S. M. Kim, Y. J. Lee, *Appl. Catal., A* **321** (2007) 109
22. J. H. de Boer, B. C. Lippens, B. G. Linsen, J. C. P. Broekhoff, A. van den Heuvel, T. J. Osinga, *J. Colloid Interface Sci.* **21** (1966) 405.



Assessment of contamination and origin of metals in mining affected river sediments: a case study of the Aries River catchment, Romania

ERIKA LEVEI¹, MICHAELA PONTA², MARIN SENILA¹, MIRELA MICLEAN¹
and TIBERIU FRENTIU^{2*}

¹INCDO-INOE 2000, Research Institute for Analytical Instrumentation, 67 Donath, 400293, Cluj-Napoca, Romania and ²Faculty of Chemistry and Chemical Engineering, Babes-Bolyai University, 11 Arany Janos, 400028, Cluj-Napoca, Romania

(Received 1 May, revised 5 August, accepted 24 August 2013)

Abstract: The study presents the current status of contamination with metals (Cu, Cr, Cd, Pb, Ni, Zn and As) and their anthropogenic or natural origin in the sediments of the Aries River Basin, Romania, affected by mining activities. The results indicated an enrichment of metals in the sediments. Different contamination levels of the Aries River and its tributaries were identified. According to sediment quality guidelines and contamination indices, the sediments from the Aries River were found to be highly contaminated with Cd, Cu and As, considerably with Zn and moderately with Pb and Ni. The right-bank tributaries were found to be more contaminated than the left-bank effluents, where only contamination with As of geogenic origin was identified. Principal Component Analysis enabled the identification of five latent factors (86 % total variability), reflecting the anthropogenic and natural origins of the metals. Arsenic, Cd and partially Pb were found to have a common anthropogenic origin, different from that of Cu. The statistical approach indicated also the geogenic origin of Pb due to its association with Ca, K, Na and Sr. Chromium and Ni were attributed to natural sources through their association with Mn, Fe, Al and Mg.

Keywords: river sediment; sediment quality guideline; contamination index; multivariate statistics.

INTRODUCTION

Although an important branch of the economy, mining has a negative reputation for polluting surface water and sediments with solid wastes and acidic or circumneutral mine drainage that may contain significant metal levels.^{1–3} Considering their toxicity and high bioaccumulation capacity, metals are among the

*Corresponding author. E-mail: ftibi@chem.ubbcluj.ro
doi: 10.2298/JSC130501086L

most common pollutants of soil, water and biota. Sediments are preferred in regular environment monitoring as they represent a major sink for contaminants, have higher metal concentrations than water and lower temporal variability.^{4–9}

Romania has a long mining history of precious (Au and Ag) and base metals (Cd, Cu, Pb and Zn), but the inappropriate management of wastes has generated long-term pollution and even accidents with transboundary effects.^{10–15} These events were the starting point for studies on water and sediment quality in mining affected catchments.^{16–18} There are several studies regarding the impact of the opencast mining of porphyry Cu deposits and underground mining of auriferous pyrites on the Aries River Basin, but the origin and distribution of the contaminants in the area are still under debate.^{19–25} The aim of this study was to assess the contamination level in relation to Romanian Sediment Quality Guidelines (RSQGs),²⁶ Consensus-Based Sediment Quality Guidelines (CBSQGs) of freshwater ecosystems²⁷ and several contamination indices, as well as to identify the origin of several metals (Cu, Cr, Cd, Pb, Ni, Zn and As) in the sediments of the Aries catchment, Romania.

MATERIALS AND METHODS

Site description

The Aries River (164 km in length) springs from the Bihorului Mountains and collects its tributaries on an area of around 3000 km². The River crosses two towns (Campeni and Baia de Aries) and several villages with a total population of 40000 inhabitants. The riverbed is surrounded by forested hills at an altitude of 1000–1200 m. The Aries Basin is of high economic importance because of the large reserves of gold and base metals and also has outstanding tourism potential through its natural reservations and caves.^{20,28} The mining activities in the area encompassed the extraction of auriferous pyrite (Baia de Aries), Cu and Au ores (Rosia Montana), porphyritic Cu (Rosia Poieni) and Fe and Mg ores (Masca Baisoara). The ores were processed by flotation, while Au was extracted by the cyanide leaching procedure in Baia de Aries. Tailings and wastewaters were stored in several tailing ponds in the floodplain of the Aries River and its right-bank tributaries. Some of the mining and ore processing facilities were demolished, while others were conserved or have been abandoned. Currently, the opencast Cu mine at Rosia Poieni is in operation and the exploitation of gold and silver ores at Rosia Montana is planned to start. Although remediation measures have been undertaken, the centuries of mining activities and the poor management of the resulting wastes have led to deterioration of the ecosystem.^{21,23}

Sampling

Fifteen spot samples from the sediment top layer (about 0–10 cm) were collected along the Aries riverbed over a distance of 92 km (Fig. 1). Sediment samples were also collected from tributaries in order to evaluate their possible contribution to the pollution of the main stream. Thus, samples were collected from 8 right-bank tributaries (Abrud, Stefanca, Muscani, Sesei, Harmaneasa, Cioara, Morilor and Rimetea), exposed in different extents to pollution by mining activities, and from 7 left-bank tributaries (Bistra, Valea Mare, Lupsa, Posaga, Ocolis, Ocolisel and Iara), situated outside the mining area. The sediment samples were collected

using plastic shovels and transported to laboratory in polyethylene bags. The bulk sediment samples were oven dried at 105 ± 5 °C, homogenized and sieved to pass through a 63- μm sieve.

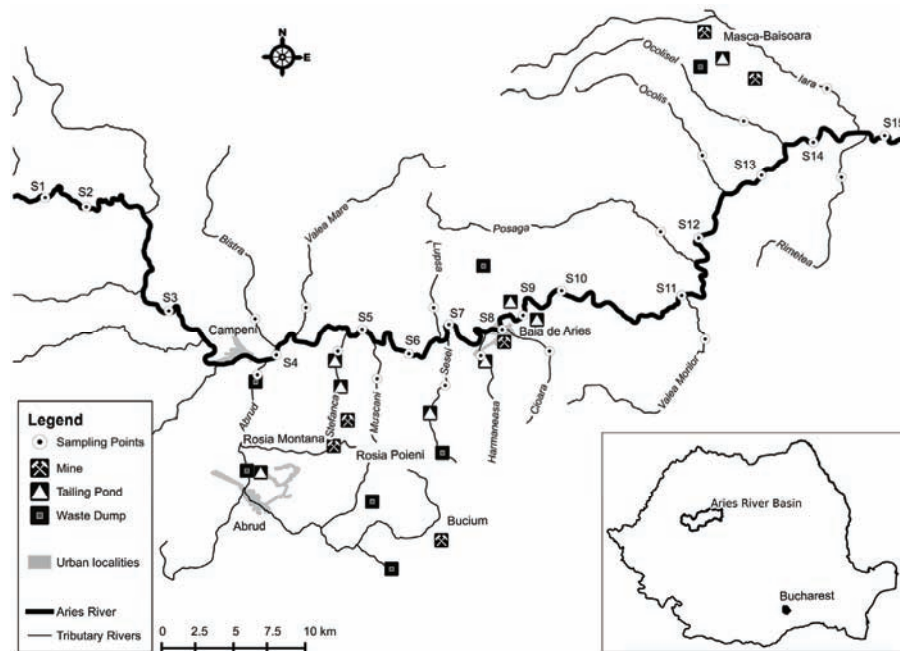


Fig. 1. Map of the sampling points and mining facilities in the Aries catchment.

Sample preparation and instrumentation

The mineral composition of the river sediments was characterized by recording X-ray powder diffraction patterns employing a high-resolution Bruker D8 Advance diffractometer (Bruker-AXS, Karlsruhe, Germany) using the CuK α line. The metal contents in the sediments were determined by inductively coupled plasma optical emission spectrometry (ICP-OES) using OPTIMA 5300DV multichannel spectrometer (Perkin-Elmer, Norwalk, CT, USA), after *aqua regia* digestion according to ISO 11466:1995.²⁹ Thus, 1 g of sediment sample was subjected to digestion with 21 mL of 37 % HCl and 7 mL of 65 % HNO₃. The mixture was allowed to react overnight at room temperature, and then boiled under reflux for 2 h. After cooling, the mixture was filtered and diluted to 100 mL with ultrapure water.

Accuracy of metals determination

The accuracy of metals determination by ICP-OES was tested by analyzing two certified reference materials (CRMs), namely BCR 701 Freshwater sediment and NCS DC 78301 River sediment purchased from LGC Promochem (Wessel, Germany). In accordance with Table I, the accuracy and precision for the determination of metals in the CRMs by ICP-OES were in the range of 92–105 % and 2.0–5.5 %, respectively.

Sediment quality guidelines and contamination indices

In order to screen sediments contamination, the metal contents were compared with the threshold values in RSQGs²⁶ complying with EU legislation. For the assessment of ecotoxic-

ological risk and to predict the potential effects of metals on sediment dwelling organisms, the metal concentrations were compared with the CBSQGs for freshwater ecosystems.²⁷ For assessment of the extent of contamination in the catchment, several indices were calculated for the metals: the enrichment factor (*EF*, Eq. (1)) according to Sinex and Helz,³⁰ the geoaccumulation index (*I_{geo}*, Eq. (2)) introduced by Muller,³¹ and the contamination factor (*CF*, Eq. (3)) and contamination degree (*CD*) according to Hakanson.³² The background level used to calculate the indices was the elemental composition of the continental crust according to Taylor and McLeenan.³³ Pb 20, Cu 25, Zn 71, As 1.5, Cd 0.098, Ni 20, Cr 35 and Fe 35000 mg kg⁻¹. Considering that Fe in sediments results mainly from natural weathering processes, it was used for the geochemical normalization of the metals:³⁴

$$EF = \frac{([Me]/[Fe])_{\text{sample}}}{([Me]/[Fe])_{\text{background}}} \quad (1)$$

where [Me]/[Fe] refers to the metal-to-Fe ratio in the sediment sample or background.

TABLE I. Comparison of the found content of metals (mg kg⁻¹, *n* = 3 parallel samples) with the indicated/certified values in the certified reference materials

Element	BCR 701 Freshwater sediment		NCS DC 78301 River sediment		Average recovery %	Pooled SD %
	Certified ^a	Found ^a	Certified ^a	Found ^a		
As	— ^b	56±6	56±5	59±5	105	4.0
Cd	11.7±1.0	10.3±1.5	2.45±0.2	2.35±0.3	92	5.5
Cr	272±20	280±12	90±4	88±5	100	2.0
Cu	275±13	276±15	53±3	52±3	99	2.3
Mn	— ^b	675±45	975±17	920±40	94	2.3
Ni	103±4	100±8	32 ^c	30±3	95	3.6
Pb	143±6	140±6	79±6	83±8	102	3.0
Zn	454±19	458±14	251 ^c	245±25	99	3.0

^aMean±*U*, where *U* expanded uncertainty for 95 % confidence level; ^bnot certified; ^cindicative value

Values of *EF* < 1 indicate no enrichment, while values >1 indicate different degrees of enrichment.

Geoaccumulation index resulted from comparing the current concentration of the elements in the sediments with their background values:

$$I_{\text{geo}} = \log_2 \left(\frac{c_n}{1.5B_n} \right) \quad (2)$$

where *c_n* is the concentration of metal examined in sediments and *B_n* is the geochemical background concentration of metal (n). Based on the *I_{geo}* values, seven pollution classes were defined, ranging from unpolluted to extremely polluted.

Contamination factor of a metal was computed by dividing its concentration in sediment by its background concentration. According to *CF* values, sediments contamination was classified as low, moderate, considerable or very high:

$$CF = \left(\frac{c_n}{B_n} \right) \quad (3)$$

Summation of CF values for seven metals (As, Cd, Cr, Cu, Ni, Pb and Zn) gave the contamination degree (CD) describing, according to Hakanson,³² the quality of the sediments. Based on the CD values, the sediments were classified into four classes corresponding to: low ($CD \leq 8$), moderate ($8 < CD \leq 16$), considerable ($16 < CD < 32$) and very high contamination ($CD > 32$).

Statistical analyses

The normality of all data was assessed by the Shapiro–Wilk test, while the Mann–Whitney U test was used to assess significant differences between the metal contents in the main stream and its tributaries.

Multivariate exploratory techniques, such as principal component analysis (PCA), hierarchical cluster analysis (HCA) and linear discriminant analysis (LDA) are widely applied to evaluate water and sediment quality through data reduction and classification.^{35–37} These techniques can be used to obtain relationships between parameters and sampling sites, or to identify the important factors and sources influencing sediment quality.³⁸ PCA was used to outline the anthropogenic or natural origin of contaminants and to assess their specific input from tributaries to the main stream. A previous study revealed that tailings deposited in the Aries River Basin pose high contamination risk for the sediments, especially by As, Cd, Cu and Pb.³⁹

HCA and LDA were used to group the sediments (sites) in relation to their degree of metal contamination. The statistical approach is useful in case of complex systems such as sediment as it offers the possibility to establish correlations or differences between multiple parameters or sites considered in a study.^{40,41} Given the complexity of real field circumstances, the study took into consideration seven metals likely to be of anthropogenic origin and metals normally present in sediments from natural sources (Na, K, Ca, Mg, Ba, Sr, Al, Fe and Mn). For the multivariate statistical analysis, all parameters were z -scale standardized (mean = 0; variance = 1) in order to avoid misclassifications arising from the different orders of magnitude of the studied parameters.⁴² In order to define the geogenic and anthropogenic origin of the contaminants, PCA was applied on the standardized data, as this method is considered very efficient for this purpose. According to the Kaiser criterion, only the PCs with eigenvalue higher than 1.0 were retained and subjected to varimax rotation. Factor loadings used to determine the relative importance of a variable as compared to other variables in a PC were classified as “strong”, “moderate” and “weak” corresponding to absolute loading value of >0.75 , 0.50–0.75, and 0.30–0.50, respectively.⁴³ Positive values on each component are related to important inputs, whereas negative values correspond to low input. Hierarchical Cluster Analysis (HCA) and LDA allow the grouping of sampling sites based on their similarities. HCA was realized by means of the Ward linkage method using squared Euclidian distance as a measure of similarity. LDA in the standard mode was applied to construct the discriminant function for an adequate classification of sediments/sites sharing similar pollution levels.⁴¹ The statistical analysis was performed using Microsoft Office Excel 2007 with XLSTAT plug-in (Addinsoft).

RESULTS AND DISCUSSION

Mineralogical composition of the sediments

The X-ray diffraction analysis emphasized the presence of silicates (quartz, SiO_2 and albite, $\text{NaAlSi}_3\text{O}_8$) as the major class of minerals (20–50 %) in all sediments. However, differences in the mineralogical composition of sediments

were observed. Muscovite ($KAl_2(Si_3Al)O_{10}(OH,F)_2$) was found as the major constituent (20–50 %) in all tributaries and as a minor constituent (5–20 %) in the Aries River sediments. Orthoclase ($AlKSi_3O_8$) and illite ($KAl_2(Si_3Al)O_{10}(OH)_2$) were identified as minor minerals (5–20 %) in the sediments of the tributaries, while in those from the Aries River, they were present only in traces (<5 %). In contrast, feldspar ($Al_2CaO_8Si_2$) and clinochlore ($(Mg,Fe,Al)_6(Si,Al)_4O_{10}(OH)_8$) were identified as minor minerals (5–20 %) in the Aries River sediments and in traces (<5 %) in the tributaries. Traces of cuprite (Cu_2O) and calcopirite ($CuFeS_2$) were found in the sediments of the Muscani and Sesei Tributaries, respectively. Effenbergerite ($BaCu(Si_4O_{10})$) was identified as a minor mineral (5–20 %) in the Muscani, Sesei and Cioara Tributaries. Anglesite ($PbSO_4$) was identified in traces (<5 %) in the sediments from sampling points S6–S10, situated in the area with maximum pollution. Minerals from the carbonate group, such as dolomite ($CaMg(CO_3)_2$) were identified as a minor component (5–20 %) in the sediments of the Aries River upstream from the pollution sources (S1–S3), while calcite ($CaCO_3$) was identified in some of sediments of the right side tributaries.

Metal contents and sediment quality

The metal concentrations in the sediments from the Aries River and its tributaries are presented in Tables II and III. Although strictly speaking, As is a metalloid, the term metal will be used in this paper to include all the elements under discussion. Examination of data revealed high variability of the Cu, Zn, Cd and Fe content in the sediments collected from the main stream. Differences among metal concentrations in sediments from the left-side tributaries were small, while sediments from the right-bank exhibited a much larger variability for As, Cd, Cu, Pb and Zn. The Shapiro–Wilk test showed that the metal contents in the sediments did not follow a normal distribution ($p < 0.05$). Thus, to evaluate the similarity or difference in the contents of each metal between the main stream and its right/left side tributaries, the non-parametric Mann–Whitney U -test was applied. According to this test, the main stream was differentiated ($p < 0.05$) from the left side tributaries, situated outside the mining area, with respect to the Pb, Cu, Zn, As and Cd contents, and from the right side tributaries that drain the mining area with respect to the Pb, Zn, Cd, Ni and Cr contents.

The guideline values for metals used for the characterization of sediment quality are presented in Table IV. According to Romanian legislation, sediments are considered unpolluted if the metal content is lower than the corresponding threshold value. According to the CBSQGs, sediments are predicted to be non-toxic if the metal concentration is lower than the corresponding threshold effect concentration (TEC), while those with a metal content exceeding the probable effect concentration values (PEC) are predicted to be toxic. Sediments with a metal concentration between the TEC and PEC values are predicted to be neither

TABLE II. Concentration (mg kg^{-1}) of metals in the sediments of the Aries River

Site	Pb	Cu	Zn	As	Cd	Ni	Cr	Mn	Fe	Al	Ca	K	Mg	Na	Sr	Ba
S1	21.2	8.69	84.7	8.23	0.256	12.3	16.2	542	14256	9945	9170	1536	6706	214	11.9	68.4
S2	17.6	7.80	77.2	9.12	0.100	13.3	14.0	305	13197	9544	9034	1484	7067	151	10.0	54.1
S3	26.6	21.2	136	14.2	0.343	16.4	20.1	589	17431	16058	7988	2604	9869	208	14.0	65.1
S4	23.2	37.2	250	13.4	0.845	53.4	33.1	1110	15173	14364	5072	1674	8146	153	14.3	86.7
S5	27.6	40.6	229	16.4	0.777	32.0	24.5	761	14247	17017	3871	2232	6380	179	16.8	86.7
S6	25.7	54.9	275	12.5	1.15	20.4	21.1	1164	13457	15396	5181	1871	8705	153	17.0	69.6
S7	25.4	180	153	13.2	0.376	18.6	15.3	486	10895	13531	2727	1755	5592	155	12.5	65.9
S8	37.3	120	179	14.0	0.818	19.3	17.7	697	11279	13417	4419	1904	7085	156	13.9	57.8
S9	33.6	195	233	16.4	0.981	19.2	14.7	789	10411	12527	3454	1550	6177	164	10.5	39.6
S10	32.1	534	594	18.2	1.57	24.3	20.6	1858	33200	22341	4516	2430	8090	187	14.7	62.4
S11	17.8	320	240	12.4	0.900	26.8	18.6	733	10593	13468	4888	2547	6588	228	22.4	71.6
S12	21.0	187	228	14.6	0.968	27.1	19.8	705	11159	15935	3853	2587	6977	189	14.8	62.3
S13	15.3	188	116	16.4	0.510	29.3	23.8	937	37900	21000	9000	3400	9150	118	15.0	54.0
S14	22.6	163	228	16.4	0.939	26.9	20.6	795	10950	15870	5536	2590	7283	166	17.6	61.8
S15	41.5	347	338	23.0	1.87	42.1	32.0	1159	40300	25204	7362	3049	8556	199	23.9	113
Min.	15.3	7.80	77.2	8.23	0.100	12.3	14.0	305	10411	9544	2127	1484	5592	118	10.0	39.6
Max.	41.5	534	594	23.0	1.87	53.4	33.1	1858	40300	25204	9170	3400	9869	228	23.9	113
Average	25.9	160	224	14.6	0.827	25.4	20.8	842	17630	15708	5738	2214	7491	175	15.3	68.0
SD	7.5	149	126	3.59	0.479	10.9	5.67	373	10375	4329	2189	588	1209	29.5	3.88	17.3

TABLE III. Concentration (mg kg^{-1}) of metals in the sediments of the tributaries of the Aries River

Site	Pb	Cu	Zn	As	Cd	Ni	Cr	Mn	Fe	Al	Ca	K	Mg	Na	Sr	Ba
Right-bank tributaries																
Abrud	2.84	10.7	734	3.05	0.305	3.30	2.07	1168	39102	20812	4950	3045	6015	285	2.90	7.50
Stefanca	13.4	68.0	69.4	11.7	0.133	18.7	10.9	416	9459	9899	4641	1711	4806	243	22.3	57.8
Muscani	95.1	581	186	12.8	0.832	12.1	10.2	513	12495	15215	2807	2646	5342	390	53.5	192
Sesei	19.8	167	59.3	10.4	0.219	5.10	6.30	109	16614	10199	2697	1614	4473	141	6.50	28.9
Harmaneasa	189	33.0	139	23.2	1.54	19.7	16.5	1523	9649	12575	52495	3510	5402	264	36.0	72.3
Cioara	37.9	19.7	108	14.5	0.268	20.2	13.2	530	9875	10489	16677	3590	5563	188	23.3	67.4
Morilor	16.1	21.0	64.0	6.08	0.205	20.8	18.7	596	9596	15133	17878	2804	5374	267	12.9	67.7
Rimetea	57.1	10.8	65.2	4.90	0.154	14.7	14.2	1480	34365	17945	54530	3533	5655	480	78.6	103
Min.	2.84	10.7	59.3	3.05	0.133	3.30	2.07	109	9459	9899	2697	1614	4473	141	2.89	7.50
Max.	189	581	734	23.2	1.54	20.8	18.7	1523	39102	20812	54530	3590	6015	480	78.6	192
Average	53.9	114	178	10.8	0.457	14.3	11.5	792	17644	14033	19584	2807	5329	282	29.5	74.6
SD	62.2	196	229	6.43	0.491	6.93	5.41	527	12092	3970	21777	788	485	108	25.7	55.5
Left-bank tributaries																
Bistra	15.4	17.0	80.6	9.26	0.095	21.0	22.7	468	11939	12842	2489	1114	7375	151	12.5	50.8
Valea Mare	30.5	21.4	62.4	6.68	0.210	8.04	14.2	282	10136	8574	3664	1212	3435	179	17.3	23.1
Lupsa	13.7	19.4	89.0	11.1	0.141	19.9	22.3	369	10621	13892	6887	2367	7123	196	22.0	60.4
Posaga	11.6	13.3	56.9	6.80	0.180	16.1	21.6	357	10461	12448	5737	1708	8180	190	12.5	45.3
Ocolis	13.4	14.2	80.4	9.00	0.120	19.5	14.6	448	9881	15711	7344	3300	8378	207	36.3	79.9
Ocolisel	16.6	17.5	67.3	12.3	0.201	16.3	18.7	324	9707	13408	7754	2567	5965	139	18.2	84.8
Iara	21.4	12.5	68.4	15.2	0.184	18.4	16.2	576	8795	13811	7977	3245	4549	146	21.2	66.1
Min.	11.6	12.5	56.9	6.68	0.095	8.04	14.2	282	8795	8574	2489	1114	3435	139	12.5	23.1
Max.	30.5	21.4	89.0	15.2	0.210	21.0	22.7	576	11939	15711	7977	3300	8378	207	36.3	84.8
Average	17.5	16.5	72.1	10.0	0.162	17.0	18.6	403	10220	12955	5979	2216	6429	173	20.0	58.6
SD	6.53	3.30	11.5	3.06	0.043	4.36	3.67	100	965	2194	2138	900	1869	27.0	8.11	21.2

TABLE IV. Guideline values for metals for characterization of sediment quality

Element	RSQGs ^a		CBSQGs ^b	
	Threshold value, mg kg ⁻¹	TEC ^c , mg kg ⁻¹	PEC ^d , mg kg ⁻¹	
Pb	85	35.8	128	
Cu	40	31.6	149	
Zn	150	121	459	
As	29	9.79	33.0	
Cd	0.8	0.99	4.98	
Ni	35	22.7	48.6	
Cr	100	43.4	111	

^aRomanian Sediment Quality Guidelines²⁶; ^bconsensus-based Sediment Quality Guidelines²⁷; ^cthreshold effect concentration; ^dprobable effect concentration

toxic nor non-toxic. The status of metal contents in the sediments according to the RSQGs and CBSQGs associated to relative frequency of occurrence (%) are exhibited in Fig. 2. Sediments in the main stream were found to be polluted with Cu, Cd and Zn. Sediments from the left-side tributaries exhibited values below

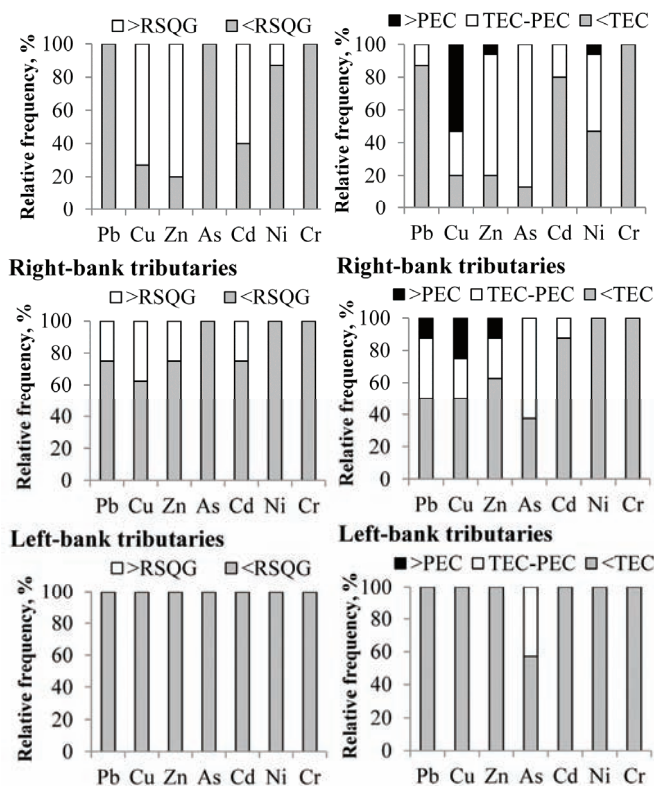


Fig. 2. Status of metal contents in the sediments of the Aries River and its tributaries in relation to the RSQGs and CBSQGs values and the relative frequency of occurrence.

the RSQGs for Pb, Cu, Zn, As, Ni, Cd, and Cr, while the *TEC* value for As was exceeded in 3 tributaries. Sediments from the right-bank tributaries revealed differences in terms of pollution and toxicity in relation to a particular contaminant. Differences in sediments ranking according to the two guidelines are because the RSQGs set the threshold values for the polluted or unpolluted status assessment, while the CBSQGs provide a basis for toxicity or non-toxicity prediction. However, good agreement between the rankings of sediments by the two guidelines was observed for Cu, Zn, Pb and Cr, while differences appeared in the case of As, Cd and Ni.

The classification of the sediments from the Aries River and its tributaries of different pollution levels according to contamination indices are presented in Figs. 3–6. Figure 3 shows the enrichment of the metals in the sediments of the Aries River and the increase in pollution from upstream to downstream, which supports the role of the river in collecting contaminants from its tributaries. Values of the $EF < 1.5$ indicate a lithological source of the element, while values

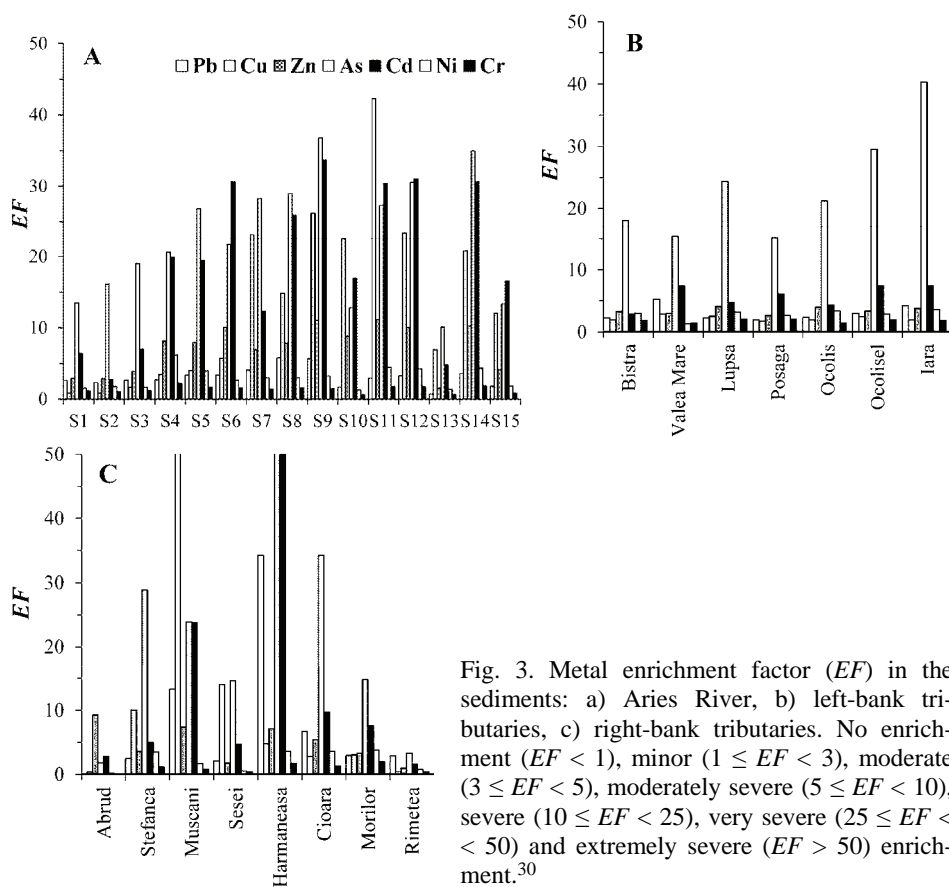


Fig. 3. Metal enrichment factor (EF) in the sediments: a) Aries River, b) left-bank tributaries, c) right-bank tributaries. No enrichment ($EF < 1$), minor ($1 \leq EF < 3$), moderate ($3 \leq EF < 5$), moderately severe ($5 \leq EF < 10$), severe ($10 \leq EF < 25$), very severe ($25 \leq EF < 50$) and extremely severe ($EF > 50$) enrichment.³⁰

of the $EF > 10$ suggests an anthropogenic origin.⁴⁴ Values of the $EF > 10$ were found for As, Cd and Cu in sediments from the Aries River, for As, Cd, Cu and Pb in the right bank tributaries and As in the left bank tributaries, suggesting anthropogenic origins of these elements.

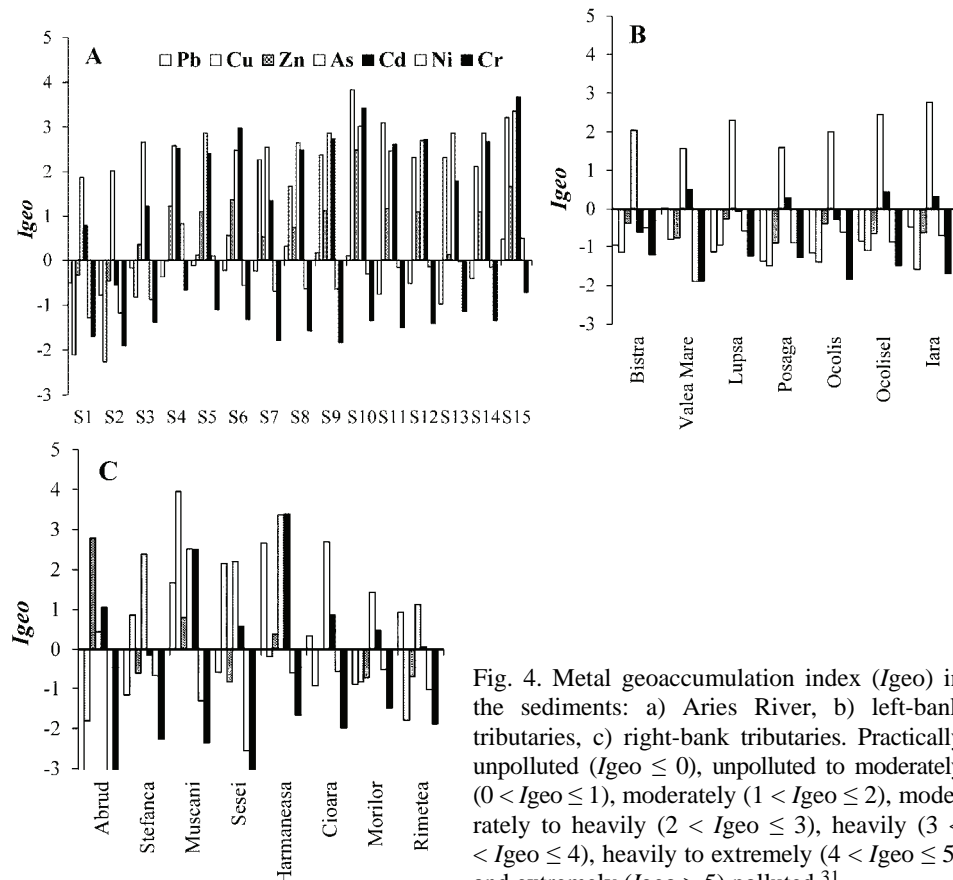


Fig. 4. Metal geoaccumulation index (I_{geo}) in the sediments: a) Aries River, b) left-bank tributaries, c) right-bank tributaries. Practically unpolluted ($I_{geo} \leq 0$), unpolluted to moderately ($0 < I_{geo} \leq 1$), moderately ($1 < I_{geo} \leq 2$), moderately to heavily ($2 < I_{geo} \leq 3$), heavily ($3 < I_{geo} \leq 4$), heavily to extremely ($4 < I_{geo} \leq 5$) and extremely ($I_{geo} > 5$) polluted.³¹

Figure 5 shows that the enrichment of metals in the sediments followed the order: Cr < Ni < Pb < Zn < Cu < Cd < As, which corresponded to different levels of contamination: very high for Cu, Cd, As ($10 < CF < 11$), considerable with Zn ($CF = 3.8$), moderate with Pb and Ni ($CF = 1.4$) and no contamination with Cr. Results indicated also the existence of local peaks, of which the most representative was S10 site with a CF values of 21 (Cu), 16 (Cd), 12 (As) and 8.4 (Zn) and an overall CD of 61. The sediments of the right-bank tributaries were found to exhibit moderate to very high degrees of contamination. The data showed different index pattern of right-bank tributaries with respect to As, Cu, Cd and Pb (Harmaneasa, Muscani, Sesei, Cioara and Stefanca). The Abrud River different-

iated itself from the other tributaries by the high Zn content in the sediment. After the confluence of the right-bank tributaries with the Aries River, an increase of the metal loading in the sediment was observed (sites S4–S7), corresponding to a considerable contamination with Cu and Zn and very high contamination with Cd and As. Sediments from the left-bank tributaries showed moderate degrees of contamination and lower metal loadings. Their classification as moderately to heavily polluted according to I_{geo} and very high contaminated according to CF was mainly due to As. Interestingly, the contamination of sediments with As was found to increase from west to east (Posaga, $CF = 4.5$; $I_{geo} = 1.6$; $EF = 15$; Ocolis, $CF = 6.0$; $I_{geo} = 2.0$, $EF = 21$; Ocolisel, $CF = 8.2$, $I_{geo} = 2.5$, $EF = 30$; Iara, $CF = 10$; $I_{geo} = 2.8$ and $EF = 40$) and the same was true for the main stream. In the absence of anthropogenic sources on the valley of the left-bank tributaries, the presence of As was attributed to the mineralogy of the local bedrock.

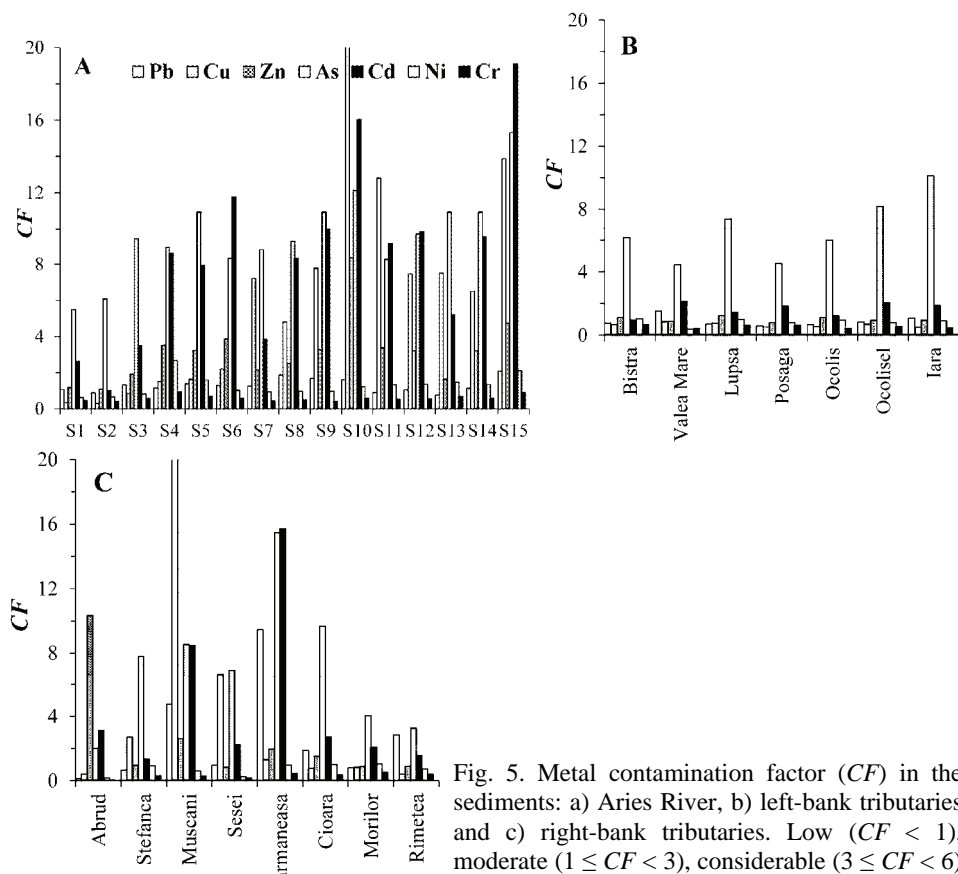


Fig. 5. Metal contamination factor (CF) in the sediments: a) Aries River, b) left-bank tributaries and c) right-bank tributaries. Low ($CF < 1$), moderate ($1 \leq CF < 3$), considerable ($3 \leq CF < 6$) and very high ($CF \geq 6$) contamination.³²

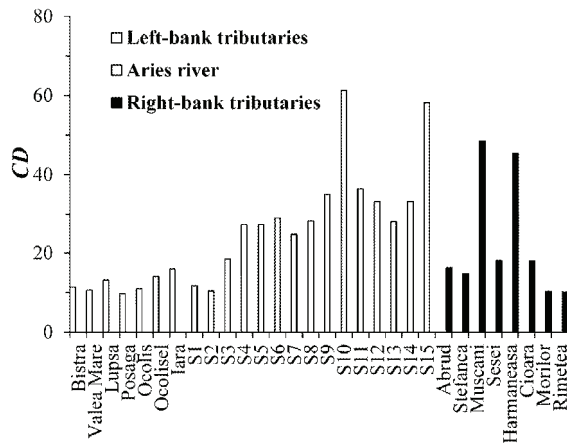


Fig. 6. Contamination degree (CD) of the sediments in the Aries River and its tributaries. Low ($CD \leq 8$), moderate ($8 < CD \leq 16$), considerable ($16 < CD < 32$) and very high ($CD > 32$) contamination degree.³²

Multivariate statistics

The varimax rotated loadings of the five PCs with eigenvalues higher than 1 of the metal contents in sediments are presented in Table V. Five latent factors cumulated 86 % of the total variance and described different sources for the metals in the sediments. The first latent factor explaining 32 % represents sediment pollution with As and Cd (strong influence) and Pb and Cu (moderate influence) of anthropogenic origin, as suggested by the lack of correlation with naturally occurring metals, such as alkaline and alkaline earth elements. This factor was ascribed to the right-bank tributaries with very highly contaminated

TABLE V. Varimax rotated factor loadings of significant PCs; * – strong influence on the latent factor; ** – moderate influence on the latent factor

Metal	PC1	PC2	PC3	PC4	PC5
Pb	0.630**	0.612**	-0.123	-0.156	0.246
Cu	0.571**	-0.412	0.351	-0.081	0.502**
Zn	0.301	-0.197	0.821*	-0.135	-0.155
As	0.809*	0.075	0.037	0.414	-0.004
Cd	0.825*	0.025	0.382	0.267	0.068
Ni	0.292	-0.035	0.117	0.834*	0.069
Cr	0.163	-0.044	0.025	0.924*	0.009
Mn	0.405	0.433	0.686**	0.154	0.018
Fe	-0.068	0.110	0.872*	0.067	0.061
Al	0.111	0.027	0.851*	0.335	0.197
Ca	0.038	0.945*	0.027	-0.077	0.152
K	0.032	0.570**	0.384	0.079	0.282
Mg	-0.071	-0.140	0.381	0.699**	-0.053
Na	-0.140	0.463	0.241	-0.371	0.651**
Sr	-0.039	0.557**	0.017	-0.067	0.755*
Ba	0.232	0.056	-0.045	0.216	0.889*
Variability, %	32	22	14	10	8

sediments, namely Harmaneasa (Pb, As and Cd), Muscani (As, Cd and Cu), Sesei (As and Cu) and Cioara and Stefanca (As). The second PC with 22 % of total variance was correlated with the natural input of Pb (moderate influence), as shown by the positive loadings with alkaline and alkaline earth elements of geogenic origin. The third factor exhibiting 14 % of the total variance was indicative for the natural origin of Zn (strong influence) in the sediments, confirmed by the concomitant positive loadings with Mn, Fe and Al. The most probable source of Zn was the Abrud River, as shown above. The fourth factor accounting for 10 % of the total variance had positive loadings with Ni and Cr of geogenic origin, since most sediments exhibited minor enrichment/low contamination with these metals. The natural source of Ni and Cr is consistent with the moderate influence of Mg on PC4, as its minerals act as host-rocks for Ni and Cr.^{45,46} In the Aries Basin, Mg minerals are associated with those belonging to the silicate and carbonate group, which explains the presence of Al in this factor, albeit with a weak influence on this factor.⁴⁵ The last PC explaining 8 % of the total variance is associated with anthropogenic contamination of sediments by Cu, especially through the Muscani and Sesei Tributaries as their sediments were found to be very high contaminated with Cu. The results are in good agreement with the mineralogical analysis. The presence of Ba in this factor is related to wastes from the processing of Cu ores.⁴⁷ The results of the HCA are displayed in Fig. 7. The cluster C1 groups the elements of geogenic origin (Pb, Ca, K, Na and Sr) and supports the idea that the natural input of Pb from bedrock in sediments is more significant than the anthropogenic source identified by PCA. The association of Zn with Mn, Fe and Al in the cluster C2 confirmed the natural origin of Zn. The cluster C3 is divided in two sub-clusters, one of which confirms the natural origin of Cr and Ni following the correlation with Mg, and the other proving the anthropogenic origin of As, Cd and Cu. A similar origin of Ni and Cr was also found in the case of mine tailings deposited in the Aries River basin.³⁹ This shows the greater influence of the anthropogenic origin of As from the right-bank tributaries compared with the natural source of the left-side tributaries on the sediments in the main stream. The natural origin of Cr, Ni, Zn and the anthropogenic origin of As, Cd and Cu identified by the PCA and CA is in accordance with that suggested by their enrichment factors.

The clustering of the sampling sites according to their contents of metals is presented in Fig. 8. The sampling sites were clustered in two groups according to the contamination degree: moderate to considerable (C1) and considerable to very high contamination (C2). This grouping is in agreement with the contaminant distribution in the studied sites and was confirmed by LDA with a 90 (C1) and 85 % (C2) prediction, respectively.

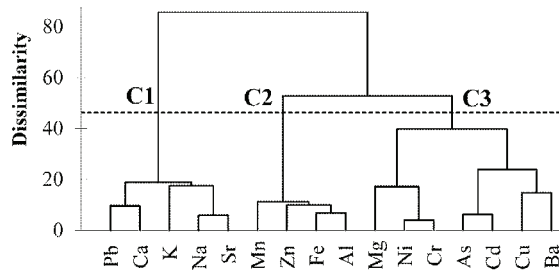


Fig. 7. Dendrogram showing the clustering of the metals in the sediments from the Aries River catchment.

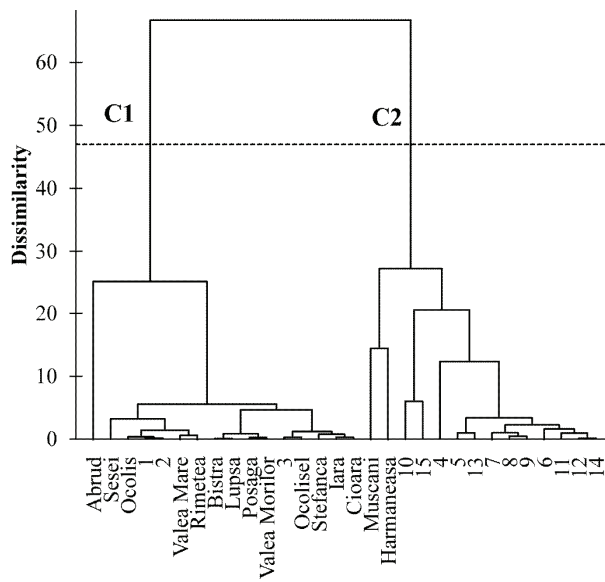


Fig. 8. Dendrogram showing the clustering of the sediments sampling sites from the Aries River catchment considering their metals contents.

CONCLUSIONS

A comprehensive insight of the current status of sediment contamination with metals and the potential origin of contaminants in the Aries River catchment has been provided. Guidelines and contamination indices were used to evaluate the contamination of the sediment, while multivariate statistical approaches allowed for the clarification of the anthropogenic or natural origin of seven metals. The obtained results indicated metal enrichments in sediment in the order $\text{Cr} < \text{Ni} < \text{Pb} < \text{Zn} < \text{Cu} < \text{Cd} < \text{As}$. The enrichment factors of the metals and the degree of contamination of the sediments in the Aries River increased from upstream to downstream with local peaks, demonstrating that the River remained a collector for pollutants coming mostly from the mine-affected right-side effluents. Sediment

ments of the Aries River were found to be very highly contaminated with Cd, Cu and As, considerably with Zn, moderately with Pb and Ni, and low with Cr. The right-bank tributaries were found to be very highly contaminated with Pb, As and Cd (Harmaneasa), As, Cd and Cu (Muscani), Cu and As (Sesei), As (Cioara and Stefanca) and Zn (Abrud). In contrast, the sediments from most of the left-side effluents were classified as very high contaminated only because of As. The PCA, HCA and LDA brought increased knowledge and contributed to a better understanding of the sediment pollution phenomena in the Aries River basin. The anthropogenic origin of As, Cd, Cu and some Pb in the main stream and the right-side tributaries was established. However, the anthropogenic source of Cu was found to be different from that of As, Cd and Pb. The geogenic input of Pb was confirmed by its association with Ca, K, Na and Sr in a common PC and cluster. The anthropogenic loading of As in the sediments from the right-side tributaries was much higher as compared to the geogenic one from the left-bank tributaries. Zinc occurred especially from natural source due to its retention on minerals containing Mn, Fe and Al and came mainly from the Abrud River. Nickel and Cr were found to be of natural origin according to their association with Mg.

Acknowledgement. This work was supported by a grant of the Romanian National Authority for Scientific Research, CNCS – UEFISCDI, Project No. PN-II-RU-PD-2011-3-0056.

ИЗВОД

ПРОЦЕНА ЗАГАЂЕЊА И ПОРЕКЛА МЕТАЛА У РЕЧНИМ СЕДИМЕНТИМА ПОГОЂЕНИХ РУДАРСТВОМ: СТУДИЈА СЛУЧАЈА ЗАХВАТА НА РЕЦИ ARIES У РУМУНИЈИ

ERIKA LEVEI¹, MICHAELA PONTA², MARIN SENILA¹, MIRELA MICLEAN¹ и TIBERIU FRENTIU²

¹INCDO-INOE 2000, Research Institute for Analytical Instrumentation, 67 Donath, 400293, Cluj-Napoca,
Romania и ²Faculty of Chemistry and Chemical Engineering, Babes-Bolyai University, 11 Arany Janos,
400028, Cluj-Napoca, Romania

Ова студија представља тренутни статус загађења металима (Cu, Cr, Cd, Pb, Ni, Zn и As) и њиховог антропогеног порекла у седиментима базена реке *Aries* у Румунији, који је погођен рударским активностима. Резултати указују на обогаћење седимената металима. Идентификовани су различити нивои загађења у реци *Aries* и њеним притокама. Према упутствима за квалитет седимената и индекса загађења, нађено је да су седименти из реке *Aries* високо загађени са Cd, Cu, As, значајно са Zn и умерено са Pb и Ni. Нађено је да су десне притоке више загађене него леве, у којима је нађен само As геолошког порекла. Статистичком PCA методом је идентификовано пет латентних фактора (са укупном варијабилношћу од 86 %), што одражава антропогено и природно порекло метала. Нађено је да As, Cd и деломично Pb имају заједничко антропогено порекло, различито од Cu. Статистички приступ је такође указао на геолошко порекло Pb, због своје повезаности са Ca, K, Na и Sr. Хром и Ni су приписани природном извору, на основу њихове повезаности са Mn, Fe, Al и Mg.

(Примљено 1. маја, ревидирано 5. августа, прихваћено 24. августа 2013)

REFERENCES

1. B. Dold, *Rev. Environ. Sci. Biotechnol.* **7** (2008) 275
2. J. Zobrist, M. Sima, D. Dogaru, M. Senila, H. Yang, C. Popescu, C. Roman, B. Abraham, L. Frei, B. Dold, D. Balteanu, *Environ. Sci. Pollut. Res. Int.* **16** (2009) 14
3. M. Sima, B. Dold, L. Frei, M. Senila, D. Balteanu, J. Zobrist, *J. Hazard. Mater.* **189** (2011) 624
4. G. Bird, P. A. Brewer, M. G. Macklin, M. Nikolova, T. Kotsev, M. Mollov, C. Swain, *Water Air Soil Pollut.* **206** (2010) 105
5. A. K. Krishna, K. R. Mohan, N. N. Murthy, *Res. J. Environ. Earth Sci.* **3** (2011) 103
6. M. Varol, *J. Hazard. Mater.* **195** (2011) 355
7. L. Djordjević, N. Živković, L. Živković, A. Djordjević, *Soil Sediment Contam.* **21** (2012) 889
8. K. T. Singh, G. N. Nayak, L. L. Fernandes, *Soil Sediment Contam.* **22** (2013) 256
9. Z. Vuković, M. Radenković, S. J. Stanković, D. Vuković, *J. Serb. Chem. Soc.* **76** (2011) 795
10. J. M. Pope, M. E. Farago, I. Thornton, E. Cordos, *Water Air Soil Pollut.* **162** (2005) 1
11. E. A. Cordos, T. Frentiu, M. Ponta, I. Marginean, B. Abraham, C. Roman, *Chem. Spec. Bioavail.* **18** (2006) 11
12. A. Rusu, G. C. Jones, P. D. Chimonides, O. W. Purvis, *Environ. Pollut.* **143** (2006) 81
13. T. Frentiu, M. Ponta, E. Levei, E. Gheorghiu, M. Benea, E. A. Cordos, *Chem. Spec. Bioavail.* **20** (2008) 99
14. E. Cordos, R. Rautiu, C. Roman, M. Ponta, T. Frentiu, A. Sarkany, L. Fodorpataki, K. Macalik, C. McCormick, D. Weiss, *Eur. J. Mineral Process. Environ. Prot.* **3** (2003) 324
15. M. Macklin, P. Brewer, D. Balteanu, T. Coulthard, B. Driga, A. Howard, S. Zaharia, *Appl. Geochem.* **18** (2003) 241
16. M. Ponta, T. Frentiu, A. Sarkany-Kiss, E. A. Cordos, *Croat. Chim. Acta* **75** (2002) 307
17. G. Bird, P. A. Brewer, M. G. Macklin, D. Balteanu, B. Driga, M. Serban, S. Zaharia, *Appl. Geochem.* **18** (2003) 1583
18. G. Bird, M. G. Macklin, P. A. Brewer, S. Zaharia, D. Balteanu, B. Driga, M. Serban, *Environ. Geochem. Health* **31** (2009) 741
19. F. L. Forray, D. K. Hallbauer, *Environ. Geol.* **39** (2000) 1372
20. M. Buza, L. Dimen, G. Pop, D. Turnock, *GeoJournal* **54** (2001) 631
21. G. Bird, P. A. Brewer, M. G. Macklin, M. Serban, D. Balteanu, B. Driga, *J. Geochem. Explor.* **86** (2005) 26
22. R. M. Florea, A. I. Stoica, G. E. Baiulescu, P. Capota, *Environ. Geol.* **48** (2005) 1132
23. M. J. Friedel, J. A. Tindall, D. Sardan, D. L. Fey, G. L. Poputa, *Reconnaissance study of water quality in the mining-affected Aries River basin, Romania*, U.S. Geological Survey Open-File Report 2008-1176, 2008
24. C. Marin, A. Tudorache, O. T. Moldovan, I. Povara, G. Rajka, *Carpath. J. Earth Environ. Sci.* **5** (2010) 13
25. O. Moldovan, E. Levei, C. Marin, M. Banciu, H. Banciu, C. Pavelescu, T. Brad, M. Cimpean, I. Meleg, S. Iepure, I. Povara, *Hydrobiologia* **669** (2011) 63
26. Romanian Ministry of Environment and Water Management, *Ministerial Order No. 161/2006 for the approval of the Normative regarding the surface water quality classification in order to establish the ecological status of water bodies*, Official Gazette, part I, 2006, p. 511 (In Romanian)
27. D. D. MacDonald, C. G. Ingersoll, T. A. Berger, *Arch. Environ. Contam. Toxicol.* **39** (2000) 20

28. V. Milu, J. L. Leroy, C. Peiffert, *Environ. Geol.* **42** (2002) 773
29. ISO 11466, *Soil quality – Extraction of trace elements soluble in aqua regia*, 1995
30. S. A. Sinex, G. R. Helz, *Environ. Geol.* **3** (1981) 315
31. G. Muller, *Umschau* **79** (1979) 778
32. L. Hakanson, *Water Res.* **14** (1995) 975
33. S. R. Taylor, S. M. McLennan, *Rev. Geophys.* **33** (1995) 241
34. S. Yilgor, F. Kucuksezgin, E. Ozel, *Bull. Environ. Contam. Toxicol.* **89** (2012) 512
35. E. Levei, T. Frentiu, M. Ponta, M. Senila, M. Miclean, C. Roman, E. Cordos, *Int. J. Environ. Anal. Chem.* **89** (2009) 635
36. T. Frentiu, M. Ponta, A. Mihaltan, E. Cordos, M. Frentiu, G. Lazaroiu, L. Traista, R. Indries, *J. Optoelectron. Adv. Mater.* **11** (2009) 697
37. H. H. Ho, R. Swennen, V. Cappuyns, E. Vassilieva, G. Neyens, M. Rajabali, T. V. Tran, *Soil Sediment Contam.* **22** (2013) 415
38. K. Nosrati, M. Van Den Eeckhaut, *Environ. Earth Sci.* **65** (2012) 331
39. E. Levei, T. Frentiu, M. Ponta, C. Tanaselia, G. Borodi, *Chem. Cent. J.* **7** (2013) 5
40. O. Abollino, M. Malandrino, A. Giacomino, E. Mentasti, *Anal. Chim. Acta* **688** (2011) 104
41. A. Giacomino, O. Abollino, M. Malandrino, E. Mentasti, *Anal. Chim. Acta* **688** (2011) 122
42. F. Zhou, H. Guo, Y. Liu, Y. Jiang, *Mar. Pollut. Bull.* **54** (2007) 745
43. K. L. Lu, C.W. Liu, C. S. Jang, *Environ. Monit. Assess.* **184** (2012) 6071
44. L. Zhang, X. Ye, H. Feng, Y. Jing, T. Ouyang, X. Yu, *Mar. Pollut. Bull.* **54** (2007) 974
45. C. Ionescu, *The Brucite–Mg(OH)₂. Mineralogy and Mineralogenesis. Brucite Deposits in Romania*, Didactica si Pedagogica, Bucuresti, 1999 (In Romanian)
46. Jeffrey, *Chemical methods of rock analysis*, Pergamon, New York, 1975
47. J. Van Deuren, T. Lloyd, S. Chhetry, R. Liou, J. Peck, *Remediation Technologies Screening Matrix and Reference Guide*, 4th ed., 2002, http://www.frtr.gov/matrix2/section2/2_8_1.html (Accessed 10 February 2012).



Sorption recovery of copper(II) and zinc(II) from aqueous chloride solutions

OLGA N. KONONOVA^{1*}, MARINA A. KUZNETSOVA¹, ALEXEY M. MEL'NIKOV¹,
NATALIYA S. KARPLYAKOVA¹ and YURY S. KONONOV²

¹Institute of Non-Ferrous Metals and Material Science, Siberian Federal University, 660041 Krasnoyarsk, Svobodny Pr. 79, Russian Federation and ²Institute of Chemistry and Chemical Technology, Siberian Department of the Russian Academy of Sciences, 660036 Krasnoyarsk, Akademgorodok 50/24, Russian Federation

(Received 11 September 2013, revised 31 March, accepted 1 April 2014)

Abstract: The present investigation was devoted to the simultaneous sorption recovery of copper(II) and zinc(II) ions on some commercial anion exchangers with different physico-chemical properties. The initial concentrations of zinc and copper were 1–3 mmol L⁻¹ and the recovery was performed in 0.01 and 2 M hydrochloric acid solutions. It was shown that the investigated anion exchangers possess good sorption and kinetic properties. After the recovery of copper and zinc from the strongly acidic solutions, their selective elution was realized by means of 2 M hydrochloric acid solution (zinc recovery) and 2 M ammonia solution (copper recovery). In the weakly acidic solutions, copper and zinc were separated during sorption, as zinc sorption did not proceed in this case. The subsequent copper(II) elution was performed using 2 M ammonia solution. The anion exchangers Purolite S985, Purolite A500 and AM-2B could be recommended for zinc and copper recovery from acidic industrial solutions and wastewater.

Keywords: anion exchange; copper; zinc; anion exchangers; hydrochloric acidic solutions.

INTRODUCTION

The rapid growth in the demand for non-ferrous metals in metallurgy and the chemical industry was followed by an increase in their production volumes.¹ The most widespread non-ferrous metals are copper and zinc, which are extensively used in electrical engineering and the chemical industry. Zinc is used for galvanization of steel products, whereas copper is applied as a catalyst, and brasses, the alloys of copper and zinc with 5–45 % zinc content, are widely used for the

*Corresponding author. E-mail: cm2@bk.ru
doi: 10.2298/JSC130911033K

production of automotive parts, chemical and heat technology equipment, bearings and jewelry.^{1–3}

Simultaneously, the growth in output of non-ferrous metals (including copper and zinc) entailed the growth in the amounts of solid and liquid wastes arising from the processing of ores and secondary raw materials. These wastes include mine and dump water of mining plants, and waste water from the facilities in which non-ferrous metals are manufactured facilities.^{2,4,5} Waste emission leads to environmental damage through toxic solutions, and to the loss of valuable components, such as copper and zinc.^{1,4,5}

This situation led to the urgent need for the utilization and decontamination of wastewaters containing heavy metal ions. A simple illustration of this could be as follows. It is known⁶ that acid washing sewages after etching usually contain about 60–120 mg L⁻¹ of copper(II) and 50–200 mg L⁻¹ of zinc. However, according to EU regulations, the maximum permissible concentrations (*MPC*) of these components are 0.5 mg L⁻¹ for copper and up to 5 mg L⁻¹ for zinc. The standards of the Russian Federation generally imply that the *MPC* values are 0.1 mg L⁻¹ for both copper and zinc, but in case of drinking water (or water for fishery purposes), the *MPC* values are more stringent, *i.e.*, 0.001 mg L⁻¹ for copper and 0.01 mg L⁻¹ for zinc.⁷ Besides being an illustration of the high quality purification requirements, this also indicates the toxicity of these components, given the strict regulations imposed on water supply. It is known that copper and zinc induce respiratory tract infections, gastrointestinal issues and functional disorders of the nervous system.⁸ Although zinc is less hazardous than copper, the content of both components in water is strictly controlled.

The basic technologies for wastewater purification from heavy metals include chemical (reagent) methods (when soluble compounds are converted into sparingly soluble ones, and the precipitates are separated), microbiological methods, and physical (sorption) methods.^{8–15} The sorption technologies are being increasingly used for sewage treatment, mostly because they imply eco-friendly processes. For these purposes, various kinds of sorbents are used: inorganic (zeolites),⁵ activated carbon,¹⁵ sorption materials based on natural compounds,^{16–18} as well as organic ion exchangers.^{19–27} Many researchers modify the sorbents, to improve their sorption properties.^{5,15,17,20,21} The ion exchange recovery of heavy metals from wastewater is realized on cation exchangers or on chelate sorbents,^{4,8,9,11,19–21} because of the presence of the cation form of the recovered ions in solution. However, it is known^{28–31} that copper(II) and zinc(II) form anionic complexes in acidic media, so that they could be adsorbed on anion exchangers. Previously, the sorption recovery of zinc from chloride and chloride–sulfate (*i.e.*, mixed) solutions was studied³² on some anion exchangers. The present work was focused on the simultaneous recovery of copper(II) and zinc(II) from chloride solutions on some anion exchangers.

EXPERIMENTAL

Solutions of copper(II) and zinc(II) with concentrations of 1–3 mmol L⁻¹ were used. Accurately weighed salt samples CuCl₂·2H₂O and ZnCl₂ were dissolved in hydrochloric acid solutions with concentrations 2 and 0.01 mol L⁻¹. The acidity of the solutions and initial concentrations of Cu²⁺ and Zn²⁺ were chosen to make the experiment conditions similar to those of real industrial conditions, *i.e.*, similar to wastewaters from the galvanic industry, or to technical solutions obtained after treatment of secondary copper–zinc raw materials.^{3,4,6} All the reagents were of analytical purification grade.

Macroporous anion exchangers with different functional groups were taken for the investigations. Their physico-chemical characteristics are presented in Table I. The selection of the anion exchangers was based on their good sorption properties towards zinc, which were revealed in a previous study.³²

TABLE I. Physico-chemical characteristics of the investigated anion exchangers

Trade name	Exchanger type	Copolymer	Functional group	Exchange capacity in the Cl ⁻ form, mmol g ⁻¹	Swelling grade g cm ⁻³	Moisture %	Manufacturer
Purolite S985	Weak base	PAc – DVB	PA	2.3	1.3	18.8	Purolite (UK)
Purolite A500	Strong base	St – DVB	QAB	2.8	1.6	20.3	Purolite (UK)
AM-2B	Intermediate base	St – DVB	SAG, TAG, QAB	3.0	2.1	32.8	Cherkassy (Ukraine)

Before use, the anion exchangers were prepared according to standard methods and loaded by 1 M HCl, to convert the resins into the Cl⁻ form.

The concentrations of non-ferrous metal ions were determined by spectrophotometrical methods: copper(II) – with rubeanic acid (ethanedithioamide)²⁸ and zinc(II) – with PAN (1-(2-pyridylazo)2-naphthol)²⁹ using a Specol 1300 spectrophotometer (Carl Zeiss, Germany). Before the determination of the zinc ions, the copper ions were masked with sodium thiosulfate.

The sorption of copper(II) and zinc(II) was studied under batch experiment conditions: resin mass, 0.2 g; volume of contacting solution, 20.0 mL; stirring in a thermostat at 20±1 °C. The equilibrium time was 24 h.

The efficiency of ion exchange recovery of copper(II) and zinc(II) was estimated by means of the recovery degree *R* / % and the distribution coefficient *D*, which were calculated as follows:

$$R = 100 \frac{c_0 - c_{eq}}{c_0} \quad (1)$$

$$D = \frac{WEC}{c_{eq}} \quad (2)$$

where *c*₀ and *c*_{eq} are the initial and equilibrium molar concentrations of zinc (copper), respectively, and *WEC* is working exchange capacity of resin for zinc (copper) in mmol g⁻¹. The latter was calculated using the equation:

$$WEC = \frac{(c_0 - c_{eq})V}{m} \quad (3)$$

where V in L is the volume of the contacting solution and m in g is the resin mass.

Moreover, the separation coefficient S of copper(II) and zinc(II) was calculated as follows:

$$S = \frac{D_{Cu}}{D_{Zn}} \quad (4)$$

where D_{Cu} and D_{Zn} are the distribution coefficients of copper and zinc, respectively.

The sorption isotherms were plotted by varying the molar ratio of resins to the amount of copper (zinc) in contacting solution.^{33,34} The apparent constants of ion exchange equilibrium were calculated based on the sorption isotherms obtained according to the law of mass action for the investigated equilibria.^{33,34}

The kinetic behavior of copper(II) and zinc(II) sorption by the investigated resins was studied by the "limited bath" method.³³⁻³⁵ The resin quantities (0.1 g) were stirred with 10.0 mL of zinc and copper solution at 20±1 °C over a period from 1 min to 24 h. The saturation times were 1, 2, 3, 5, 15, 20, 30 and 45 min and 1, 2, 3, 6 and 24 h. The suspensions were intensively stirred (more than 800 rev min⁻¹). After a certain time, the resins and solutions were quickly separated by filtration through a porous glass filter. Then the concentrations of copper and zinc were determined in the solutions by the spectrophotometrical methods. Using the obtained results, the saturation degree F was calculated using the equation:

$$F = \frac{Q_t}{Q_\infty} \quad (5)$$

where Q_t and Q_∞ in mmol are the amounts of copper (zinc) sorbed at time t and at equilibrium, respectively.

Then the kinetic curves were plotted as dependences $F = f(t)$, and the half-exchange times, $t_{1/2}$ in s, were determined from these curves at $F = 0.5$. Subsequently, the diffusion coefficients of copper and zinc ions in a resin grain, \bar{D}_S in cm² s⁻¹, were calculated from the following formula:

$$\bar{D}_S = \frac{r^2}{4\pi^2 t_{1/2}} \quad (6)$$

where r in cm is the radius of the resin grain.

Moreover, the process rate, v in mmol g⁻¹·s⁻¹, was calculated from the equation:

$$v = \frac{a_i}{t_i} \quad (7)$$

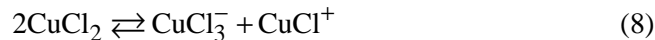
where a_i in mmol is the quantity of copper (zinc) sorbed per 1 g of the resin at time t_i in s.

The obtained results were statistically processed by standard methods.^{36,37} The average experimental error was less than 6 %.

RESULTS AND DISCUSSION

As mentioned above, the ion exchange recovery of copper(II) and zinc(II) is usually realized on cation exchangers or chelate sorbents. However, the ionic state of these elements depends on the acidity of the medium.²⁸⁻³¹ Thus, cop-

per(II) is present in solution in the form of complexes $[\text{CuCl}_4]^{2-}$ when the HCl concentration is 1–4 mol L⁻¹, but in stronger acidic solutions (5–10 M HCl) its polymeric species $[\text{Cu}_2\text{Cl}_6]^{2-}$ are formed.^{28,31} With dilution and decrease in the acidity, the complexes $[\text{Cu}(\text{H}_2\text{O})_6]^{2+}$ appear in the system. In weaker acidic media in the presence of chloride ions (0.5–1 mol L⁻¹), the following transformation occurs:³⁸



The ionic state of zinc also depends on the acidity of the medium.^{29,31} For instance, complexes $[\text{ZnCl}_4]^{2-}$ are present in strong acidic solutions (1–6 M HCl). On decreasing the acidity to 0.01–0.001 M HCl, the formation of the species $[\text{ZnCl}]^+$ and $[\text{ZnCl}_2]^0$ occurs. These species co-exist with the complex $[\text{ZnCl}_4(\text{H}_2\text{O})_2]^{2-}$.

Therefore, the presence of anionic complexes of copper(II) and zinc(II) in acidic solutions gives an opportunity to use anion exchangers for their recovery. In this work, the simultaneous sorption of Cu(II) and Zn(II) on anion exchangers with different basicity (Table I) was studied, which is a matter of scientific and practical importance.

The results of the sorption recovery of copper and zinc on the investigated anion exchangers from strong and weak acidic solutions for various initial concentrations are presented in Table II. It can be seen from these data that zinc was not adsorbed from weak acidic media when copper was present (regardless of initial concentrations of both ions). However, in a previous study,³² the recovery of 53–71 % zinc on the same anion exchangers from individual weak acidic solu-

TABLE II. Simultaneous recovery of copper(II) and zinc(II) from chloride solutions of different acidity on the investigated anion exchangers

Trade name	$c_0(\text{HCl})$ mol L ⁻¹	Initial concentrations of copper(II) and zinc(II)											
		$c_0(\text{Cu}) = c_0(\text{Zn}) = 3 \text{ mmol L}^{-1}$				$c_0(\text{Cu}) = c_0(\text{Zn}) = 1 \text{ mmol L}^{-1}$				$c_0(\text{Cu}) = 3 \text{ mmol L}^{-1}; c_0(\text{Zn}) = 1 \text{ mmol L}^{-1}$			
		Zn(II)		Cu(II)		Zn(II)		Cu(II)		Zn(II)		Cu(II)	
Purolite	2	R / %	D	R / %	D	R / %	D	R / %	D	R / %	D	R / %	D
		86	345	91	408	74	228	90	399	59	168	95	485
S985		±5	±20	±5	±25	±4	±14	±6	±20	±3	±10	±5	±29
Purolite	0.01	74	232	81	327	—	—	89	378	—	—	95	491
A500		±4	±12	±5	±20			±5	±23			±5	±30
AM-2B		63	198	90	405	45	115	85	365	63	189	85	361
		±3	±10	±5	±24	±3	±7	±5	±22	±3	±11	±5	±22
Purolite		—	—	97	485	—	—	95	479	—	—	95	489
S985				±3	±29			±5	±29			±5	±29
Purolite		—	—	94	479	—	—	93	465	—	—	94	476
A500				±5	±24			±5	±27			±5	±29
AM-2B		—	—	95	481	—	—	95	484	—	—	95	483
				±5	±28			±5	±29			±5	±29

tions was observed. This indicates to the joint action of simultaneously sorbed ions, leading to the increase in the selectivity of the resins to copper(II). The probable reason is an acid effect, affecting the anion exchanger phase and facilitating the sorption of the component with more stable anionic complexes.³⁹ Given that zinc in weak acidic media is present not only in the form of anionic complexes, but also in the form of cationic and neutral species, the affinity of anionic complexes of copper(II) to the anion exchanger is greater, so that the sorption centers are occupied by copper and copper is recovered almost completely. From the practical point of view, this facilitates the complete separation of copper and zinc in dependence on the stage of their sorption on investigated anion exchangers.

In strong acidic solutions, a similar result was obtained for the strong basic anion exchanger Purolite A500 during zinc and copper sorption at 1 mmol L⁻¹ initial concentration of zinc, whereas when its concentration was 3 mmol L⁻¹, its sorption recovery was observed (Table II). Probably the decrease in the initial zinc concentration in the presence of copper(II) reduces the affinity of the anion exchanger for zinc and improves its affinity for copper. Overall, the sorption recovery of copper(II) and zinc(II) in strong acidic media was affected by the functional groups of the investigated anion exchangers. The greatest affinity for copper(II) ions was revealed for the complex-forming polyamine anion exchanger Purolite S985 (Table II). In addition, the degree recovery of copper(II) also depended on the initial concentrations of the components, and with decreasing zinc concentration, it grew to almost complete recovery. In turn, the recovery of zinc depended positively on its initial concentration.

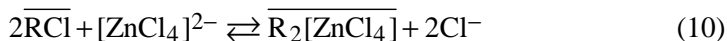
Therefore, the obtained data for simultaneous recovery of copper(II) and zinc(II) demonstrated the good sorption properties of investigated anion exchangers, and also indicated the possibilities for separation of copper and zinc during their sorption from weak acidic solutions (or from strong acidic solutions onto the strong basic anion exchanger Purolite A500).

The separation coefficients presented in Table III also indicate that copper(II) and zinc(II) ions could be separated during their sorption from 2 M HCl solutions. It can be seen from the data that all the values exceeded 1 and that the anion exchanger Purolite S985 provides the most favorable conditions for separation at initial zinc concentration 1 mmol L⁻¹ (Table III).

TABLE III. Separation coefficients of copper(II) and zinc(II) during their recovery from strong acidic solutions on the investigated anion exchangers ($c_0(\text{HCl}) = 2 \text{ mol L}^{-1}$)

Trade name	Initial concentrations of copper(II) and zinc(II)		
	$c_0(\text{Cu}) = c_0(\text{Zn}) = 3 \text{ mmol L}^{-1}$	$c_0(\text{Cu}) = c_0(\text{Zn}) = 1 \text{ mmol L}^{-1}$	$c_0(\text{Cu}) = 3 \text{ mmol L}^{-1}; c_0(\text{Zn}) = 1 \text{ mmol L}^{-1}$
Purolite S985	1.17±0.07	3.47±0.21	3.07±0.18
Purolite A500	1.41±0.08	—	—
AM-2B	2.06±0.12	1.59±0.11	1.86±0.11

Therefore, taking into account the ionic state of zinc and copper and the results on their sorption recovery, it could be concluded that the sorption of copper and zinc from strong acidic solutions on the investigated anion exchangers proceeded as follows:



where R indicates the resin phase and the bar indicates the sorbate. In weak acidic medium, the sorption recovery of copper(II) proceeded according to Eq. (9).

The sorption isotherms for the simultaneous recovery of copper(II) and zinc(II) from strong acidic solutions are presented in Fig. 1 for an initial concentration of 3 mmol L⁻¹ for both ions in the contacting solution. It should be noted that the curves obtained for the other concentrations of copper and zinc were similar to those presented in Fig. 1.

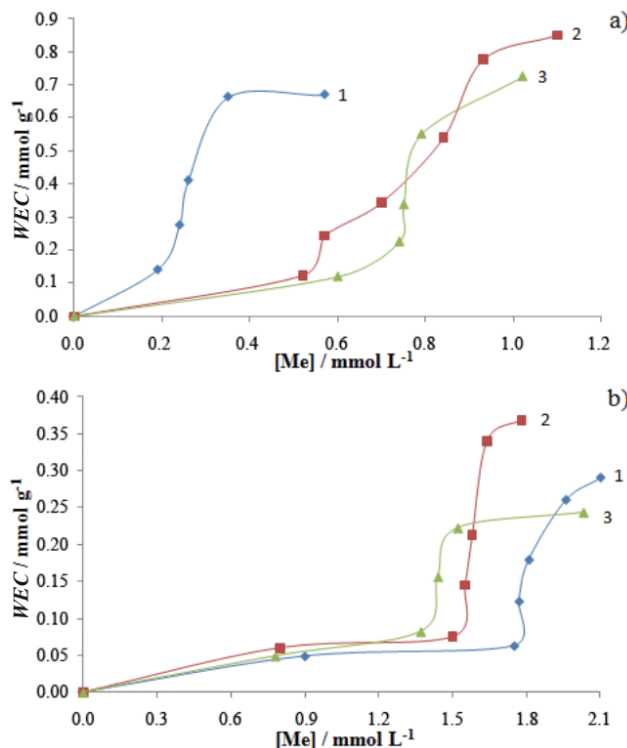


Fig. 1. Isotherms of copper sorption in the presence of zinc (a) and of zinc sorption in the presence of copper (b) from strong acidic chloride solutions on the investigated anion exchangers. $c_0(\text{Cu}) = c_0(\text{Zn}) = 3 \text{ mmol L}^{-1}$; $c_0(\text{HCl}) = 2 \text{ mol L}^{-1}$; 1 – Purolite S985; 2 – Purolite A500; 3 – AM-2B; [Me] is the equilibrium concentration of copper (zinc) in the contacting solutions; WEC is working exchange capacity for copper (zinc) at equilibrium.

It is known^{33,34} that the shape of the sorption isotherms is evidence of the sorption selectivity. As could be seen in Fig. 1, the sorption isotherms were S-shaped curves, which were steep upward sloping and almost parallel to the ordinate axis. This is evidence of the high selectivity of the copper and zinc recovery.

Using the isotherms, the apparent constants of the ion exchange equilibria (9) and (10) were calculated and the obtained data are presented in Table IV. These constants correlate with the selectivity of the investigated anion exchangers, since they define free energy and, consequently, determine the ion exchange affinity.^{33,34} It can be seen from Table IV that the apparent constants show the high affinity of the anion exchangers for zinc ions, and higher affinity for copper(II) ions.

TABLE IV. Apparent constants of the ion exchange equilibrium during copper(II) and zinc(II) recovery from strong acidic chloride solutions on the investigated anion exchangers ($c_0(\text{HCl}) = 2 \text{ mol L}^{-1}$)

Trade name	Initial concentrations of copper(II) and zinc(II)					
	$c_0(\text{Cu}) = c_0(\text{Zn}) = 3 \text{ mmol L}^{-1}$		$c_0(\text{Cu}) = c_0(\text{Zn}) = 1 \text{ mmol L}^{-1}$		$c_0(\text{Cu}) = 3 \text{ mmol L}^{-1}; c_0(\text{Zn}) = 1 \text{ mmol L}^{-1}$	
	Cu(II)	Zn(II)	Cu(II)	Zn(II)	Cu(II)	Zn(II)
Purolite S985	55.1±3.3	38.2±2.3	57.9±3.5	31.5±1.9	62.3±3.1	29.5±1.8
Purolite A500	43.1±2.2	30.5±1.8	46.2±2.3	—	61.5±3.7	—
AM-2B	58.4±3.5	27.3±1.6	36.0±1.8	18.7±1.1	51.2±3.1	30.7±1.8

Furthermore, the kinetics of the recovery of copper(II) and zinc(II) from weak and strong acidic chloride solutions on anion exchangers were studied. It should be noted that the rate of experiment is very important for a number of practical tasks, such as sorption optimization and selection of the best available sorbent for a particular case.^{33–35}

The dependence of ion exchange rate on time during the simultaneous recovery of copper(II) and zinc(II) on the anion exchanger Purolite S985 is shown in Fig. 2. It could be seen that the process rate increased sharply in first seconds of contact between the resin and solution and then decreased gradually with the saturation of the sorbent, reaching equilibrium over 24 h. Moreover, the sorption rate of copper(II) was higher than that of zinc(II) (Fig. 2). It should be noted that in approximately 1.5 h, the saturation of anion exchanger Purolite S985 from strong acidic chloride solution reaches ≈75 % for copper and ≈60 % for zinc of the equilibrium exchange capacity of the resin for these ions. For the anion exchangers Purolite A500 and AM-2B, these values were slightly lower and amounted to 68–70 % for copper and 48–52 % for zinc. Therefore, it could be concluded that the saturation rates of the resins were high and the investigated sorbents possessed good kinetic properties.

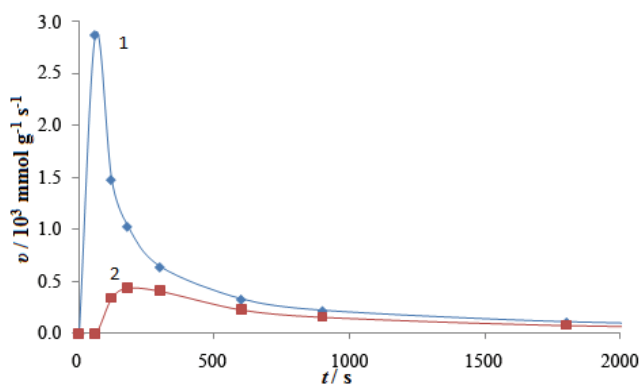


Fig. 2. Kinetic curves of anion exchanger Purolite S985 saturation during simultaneous recovery of copper (1) and zinc (2) from strong acidic solutions.
 $c_0(\text{Cu}) = c_0(\text{Zn}) = 3 \text{ mmol L}^{-1}$; $c_0(\text{HCl}) = 2 \text{ mol L}^{-1}$.

The calculated main kinetic parameters – half-exchange time and diffusion coefficients – are presented in Table V. The order of diffusion coefficients complies with the data obtained previously^{40–42} for the kinetics on the selected ion exchangers. The values of half-exchange times indicate the good kinetic properties of the investigated anion exchangers.⁴³

TABLE V. Kinetic parameters during simultaneous recovery of copper(II) and zinc(II) from strong acidic chloride solutions on anion exchangers investigated $c_0(\text{Cu}) = c_0(\text{Zn}) = 3 \text{ mmol L}^{-1}$; $c_0(\text{HCl}) = 2 \text{ mol L}^{-1}$

Trade name	Ion			
	Cu(II)	Zn(II)	Cu(II)	Zn(II)
	$t_{1/2} / \text{s}$	$\bar{D}_S \times 10^8 / \text{cm}^2 \text{ s}^{-1}$	$t_{1/2} / \text{s}$	$\bar{D}_S \times 10^8 / \text{cm}^2 \text{ s}^{-1}$
Purolite S985	820±49	6.91±0.35	1207±72	1.79±0.11
AM-2B	945±57	4.82±0.24	1568±94	1.68±0.11

Furthermore, the desorption of copper and zinc after their simultaneous recovery from chloride solutions on anion exchangers were studied. The system with 3 mmol L^{-1} initial concentrations of copper and zinc in strong acidic solution was chosen for the investigation. A solution of hydrochloric acid solution (2 mol L^{-1}) was selected as the eluent, as solutions of mineral acids are, as a rule, applied for desorption of non-ferrous metals.^{21–27,38} The results are summarized in Table VI.

It can be seen from these data that zinc was eluted practically completely, whereas copper desorption proceeds to the level of experimental error. Obviously, the high desorption of zinc could be explained by the lower selectivity of the investigated anion exchangers for zinc, as discussed above when considering the sorption of copper and zinc.

TABLE VI. Desorption degree, %, using 2 M HCl. of copper and zinc after their simultaneous recovery on the investigated anion exchangers. The sorption was realized at $c_0(\text{Cu}) = c_0(\text{Zn}) = 3 \text{ mmol L}^{-1}$ from a strong acidic solution

Trade name	Ion	
	Cu(II)	Zn(II)
Purolite S985	6	96±4
Purolite A500	6	96±4
AM-2B	6	95±5

The subsequent recovery of copper(II) was performed in the systems where copper remained in the resin after zinc removal, as well as in weak acidic solutions where zinc was not sorbed. A solution of ammonia (2 mol L⁻¹) was chosen as the eluent, because copper and ammonia form stable complexes.^{28,44} The results are presented in Table VII.

TABLE VII. Desorption degree, %, of copper(II) from the investigated anion exchangers using 2 mol L⁻¹ ammonia solution. The sorption was performed at $c_0(\text{Cu}) = c_0(\text{Zn}) = 3 \text{ mmol L}^{-1}$ from weak and strong acidic solutions; system A – desorption after elution of Zn(II) (strong acidic solutions); system B – desorption after Cu(II) sorption from weak acidic solutions (sorption of zinc was not observed)

Trade name	System	
	A	B
Purolite S985	95±5	95±5
Purolite A500	≈100	≈100
AM-2B	94±5	95±5

It can be seen from these data that complete elution of copper(II) in the form of complexes with ammonia occurred. After that, the anion exchanger was converted to the hydroxyl form. The resin in hydroxyl form could be either repeatedly used, or converted into the chloride form.

Therefore, the simultaneous sorption of copper and zinc from strong acidic chloride solutions requires the selective elution for their complete separation. In the cases of copper and zinc recovery from weak acidic chloride solutions, their separation occurs in the sorption stage, and subsequently, it is necessary to elute copper only.

Thus, the investigated anion exchangers could be recommended for the purification of acidic sewages from copper and zinc ions.

CONCLUSIONS

Sorption recovery of copper(II) and zinc(II) from weak and strong acidic chloride solutions was investigated at different ratios of initial concentrations of components on anion exchangers with various physico-chemical properties. It was revealed that the investigated resins possess high sorption ability for copper(II) ions, regardless of the basicity of the resins. It was determined that

zinc ions were not adsorbed on the investigated anion exchangers during the simultaneous recovery of copper(II) and zinc(II) from weak acidic solutions. This indicated an opportunity for the separation of copper and zinc.

The apparent constants of the ion exchange equilibrium with the participation of copper(II) and zinc(II) ions were calculated for the investigated anion exchangers. The values of these constants showed the high selectivity of the sorption process, especially towards copper(II). It was shown that investigated anion exchangers possessed good kinetic properties, since the process rate was high for both Cu(II) and Zn(II), but was higher during copper(II) recovery.

Desorption of copper(II) and zinc(II) was performed after their simultaneous recovery on the investigated anion exchangers. It was shown that zinc ions were completely eluted using 2 M hydrochloric acid, whereas copper remained in the sorbent phase. Then copper(II) could be removed by using a 2 mol L⁻¹ ammonia solution.

Based on the obtained experimental data, the investigated anion exchangers (Purolite S985, Purolite A500 and AM-2B) could be recommended for purification of acidic sewages from copper and zinc ions. The novelty of the suggested method is the complete recovery of copper and zinc ions, in their simultaneous presence, from strong and weak acidic chloride solutions, as well as the complete separation of these ions by subsequent elution.

ИЗВОД

СОРПЦИОНО ИЗДВАЈАЊЕ БАКРА(II) И ЦИНКА(II) ИЗ ХЛОРИДНИХ ВОДЕНИХ РАСТВОРА

OLGA N. KONONOVA¹, MARINA A. KUZNETSOVA¹, ALEXEY M. MEL'NIKOV¹, NATALIYA S. KARPLYAKOVA¹
и YURY S. KONONOV²

¹Institute of Non-Ferrous Metals and Material Science, Siberian Federal University, 660041 Krasnoyarsk,
Svobodny Pr. 79, Russian Federation and ²Institute of Chemistry and Chemical Technology, Siberian Department of the Russian Academy of Science, 660036 Krasnoyarsk, Akademgorodok 50/24, Russian Federation

Ово испитивање је обухватило истовремено сорпционо јона бакра(II) и цинка(II) на неким анјонским измењивачима са различитим физичкохемијским својствима. Почетне концентрације цинка и бакра су биле 1–3 mmol L⁻¹, а издавање је изведено у 0,01 М и 2 М растворима хлороводоничне киселине. Показано је да испитивани анјонски измењивачи имају добра сорпциона и кинетичка својства. Након издавања из јако киселих растворова, бакар и цинк су селективно елуирани помоћу 2 М раствором хлороводоничне киселине (издавање цинка) и 2 М раствором амонијака (издавање бакра). У слабо киселим растворима, бакар и цинк су раздвојени током сорпције, пошто није долазило до сорпције цинка у овом случају. Елуирање бакра(II) је затим извођено 2 М раствором амонијака. Анјонски измењивачи Purolite S985, Purolite A500 и AM-2B се могу препоручити за издавање цинка и бакра из киселих индустриских растворова и отпадних вода.

(Примљено 11. септембра 2013, ревидирано 31. марта, прихваћено 1. априла 2014)

REFERENCES

1. A. P. Stavskiy, *Mineral Raw Materials: from the Bowels of the Earth to the Market. Non-Ferrous Metals*, Nauchny Mir, Moscow, 2011, pp. 125–141
2. A. I. Volkhin, E. I. Elisseev, V. P. Zhukov, B. N. Smirnov, *Anode and Cathode Copper*, Yuzhno-Uralskoe Knizhnoe Izdatel'stvo, Chelyabinsk, 2001, pp. 34–39
3. Y. V. Kolesov, L. F. Tazetdinova, A. I. Zagudaev, E. A. Stepanov, B. N. Smirnov, *A comparative analysis of technology of production of cathode copper from primary and secondary mineral raw materials*, in *Proceedings of the 4th International Congress “Non-Ferrous Metals – 2012”*, Krasnoyarsk, Russia, 2012, p. 88
4. A. D. Besser, *Ecological aspects of production of secondary zinc*. *Proceedings of the 1st International Congress “Non-Ferrous Metals in Siberia”*, Krasnoyarsk, Russia, 2009, p. 465
5. I. V. Kunilova, *PhD Thesis*, IPKON RAS, Moscow, 2007
6. I. F. Khudyakov, A. P. Doroshkevich, S. V. Karelov, *Metallurgy of Non-Ferrous Heavy Metals*, Nauka, Moscow, 1990, p. 275
7. G. S. Fomin, *Water: Control of Chemical, Bacterial and Radiation Safety in Accordance with International Standards*, Protektor, Moscow, 2010, pp. 156–192
8. N. S. Serpokkrylov, E. V. Vil'son, S. V. Getmantsev, A. A. Marochkin, *Ecology of Waste Water Purification by Physico-Chemical Methods*. Izdatel'stvo Assotsiatsii Stroitel'nykh Vusov, Moscow, 2008, pp. 3–68
9. S. N. Glyadenov, *Ekologiya I Promyshlennost Rossii* **9** (2001) 15
10. C. Binnie, M. Kimber, G. Smethurst, *Basic Water Treatment*. MPG Books, Bodmin, Cornwall, 2002, pp. 14–28
11. N. P. Cheremissinoff, *Handbook of Water and Wastewater Treatment Technologies*, Butterworth-Heinemann, Woburn, MA, 2002, pp. 5–91
12. P. A. Kozlov, L. A. Kazanbaev, A. V. Zatonskiy, V. F. Travkin, *Extraction-electrolysis Methods for Processing of Zinc Raw Materials*, Ruda I Metally, Moscow, 2008, pp. 12–55
13. T. Arko, S. Bartlett, K. Campbell, R. Lockett, L. Pettyjohn, S. Sparkman, *The Book on Effective Water Treatment*, HaloSource, Inc., Bothell, WA, 2009, pp. 25–78
14. F. R. Spellman, *Spellman's Standard Handbook for Wastewater Operators*, CRC Press, Taylor and Francis Group, Boca Raton, FL, 2011, pp. 56–243
15. M. Prascakova, M. Kusnierova, A. Luptakova, L. Ivaničova, *NATO Science for Peace and Security, series C: Environmental Security*, 2010, p. 259
16. R. Vulkan, U. Yermiyahu, U. Mingelgrin, G. Rytwo, T. V. Kinraide, *J. Membr. Biol.* **2002** (2004) 97
17. R. Shawabkeh, A. Al-Harahsheh, A. Al-Otoom, *Sep. Purif. Technol.* **40** (2004) 251
18. V. Sevel, A. Bilge, *J. Hazard. Mater.* **149** (2007) 226
19. M. S. Walud, A. G. Hatem, F. H. Nowar, *J. Eng.* **18** (2001) 1042
20. V. M. Ivanov, E. V. Antonova, E. N. Uskova, *Vestnik MGU, Seriya Khimiya* **50** (2009) 169
21. R. Z. Zeynalov, S. D. Tataeva, N. I. Ataeva, *Analitika I Kontrol* **17** (2013) 89
22. I. N. Parshina, A. V. Stryapkov, *Vestnik OGU* **5** (2003) 107
23. A. M. Akimbaeva, E. F. Ergozhin, A. D. Tovasarov, *Uspekhi Sovremennoogo Estestvoznaniya* **4** (2006) 27
24. L. A. Pimenova, E. L. Nesterova, *Fundamentalnye Issledoveniya* **4** (2008) 24
25. N. N. Basargin, E. R. Oskotskaya, A. V. Chebrova, Y. G. Rozovskiy, *Russ. J. Anal. Chem.* **63** (2008) 231
26. R. M. Alosmanov, *Vestnik MGU, Seriya Khimiya* **52** (2011) 145

27. L. K. Neudachina, A. V. Pestov, N. V. Baranova, V. A. Startsev, *Analitika I Kontrol* **15** (2011) 238
28. V. I. Podchanova, L. N. Simonova, *Analytical Chemistry of Copper*, Nauka, Moscow, 1990, pp. 62–66
29. V. P. Zhivopistsev, V. A. Seleznyova, *Analytical Chemistry of Zinc*, Nauka, Moscow, 1975, pp. 44–47
30. A. A. Drozdov, V. P. Zlomanov, F. M. Spiridonov, G. N. Mazo, *Inorganic Chemistry of Transition Elements*, Akademiya, Moscow, 2007, p. 197
31. F. A. Cotton, C. Wilkinson, *Advanced Inorganic Chemistry. A Comprehensive Text*, Wiley, New York, 1969, pp. 211–487
32. O. N. Kononova, N. V. Mikhaylova, A. M. Mel'nikov, Y. S. Kononov, *Desalination* **274** (2011) 150
33. F. Helfferich, *Ion Exchange*, McGraw Hill, New York, 1962, p. 481
34. Y. A. Kokotov, V. A. Pasechnik, *Ion Exchange Equilibrium and Kinetics of Ion Exchange*, Khimiya, Leningrad, 1979, p. 374
35. F. Helfferich, In *Ion Exchange. A Series of Advances*, J. A. Marinsky, Ed., McGraw Hill, Buffalo, New York, 1966, p. 281
36. D. C. Harris, *Quantitative Chemical Analysis*, W. H. Freeman, New York, 2007, pp. 51–64
37. J. H. Pollard, *Handbook of Numerical and Statistical Techniques*, Cambridge University Press, Cambridge, 1977, p. 374
38. K. B. Lebedev, E. I. Kazantsev, V. M. Rosmanov, V. S. Pakholkov, V. A. Chemezov, *Ion Exchangers in Non-Ferrous Metallurgy*, Metallurgiya, Moscow, 1975, pp. 219–254
39. R. M. Diamond, D. C. Whitney, In *Ion Exchange. A Series of Advances*, J. A. Marinsky, Ed., McGraw Hill, Buffalo, New York, 1966, p. 174
40. K. M. Saldadze, V. D. Kopylova-Valova, *Complex-forming Ion Exchangers*, Nauka, Moscow, 1980, p. 336
41. R. Hering, *Chelatbildende Ionenaustauscher*, Akademie-Verlag, Berlin, 1967, p. 268
42. G. V. Myasoedova, S. B. Savvin, *Chelate-forming Ion Exchangers*, Nauka, Moscow, 1984, p. 211
43. T. E. Mitchenko, N. V. Makarova, *Sorbtionnye I Khromatograficheskie Protsessy* **1** (2001) 56
44. Y. Y. Lurie, *Handbook on Analytical Chemistry*, Khimiya, Moscow, 1989, p. 479.